INVESTING THE MINERALOGY AND MORPHOLOGY OF SUBGLACIAL VOLCANOES ON EARTH AND MARS

by

Sheridan Elise Ackiss

A Dissertation

Submitted to the Faculty of Purdue University

In Partial Fulfillment of the Requirements for the degree of

Doctor of Philosophy

Department of Earth, Atmospheric, & Planetary Sciences

West Lafayette, Indiana

May 2019

THE PURDUE UNIVERSITY GRADUATE SCHOOL
STATEMENT OF COMMITTEE APPROVAL

Dr. Darryl Granger, Chair
Department of Earth, Atmospheric, and Planetary Sciences
Dr. Briony Horgan, Advisor
Department of Earth, Atmospheric, and Planetary Sciences
Dr. Michelle Thompson
Department of Earth, Atmospheric, and Planetary Sciences
Dr. Joseph Michalski
Department of Earth Sciences, The University of Hong Kong

Approved by:
Dr. Darryl Granger
Head of the Graduate Program

This Dissertation is Dedicated to:

My grandparents, Guy and Evelyn Keenum.

Thank you for instilling in me a love of learning and a respect for education.

ACKNOWLEDGMENTS

It takes a village.

I am excited to introduce this thesis with these acknowledgements. It's the one place where I'll be able to speak colloquially and pay gratitude for those who I truly could not have done this without. There's a lot so hang on tight!

Perhaps the most important people that need to be mentioned are my family members. This body of work is dedicated to them but I think they also deserve to be thanked and acknowledged. My grandfather, **Lieutenant Commander Guy Keenum**, was the person who instilled the importance of education in me. I distinctly remember being shamed in the living room for not making the Honor Roll when it was announced in our town's local newspaper. Thank you, Pop. I miss you with literally all of me and I did this for you. There were so many times when I wanted to quit but I made you a promise that I had to keep. My grandmother, **Mrs. Evelyn Radford Keenum**, gave me all the spunk and fire I needed to keep the promise that I made Pop. I remember driving everywhere with Nana as she asked me math questions and had me "do it in my head" even when I was convinced that I absolutely could not. Thank you for the push and for believing in me. My aunts and uncles, **Mr. Robert Keenum, Dr. Deborah Keenum, Dr. Amy Keenum, Dr. Robert Wittig, Lieutenant Colonel Karen Schwartz, and Major Phil Schwartz**, paved the way for me to be successful by being the most badass and successful people I know. I am thankful to have been raised around them. My cousins were and continue to be the siblings I never had. They inspired me to keep going with my education as I humbly accepted that I was someone they looked up to. Here's to you: **Mr. Clint Garrett, Mr. Ian Garrett, (soon-to-be) Dr. Ishi Keenum, Mr. Guy Keenum, Mr. Elo Wittig,** and **Ms. Elise Keenum**. I love you all more than you could possibly know.

For family, there's one more person who I believe deserves an entire paragraph to show how incredibly amazing he truly is. To the man that I will soon call my husband, **Mr. Tucker Moore**, I wholeheartedly believe that I would not be where I am today without you. You saved me. You made me a better person - the person I always wanted to be. You showed me what unconditional love looks like. I am sorry for grad school. Grad school is the absolute worst. But look at us now. I am so excited for our future. Thank you and I love you.

Professionally, it was my time at NASA Goddard Space Flight Center that convinced me that I was capable of being a scientist… and gasp… going to graduate school. This was a concept I'd never before thought of but in the company of those people, it felt possible. I surely would not be writing this today if it weren't for **Dr. David Chuss, Dr. Karwan Rostem, and Dr. Nate Lourie**. To Dave, thank you for believing in me, even when I didn't believe in myself and for investing your time in, what I am sure seemed like, an unlikely candidate for the job. To Karwan, thank you for teaching me to never use the word "countless" in a manuscript and for always being honest. Your honesty with my writing, my research, and my weight (lol) has always been truly appreciated. To Nate, thank you for teaching me the ways of the lab. Without you, I would have been lost and unsuccessful.

It's a small world, the one we live in. If it weren't for my connection with Dave, I wouldn't have been able to work with **Dr. James Wray** at the Georgia Institute of Technology. To James, thank you for showing me that there existed a niche in which I belonged. Thank you for investing all of your time (quite literally – sorry about those 2-3 hour long meetings I always kept you in!) in actually teaching me. Your presence at Georgia Tech is/was a breath of fresh air for me. You were a light in that very dark tunnel that was Tech. #IGotOut #GoJackets!

James hooked me up with the best job I could have ever asked for post-graduation. After trying to convince me that I "really should just email the Principal Investigator of the Mars Reconnaissance Orbiter (MRO) Compact Reconnaissance Imaging Spectrometer for Mars (CRISM) because it's no big deal" (ummmm, oh, yeah, ok James… that's a huge deal!) and me saying "Yeah… ok… I'll do that tomorrow" and finally James just emailing him for me, I got a job at the Johns Hopkins University Applied Physics Laboratory with **Dr. Scott Murchie**. But a job with Scott isn't just a job with Scott. I was also fortunate enough to work with **Dr. Kim Seelos, Dr. Frank Seelos,** and **Dr. Debra Buczkowski**. To Scott, you are the epitome of the "Best Boss Ever." Thank you for being open, receptive, supportive, and humble. Whether you knew it or not, you played a very important role in my life – one that ranged from boss to father figure to friend. I hope that I can one day be like you and I do not say that lightly. To Kim, thank you for being you. I am not really sure how to put into words what I appreciate about you. I look at you and I think "That could be me." I think you have such a perfect life – a beautiful family, a great job, a heart of gold, and you're pretty funny. :) If you and I were at the same places in our lives, I'd make you my very best friend. To Frank, thank you for teaching me about things that I

never thought I'd be able to comprehend and for trusting in my abilities. I know you weren't officially one of my mentors… but let's admit it, you basically were! To Debra, thank you for showing me what a strong woman in our field looks like. You are a badass. I channeled your strength through grad school and let me just say "THANK YOU" because I needed that!

Frank put me in touch with **Dr. Briony Horgan** who would become my advisor at Purdue University. But I think it was fate that honestly brought us together. A few years prior to my official introduction to Briony, I was talking to a graduate student at Georgia Tech who said, "You know, you really should work with Briony. She would be the perfect advisor for you. It's just too bad she's not a professor." And then, BAM! There she was, a professor, right when I needed an advisor. To Briony, thank you for letting me be me. I know I am strong-willed and sassy and quite honestly, way too much to handle sometimes, but you let me be exactly what I needed to be to get through graduate school. I am forever grateful for that. You also made me an exponentially better writer.

To those who professionally impacted me but weren't advisors, you deserve just as much acknowledgement. To **Dr. Richard Tollo** and **Dr. Ken Ridgway**, thank you both for never laughing at my silly geology questions. You two became the definition of a "safe space" for me at George Washington and Purdue, respectively. You two are truly the best professors I have ever been lucky enough to have. To **Dr. Jon Harbor**, you were the person I needed to meet to finish graduate school. I would have quit if it wasn't for you. Thank you. To **Dr. Stephanie Masta Zywicki**, you taught me that it is most definitely the right thing to stand up for what you believe in. You always make me feel like I am making the right move, even when those moves felt very wrong.

To the administrative staff of the Purdue EAPS Department, there are two people that deserve big shout-outs. Thank you to **Dr. Barbara Gibson** for finding round-about ways for me to get teaching experience and for the secret meetings we had in your office. They really helped me out and made me feel like I was part of the resistance. To **Ms. Stacie Cordell**, thank you for being my go to gal! But really though. Literally from before Day 1, you were helping me out with all things financial and Purdue. You are an absolute gift to the department and they honestly do not deserve you. Much love to you, lady.

And to my "work friends" who I made along this crazy ride. **Dr. Hannah Susorney**, you are forever my life partner – even if you are married and we are oceans apart. To **(soon-to-be)**

Dr. Morgan Shusterman and **(soon-to-be) Dr. Mallory Kinczyk**, without you guys, I'd have to actually attend the meetings at conferences… who even does that? Thank you for also showing me that this experience is not as isolating as the gatekeepers try to make it. We have each other. We got this. **Dr. Tommy Lovell** and **Dr. Haylee Dickinson-Lovell**, I definitely would have quit grad school if it weren't for you two telling me how it goes each step of the way and for always supporting me and giving me a (metaphorical) shoulder to (actually) cry on. **Dr. Tim Berry**, thank you for walking through the shadows of darkness with me. You're a true friend. **(Soon-to-be) Dr. Jordyn Miller**, you are the yin to my yang and I appreciate every part of your soul. You have taught me so much and changed me for the better. To my girl gang: **(soon-to-be) Dr. Megan Saalfeld** and **Ms. Jess McGuire**… I actually don't think I can put into words what you two have become to me. I could try but it would be just… such a joke. You guys are my people. I am so excited to venture through this life with you two and for our annual meet ups in the most exotic locations.

So, there you have it. These people are my village. And I absolutely could never thank them enough.

TABLE OF CONTENTS

LIST OF TABLES

LIST OF FIGURES

ABSTRACT

Author: Ackiss, Sheridan, E. PhD
Institution: Purdue University
Degree Received: May 2019
Title: Investing the Mineralogy and Morphology of Subglacial Volcanoes on Earth and Mars
Committee Chair: Briony Horgan

In this dissertation, we have examined mineral assemblages and geomorphologic features in the Sisyphi Planum region of Mars, as well as examined the mineral assemblage of palagonite in Iceland. Chapter 2 is focused on the mineral assemblages detected on possible glaciovolcanic edifices in the Sisyphi Planum region of Mars. Minerals were identified utilizing visible/near-infrared orbital spectra from the Compact Reconnaissance Imaging Spectrometer for Mars (CRISM). Analysis of eleven CRISM images located on the volcanic edifices revealed three distinct spectral classes in the region which are interpreted to be: gypsum-dominated, smectite-zeolite- iron oxide-dominated (possibly palagonite), and polyhydrated sulfate-dominated material. The possible palagonite detections on the volcanic edifices, the geomorphology of the region, and the analogous terrestrial mineralogy of subglacial eruptions strongly suggests the formation of these minerals during subglacial eruptions or associated hydrothermal systems. This implies that thick water ice sheets were present in this region in the late Noachian or early Hesperian, and that the subglacial hydrothermal systems could have supported habitable environments with excellent biosignature preservation potential. Chapter 3 is focused on evaluating the variability of the composition and crystallinity of palagonite on Earth in order to inform efforts to identify it on Mars. We hypothesized that variability in palagonite composition and crystallinity could occur due to differences in environmental conditions during formation. Palagonite samples were collected in Iceland at subglacial volcanic sites around Reykjavík in the Western Volcanic Zone, on the southern coast in the Eastern Volcanic Zone, and from the Herðubreið tuya and Askja volcano in the Northern Volcanic Zone. Visible/near-infrared reflectance spectroscopy, thermal-infrared emission spectroscopy, and quantitative XRD were used to assess the bulk mineralogy, crystallinity, and clay composition of all samples. Results show the sampled palagonites contain partially devitrified glass, unaltered glass, and secondary minerals including clay minerals, poorly crystalline ferric oxides, and zeolites. However, one

sample (SCoast01) shows a vastly different mineral assemblage in all sample techniques, including well-crystalline Fe/Mg-clays as opposed to the poorly-crystalline Al-clays observed in our other samples. Based on previous studies of subaqueous palagonites and the location this sample was collected from, we hypothesize that the SCoast01 sample was formed in a submarine environment rather than subglacial. This suggests that it may be possible to differentiate submarine vs. subglacial palagonite on Earth based on composition and from remote sensing observations on Mars. Chapter 4 is a geomorphologic study of the Sisyphi Planum region of Mars where we identified and classified the tops of the Sisyphi Montes as well as geomorphologically mapped the Sisyphi Planum region. Here, we address an overarching question: What is the relationship between the Sisyphi Montes and the ice in this region? To do this, we identified 106 edifices in the region and classified them into five categories: 1) flat topped, 2) rounded tops, 3) sharp peaks, 4) cratered peaks, and 5) height less than 300 meters – a "catch-all" category for all features below the specified height, which exhibit less distinctive morphologies in MOLA topography. While many of the edifices could be sub-glacial in origin, we find that the only morphologic class that exhibits uniquely subglacial morphologies are the flat-topped edifices. These edifices are similar to terrestrial tuyas, which form when a subglacial volcano breaches an ice sheet and erupts a plateau of sub-aerial lavas. Based on the geomorphologic map and topographic data, we have shown that flat-topped edifices are all located outside of regions that we map as the Mantled Unit, which we infer to be related to the Dorsa Argentina Formation. The combination of the flat topped edifices and their location outside of the mapped ice-related regions strongly suggests that the ice in the region was once more extensive than what is currently observed. While this has been proposed in the past, it has not been documented how far the ice sheet could have extended. Here we show that the ice must have extended to at least as far as the flat topped edifices in the region. The combination of these chapters using both mineralogy and morphology suggest that the Sisyphi Planum region of Mars was subglacial in origin.

CHAPTER 1. INTRODUCTION

The paleoclimate of Mars, whether it was "warm and wet" or "cold and icy", has been highly debated [*Pollack et al.*, 1987; *Baker and Strom*, 1991; *Squyres and Kasting*, 1994; *Haberle*, 1998; *Craddock and Howard*, 2002; *Gaidos and Marion*, 2003; *Sackmann and Boothroyd*, 2003; *McEwen et al.*, 2007; *Fairén*, 2010; *Head*, 2013; *Head and Marchant*, 2014; *Cassanelli and Head*, 2015; *Fastook and Head*, 2015; *Wordsworth et al.*, 2015]. The presence of features made by water such as valley networks, inverted channels, and Glacier-Like Features have been used to show that the history of water on Mars could have been frozen or liquid, supporting both sides of this climatic argument [*Kargel and Strom*, 1992; *Gulick*, 2001; *Harrison and Grimm*, 2002; *Malin and Edgett*, 2003; *Mangold et al.*, 2004; *Arfstrom and Hartmann*, 2005; *Forget et al.*, 2006].

In addition to water, volcanism has also been used to investigate the martian paleoclimate. The problem of the "faint young sun," where the sun was too faint to be capable of producing enough heat to warm a plant, has pushed the addition of volcanic outgassing into the atmosphere to explore the probability of liquid water on the surface [*Pollack et al.*, 1987; *Haberle*, 1998; *Jakosky and Phillips*, 2001; *Halevy et al.*, 2007; *Halevy and Head*, 2014]. The interaction between water, volcanism, and the possible climatic shift that happened when both of these processes were active has raised many questions: 1) What environment did volcanism happen in?; 2) Was the water liquid, frozen, or not present during volcanic events?; and 3) What kind of landscapes did these processes leave behind? Understanding these questions is critical for investigating the evolution of early Mars and its paleoclimate.

While the "warm and wet" Mars hypothesis has been studied in detail, the "cold and icy" Mars hypothesis still has some fundamental knowledge gaps. One of the biggest unknowns in this hypothesis is: Are the volcanic morphologies and mineralogies of Noachian Mars consistent with volcanism on a "snowball Mars"? One way to answer this question is to study the Sisyphi Planum region of Mars, a Noachian-aged region nestled between the Argyre and Hellas basins near the south pole. This region contains the Sisyphi Montes, which are edifices interpreted to be subglacial volcanoes [*Ghatan and Head*, 2002], so understanding the processes that shaped this region will address key questions about the relationship between water and volcanism. The primary objective of this body of work is to determine whether or not the Sisyphi Montes are consistent with subglacial volcanism by examining mineral assemblages and morphologies from orbit using three specific tasks (each forming a separate chapter):

1) Characterize the spectral signatures of the Sisyphi Montes, Mars edifices and use inferred mineral assemblages from the terrestrial literature to test the hypothesis of whether or not the edifices were formed subglacially.

2) Characterize the mineralogy of subglacial Icelandic palagonite by using a combination of laboratory techniques to compare and contrast to mineralogic findings on Mars from Chapter 1.

3) Geomorphologic mapping and analysis of the Sisyphi Montes region of Mars by using a multitude of remote sensing datasets to characterize the overall geology of the region.

This research will provide the first assessment of the compositional and mineralogical diversity of subglacially-formed palagonites on Earth, as well as the first comprehensive geomorphologic map of the Sisyphi Montes region, helping to constrain the paleoclimate of the martian south polar region. These results will provide novel insight into regional volcanic and glacial processes.

1.1 Background and Relevant Studies

1.1.1 Overview of Subglacial Volcanism

Subglacial volcanoes on Earth are formed through complex processes. Single vent eruptions lead to flat-topped, steep-sided edifices (often referred to as tuyas or table mountains), while multiple vent eruptions that create long linear ridges are called tindars. Subglacial eruptions can be composed of both rhyolitic and basaltic magmas [*Tuffen et al.*, 2002, 2007; *Jakobsson and Gudmundsson*, 2008; *Benn and Evans*, 2014]. Volcanic eruptions in this environment create a unique stratigraphic sequence of three lithostratigraphic units, which was originally defined within the Móberg Formation in Iceland. The basal unit is composed of fragmented subaqueous pillow lavas, which is overlain by a middle unit composed of hyaloclastite: an altered, vesicular, and glassy hydroclastic tephra of basaltic and intermediate composition. These are both overlain by the top unit of subaerial lava flows, although this unit is not always present [Tuffen, 2007; Jakobsson and Gudmundsson, 2008].

The basal unit is thought to be formed between 100 and 500 meters below the ice surface under pressures ranging from 1-2 MPa and greater than 5 MPa [*Moore and Schilling*, 1973; *Gudmundsson et al.*, 2004]. Pillow lava is usually emplaced when there is a high confining pressure [*Gudmundsson et al.*, 2004; *Tuffen*, 2007; *Jakobsson and Gudmundsson*, 2008] which suppresses vesiculation and explosivity [*Zimanowski et al.*, 1997]. Because of the high confining pressure, the edifice made of pillow lavas is surrounded by a very thin layer of meltwater (the water created from the heating of the ice). The layer is so thin that the eruption is forced to be made intrusively, where the fed magma is quenched inside the edifice and does not interact with the meltwater. Because the meltwater is only interacting with the mostly hardened pillow lavas, the melting rate of the surrounding ice will be much slower [*Tuffen*, 2007]. At this stage, the surface ice is mostly smooth and non-responsive to the activity below [*Gudmundsson et al.*, 2004].

As the meltwater reservoir expands, the water pressure is greatly reduced [*Höskuldsson and Sparks*, 1997; *Jakobsson and Gudmundsson*, 2008] and the eruption transitions into a highly explosive Surtseyan eruption [*Gudmundsson et al.*, 2004; *Tuffen*, 2007]. This creates the next unit, which is made of hyaloclastites (hydrated tuff-like breccias) and hyalotuffs (explosively formed fragments of glass) [*Smellie and Skilling*, 1994; *Benn and Evans*, 2014]. This transition in eruption type occurs due to the low amount of magma discharge [*Tuffen*, 2007]. The hyaloclastites spread and create a larger surface area allowing rapid heat loss. Heat is then easily transferred into the meltwater reservoir [*Zimanowski et al.*, 1997], further melting the surrounding ice and continuously growing the meltwater reservoir. Steam is sometimes present [*Tuffen et al.*, 2002]. At this stage, the surface ice begins to act brittle and creates concentric fractures that cave in towards the meltwater reservoir. This is referred to as the ice cauldron [*Gudmundsson et al.*, 2004].

Eventually, the meltwater reservoir becomes so large that the ice cauldron collapses inward towards the edifice, exposing the meltwater reservoir and allowing the breach of both the reservoir and the explosive lava, releasing plumes of gasses and jets of hyaloclastites [*Smellie*, 2001; *Gudmundsson et al.*, 2004]. As the meltwater pours out of the opened ice cauldron, the water dissipates across the surface of the ice causing the Surtseyan eruption to halt and the Hawaiian eruption to start [*Gudmundsson et al.*, 2004; *Jakobsson and Gudmundsson*, 2008; *Benn and Evans*, 2014]. The Hawaiian eruption builds the final unit in the Móberg Formation: the subaerial flows. It is these final top flows that create the classic flat-topped shape of the tuya. In addition to flowing over the surface of the ice, the meltwater can also be released at the basal layer, flowing along the contact of the ice and the bedrock. If the basal water pressure is too high, a rapid release of meltwater will occur causing a jökulhlaup (a glacial outburst flood). It is important to note that the dissipated meltwater washes away less than 10% of the erupted products [*Gudmundsson et al.*, 2004].

Glaciovolcanic environments are high-energy and unstable, causing the creation of variable morphologies. The stratigraphic sequence that is created is also variable depending on the thickness of the ice, the explosivity of the magma, and the amount of ice that is able to be melted [*Russell et al.*, 2014].

1.1.2 Palagonite in Subglacial Volcanism and its Role as a Martian Analog

Palagonite is the first stable product of glass alteration at high water: rock ratios and low hydothermal temperatures (typically <120°C). It is a mixture of different mineral phases including clays, zeolites, and oxides and is initially amorphous [*Allen et al.*, 1981; *Morris et al.*, 1990; *Stroncik and Schmincke*, 2002; *Michalski et al.*, 2005]. Palagonitized outcrops (pillow basalts and hyaloclastites) are usually yellow to brown in color and look vastly different from fresh black basalt. Palagonite is thought to form from a dissolution-precipitation process of glass where the primary material is dissolved and the secondary phases are precipitated out. As palagonite ages, it evolves into gel-palagonite. Gel-palagonite is still amorphous and made of concentric layers. Gel-palagonite later evolves into fibro-palagonite, which is a mixture of amorphous gel-palagonite and crystallized smectites [*Stroncik and Schmincke*, 2002]. However, the formation, evolution, and mineralogic composition of palagonite is still highly debated.

Subglacial volcanoes form from different magma sources [*Tuffen et al.*, 2002; *Tuffen*, 2007; *Benn and Evans*, 2014] and within environments with variable water chemistries [*Gudmundsson et al.*, 2004; *Jakobsson and Gudmundsson*, 2008], causing the mineralogic composition of palagonite to vary with each specific volcano that it is formed in/near. While some studies have shown that palagonites from both hyaloclastites and hyalotuffs are similar in texture and composition [*Drief and Schiffman*, 2004] and all subglacially-formed hyalotuffs are ubiquitously palagonitized [*Jones*, 1968; *Furnes*, 1978], others have shown that there are mineralogic differences as seen in visible and near-infrared spectroscopy [*Farrand et al.*, 2016], X-ray diffractograms [*Warner and Farmer*, 2010], electron microprobe, and scanning electron microprobe measurements [*Massey*, 2017].

Icelandic and Hawaiian materials, most commonly palagonite, have long been used as an analog to martian soil. Mars is a basaltic sedimentary planet [*Malin and Edgett*, 2000] with evidence for both volcanic and alteration processes. It is hypothesized to have had weathering conditions similar to those on Earth [*Golden et al.*, 1993]. Because of this, as well as based on the visible/near-infrared spectral properties and geochemistry of martian soils measured by Pathfinder, palagonite has been used as a "classic" or "ideal" analog to martian soil [*Farrand and Singer*, 1992; *Golden et al.*, 1993; *Cooper and Mustard*, 2001; *Bishop et al.*, 2002; *Warner and Farmer*, 2010; *Cousins et al.*, 2013]. *Farrand and Singer* [1992] determined that visible and near-infrared spectroscopy is sensitive to hydration and palagonite content in basaltic tephra. Later, *Bishop et al.*, [2002a] showed that Icelandic palagonite tuffs shared similar spectral absorptions to the bright martian soils measured by Pathfinder and the martian dust measured by Mariner missions. This type of spectroscopy is now one of the main methods used to determine mineralogy on Mars from orbit [*Bibring et al.*, 2004; *Murchie et al.*, 2007].

However, this use of palagonite as a Mars analog material is based on a limited range of observations and a poor understanding of how palagonite forms. Indeed, martian soil is unlikely to actually be palagonite. Thermal emission spectroscopy studies show that the modeled assemblages for the surface are more consistent with a silicate mineral, such as a plagioclase feldspar (or a mineral with a similar crystallographic structure), than with a palagonite based on a transparency feature at ~825cm^{-1} [*Ruff and Christensen*, 2002]. In addition, a martian surface covered mostly in palagonite isn't consistent with observed spectral or morphologic features of the planet. A palagonite-covered Mars would resemble Iceland, where palagonite outcrops are widespread [*Jakobsson and Gudmundsson*, 2008]. Instead, morphologic features consistent with subglacial/submarine environments are seen only in a few locations [*Ghatan and Head*, 2002; *Rampey et al.*, 2007; *Martínez-Alonso et al.*, 2011; *Scanlon et al.*, 2014] and after 12 years in orbit, the Mars Reconnaissance Orbiter (MRO) Compact Reconnaissance Imaging Spectrometer for Mars (CRISM) [*Murchie et al.*, 2007] has yet to definitely identify palagonite on the surface. The confident identification of palagonite on Mars would be a signature of subaqueous and/or subglacial volcanism, rather than just low-temperature weathering of basalt.

1.1.3 The Sisyphi Montes Region of Mars

The Sisyphi Montes (55-75^{0}S and 35-345^{0}E) are a group of over 100 isolated edifices within Sisyphi Planum [*Campbell et al.*, 2016], a region of low and smooth topography located between the Argyre and Hellas impact basins. A subset of the Sisyphi Montes are located within the Dorsa Argentea Formation (DAF) – a unit hypothesized to be the remnant of an ancient middle-Hesperian ice sheet of unknown composition [*Tanaka and Scott, D.L.*, 1987; *Wordsworth et al.*, 2013]. The DAF is composed of pitted terrains, sinuous ridges, and plains units with lobate margins [*Tanaka and Scott, D.L.*, 1987; *Head and Pratt*, 2001; *Kolb and Tanaka*, 2001] and covers a combined area of ~1.5x10^6 km^2 [*Head and Pratt*, 2001] north and west of the south pole.

MARSIS (Mars Advanced Radar for Subsurface and Ionospheric Sounding) [*Picardi et al.*, 2004] detections of shallow subsurface ice interfaces in this area are highly correlated with the DAF, suggesting remnant subsurface ice is still present within the formation [*Plaut et al.*, 2007]. This ice is generally assumed to be water ice, although the composition, whether CO_2 or H_2O ice, has not been directly confirmed [*Tanaka and Scott, D.L.*, 1987; *Ghatan and Head*, 2002; *Plaut et al.*, 2007; *Carr and Head*, 2010; *Wordsworth et al.*, 2013]. If the Sisyphi Montes were formed as subglacial volcanoes, this would suggest that either the DAF or an earlier ancient ice sheet extended throughout the Sisyphi Montes region [*Plaut et al.*, 2007; *Scanlon and Head*, 2014].

The Sisyphi Montes initially included 17 high and rugged mountainous edifices [*Tanaka and Scott, D.L.*, 1987] mapped primarily within the DAF [*Tanaka and Scott, D.L.*, 1987; *Head and Pratt*, 2001; *Kolb and Tanaka*, 2001]. Due to limited image resolution, the age and origin of the edifices could not be determined. Later studies expanded the number of edifices to 22 [*Ghatan and Head*, 2002] and examined three possible origins related to impact cratering, tectonism, and volcanism. Based on the unique steep-sided, flat-topped morphology of the edifices, *Ghatan and Head* [2002] hypothesized that the edifices were volcanoes that formed subglacially, erupting underneath an extensive, possibly Hesperian-aged, ice sheet. Further studies expanded the volcano count yet again to >40 features [*Rodriguez and Tanaka*, 2006], classifying the structures based on their morphology and proximity to both the Sisyphi Planum and Hellas basin. Because some of the Sisyphi Montes structures are encircled by local moat-like features with raised rims, *Rodriguez and Tanaka* [2006] hypothesized that the edifices were formed due to a combination of volcanic and impact-related processes. Based on the close proximity of the Sisyphi Montes to the Hellas basin, they proposed that the magma that created the structures was sourced from magma bodies intersecting large impact-induced zones of crustal weakness circumferential to the Hellas basin. These zones then caused sub-crustal fault zones and the structures themselves were made from enhanced volcanic activity from subsequent smaller impacts.

The two main hypotheses for the formation of the edifices in the Sisyphi Montes region have been based on morphologic studies. *Ghatan and Head* [2002] proposed a subglacial origin while *Rodriguez and Tanaka* [2006] proposed an impact-induced subaerial origin. Visible/near-infrared spectral surveys have revealed that the Sisyphi Montes exhibit spectral signatures consistent with polyhydrated sulfates [*Wray et al.*, 2009]. These signatures are correlated with the presence of boulders in high-resolution imagery, and are attributed to either volcanic hydrothermal or acid fog alteration [*Wray et al.*, 2009; *Ackiss and Wray*, 2014]. A more recent mineralogic survey of the southern high latitudes showed that while hydrated sulfates and other hydrated phases of unknown composition are widespread, the sulfate signatures within Sisyphi Planum are strongest on the Sisyphi Montes. This observation suggests that the sulfates may have been produced in association with volcanic activity and later transported into the surrounding plains [*Ackiss and Wray*, 2014].

1.1.4 Significance

This research emphasizes the importance in understanding the history of the Sisyphi Montes region, a region that played a part in the history of ice near the martian south pole. It provides regional information about the Dorsa Argentea Formation, as well as surrounding volcanic features. Overall, the work here strives to answer the questions:

1) Is the mineralogy of the Sisyphi Montes region consistent with a subaerial, submarine, or subglacial origin?
2) Can the spectral variability of Icelandic palagonites be used to constrain the identification of palagonite on the martian surface?
3) What formation environments are the features surrounding the Sisyphi Montes edifices consistent with?

4) Are the volcanic morphologies and mineralogies of Noachian Mars consistent with volcanism on a "snowball Mars"?

In particular, this research will provide new information pertaining to the martian paleoclimate, possibly helping to address the validity of the current "warm and wet" [*Craddock and Howard*, 2002] and "cold and icy" [*Wordsworth et al.*, 2013, 2015] climate models. The results from this study will provide novel insight into regional volcanic and glacial processes.

1.2 References

Ackiss, S. E., and J. J. Wray (2014), Occurrences of possible hydrated sulfates in the southern high latitudes of Mars, Icarus, 243, 311–324, doi:10.1016/j.icarus.2014.08.016.

Allen, C. C., J. L. Gooding, M. Jercinovic, and K. Keil (1981), Altered basaltic glass: A terrestrial analog to the soil of Mars, Icarus, 45(2), 347–369, doi:10.1016/0019-1035(81)90040-3.

Arfstrom, J., and W. K. Hartmann (2005), Martian flow features, moraine-like ridges, and gullies: Terrestrial analogs and interrelationships, Icarus, 174(2), 321–335, doi:10.1016/j.icarus.2004.05.026.

Baker, V. R., and R. G. Strom (1991), Ancient oceans, ice sheets and the hydrological cycle on Mars, Nature, 352(6336), 589.

Benn, D., and D. J. A. Evans (2014), Glaciers and Glaciation, 2nd Edition, Routledge, London and New York.

Bibring, J.-P. et al. (2004), OMEGA: Observatoire pour la Minéralogie, l'Eau, les Glaces et l'Activité, vol. 1240, pp. 37–49.

Bishop, J. L., P. Schiffman, and R. Southard (2002), Geochemical and mineralogical analyses of palagonitic tuffs and altered rinds of pillow basalts in Iceland and applications to Mars, Geol. Soc. Lond. Spec. Publ., 202(1), 371–392, doi:10.1144/GSL.SP.2002.202.01.19.

Campbell, A., S. Ackiss, and B. H. Horgan (2016), Morphology of possible subglacial volcanoes in the Sysphi Montes region of Mars, vol. 47, p. 1554.

Carr, M. H., and J. W. Head (2010), Geologic history of Mars, Earth Planet. Sci. Lett., 294(3), 185–203.

Craddock, R. A., and A. D. Howard (2002), The case for rainfall on a warm, wet early Mars, J. Geophys. Res. Planets, 107(E11).

Cooper, C. D., and J. F. Mustard (2001), TES Observations of the Global Distribution of Sulfate on Mars, vol. 32, p. 2048.

Cousins, C. R. et al. (2013), Glaciovolcanic hydrothermal environments in Iceland and implications for their detection on Mars, J. Volcanol. Geotherm. Res., 256, 61–77, doi:10.1016/j.jvolgeores.2013.02.009.

Drief, A., and P. Schiffman (2004), Very Low-Temperature Alteration of Sideromelane in Hyaloclastites and Hyalotuffs from Kilauea and Mauna Kea Volcanoes: Implications for the Mechanism of Palagonite Formation, Clays Clay Miner., 52(5), 622–634, doi:10.1346/CCMN.2004.0520508.

Fairén, A. G. (2010), A cold and wet Mars, Icarus, 208(1), 165–175, doi:10.1016/j.icarus.2010.01.006.

Farrand, W.H., Wright, S.P., Rogers, A.D., Glotch, T.D., 2016. Basaltic glass formed from hydrovolcanism and impact processes: Characterization and clues for detection of mode of origin from VNIR through MWIR reflectance and emission spectroscopy. Icarus 275, 16–28.

Farrand, W. H., and R. B. Singer (1992), Alteration of hydrovolcanic basaltic ash: Observations with visible and near-infrared spectrometry, J. Geophys. Res. Solid Earth, 97(B12), 17393–17408.

Fastook, J. L., and J. W. Head (2015), Glaciation in the Late Noachian Icy Highlands: Ice accumulation, distribution, flow rates, basal melting, and top-down melting rates and patterns, Planet. Space Sci., 106, 82–98.

Forget, F., R. M. Haberle, F. Montmessin, B. Levrard, and J. W. Head (2006), Formation of glaciers on Mars by atmospheric precipitation at high obliquity, science, 311(5759), 368–371.

Furnes, H. (1978), Element mobility during palagonitization of a subglacial hyaloclastite in Iceland, Chem. Geol., 22, 249–264, doi:10.1016/0009-2541(78)90034-7.

Gaidos, E., and G. Marion (2003), Geological and geochemical legacy of a cold early Mars, J. Geophys. Res. Planets, 108(E6), 5055, doi:10.1029/2002JE002000.

Ghatan, G. J., and J. W. Head (2002), Candidate subglacial volcanoes in the south polar region of Mars: Morphology, morphometry, and eruption conditions, J. Geophys. Res. Planets, 107, 5048, doi:10.1029/2001JE001519.

Golden, D. C., R. V. Morris, D. W. Ming, H. V. Lauer, and S. R. Yang (1993), Mineralogy of three slightly palagonitized basaltic tephra samples from the summit of Mauna Kea, Hawaii, J. Geophys. Res. Planets, 98(E2), 3401–3411, doi:10.1029/92JE02590.

Gudmundsson, M. T., F. Sigmundsson, H. Björnsson, and T. Högnadóttir (2004), The 1996 eruption at Gjálp, Vatnajökull ice cap, Iceland: efficiency of heat transfer, ice deformation and subglacial water pressure, Bull. Volcanol., 66(1), 46–65, doi:10.1007/s00445-003-0295-9.

Gulick, V. C. (2001), Origin of the valley networks on Mars: A hydrological perspective, Geomorphology, 37(3), 241–268.

Haberle, R. M. (1998), Early Mars climate models, J. Geophys. Res., 103(28), 467–479.

Halevy, I., M. T. Zuber, and D. P. Schrag (2007), A Sulfur Dioxide Climate Feedback on Early Mars, Science, 318(5858), 1903–1907, doi:10.1126/science.1147039.

Halevy, I., and J. W. Head (2014), Episodic warming of early Mars by punctuated volcanism, Nat. Geosci., 7(12), 865–868, doi:10.1038/ngeo2293.

Harrison, K. P., and R. E. Grimm (2002), Controls on Martian hydrothermal systems: Application to valley network and magnetic anomaly formation, J. Geophys. Res. Planets, 107(E5), 1–1, doi:10.1029/2001JE001616.

Head, J. (2013), The Early Climate History of Mars: “Warm and Wet” or “Cold and Icy”?, vol. 15, pp. EGU2013-10106.

Head, J. W., and D. R. Marchant (2014), The climate history of early Mars: insights from the Antarctic McMurdo Dry Valleys hydrologic system, Antarct. Sci., 26(06), 774–800.

Head, J. W., and S. Pratt (2001), Extensive Hesperian-aged south polar ice sheet on Mars: Evidence for massive melting and retreat, and lateral flow and ponding of meltwater, J. Geophys. Res. Planets, 106(E6), 12275–12299, doi:10.1029/2000JE001359.

Höskuldsson, A., and R. S. J. Sparks (1997), Thermodynamics and fluid dynamics of effusive subglacial eruptions, Bull. Volcanol., 59(3), 219–230, doi:10.1007/s004450050187.

Jakobsson, S., and M. Gudmundsson (2008), Subglacial and intraglacial volcanic formations in Iceland, Jökull, 58, 179–196.

Jakosky, B. M., and R. J. Phillips (2001), Mars’ volatile and climate history, Nature, 412(6843), 237–244, doi:10.1038/35084184.

Jones, J. G. (1968), Intraglacial volcanoes of the Laugarvatn region, south-west Iceland—I, Q. J. Geol. Soc., 124(1–4), 197–211, doi:10.1144/gsjgs.124.1.0197.

Kolb, E. J., and K. L. Tanaka (2001), Geologic History of the Polar Regions of Mars Based on Mars Global Surveyor Data. II. Amazonian Period, Icarus, 154, 22–39, doi:10.1006/icar.2001.6676.

Malin, M. C., and K. S. Edgett (2000), Sedimentary Rocks of Early Mars, Science, 290(5498), 1927–1937, doi:10.1126/science.290.5498.1927.

Malin, M. C., and K. S. Edgett (2003), Evidence for persistent flow and aqueous sedimentation on early Mars, Science, 302(5652), 1931–1934.

Mangold, N., C. Quantin, V. Ansan, C. Delacourt, and P. Allemand (2004), Evidence for precipitation on Mars from dendritic valleys in the Valles Marineris area, Science, 305(5680), 78–81.

Martínez-Alonso, S., M. T. Mellon, M. E. Banks, L. P. Keszthelyi, and A. S. McEwen (2011), Evidence of volcanic and glacial activity in Chryse and Acidalia Planitiae, Mars, Icarus, 212(2), 597–621, doi:10.1016/j.icarus.2011.01.004.

Massey, E. (2017), A comparative study of glaciovolcanic palagonitization of tholeiitic and alkaline sideromelane at Helgafell, Iceland and Wells Gray-Clearwater Volcanic Field, BC Canada, Assoc. Miner. Explor. Br. Columbia.

McEwen, A. S. et al. (2007), A Closer Look at Water-Related Geologic Activity on Mars, Science, 317, 1706, doi:10.1126/science.1143987.

Michalski, J. R., M. D. Kraft, T. G. Sharp, and P. R. Christensen (2005), Palagonite-like Alteration Products on the Earth and Mars I: Spectroscopy (0.4-25 microns) of Weathered Basalts and Silicate Alteration Products, vol. 36.

Moore, J. G., and J.-G. Schilling (1973), Vesicles, water, and sulfur in Reykjanes Ridge basalts, Contrib. Mineral. Petrol., 41(2), 105–118, doi:10.1007/BF00375036.

Morris, R. V., J. L. Gooding, H. V. Lauer, and R. B. Singer (1990), Origins of Marslike spectral and magnetic properties of a Hawaiian palagonitic soil, J. Geophys. Res. Solid Earth, 95(B9), 14427–14434, doi:10.1029/JB095iB09p14427.

Murchie, S. et al. (2007), Compact Reconnaissance Imaging Spectrometer for Mars (CRISM) on Mars Reconnaissance Orbiter (MRO), J. Geophys. Res. Planets, 112, doi:10.1029/2006JE002682.

Picardi, G. et al. (2004), Performance and surface scattering models for the Mars Advanced Radar for Subsurface and Ionosphere Sounding (MARSIS), Planet. Space Sci., 52(1–3), 149–156, doi:10.1016/j.pss.2003.08.020.

Plaut, J. J., A. Ivanov, A. Safaeinili, S. M. Milkovich, G. Picardi, R. Seu, and R. Phillips (2007), Radar Sounding of Subsurface Layers in the South Polar Plains of Mars: Correlation with the Dorsa Argentea Formation, vol. 38, p. 2144.

Pollack, J. B., J. F. Kasting, S. M. Richardson, and K. Poliakoff (1987), The case for a wet, warm climate on early Mars, Icarus, 71(2), 203–224, doi:10.1016/0019-1035(87)90147-3.

Rampey, M. L., K. A. Milam, H. Y. McSween, J. E. Moersch, and P. R. Christensen (2007), Identity and emplacement of domical structures in the western Arcadia Planitia, Mars, J. Geophys. Res. Planets, 112(E6).

Rodriguez, J. A. P., and K. L. Tanaka (2006), Sisyphi Montes and Southwest Hellas Paterae: Possible Impact, Cryotectonic, Volcanic, and Mantle Tectonic Processes and Hellas Basin Rings, LPI Contrib., 1323, 8066.

Ruff, S. W., and P. R. Christensen (2002), Bright and dark regions on Mars: Particle size and mineralogical characteristics based on Thermal Emission Spectrometer data, J. Geophys. Res. Planets, 107(E12), 5119, doi:10.1029/2001JE001580.

Russell, J. K., B. R. Edwards, L. Porritt, and C. Ryane (2014), Tuyas: a descriptive genetic classification, Quat. Sci. Rev., 87, 70–81, doi:10.1016/j.quascirev.2014.01.001.

Sackmann, I.-J., and A. I. Boothroyd (2003), Our Sun. V. A bright young Sun consistent with helioseismology and warm temperatures on ancient Earth and Mars, Astrophys. J., 583(2), 1024.

Scanlon, K. E., and J. W. Head (2014), The Dorsa Argentea Formation: Synthesis of Glacial Features and History of Late Noachian-Early Hesperian Martian Climate Change, vol. 45, p. 1477.

Smellie, J. L., and I. P. Skilling (1994), Products of subglacial volcanic eruptions under different ice thicknesses: two examples from Antarctica, Sediment. Geol., 91(1), 115–129, doi:10.1016/0037-0738(94)90125-2.

Stroncik, N. A., and H.-U. Schmincke (2002), Palagonite – a review, Int. J. Earth Sci., 91(4), 680–697, doi:10.1007/s00531-001-0238-7.

Squyres, S., and J. F. Kasting (1994), Early Mars, Science, 265(5173), 744–749.

Tanaka, K. L., and Scott, D.L. (1987), Geologic Maps of the Polar Regions of Mars, U. S. Geol. Surv., Miscellaneous Investigations(Series Map I-802-C, Scale 1:15,000,000).

Tuffen, H. (2007), Models of ice melting and edifice growth at the onset of subglacial basaltic eruptions, J. Geophys. Res. Solid Earth, 112(B3), B03203, doi:10.1029/2006JB004523.

Tuffen, H., D. W. McGarvie, J. S. Gilbert, and H. Pinkerton (2002), Physical volcanology of a subglacial-to-emergent rhyolitic tuya at Rauðufossafjöll, Torfajökull, Iceland, Geol. Soc. Lond. Spec. Publ., 202(1), 213–236, doi:10.1144/GSL.SP.2002.202.01.11.

Warner, N. H., and J. D. Farmer (2010), Subglacial Hydrothermal Alteration Minerals in Jökulhlaup Deposits of Southern Iceland, with Implications for Detecting Past or Present Habitable Environments on Mars, Astrobiology, 10(5), 523–547, doi:10.1089/ast.2009.0425.

Wordsworth, R., F. Forget, E. Millour, J. W. Head, J.-B. Madeleine, and B. Charnay (2013), Global modelling of the early martian climate under a denser CO2 atmosphere: Water cycle and ice evolution, Icarus, 222(1), 1–19, doi:10.1016/j.icarus.2012.09.036.

Wordsworth, R. D., L. Kerber, R. T. Pierrehumbert, F. Forget, and J. W. Head (2015), Comparison of “warm and wet” and “cold and icy” scenarios for early Mars in a 3-D climate model, J. Geophys. Res. Planets, 120(6), 2015JE004787, doi:10.1002/2015JE004787.

Wray, J. J., S. L. Murchie, S. W. Squyres, F. P. Seelos, and L. L. Tornabene (2009), Diverse aqueous environments on ancient Mars revealed in the southern highlands, Geology, 37, 1043–1046, doi:10.1130/G30331A.1.

Zimanowski, B., R. Büttner, and V. Lorenz (1997), Premixing of magma and water in MFCI experiments, Bull. Volcanol., 58(6), 491–495, doi:10.1007/s004450050157.

CHAPTER 2. MINERALOGIC EVIDENCE FOR SUBGLACIAL VOLCANISM IN THE SISYPHI MONTES REGION OF MARS

This chapter is published in peer-reviewed Elsevier Icarus and can be found here:
S. Ackiss, B. Horgan, F. Seelos, W. Farrand, J. Wray, Mineralogic evidence for subglacial volcanism in the Sisyphi Montes region of Mars, Icarus, Volume 311, 2018, Pages 357-370, ISSN 0019-1035, https://doi.org/10.1016/j.icarus.2018.03.026.
(http://www.sciencedirect.com/science/article/pii/S0019103517308059) Keywords: Mineralogy; Volcanism; Geological processes; Mars; Surface; Spectroscopy

2.1 Introduction

The paleoclimate of Noachian Mars prior to 3.7 billion years ago has been highly debated, and there is no current consensus on whether it was “warm and wet” or “cold and icy” [*Pollack et al.*, 1987; *Baker and Strom*, 1991; *Squyres and Kasting*, 1994; *Haberle*, 1998; *Craddock and Howard*, 2002; *Gaidos and Marion*, 2003; *Sackmann and Boothroyd*, 2003; *McEwen et al.*, 2007; *Fairén*, 2010; *Head*, 2013; *Head and Marchant*, 2014; *Cassanelli and Head*, 2015; *Fastook and Head*, 2015; *Wordsworth et al.*, 2015]. The presence of features made by liquid water such as valley networks, deltas, and lake deposits, as well as minerals formed in aqueous environments [e.g. *Bibring et al.*, 2006; *Ehlmann et al.*, 2011; *Grotzinger et al.*, 2015] indicate that liquid water must have been present on Mars. However, paleoclimate models have been unable to produce warm climatic conditions that would allow liquid water to be stable on the surface [*Kargel and Strom*, 1992; *Gulick*, 2001; *Harrison and Grimm*, 2002; *Malin and Edgett*, 2003; *Mangold et al.*, 2004; *Arfstrom and Hartmann*, 2005; *Forget et al.*, 2006]. Volcanism was prevalent during Mars’ early history [*Robbins et al.*, 2013], and the addition of volcanic gases into the atmosphere has not been able to adequately increase the probability of liquid water on the surface [*Pollack et al.*, 1987; *Haberle*, 1998; *Jakosky and Phillips*, 2001; *Halevy et al.*, 2007; *Halevy and Head*, 2014]. Instead of liquid water, the paleoclimate models predict cold and icy conditions leading to the deposition of snow and ice in the southern highlands. In this scenario, climatic conditions would still need to be perturbed to cause significant top-down melting of the glaciated regions to produce the observed fluvial and lacustrine features [*Fastook and Head*, 2015].

While the “warm and wet” Mars hypothesis has been studied in detail, it has not yet been shown whether or not the “cold and icy” Mars hypothesis is broadly consistent with the mineralogy of surface features from this time period. Considering the extent of volcanism on early Mars, we propose a novel test for the “cold and icy” early Mars hypothesis: Are the volcanic mineralogies of Noachian Mars consistent with volcanism on a “snowball Mars”? If ice was present for extended periods on the surface of ancient Mars, we should expect to see morphological and mineralogical evidence for ice-magma interactions in the Noachian geologic record; however, it is unclear what mineral assemblages due to ice-magma interactions would be observed from orbit. In this study, we investigate the mineralogy of a well-preserved hypothesized glaciovolcanic field on Mars to address questions such as: What are the minerals produced by glaciovolcanism on Mars? And more specifically, what are their spectral properties as detected by the Mars Reconnaissance Orbiter (MRO) Compact Reconnaissance Imaging Spectrometer for Mars (CRISM)? The answers to these questions can help to place constraints on the presence (i.e. mineralogy) and depth (derived from the height of the subglacial edifice) of ice in volcanic terrains on ancient Mars.

The Sisyphi Planum region of Mars is a high-latitude late Noachian to late Hesperian-aged [*Tanaka and Scott*, 1987] region near the south pole, nestled between the Argyre and Hellas basins. This region contains the Sisyphi Montes, which is a group of edifices interpreted to be subglacial in origin [*Ghatan and Head*, 2002]. The primary objective of this work is to determine whether or not the spectral signatures of the Sisyphi Planum region are consistent with glaciovolcanism by using the spectral signatures to determine mineral assemblages and comparing those mineral assemblages to those from volcanically altered environments on Earth with different water-to-rock ratios, temperatures, and pressures. If the Sisyphi Montes do indeed exhibit mineral assemblages that are consistent with glaciovolcanism, then this region can be used as a type location for ice-magma interactions on Mars and to constrain the past presence of glaciers in this area.

2.2 Background

2.2.1 Mineralogy of Terrestrial (Earth) Volcanic Environments

Glaciovolcanism creates distinct mineral assemblages compared to other modes of alteration in volcanic terrains. Here, we summarize the mineralogy of four volcanic alteration regimes on Earth including: subglacial eruptions and associated hydrothermal systems, subglacial weathering, subaerial hydrothermal systems, and subaerial weathering. Because different assemblages of alteration minerals form in these different environments, detailed mineralogic studies can help to constrain formation environments on Mars.

In volcanic eruptions beneath ice sheets and glaciers on Earth, the combination of heat and large quantities of melt water lead to the production of unique morphologies. These morphologies include “tuyas” or table mountains that are steep sided and flat topped edifices and “tindars” or ridges that are flat-topped and linear (both of which are flat-topped due to sub-aerial lava flows erupting after the edifice breaches the ice sheet). Subglacial mounds, which are conical in shape, are made when the eruption does not breach the ice-sheet causing the tops to remain curvilinear instead of becoming flat [*Russell et al.*, 2014]. This environment creates a unique stratigraphic sequence with pillow basalts at the base, hyaloclastites and pyroclastic breccias in the middle, and capped by subaerial lava flows [*Tuffen,* 2007; *Jakobsson and Gudmundsson,* 2008; *Russell et al.*, 2014]. The mineralogy produced during these eruptions is also unique because of the interaction of the hot lava and cold glacial meltwater. This process involves the quenching of magma to form basaltic glass (sideromelane) as well as *in situ* hydrothermal alteration of the sideromelane forming amorphous to poorly crystalline rinds of palagonite, which cement the fragments into a hyaloclastite rock [*Stroncik and Schmincke,* 2002; *Drief and Schiffman,* 2004; *Massey et al,* 2017]. This process creates an ideal location for microbial habitats because hydrothermal deposits can preserve biosignatures in their crystalline structures [*Cousins et al.*, 2013].

While glaciovolcanic hydrothermal alteration produces a diverse suite of minerals, there have been few detailed studies of this mineralogy. Samples from British Columbia, Canada have shown that subglacial eruptions are associated with authigenic mineralization including clay minerals and zeolites, and that this alteration assemblage stoichiometrically resembles smectites [*Jercinovic et al.,* 1990]. Smectites, hematite, sideromelane, and erionite (zeolite) are observed in subglacial volcanic deposits emplaced emplaced in Hawaii [Golden et al., 1993] and Iceland

[*Bishop et al.*, 2002b] during the Pleistocene. Glaciovolcanic materials from Icelandic outwash deposits have been shown to contain zeolites (heulandite, laumonite, stilbite, and analcime) and phyllosilicates (illite, kaolinite, and smectites) [*Warner and Farmer*, 2010], while *in situ* deposits from glaciovolcanic hydrothermal sites can also contain sulfates (gypsum, alunogen, and jarosite) and iron oxides (hematite and goethite) [*Cousins et al.*, 2013]. Zeolites are an important product of subglacial eruptions, and X-ray powder diffraction studies have shown that the zeolites crystallize in low-temperature, closed system conditions during the process of the eruption and are thus authigenic [*Jercinovic et al.*, 1990; *Utada*, 2001; *Warner and Farmer*, 2010]. Other studies that have specifically studied sideromelane and palagonite have observed zeolites forming in-situ as late-stage minerals, especially in vesicles and voids [Stroncik and Schmincke, 2001].

Collectively, the assemblage of minerals produced during subglacial or subaqueous hydrothermal alteration of sideromelane is referred to as palagonite. Thus, palagonite is not a mineral, but rather an assemblage of minerals and mineraloids formed from alteration of basaltic glass (sideromelane) [*Massey et al.*, 2017] including clay minerals, zeolites, iron oxides, and basaltic glass. In its early stages, palagonite is an amorphous gel thought to form during dissolution-precipitation of sideromelane where the primary material is dissolved and the secondary phases are precipitated at the contact with the sideromelane [Stroncik and Schmincke, 2002]. As palagonite ages, it evolves into fibro-palagonite, which is a mixture of amorphous gel-palagonite and crystalline smectites. Jercinovic et al., [1990] proposes that zeolites are formed in the middle phase of palagonite alteration as it progresses from 1) saponite (smectite), to 2) zeolites in the order of phillipsite to chabazite, and 3) finally to nontronite (smectite). However, the details of the formation, evolution, and mineralogic composition of palagonite are still highly debated [*Stroncik and Schmincke*, 2002; *Drief and Schiffman*, 2004].

Palagonite is commonly misinterpreted as a weathering product produced during subaerial oxidation and weathering of volcanic rocks [*Hay and Iijima*, 1968; *Hay and Jones*, 1972; *Gooding and Keil*, 1978; *Singer*, 1982; *Banin and Margulies*, 1983]; however, the terrestrial literature specifically defines palagonite as a poorly crystalline, hydrated, and oxidized hydrothermal alteration product of sideromelane made exclusively at relatively low-temperatures (typically <120°C) and high water-to-rock ratios [*Allen et al.*, 1981; *Morris et al.*, 1990; *Stroncik and Schmincke*, 2002; *Michalski et al.*, 2005; *Warner and Farmer*, 2010; *Cousins et al.*, 2013].

Schiffman et al., [2000] and Pauly et al. [2011] have proposed that palagonite may form under two fundamentally different temperature regimes: high-temperature and low-temperature. High-temperature, hydrothermal palagonitization occurs during and directly following an eruption, resulting in thin rinds and few zeolites due to the short duration of alteration [*Schiffman et al.*, 2000]. In contrast, porosity and water content decrease over time during low-temperature, diagenetic palagonitization [*Pauly et al.*, 2011]; however, this type of alteration may be difficult to distinguish from typical early diagenesis and has not been shown to produce the same mineral assemblages as high temperature alteration. Because palagonite requires the presence of basaltic glass, low temperatures, and high water-to-rock ratios, the main environments in which it forms are subglacial and submarine (at a range of depths, including sublacustrine) volcanic eruptions. In general, submarine volcanism produces similar alteration mineral assemblages as glaciovolcanism [*Jakobsson*, 1978; *Jakobsson and Moore*, 1986], but very different volcanic morphologies [*Mitchell et al.*, 2002; *Jakobsson and Gudmundsson*, 2008; *Russell et al.*, 2014; *Romagnoli and Jakobsson*, 2015].

Subglacial chemical weathering is driven by low-temperature (typically ~0°C) glacial meltwater and has primarily been studied in felsic volcanic terrains [*Anderson*, 2005]. Recent studies suggest that alteration mineral assemblages in these environments are determined by the bedrock composition. On carbonate and granitic bedrock, subglacial weathering is driven by carbonate dissolution, then sulfide oxidation, which causes silicate weathering [*Anderson*, 2005]. Based on the geochemistry of simulated subglacial fluids, these fluids could produce kaolinite along with very low sulfate concentrations [*Crompton et al.*, 2015]. In contrast, recent studies of subglacial weathering of mafic volcanic terrains have shown that sediments generated by small alpine glaciers on mafic volcanic edifices include no significant crystalline alteration phases produced by subglacial alteration in that environment. Instead, alteration products in this environment are silica-dominated, hydrated, and poorly crystalline [*Rampe et al.*, 2017; *Smith et al.*, 2017], and the spectrally dominant phase in rock coatings and sediments is hydrated silica [*Scudder et al.*, 2017]. Based on geochemical studies across multiple volcanic systems, the silica content of glacial meltwaters increases as the bedrock becomes more mafic. This is because mafic rocks contain more soluble silicates (e.g. olivine and pyroxene) than felsic rocks (e.g. quartz and feldspar) [*McLennan et al.*, 2003]. This has been observed in glacial outwash at the Three Sisters volcanic complex in Oregon, USA, suggesting that poorly crystalline silica precipitates would be the most likely signature of glacial alteration on Mars [*Rutledge et al.* submitted]. Sulfates have been observed associated with glacial systems in Svalbard, where physical abrasion from the movement of the glacier leaves insoluble products of chemical weathering behind (e.g. Fe and Al) and transports soluble chemical weathering products (SO_4, HCO_2, Ca, and Mg) [*Szynkiewicz et al.*, 2013]. These products then concentrate, freeze, and evaporate and precipitate salt efflorescence (e.g. calcite, gypsum, Ca-Mg sulfates) in the proglacial zone [*Szynkiewicz et al.*, 2013]. Preliminary analysis of subglacial sediments from the Antarctic ice sheet suggest that phyllosilicate formation might be possible in that much larger and long-lived subglacial system, but additional work is needed to confirm this hypothesis [*Graly et al.*, 2017]. The primary difference between hydrothermal alteration during glaciovolcanism and subglacial weathering is the general lack of crystalline weathering products in subglacially weathered rocks and sediments.

Subaerial volcanism (e.g. stratovolcanoes, shield and post-shield volcanoes, and cinder cones) is often accompanied by hydrothermal alteration and high-temperature oxidation. These processes typically produce variable alteration mineral assemblages, including clay minerals (kaolinite, Al-montmorillonite, saponite, illite) [*Ugolini*, 1974; *Swayze et al.*, 2002], sulfates (gypsum, jarosite), carbonates, silica [*Rice et al.*, 2013], and Fe-oxides (hematite, goethite, ferrihydrite), where clay minerals are often present at high abundances (ranging from ~20-80%) and dominate the visible/near-infrared spectra of hydrothermally altered basalt [*Swayze et al.*, 2002; *Ehlmann et al.*, 2012]. Additionally, the circulation of hydrothermal fluids causes the precipitation of zeolites (e.g. phillipsite and gismondine) in voids [Ehlmann et al., 2012] and causes glass and phenocrysts in cinder cones to weather to alunite and smectites [*Wolfe et al.*, 1997]. While both subglacial and subaerial volcanism cause hydrothermal alteration, one key difference between the two systems is that hydrothermal alteration primarily produces void-filling zeolites in pre-existing rocks, which only comprise a small volumetric abundance (≤10%) in subaerial systems [*Ehlmann et al.*, 2012; *Gelves et al.*, 2016], whereas zeolites can be abundant throughout the bulk of altered sediments produced during glaciovolcanism.

Subaerial weathering is driven by leaching due to infiltration of rainfall and snowmelt into rocks and soils, and the alteration mineral assemblage in these environments is highly dependent on climate and duration of alteration. In very humid climates like Japan and Iceland, subaerial weathering of volcanic terrain is initially dominated by poorly crystalline materials (e.g. allophane, imoglite, and ferrihydrite) formed due to the rapid weathering of glassy materials [*Claridge*, 1965; *Singer*, 1974, 1980; *Arnalds and Kimble*, 2001; *Arnalds*, 2004; *Ugolini and Bockheim*, 2008], which mature into more crystalline clay minerals and oxides (e.g., halloysite, kaolinite, gibbsite) over a period of tens of thousands to millions of years [*Ugolini and Dahlgren*, 2002; *Ziegler et al.*, 2003; *Tsai et al.*, 2010]. More arid environments generally do not form poorly crystalline precursors in such high abundances and assemblages are instead dominated by crystalline clay minerals, including smectites, kaolinite, halloysite [*Delvaux et al.*, 1989; *Alexander et al.*, 1993], as well as iron oxides (hematite, goethite) [*Delvaux et al.*, 1989]. In Antarctica, subaerial weathering of lavas in permafrost can produce Fe-oxide surface stains, sulfates, vug-filling zeolites, and carbonate (calcite). Phyllosilicates (Mg-montmorillonite) have also been observed in association with Antarctic permafrost, although they are extremely rare and phyllosilicates likely play a minor role in weathering above dry permafrost [*Berkley and Drake*, 1981]. While zeolitization due to burial diagenesis of volcanic tephra and volcanic soils can create spectrally detectable zeolites [*Horgan et al.*, 2017], zeolites are not commonly found in modern soils [*Retallack*, 2008]. Overall, phyllosilicates like smectite and kaolinite are the two most prevalent minerals found in soils formed in volcanic environments [*Singer*, 1980; *Sheldon and Tabor*, 2009].

Based on the most common mineral assemblages of these environments, we hypothesize that spectral signatures would be dominated by a few key phases in each environment (Table 1). In general, we hypothesize that zeolites and smectites spectrally dominate subglacial hydrothermal volcanic regions [*Swayze et al.*, 2002; *Paque et al.*, 2016], silica spectrally dominates subglacial weathering environments [*Scudder et al.*, 2017], clay minerals spectrally dominate subaerial hydrothermal volcanic regions [*Ehlmann et al.*, 2012], and clay minerals, specifically smectites and kaolinite, also spectrally dominate subaerial weathering environments [*Delvaux et al.*, 1989; *Alexander et al.*, 1993]. These mineralogies will be used to compare to the minerals identified on Mars to pinpoint the past weathering environments of our martian study.

2.2.2 Study Region: The Sisyphi Planum Montes

The Sisyphi Montes (55-75°S and 35-345°E) are a group of over 100 isolated edifices [*Campbell et al.*, 2016] within Sisyphi Planum, a region of low and smooth topography located between the Argyre and Hellas impact basins (Figure 1). A subset of the Sisyphi Montes are located within the Dorsa Argentea Formation (DAF) – a unit hypothesized to be the remnant of an ancient middle-Hesperian ice sheet of unknown composition (Figure 1) [*Tanaka and Scott*, 1987; *Wordsworth et al.*, 2013]. The DAF is composed of pitted terrains, sinuous ridges, and plains units with lobate margins [*Tanaka and Scott*, 1987; *Head and Pratt*, 2001; *Kolb and Tanaka*, 2001] and covers a combined area of ~1.5×10^6 km^2 [*Head and Pratt*, 2001]. MARSIS (Mars Advanced Radar for Subsurface and Ionospheric Sounding) [*Picardi et al.*, 2004] detections of shallow subsurface ice interfaces in this area are highly correlated with the DAF, suggesting remnant subsurface ice is still present within the DAF [*Plaut et al.*, 2007]. This ice is generally assumed to be water ice [*Wordsworth et al.*, 2013], although the composition, whether CO_2 or water ice, has not been directly confirmed [*Tanaka and Scott*, 1987; *Ghatan and Head*, 2002; *Plaut et al.*, 2007; *Carr and Head*, 2010]. If the Sisyphi Montes were formed as glaciovolcanoes, this would suggest that either the ice sheet that produced the DAF or an earlier ancient ice sheet extended throughout the Sisyphi Planum region [*Plaut et al.*, 2007; *Scanlon and Head*, 2014].

The Sisyphi Montes initially included 17 high and rugged mountainous edifices [*Tanaka and Scott*, 1987] mapped primarily within the DAF [*Tanaka and Scott*, 1987; *Head and Pratt*, 2001; *Kolb and Tanaka*, 2001]. Due to limited image resolution, the age and origin of the edifices could not be determined. Later studies expanded the number of edifices to 22 [*Ghatan and Head*, 2002] and examined three possible origins related to impact cratering, tectonism, and volcanism. Based on the unique steep-sided and flat-topped morphology of the edifices, Ghatan and Head [2002] hypothesized that the edifices were volcanoes that formed subglacially, erupting underneath an extensive Hesperian-aged ice sheet. Further studies expanded the volcano count to >40 features [*Rodriguez and Tanaka*, 2006], classifying the structures by their morphology and proximity to both the Sisyphi Planum and Hellas basin. Because some of the Sisyphi Montes are encircled by local moat-like features with raised rims, Rodriguez and Tanaka [2006] hypothesized that the edifices were formed due to a combination of volcanic and impact-related processes. They proposed that the magma that created the structures was sourced from magma bodies intersecting large impact-induced zones of crustal weakness circumferential to the Hellas basin. The magma was then brought to the surface by subsequent small impacts, building edifices in the centers of the smaller impact craters [*Rodriguez and Tanaka*, 2006]. While no other hypotheses about the formation of the region have been proposed, more detailed studies of the edifices have been conducted and report >100 edifices within the Sisyphi Planum region [*Campbell et al.*, 2016].

Chemical signatures from the Mars Odyssey Gamma Ray and Neutron Spectrometer (GRS) shows that sulfates are the most likely phases in the southern hemisphere midlatitudes [*Karunatillake et al.,* 2016]. Visible/near-infrared spectral surveys have revealed that the Sisyphi Montes exhibit spectral signatures consistent with olivine, pyroxene [*Farrand et al.*, 2008], and polyhydrated sulfates [*Wray et al.*, 2009; *Ackiss and Wray*, 2014]. Sulfate signatures are correlated with the presence of boulders in high-resolution imagery, and are attributed to either volcanic hydrothermal or acid fog alteration [*Wray et al.*, 2009]. A more recent mineralogic survey of the southern high latitudes showed that while hydrated sulfates and other hydrated phases of unknown composition are widespread at high-latitudes, the sulfate signatures within Sisyphi Planum are strongest on the Sisyphi Montes. This observation suggests that the sulfates may have been produced in association with volcanic activity and later transported into the Sisyphi Planum plains [*Ackiss and Wray*, 2014].

2.2.3 Possible Occurrences of Other Subglacial Volcanic Landforms on Mars

The Sisyphi Montes region was chosen to be the region of study because it is a region of excellent morphologic preservation of edifices with morphologies similar to subglacial volcanoes on Earth [*Ghatan and Head*, 2002; *Russel et al.*, 2014]. There are, however, other landforms elsewhere on Mars that have been hypothesized to be derived from subglacial volcanism based on their morphologies [*Cousins and Crawford,* 2011], including in the northern plains [*Fagan et al.*, 2010; *Mouginis-Mark et al.*, 2016]. Mounds, mesas, and buttes in Chryse and Acidalia Planitia appear to be rocky with horizontal layering [*Martínez-Alonso et al.*, 2011]. Cones are often observed on the summit of these edifices, providing further evidence that they may be volcanic in origin [*Martínez-Alonso et al.*, 2011]. These edifices are surrounded by features interpreted to be subglacial such as formations resembling terrestrial drumlins, eskers, kettle holes, and inverted valleys [*Martínez-Alonso et al.*, 2011]. Mid-latitude volcanic regions, such as Arsia Mons, also exhibit evidence of subglacial volcanic activity. Fan-shaped deposits around Arsia Mons contain steep-sided mounds, steep-sided flow-like landforms with depressed craters, digitate flows, and steep-sided flat-topped plateau features. Collectively, these features are interpreted to be subglacial pillow sheets, hyaloclastite mounds, ice-confined flows, and tuyas [*Scanlon et al.*, 2014]. While there have been extensive morphologic studies of these sites, mineralogic studies have not been conducted due to the low signal-to-noise ratios of CRISM data in the high latitudes [*Ackiss and Wray*, 2014] and the extensive dust coverage [*Seelos et al.*, 2012]

2.3 Methodology

The MRO CRISM instrument is a hyperspectral imaging spectrometer with two detectors, a short wavelength detector ranging from 0.36 to 1.05 µm and a long wavelength detector spanning 1.00 to 3.92 µm, that when combined have 544 bands in the visible/near-infrared [*Murchie et al.*, 2007]. CRISM has a gimbaled hyperspectral mode that provides 20 or 40 m/pixel observations that are also 10 km wide and can be 3, 10, or 20 km long depending on the specific observing mode (Half Resolution Short (HRS), Full Resolution Targeted (FRT), Half Resolution Targeted (HRL), respectively). In targeted mode, CRISM utilizes a gimbal to compensate for ground track motion, which results in an hourglass footprint when map-projected. For this study, hyperspectral targeted (FRT and HRL) CRISM observations were processed to prototype Map-Projected Targeted Reduced Data Records (MTRDRs) [*Seelos et al.*, 2011]. MTRDRs include photometric and atmospheric corrections as well as wavelength-dependent empirical corrections to compensate for spectral smile and gimbal-induced residuals. Both visible and near-infrared image cubes are then combined into one product with summary parameters calculated prior to map projection [*Viviano-Beck et al.*, 2014].

All CRISM hyperspectral targeted images between 55-75° S and 35-345° E (the Sisyphi Planum region) located on an edifice and acquired with a solar longitude (Ls) between 180-360° and detector temperature less than -145.65° C (for long wavelength detector observations) were downloaded and processed through the MTRDR pipeline. Ls 180-360° marks southern summer, decreasing the chance of CO_2 ice and frost in the region during the time of observation. Observations taken above -145.65° C have a low signal-to-noise ratio making absorption band identification and interpretation more complex. Twenty-four images met the above criteria; however, only 11 of those images were usable in this study (Table 2 and Supplemental Table 1). Two of the 24 images did not have both the short and long wavelength detector temperature observations, which are required for the MTRDR joining process, and thus were excluded from the study. Eleven of the 24 images were either spectrally bland, exhibited high atmospheric opacity, or CO_2 ice/frost was present.

CRISM's wavelength range is sensitive to the electronic transitions of ferric and ferrous iron in minerals from 0.4 to ~1 µm as well as the overtones and/or combination tones of fundamental molecular vibrations in minerals from ~1 µm to ~4 µm. Molecular vibrations depend on specific mineral crystal structures, thus the vibrations of similar molecules in different minerals can produce features at different wavelength positions [e.g. *Hunt et al.*, 1973]. CRISM and laboratory reference spectra in this study were evaluated for the presence of mineral absorption bands between 0.42 to 2.60 µm to target bands in Fe oxide minerals, phyllosilicates, hydrated silica, and sulfate phases. Qualitative comparison of scene spectral endmembers to library reference spectra allows identification of specific mineral species. To reduce noise and emphasize diagnostic absorption features, several to 10s of pixels from an outcrop of interest are averaged together and ratioed to a similar-sized, spectrally neutral, and in-column averaged spectrum. After the spectra were ratioed, a boxcar smooth was performed on the spectra, where each wavelength data point was replaced with an average of the 3 neighboring data points. This further reduces the amount of small noise in the final product.

Fifteen spectral summary parameters [*Viviano-Beck et al.*, 2014] designed to detect specific absorption bands were mapped individually to identify regions of interest within each scene. The summary parameters used in this study were focused on primary, mafic minerals including olivines and pyroxenes as well as secondary alteration minerals such as Fe-oxides, salts, and phyllosilicates. BD530_2 and BD920_2 are designed to detect crystalline ferric minerals and were used to identify regions containing Fe-oxides. R1330, which measures the albedo of the surface, was not used to study mineralogy but instead used to compare mineralogic signatures to morphologic features in the scene. OLINDEX3, LCPINDEX2, and HCPINDEX2 were used to identify regions containing primary minerals such as olivine, orthopyroxene (low-calcium pyroxene), and clinopyroxene (high-calcium pyroxene), respectively. Sulfate salts were evaluated using a suite of parameters including BD1750_2, which can detect the 1.75 µm band of gypsum and alunite, BD1900_2, which can detect the 1.9 µm band due to H_2O in polyhydrated sulfates and other hydrated minerals, BD2100_2, which can detect the 2.1 µm band due to H_2O in monohydrated sulfates, and SINDEX2, which can detect the convexity induced at 2.29 µm caused by the presence of both the 1.9 or 2.1 and 2.4 µm sulfate bands. Al-OH alteration minerals (e.g., phyllosilicates and zeolites) were mapped using D2200 whereas hydroxylated Fe/Mg silicates were mapped using D2300. MIN2345_2537 mostly highlights Ca/Fe carbonates but also identifies the OH and SO combination vibrations in OH-bearing sulfates [*Cloutis et al.*, 2006] and mixtures of hydroxylated silicates and zeolites. The surface was examined for both CO_2 and H_2O ice using the BD1435 and BD1500_2 parameters, respectively.

2.4 Results

The 11 CRISM images used in this study cover five edifices in Sisyphi Planum. Based on analysis of these images, we have identified three distinct spectral classes in the region (Figure 2). These classes are interpreted to be surfaces spectrally dominated by (1) gypsum, (2) polyhydrated sulfate (or zeolite), and (3) a smectite-zeolite-iron oxide mixture. Out of the five edifices with clear hydrated mineral signatures, 3 exhibit spectra from more than one class (Figure 2). Two of the edifices have a combination of Classes 2 (polyhydrated sulfate) and 3 (smectite-zeolite-iron oxide mixture) while one edifice has a combination of Classes 1 (gypsum) and 2 (polyhydrated sulfate).

2.4.1 Class 1: Gypsum-dominated Spectra

Spectra in this class exhibit absorption bands in the visible and near-infrared at 0.52, 0.91 1.21, 1.43, 1.75, 1.92, 2.22, and 2.47 μm in CRISM images FRT00007E11 and FRT00007AE6 (Figures 2 and 3). At visible wavelengths, the spectra have weak and variable absorptions at 0.52 and 0.91 μm; however, the 0.91 μm is the most consistently observed feature. The ~1.4 and ~2.4 μm features tend to be broad while the ~1.9 μm feature is narrow. All of the absorption bands are relatively strong. This combination of near-infrared (NIR) bands is uniquely consistent with laboratory spectra of gypsum and the majority of these bands are attributed to water, which is an integral part of gypsum's crystalline structure ($CaSO4•2(H2O)$) [*Clark et al.*, 1990]. The visible bands are consistent with a variety of Fe-oxide minerals including lepidocrocite, goethite, and akaganeite. Gypsum is an especially strong absorber at NIR wavelengths. With as little as 5 wt.%, the 1.9 μm hydration band of gypsum can be detected in a mixture with basalt [*Horgan et al.*, 2009] and the NIR signature will be completely dominated by gypsum [*Howari et al.*, 2002; *Cloutis et al.*, 2008]. Additionally, the association of iron-oxides and sulfates is consistent with assemblages observed in other regions of Mars (e.g. Candor and Capri Chasmas) [*Bibring et al.*, 2007].

We only observe these absorption bands on one edifice in the region (-63.54ºS, 17.65ºE; edifice 18 as named in Ghatan and Head, [2002]), although the detection is strong and correlates well with morphology. CRISM images FRT00007E11 and FRT00007AE6 and associated MRO High Resolution Imaging Science Experiment (HiRISE) images have been studied in detail previously and show that sulfate (gypsum and polyhydrated sulfate) signatures correlate with boulders eroding from curvilinear structures [*Wray et al.*, 2009; *Ackiss and Wray*, 2014]. Note that the CRISM images (FRT0007E11 and FRT0007AE6) are not located on the top of the main edifice (edifice 18). Instead, the images are centered on a mound leading up the flank of edifice 18. It is unknown if this mound was formed during the initial formation of the main edifice or if it is a secondary feature (Figure 3).

2.4.2 Class 2: Polyhydrated Sulfate-dominated Spectra

Spectra in this class have absorptions at 0.52, 1.9, and 2.5 μm and roughly half of the spectra also exhibit absorptions at 0.93 and 1.43 μm (Figures 2 and 3). The ~1.9 and ~2.5 μm bands are the strongest absorptions. These features are observed in CRISM images FRT00007E11, FRT00007AE6, HRL00011898, FRT000079E4, FRT00007EB5, HRL000126C5, and HRL000086DE. Observations in CRISM images FRT00007E11, FRT00007AE6, HRL00011898 contain all absorption bands listed above and are located on edifice 18 (Figure 2, top 3 red spectra), whereas CRISM images FRT000079E4, FRT00007EB5, HRL000126C5, and HRL000086DE only contain the 0.52, 1.9, and 2.5 μm absorptions (Figure 2, bottom 4 spectra ranging in color from yellow to black). These broad absorption features are caused by the overlapping bands of water molecules in different bonding configurations [*Crowley*, 1990]. In general, the combination of these bands could indicate either polyhydrated sulfates or zeolites, which are difficult to distinguish spectrally. However, we observe that the ~1.4 μm absorption bands are centered at shorter wavelengths than are typical for zeolites (e.g. 1.43 versus 1.48 μm), and are thus more consistent with a polyhydrated sulfate interpretation [*Cloutis et al.*, 2002, 2006; *Viviano-Beck et al.*, 2014]. We suggest that the signatures in CRISM images FRT00007E11, FRT00007AE6, HRL00011898 are most consistent with polyhydrated Mg-sulfates (Figure 2, top 3 red spectra). CRISM images FRT000079E4, FRT00007EB5, HRL000126C5, and HRL000086DE contain spectra with weaker 1.9 and 2.5 micron bands and no detectable 1.4 micron band. These bands alone are not conclusive enough to definitively define the type of mineral but they are *most consistent* with a polyhydrated sulfate interpretation (Figure 2, bottom 4 spectra ranging in color from yellow to black). A strong red slope in the visible combined with the ~0.5 and 0.93 μm absorption bands in some spectra implies the presence of iron-oxide minerals. As in the previous spectral class, this combination of bands is consistent with a variety of Fe-oxide minerals including lepidocrocite, goethite, and akaganeite.

This class of spectra is located on four edifices examined in the region. The strongest absorptions are seen on edifice 18 (Figure 3) with weaker absorptions on edifice 7 (63.453^{0}S, 2.690^{0}E), edifice 4 (59.943^{0}S, 1.845^{0}E), and edifice 11 (66.501^{0}S, 4.061^{0}E), respectively. Half of the edifices exhibit this class of spectra on their flanks (edifice 7 and 4), while the other half of the edifices exhibit these spectra on their tops (edifice 11 and 18). All of the occurrences of this class are correlated with larger morphological features (e.g., ridges and boulders).

2.4.3 Class 3: Smectite-zeolite-iron oxide-dominated Spectra

Spectra in this class exhibit absorptions at 0.54, 0.94, 1.45, 1.78, 1.93, 2.21, and 2.46 μm in CRISM images FRT00007588, FRT00007A8C, FRT00006DE7, HRL000122A0, and HRL000086DE. The absorptions at 1.93, 2.21, and 2.49 μm are relatively broad while roughly half of the spectra exhibit 1.45 and 1.78 μm bands (Figures 2 and 4). All spectra exhibit variable band depths but similar overall spectral character including band shape. The combination of these bands is not unique to one specific type of mineral and suggests a few possible interpretations. The absorption at 0.54 μm is consistent with hematite while the absorption at 0.94 μm is consistent with goethite or lepidocrocite, suggesting a mixture of oxides or other ferric phases. Aluminum smectites are indicated by a strong 2.21 μm band made by a 2Al-OH combination overtone [*Bishop et al.*, 2002a, 2008, p.2002; *Ehlmann et al.*, 2009]. While the 2.21 μm band is also found in spectra of hydrated silica due to SiOH-bending and OH-stretching, it is typically part of a doublet band with another, usually weaker absorption at ~2.26 μm that can create a highly asymmetric band [*Herzberg*, 1945; *Bayly et al.*, 1963; *Langer and Flörke*, 1974; *Rice et al.*, 2013]. As we typically do not see this doublet feature or an asymmetric band, our spectra seem more consistent with Al-phyllosilicates, most likely an Al-smectite like montmorillonite.

Zeolites exhibit strong absorptions at ~1.4, ~1.9, and ~2.5 μm and weaker bands at ~1.78 and, more rarely, ~2.2 μm (although these two bands are not often seen in combination) [*Cloutis et al.*, 2002; *Clark et al.*, 2007]. The absorption bands at ~1.4, ~1.9, and ~1.78 μm that are characteristic of zeolite are due to water bound in the molecular structure [*Cloutis et al.*, 2002; *Clark et al.*, 2007; *Ehlmann et al.*, 2009; *Rice et al.*, 2013; *Viviano-Beck et al.*, 2014] and will not be observed unless the material is sufficiently hydrated. Thus, the identification of zeolites has been shown to be difficult based on visible and near-infrared (VNIR) spectroscopy alone because of their similarity to other hydrated minerals (e.g. sulfates and silica [*Ehlmann et al.*, 2009]); however, zeolites can be distinguished by careful analysis of their hydration absorption bands, as they are usually shifted towards longer wavelengths compared to hydrated sulfates and silica [*Cloutis et al.*, 2002; *Viviano-Beck et al.*, 2014]. As discussed in Class 2, absorptions shifted to longer wavelengths are more consistent with a zeolite interpretation. Here, we see the 1.45 and the 1.78 μm bands, which are at longer wavelengths than what is observed in Class 2.

Thus, we interpret this spectral class as a mixture of phases, including smectites, zeolites, and Fe-oxides (Figures 2 and 4). This assemblage is consistent with the most commonly observed mineral assemblage of palagonite [*Allen et al.*, 1981; *Morris et al.*, 1990; *Farrand and Singer*, 1992; *Stroncik and Schmincke*, 2002; *Michalski et al.*, 2005; *Warner and Farmer*, 2010; *Cousins et al.*, 2013; *Massey et al.*, 2017], and, indeed, laboratory spectra of terrestrial palagonites are a good match for spectra in this class (Figure 4).

The five CRISM images that are included in this class are located on three edifices in the region: HRL000086DE on edifice 4, HRL000122A0 on edifice 11, and FRT00007588, FRT00007A8C, and FRT00006DE7 on edifice 15 (Figure 4). All of the images in this class are located on the tops of the edifices. Ackiss and Wray, [2014] document the association of hydrated material on edifice 15 and the nearby Sisyphi Cavi, proposing that volcano-induced meltwater could have drained westward towards the Cavi. This interpretation is consistent with the overall morphology, which is similar to braided stream channels on Earth made by large meltwater events (jökulhlaup) [*Warner and Farmer*, 2010].

2.5 Discussion

Here we have examined the mineralogies of edifices in the Sispyhi Planum region to answer the question: What mineral assemblages would be present on Noachian Mars if volcanism occurred on an ancient "Snowball Mars"? Overall, the results of this study have shown that the most prevalent mineral assemblages on the Sisyphi Montes are 1) gypsum-dominated, 2) polyhydrated sulfate-dominated, and 3) smectite-zeolite-iron oxide-dominated. This diverse range of alteration minerals probably cannot be attributed to just surface weathering without invoking highly variable conditions across and between the edifices. Instead, given the volcanic context, these mineral assemblages are broadly consistent with hydrothermal alteration in a volcanic environment and therefore could be associated with either subglacial or subaerial volcanism (Table 1). Additionally, the Sisyphi Montes are flat-topped and steep sided edifices, as detailed by Ghatan and Head [2002] and Campbell et al., [2016], which is consistent with classic terrestrial subglacial volcanic morphologies [*Russell et al.*, 2014]. Combining the mineralogy results reported here with the previously reported morphology of the region presents a strong case for a subglacial hydrothermal environment.

In terrestrial systems, sulfates (and specifically gypsum) are found in a variety of subglacial and subaerial volcanic environments. Alunogen (an Al polyhydratred sulfate) and gypsum in combination have been identified in some samples from glaciovolcanic hydrothermal sites in Iceland, and are hypothesized to be formed during later lower temperature alteration of palagonite [*Cousins et al.*, 2013]. Thus, a similar early diagenetic sulfate formation mechanism could explain our sulfate detections in the Sisyphi Montes. In Svalbard, physical abrasion from the movement of the glaciers has been shown to leave insoluble products of chemical weathering behind (e.g., Fe and Al) whereas soluble chemical weathering products (SO_4, HCO_2, Ca, and Mg) are transported [*Szynkiewicz et al.*, 2013]. These products then concentrate, freeze, and evaporate and precipitate salt efflorescence (e.g. calcite, gypsum, Ca-Mg sulfates) in the proglacial zone [*Szynkiewicz et al.*, 2013] and thus are the expected observable minerals in a glacial outwash deposit (jökulhlaup). This process, with the addition of wind erosion, is the proposed hypothesis for the creation of the gypsum dunes in the northern circumpolar region of Mars [*Szynkiewicz et al.*, 2013]. Thus, the sulfate outcrops in this study could be related to a subglacial process; however, it is also possible that they could have been formed during other volcanic processes (e.g., subaerial hydrothermal alteration) after the edifice was constructed.

The smectite-zeolite-iron oxide-rich mixture that we report here is the most consistent with a specifically glaciovolcanic hydrothermal environment. This mixture contains detectable and thus most likely volumetrically abundant zeolites (i.e., not just vug-filling), the detection of which, along with smectites and iron oxides, makes a strong case for palagonite. While zeolites are commonly formed by many types of aqueous processes, including under both hydrothermal and diagenetic conditions, they are most commonly formed in voids and vesicles. However, the zeolites observed here are likely not vesicle-filling zeolites as these would be present in such small amounts (≤10%) [*Ehlmann et al.*, 2012; *Gelves et al.*, 2016] that they most likely would not be detectable at CRISM resolution. Because the zeolites are in high abundance and are associated with smectites, iron oxides, and sometimes sulfates, a valid interpretation for the mineral assemblage would be palagonite. Palagonite has been shown to be comprised of secondary crystalline and poorly crystalline hydrated and oxidized hydrothermal alteration products of sideromelane formed at low-temperatures and high water-to-rock ratios [*Allen et al.*, 1981; *Morris et al.*, 1990; *Stroncik and Schmincke*, 2002; *Michalski et al.*, 2005; *Warner and Farmer*, 2010; *Cousins et al.*, 2013] and is commonly found in submarine and subglacial volcanic environments. Thus, the potential identification of palagonite on the Sisyphi Montes strengthens the case for a subglacial origin for these edifices. Based on their excellent morphologic preservation and diverse mineral signatures, the Sisyphi Montes could serve as a type example for ice-magma processes on Mars.

Thus, the mineral assemblages that we have identified in the Sisyphi Montes (gypsum; polyhydrated sulfates; smectites, zeolites, and iron oxides) could all have formed in a subglacial hydrothermal environment. However, the alteration history may have been more complex. While the palagonite assemblage (smectites, zeolites, and iron oxides) did most likely form during subglacial eruption and emplacement of the edifices, the sulfates could have formed later, due to either subaerial hydrothermal activity or subglacial weathering.

Submarine and glaciovolcanic hydrothermal systems like those we hypothesize formed the Sisyphi Montes are extremely habitable environments. In submarine environments, hydrothermal vents (e.g., black smokers) harbor rich communities of microbial life. The chemistries at the vents correlates well with inferred metabolic processes of modern prokaryotic autotrophs leading to the hypothesis that these vents could have facilitated the origin of life [*Martin et al.*, 2008]. The dissolution and alteration of sideromelane that forms rocks and minerals like palagonite and sulfates, respectively, also feeds diverse chemotrophic organisms [*Alt and Mata*, 2000; *Benzerara et al.*, 2007]. Seafloor basalt and sideromelane has been observed to have pore space that may have previously been occupied by microbes and subsequently filled with other minerals – a possible biosignature that could be preserved in the geologic record [*Alt and Mata*, 2000; *Benzerara et al.*, 2007]. Similarly, subglacial hydrothermal systems maintain abundant water and high temperatures around the volcanic vents. Regions where life in the subglacial environment could coalesce include the vent/edifice and the meltwater lake that is generated in this process [*Cousins and Crawford*, 2011]. This location creates an ideal location for microbial habitats because hydrothermal deposits can preserve biosignatures in their crystalline structures [*Cousins et al.*, 2013]. Additionally, the metabolisms of subglacial microbial populations are consistent with the aqueous geochemistry of glacial melt, leading to the idea that microbial activity plays an important role in the solute flux of glaciers [*Skidmore et al.*, 2005; *Tranter et al.*, 2005].

Similar habitable subglacial hydrothermal environments could have existed elsewhere on Mars, in particular in the northern plains [*Fagan et al.*, 2010; *Mouginis-Mark et al.*, 2016]. Chryse and Acidalia Planitia have edifices that exhibit horizontal layering with cones on their summit [*Martínez-Alonso et al.*, 2011]. Fan-shaped deposits around Arsia Mons contain steep-sided mounds, steep-sided flow-like landforms with depressed craters, digitate flows, and steep-sided flat-topped plateau features collectively interpreted to be subglacial pillow sheets, hyaloclastite mounds, ice-confined flows, and tuyas [*Scanlon et al.*, 2014]. However, these features are all in Amazonian and Hesperian terrains, and no clear subglacial morphologies have yet been identified to date in Noachian terrains, a time when they are expected to have occurred [Robbins et al., 2013; Cassanelli and Head, 2015; Fastook and Head, 2015].

This lack of obvious subglacial geomorphologic features dating to the late Noachian may be inconsistent with the Late Noachian Icy Highlands model. As volcanism was prevalent during that time [Robbins et al., 2013], and it is postulated that ice sheets were widespread [Cassanelli and Head, 2015; Fastook and Head, 2015], ice-magma interactions should have been common on Mars during the Noachian. However, the lack of clear Noachian glaciovolcanoes from this time period could also be due to erosion and degradation, so a mineralogical survey for spectral signatures similar to those in the Sysiphi Montes may help us to better identify these features.

The presence or lack of mineralogical and/or morphological evidence of ice-magma interactions could be a good test for the Late Noachian Icy Highlands Model [*Fastook and Head*, 2015].

2.6 Conclusion

In this study, we identified and examined the mineral assemblages detectable from orbit on possible glaciovolcanic edifices in the Sisyphi Planum region of Mars, a high-latitude region in the southern highlands nestled between the Argyre and Hellas impact basins. Analysis of 11 CRISM images located on the volcanic edifices revealed three distinct spectral classes in the region which are interpreted to be: gypsum-dominated, smectite-zeolite-iron oxide-dominated (possibly palagonite), and polyhydrated sulfate-dominated material. These new mineral identifications would not have been possible without the enhanced CRISM MTRDR processing and filtering techniques [*Seelos et al.*, 2011].

The combination of these three spectral classes located on the volcanic edifices as well as the geomorphology of the region strongly suggests the formation of these minerals during an subglacial eruption or during alteration in associated hydrothermal systems. A key component of these findings is the possible identification of palagonite, indicating water-magma interactions, based on the spectral identification of an assemblage of smectites, zeolites, and iron oxides.

The identification of glaciovolcanic hydrothermal systems has significant implications for the long-term habitability of Mars. Locations of ice-magma interactions are present from the Noachian (in Sisyphi Planum) through the Amazonian (in Acidalia Planitia), suggesting that habitable surface environments spanned much of Mars' history. Because of the excellent morphological preservation of the Sisyphi Montes and their morphological and mineralogical similarities to terrestrial subglacial volcanoes, this region can be used as a type location for glaciovolcanism on Mars. We can use the mineral assemblage of Sisyphi Planum to examine other locations on Mars to determine how common glaciovolcanic processes have been in the martian geologic record.

2.7 Acknowledgements and Data

This work was supported by the NASA Earth and Space Science Fellowship. We would like to thank the CRISM team for a spectacular dataset, the CRISM PDS and team for the data used in this study, the Data Center Hub (https://datacenterhub.org/projects/ackiss2018sisyphimontes), where the data from this manuscript is stored, and Liz Rampe and an anonymous reviewer for the useful feedback.

2.8 References

Ackiss, S. E., and J. J. Wray (2014), Occurrences of possible hydrated sulfates in the southern high latitudes of Mars, *Icarus*, *243*, 311–324, doi:10.1016/j.icarus.2014.08.016.

Alexander, E. B., J. I. Mallory, and W. L. Colwell (1993), Soil-elevation relationships on a volcanic plateau in the southern Cascade Range, northern California, USA, *Catena*, *20*(1–2), 113–128.

Allen, C. C., J. L. Gooding, M. Jercinovic, and K. Keil (1981), Altered basaltic glass: A terrestrial analog to the soil of Mars, *Icarus*, *45*(2), 347–369, doi:10.1016/0019-1035(81)90040-3.

Alt, J. C., and P. Mata (2000), On the role of microbes in the alteration of submarine basaltic glass: a TEM study, *Earth Planet. Sci. Lett.*, *181*(3), 301–313, doi:10.1016/S0012-821X(00)00204-1.

Anderson, S. P. (2005), Glaciers show direct linkage between erosion rate and chemical weathering fluxes, *Geomorphology*, *67*(1), 147–157.

Arfstrom, J., and W. K. Hartmann (2005), Martian flow features, moraine-like ridges, and gullies: Terrestrial analogs and interrelationships, *Icarus*, *174*(2), 321–335, doi:10.1016/j.icarus.2004.05.026.

Arnalds, O. (2004), Volcanic soils of Iceland, *CATENA*, *56*(1–3), 3–20, doi:10.1016/j.catena.2003.10.002.

Arnalds, O., and J. Kimble (2001), Andisols of deserts in Iceland, *Soil Sci. Soc. Am. J.*, *65*(6), 1778–1786.

Baker, V. R., and R. G. Strom (1991), Ancient oceans, ice sheets and the hydrological cycle on Mars, *Nature*, *352*(6336), 589.

Banin, A., and L. Margulies (1983), Simulation of Viking biology experiments suggests smectites not palagonites, as martian soil analogues, *Nature*, *305*(5934), 523–525, doi:10.1038/305523a0.

Bayly, J. G., V. B. Kartha, and W. H. Stevens (1963), The absorption spectra of liquid phase H2O, HDO and D2O from 0· 7 μm to 10 μm, *Infrared Phys.*, *3*(4), 211–222.

Benzerara, K., N. Menguy, N. R. Banerjee, T. Tyliszczak, G. E. Brown Jr., and F. Guyot (2007), Alteration of submarine basaltic glass from the Ontong Java Plateau: A STXM and TEM study, *Earth Planet. Sci. Lett.*, *260*(1–2), 187–200, doi:10.1016/j.epsl.2007.05.029.

Berkley, J. L., and M. J. Drake (1981), Weathering of Mars: Antarctic analog studies, *Icarus*, *45*(1), 231–249, doi:10.1016/0019-1035(81)90016-6.

Bibring, J.-P., S. W. Squyres, and R. E. Arvidson (2006), Merging Views on Mars, *Science*, *313*(5795), 1899–1901, doi:10.1126/science.1132311.

Bibring, J.-P. et al. (2007), Coupled Ferric Oxides and Sulfates on the Martian Surface, *Science*, *317*, 1206, doi:10.1126/science.1144174.

Bishop, J., J. Madejová, P. Komadel, and H. Fröschl (2002a), The influence of structural Fe, Al and Mg on the infrared OH bands in spectra of dioctahedral smectites, *Clay Miner.*, *37*(4), 607–616.

Bishop, J. L., P. Schiffman, and R. Southard (2002b), Geochemical and mineralogical analyses of palagonitic tuffs and altered rinds of pillow basalts in Iceland and applications to Mars, *Geol. Soc. Lond. Spec. Publ.*, *202*(1), 371–392, doi:10.1144/GSL.SP.2002.202.01.19.

Bishop, J. L., M. D. Lane, M. D. Dyar, and A. J. Brown (2008), Reflectance and emission spectroscopy study of four groups of phyllosilicates: Smectites, kaolinite-serpentines, chlorites and micas, *Clay Miner.*, *43*(1), 35–54.

Campbell, A., S. Ackiss, and B. H. Horgan (2016), Morphology of possible subglacial volcanoes in the Sysphi Montes region of Mars, vol. 47, p. 1554.

Carr, M. H., and J. W. Head (2010), Geologic history of Mars, *Earth Planet. Sci. Lett.*, *294*(3), 185–203.

Cassanelli, J. P., and J. W. Head (2015), Firn densification in a Late Noachian "icy highlands" Mars: Implications for ice sheet evolution and thermal response, *Icarus*, *253*, 243–255, doi:10.1016/j.icarus.2015.03.004.

Claridge, G. G. C. (1965), The clay mineralogy and chemistry of some soils from the Ross Dependency, Antarctica, *N. Z. J. Geol. Geophys.*, *8*(2), 186–220.

Clark, Roger N., et al. "High spectral resolution reflectance spectroscopy of minerals." *Journal of Geophysical Research: Solid Earth* 95.B8 (1990): 12653-12680.

Clark, R., G. A. Swayze, R. Wise, E. Livo, T. Hoefen, R. Kokaly, and S. J. Sutley (2007), USGS digital spectral library splib06a: U.S. Geological Survey, *Digit. Data Ser. 231*.

Cloutis, E. A., P. M. Asher, and S. A. Mertzman (2002), Spectral reflectance properties of zeolites and remote sensing implications, *J. Geophys. Res. Planets*, *107*(E9), 5067, doi:10.1029/2000JE001467.

Cloutis, E. A. et al. (2006), Detection and discrimination of sulfate minerals using reflectance spectroscopy, *Icarus*, *184*, 121–157, doi:10.1016/j.icarus.2006.04.003.

Cloutis, E. A., M. A. Craig, R. V. Kruzelecky, W. R. Jamroz, A. Scott, F. C. Hawthorne, and S. A. Mertzman (2008), Spectral reflectance properties of minerals exposed to simulated Mars surface conditions, *Icarus*, *195*(1), 140–168, doi:10.1016/j.icarus.2007.10.028.

Cousins, C. R., and I. A. Crawford (2011), Volcano-Ice Interaction as a Microbial Habitat on Earth and Mars, *Astrobiology*, *11*, 695–710, doi:10.1089/ast.2010.0550.

Cousins, C. R. et al. (2013), Glaciovolcanic hydrothermal environments in Iceland and implications for their detection on Mars, *J. Volcanol. Geotherm. Res.*, *256*, 61–77, doi:10.1016/j.jvolgeores.2013.02.009.

Craddock, R. A., and A. D. Howard (2002), The case for rainfall on a warm, wet early Mars, *J. Geophys. Res. Planets*, *107*(E11).

Crompton, J. W., G. E. Flowers, D. Kirste, B. Hagedorn, and M. J. Sharp (2015), Clay mineral precipitation and low silica in glacier meltwaters explored through reaction-path modelling, *J. Glaciol.*, *61*(230), 1061–1078.

Crowley, James K. "Visible and near-infrared (0.4–2.5 μm) reflectance spectra of Playa evaporite minerals." *Journal of Geophysical Research: Solid Earth* 96.B10 (1991): 16231-16240.

Delvaux, B., A. J. Herbillon, and L. Vielvoye (1989), Characterization of a weathering sequence of soils derived from volcanic ash in Cameroon. Taxonomic, mineralogical and agronomic implications, *Geoderma*, *45*(3), 375–388, doi:10.1016/0016-7061(89)90017-7.

Ehlmann, B. L. et al. (2009), Identification of hydrated silicate minerals on Mars using MRO-CRISM: Geologic context near Nili Fossae and implications for aqueous alteration, *J. Geophys. Res. Planets*, *114*, doi:10.1029/2009JE003339.

Ehlmann, B. L., J. F. Mustard, S. L. Murchie, J.-P. Bibring, A. Meunier, A. A. Fraeman, and Y. Langevin (2011), Subsurface water and clay mineral formation during the early history of Mars, *Nature*, *479*(7371), 53–60, doi:10.1038/nature10582.

Ehlmann, B. L., D. L. Bish, S. W. Ruff, and J. F. Mustard (2012), Mineralogy and chemistry of altered Icelandic basalts: Application to clay mineral detection and understanding aqueous environments on Mars, *J. Geophys. Res. Planets*, *117*, E00J16, doi:10.1029/2012JE004156.

Fagan, A. L., S. E. H. Sakimoto, and S. S. Hughes (2010), Formation constraints on Martian north polar volcanic edifices, *J. Geophys. Res. Planets*, *115*(E7).

Fairén, A. G. (2010), A cold and wet Mars, *Icarus*, *208*(1), 165–175, doi:10.1016/j.icarus.2010.01.006.

Farrand, W. H., M. D. Lane, and B. R. Edwards (2008), North and South: Possible Tuyas and Hyaloclastite Hills on the Northern Plains and in the Southern Dorsa Argentea Region of Mars, vol. 39, p. 1761.

Fastook, J. L., and J. W. Head (2015), Glaciation in the Late Noachian Icy Highlands: Ice accumulation, distribution, flow rates, basal melting, and top-down melting rates and patterns, *Planet. Space Sci.*, *106*, 82–98.

Forget, F., R. M. Haberle, F. Montmessin, B. Levrard, and J. W. Head (2006), Formation of glaciers on Mars by atmospheric precipitation at high obliquity, *science*, *311*(5759), 368–371.

Gaidos, E., and G. Marion (2003), Geological and geochemical legacy of a cold early Mars, *J. Geophys. Res. Planets*, *108*(E6), 5055, doi:10.1029/2002JE002000.

Gelves, J.F., Gallego, G.S., Marquez, M.A., 2016. Mineralogical characterization of zeolites present on basaltic rocks from Combia geological formation, La Pintada (Colombia). Microporous and Mesoporous Materials 235, 9–19. doi:10.1016/j.micromeso.2016.07.035

Ghatan, G. J., and J. W. Head (2002), Candidate subglacial volcanoes in the south polar region of Mars: Morphology, morphometry, and eruption conditions, *J. Geophys. Res. Planets*, *107*, 5048, doi:10.1029/2001JE001519.

Golden, D. C., R. V. Morris, D. W. Ming, H. V. Lauer, and S. R. Yang (1993), Mineralogy of three slightly palagonitized basaltic tephra samples from the summit of Mauna Kea, Hawaii, *J. Geophys. Res. Planets*, *98*(E2), 3401–3411, doi:10.1029/92JE02590.

Gooding, J. L., and K. Keil (1978), Alteration of glass as a possible source of clay minerals on Mars, *Geophys. Res. Lett.*, *5*(8), 727–730, doi:10.1029/GL005i008p00727.

Graly, J., K. Licht, and D. L. Bish (2017), Subglacial and Interglacial Chemical Weathering in the Transantarctic Mountains, Available from: https://goldschmidt.info/2017/abstracts/abstractView?id=2017003488 (Accessed 24 August 2017)

Grotzinger, J. P., S. Gupta, M. C. Malin, D. M. Rubin, J. Schieber, K. Siebach, D. Y. Sumner et al. "Deposition, exhumation, and paleoclimate of an ancient lake deposit, Gale crater, Mars." *Science* 350, no. 6257 (2015): aac7575.

Gulick, V. C. (2001), Origin of the valley networks on Mars: A hydrological perspective, *Geomorphology*, *37*(3), 241–268.

Haberle, R. M. (1998), Early Mars climate models, *J. Geophys. Res.*, *103*(28), 467–479.

Halevy, I., and J. W. Head (2014), Episodic warming of early Mars by punctuated volcanism, *Nat. Geosci.*, *7*(12), 865–868, doi:10.1038/ngeo2293.

Halevy, I., M. T. Zuber, and D. P. Schrag (2007), A Sulfur Dioxide Climate Feedback on Early Mars, *Science*, *318*(5858), 1903–1907, doi:10.1126/science.1147039.

Harrison, K. P., and R. E. Grimm (2002), Controls on Martian hydrothermal systems: Application to valley network and magnetic anomaly formation, *J. Geophys. Res. Planets*, *107*(E5), 1–1, doi:10.1029/2001JE001616.

Hay, R. L., and A. Iijima (1968), Nature and Origin of Palagonite Tuffs of the Honolulu Group on Oahu, Hawaii, *Geol. Soc. Am. Mem.*, *116*, 331–376, doi:10.1130/MEM116-p331.

Hay, R. L., and B. F. Jones (1972), Weathering of Basaltic Tephra on the Island of Hawaii, *Geol. Soc. Am. Bull.*, *83*(2), 317–332, doi:10.1130/0016-7606(1972)83[317:WOBTOT]2.0.CO;2.

Head, J. (2013), The Early Climate History of Mars: “Warm and Wet” or “Cold and Icy”?, vol. 15, pp. EGU2013-10106.

Head, J. W., and D. R. Marchant (2014), The climate history of early Mars: insights from the Antarctic McMurdo Dry Valleys hydrologic system, *Antarct. Sci.*, *26*(06), 774–800.

Head, J. W., and S. Pratt (2001), Extensive Hesperian-aged south polar ice sheet on Mars: Evidence for massive melting and retreat, and lateral flow and ponding of meltwater, *J. Geophys. Res. Planets*, *106*(E6), 12275–12299, doi:10.1029/2000JE001359.

Herzberg, G. (1945), *Molecular Spectra and Molecular Structure: Infrared and Raman Spectra of Polyatomic Molecules; by Gerhard Herzberg*, Van Nostrand Reinhold.

Horgan, B. H., J. F. Bell, E. Z. Noe Dobrea, E. A. Cloutis, D. T. Bailey, M. A. Craig, L. H. Roach, and J. F. Mustard (2009), Distribution of hydrated minerals in the north polar region of Mars, *J. Geophys. Res. Planets*, *114*, 1005, doi:10.1029/2008JE003187.

Horgan, B. H. N., R. Smith, O. A. Chadwick, and G. J. Retallack (2017), THE EFFECTS OF CLIMATE, ENVIRONMENT, AND DIAGENESIS ON THE SPECTRAL PROPERTIES OF VOLCANIC SOILS, GSA.

Howari, F. M., P. C. Goodell, and S. Miyamoto (2002), Spectral Properties of Salt Crusts Formed on Saline Soils, *J. Environ. Qual.*, *31*(5), 1453, doi:10.2134/jeq2002.1453.

Hunt, G. R., J. W. Salisbury, and C. J. Lenhoff (1973), Visible and near infrared spectra of minerals and rocks. VI. Additional silicates, *Mod. Geol.*, *4*, 85–106.

Jakobsson, S. (1978), Environmental factors controlling the palagonization of the Surtsey tephra, Iceland, *Bull Geol Soc Den.*, *27*(Special Issue), 91–105.

Jakobsson, S., and M. Gudmundsson (2008), Subglacial and intraglacial volcanic formations in Iceland, *Jökull*, *58*, 179–196.

Jakobsson, S. P., and J. G. Moore (1986), Hydrothermal minerals and alteration rates at Surtsey volcano, Iceland, *Geol. Soc. Am. Bull.*, *97*(5), 648–659, doi:10.1130/0016-7606(1986)97<648:HMAARA>2.0.CO;2.

Jakosky, B. M., and R. J. Phillips (2001), Mars' volatile and climate history, *Nature*, *412*(6843), 237–244, doi:10.1038/35084184.

Jercinovic, M. J., K. Keil, M. R. Smith, and R. A. Schmitt. "Alteration of basaltic glasses from north-central British Columbia, Canada." *Geochimica et Cosmochimica Acta* 54, no. 10 (1990): 2679-2696.

Kargel, J. S., and R. G. Strom (1992), Ancient glaciation on Mars, *Geology*, *20*(1), 3–7, doi:10.1130/0091-7613(1992)020<0003:AGOM>2.3.CO;2.

Karunatillake, S., Wray, J.J., Gasnault, O., McLennan, S.M., Deanne Rogers, A., Squyres, S.W., Boynton, W.V., Skok, J.R., Button, N.E., Ojha, L., 2016. The association of hydrogen with sulfur on Mars across latitudes, longitudes, and compositional extremes. J. Geophys. Res. Planets 121, 2016JE005016. doi:10.1002/2016JE005016

Kolb, E. J., and K. L. Tanaka (2001), Geologic History of the Polar Regions of Mars Based on Mars Global Surveyor Data. II. Amazonian Period, *Icarus*, *154*, 22–39, doi:10.1006/icar.2001.6676.

Langer, K., and O. W. Flörke (1974), Near infrared absorption spectra (4000–9000 cm− 1) of opals and the role of "water" in these SiO 2· nH 2 O minerals, *Fortschritte Mineral.*, *52*(1), 17–51.

Malin, M. C., and K. S. Edgett (2003), Evidence for persistent flow and aqueous sedimentation on early Mars, *Science*, *302*(5652), 1931–1934.

Mangold, N., C. Quantin, V. Ansan, C. Delacourt, and P. Allemand (2004), Evidence for precipitation on Mars from dendritic valleys in the Valles Marineris area, *Science*, *305*(5680), 78–81.

Martin, W., J. Baross, D. Kelley, and M. J. Russell (2008), Hydrothermal vents and the origin of life, *Nat. Rev. Microbiol.*, *6*(11), 805.

Martínez-Alonso, S., M. T. Mellon, M. E. Banks, L. P. Keszthelyi, and A. S. McEwen (2011), Evidence of volcanic and glacial activity in Chryse and Acidalia Planitiae, Mars, *Icarus*, *212*(2), 597–621, doi:10.1016/j.icarus.2011.01.004.

Massey, E. A., Greenough, J. D., and Edwards, B. R. A. (2017). comparative study of glaciovolcanic palagonitization of tholeiitic and alkaline sideromelane at Helgafell, Iceland and Wells Gray, BC Canada (Master's thesis). Retrieved from https://circle.ubc.ca

McEwen, A. S. et al. (2007), A Closer Look at Water-Related Geologic Activity on Mars, *Science*, *317*, 1706, doi:10.1126/science.1143987.

Michalski, J. R., M. D. Kraft, T. G. Sharp, and P. R. Christensen (2005), Palagonite-like Alteration Products on the Earth and Mars I: Spectroscopy (0.4-25 microns) of Weathered Basalts and Silicate Alteration Products, vol. 36.

Mitchell, N. C., D. G. Masson, A. B. Watts, M. J. Gee, and R. Urgeles (2002), The morphology of the submarine flanks of volcanic ocean islands: a comparative study of the Canary and Hawaiian hotspot islands, *J. Volcanol. Geotherm. Res.*, *115*(1), 83–107.

Morris, R. V., J. L. Gooding, H. V. Lauer, and R. B. Singer (1990), Origins of Marslike spectral and magnetic properties of a Hawaiian palagonitic soil, *J. Geophys. Res. Solid Earth*, *95*(B9), 14427–14434, doi:10.1029/JB095iB09p14427.

Mouginis-Mark, P.J., Wilson, L., 2016. Possible sub-glacial eruptions in the Galaxias Quadrangle, Mars. Icarus 267, 68–85. doi:10.1016/j.icarus.2015.11.025

Murchie, S. et al. (2007), Compact Reconnaissance Imaging Spectrometer for Mars (CRISM) on Mars Reconnaissance Orbiter (MRO), *J. Geophys. Res. Planets*, *112*, doi:10.1029/2006JE002682.

Pauly, Bruce D., Peter Schiffman, Robert A. Zierenberg, and David A. Clague. "Environmental and chemical controls on palagonitization." *Geochemistry, Geophysics, Geosystems* 12, no. 12 (2011).

Paque, M., Detienne, M., Maters, E. C., & Delmelle, P. (2016). Smectites and zeolites in ash from the 2010 summit eruption of Eyjafjallajökull volcano, Iceland. Bulletin of Volcanology, 78, 61. doi: 10.1007/s00445-016-1056-x

Picardi, G. et al. (2004), Performance and surface scattering models for the Mars Advanced Radar for Subsurface and Ionosphere Sounding (MARSIS), *Planet. Space Sci.*, *52*(1–3), 149–156, doi:10.1016/j.pss.2003.08.020.

Plaut, J. J., A. Ivanov, A. Safaeinili, S. M. Milkovich, G. Picardi, R. Seu, and R. Phillips (2007), Radar Sounding of Subsurface Layers in the South Polar Plains of Mars: Correlation with the Dorsa Argentea Formation, vol. 38, p. 2144.

Pollack, J. B., J. F. Kasting, S. M. Richardson, and K. Poliakoff (1987), The case for a wet, warm climate on early Mars, *Icarus*, *71*(2), 203–224, doi:10.1016/0019-1035(87)90147-3.

Rampe, E. B., B. Horgan, N. Scudder, R. J. Smith, and A. M. Rutledge (2017), Mineralogy of Rock Flour in Glaciated Volcanic Terrains: An Analog for a Cold and Icy Early Mars, vol. 48, p. 2437.

Retallack, G. J. (2008), *Soils of the past: an introduction to paleopedology*, John Wiley & Sons.

Rice, M. S., E. A. Cloutis, J. F. Bell III, D. L. Bish, B. H. Horgan, S. A. Mertzman, M. A. Craig, R. W. Renaut, B. Gautason, and B. Mountain (2013), Reflectance spectra diversity of silica-rich materials: Sensitivity to environment and implications for detections on Mars, *Icarus*, *223*(1), 499–533, doi:10.1016/j.icarus.2012.09.021.

Robbins, S. J., B. M. Hynek, R. J. Lillis, and W. F. Bottke (2013), Large impact crater histories of Mars: The effect of different model crater age techniques, *Icarus*, *225*, 173–184, doi:10.1016/j.icarus.2013.03.019.

Rodriguez, J. A. P., and K. L. Tanaka (2006), Sisyphi Montes and Southwest Hellas Paterae: Possible Impact, Cryotectonic, Volcanic, and Mantle Tectonic Processes and Hellas Basin Rings, *LPI Contrib.*, *1323*, 8066.

Romagnoli, C., and S. P. Jakobsson (2015), Post-eruptive morphological evolution of island volcanoes: Surtsey as a modern case study, *Geomorphology*, *250*, 384–396, doi:10.1016/j.geomorph.2015.09.016.

Russell, J. K., B. R. Edwards, L. Porritt, and C. Ryane (2014), Tuyas: a descriptive genetic classification, *Quat. Sci. Rev.*, *87*, 70–81, doi:10.1016/j.quascirev.2014.01.001.

Sackmann, I.-J., and A. I. Boothroyd (2003), Our Sun. V. A bright young Sun consistent with helioseismology and warm temperatures on ancient Earth and Mars, *Astrophys. J.*, *583*(2), 1024.

Scanlon, K. E., and J. W. Head (2014), The Dorsa Argentea Formation: Synthesis of Glacial Features and History of Late Noachian-Early Hesperian Martian Climate Change, vol. 45, p. 1477.

Scanlon, K. E., J. W. Head, L. Wilson, and D. R. Marchant (2014), Volcano–ice interactions in the Arsia Mons tropical mountain glacier deposits, *Icarus*, *237*, 315–339, doi:10.1016/j.icarus.2014.04.024.

Schiffman, Peter, Howard J. Spero, R. J. Southard, and D. A. Swanson. "Controls on palagonitization versus pedogenic weathering of basaltic tephra: Evidence from the consolidation and geochemistry of the Keanakako'i Ash Member, Kilauea Volcano." *Geochemistry, Geophysics, Geosystems* 1, no. 8 (2000).

Scudder, N. A., B. Horgan, A. M. Rutledge, and E. B. Rampe (2017), Using Composition to Trace Glacial, Fluvial, and Aeolian Sediment Transport in a Mars-Analog Glaciated Volcanic System, vol. 48, p. 2625.

Seelos, F. P., S. L. Murchie, D. C. Humm, O. S. Barnouin, F. Morgan, H. W. Taylor, C. Hash, and CRISM Team (2011), CRISM Data Processing and Analysis Products Update — Calibration, Correction, and Visualization, vol. 42, p. 1438.

Seelos, K. D., N. T. Bridges, J. C. Andrews-Hanna, F. P. Seelos, and S. L. Murchie (2012), Investigation of Anomalous Terrains on the West Flank of Olympus Mons using CRISM Data, *AGU Fall Meet. Abstr.*, *11*.

Sheldon, N. D., and N. J. Tabor (2009), Quantitative paleoenvironmental and paleoclimatic reconstruction using paleosols, *Earth-Sci. Rev.*, *95*(1–2), 1–52, doi:10.1016/j.earscirev.2009.03.004.

Singer, A. (1974), Mineralogy of palagonitic material from the Golan Heights, Israel, *Clays Clay Miner.*, *22*(3), 231–240.

Singer, A. (1980), The paleoclimatic interpretation of clay minerals in soils and weathering profiles, *Earth-Sci. Rev.*, *15*(4), 303–326.

Singer, R. B. (1982), Spectral evidence for the mineralogy of high-albedo soils and dust on Mars, *J. Geophys. Res. Solid Earth*, *87*(B12), 10159–10168, doi:10.1029/JB087iB12p10159.

Skidmore, M., S. P. Anderson, M. Sharp, J. Foght, and B. D. Lanoil (2005), Comparison of Microbial Community Compositions of Two Subglacial Environments Reveals a Possible Role for Microbes in Chemical Weathering Processes, *Appl. Environ. Microbiol.*, *71*(11), 6986–6997, doi:10.1128/AEM.71.11.6986-6997.2005.

Smith, R. J., B. Horgan, E. Rampe, E. Dehouck, and R. V. Morris (2017), X-Ray Amorphous Phases in Terrestrial Analog Volcanic Sediments: Implications for Amorphous Phases in Gale Crater, Mars, vol. 48, p. 2465.

Squyres, S., and J. F. Kasting (1994), Early Mars, *Science*, *265*(5173), 744–749.

Stroncik, N. A. & Schmincke, H. U. (2001). Evolution of palagonite: Crystallization, chemical changes, and element budget. Geochemistry Geophysics Geosystems, 2. doi: 10.1029/2000GC000102

Stroncik, N. A., and H.-U. Schmincke (2002), Palagonite – a review, *Int. J. Earth Sci.*, *91*(4), 680–697, doi:10.1007/s00531-001-0238-7.

Swayze, G. A., R. C. Clark, S. J. Sutley, C. A. Gent, B. W. Rockwell, D. L. Blaney, M. J. Post, and B. P. Farm (2002), Mineral Mapping Mauna Kea and Mauna Loa Shield Volcanos on Hawaii Using AVIRIS Data and the USGS Tetracorder Spectral Identification System: Lessons Applicable to the Search for Relict Martian Hydrothermal Systems, *Proc. 11th JPL Airborne Earth Space Workshop*, (JPL Publication 03-4).

Szynkiewicz, Anna, et al. "The polar sulfur cycle in the Werenskioldbreen, Spitsbergen: Possible implications for understanding the deposition of sulfate minerals in the North Polar Region of Mars." *Geochimica et Cosmochimica Acta* 106 (2013): 326-343.

Tanaka, K. L., and Scott (1987), Geologic Maps of the Polar Regions of Mars, *U. S. Geol. Surv., Miscellaneous Investigations*(Series Map I-802-C, Scale 1:15,000,000).

Tranter, M., M. Skidmore, and J. Wadham (2005), Hydrological controls on microbial communities in subglacial environments, *Hydrol. Process.*, *19*(4), 995–998, doi:10.1002/hyp.5854.

Tsai, C. C., Z. S. Chen, C. I. Kao, F. Ottner, S. J. Kao, and F. Zehetner (2010), Pedogenic development of volcanic ash soils along a climosequence in Northern Taiwan, *Geoderma*, *156*(1), 48–59.

Tuffen, H. (2007), Models of ice melting and edifice growth at the onset of subglacial basaltic eruptions, *J. Geophys. Res. Solid Earth*, *112*(B3), B03203, doi:10.1029/2006JB004523.

Ugolini, F. C. (1974), Hydrothermal origin of the clays from the upper slopes of Mauna Kea, Hawaii., *Clays Clay Min.*, *22*, 189–194.

Ugolini, F. C., and J. G. Bockheim (2008), Antarctic soils and soil formation in a changing environment: a review, *Geoderma*, *144*(1), 1–8.

Ugolini, F. C., and R. A. Dahlgren (2002), Soil development in volcanic ash, *Glob. Environ. Res.-Engl. Ed.-*, *6*(2), 69–82.

Utada, M. (2001), Zeolites in Hydrothermally Altered Rocks, *Rev. Mineral. Geochem.*, *45*(1), 305–322, doi:10.2138/rmg.2001.45.10.

Viviano-Beck, C. E. et al. (2014), Revised CRISM spectral parameters and summary products based on the currently detected mineral diversity on Mars, *J. Geophys. Res. Planets*, *119*(6), 2014JE004627, doi:10.1002/2014JE004627.

Warner, N. H., and J. D. Farmer (2010), Subglacial Hydrothermal Alteration Minerals in Jökulhlaup Deposits of Southern Iceland, with Implications for Detecting Past or Present Habitable Environments on Mars, *Astrobiology*, *10*(5), 523–547, doi:10.1089/ast.2009.0425.

Wolfe, E. W., W. S. Wise, and G. B. Dalrymple (1997), *The geology and petrology of Mauna Kea Volcano, Hawaii; a study of postshield volcanism*, USGPO,.

Wordsworth, R., F. Forget, E. Millour, J. W. Head, J.-B. Madeleine, and B. Charnay (2013), Global modelling of the early martian climate under a denser CO2 atmosphere: Water cycle and ice evolution, *Icarus*, *222*(1), 1–19, doi:10.1016/j.icarus.2012.09.036.

Wordsworth, R. D., L. Kerber, R. T. Pierrehumbert, F. Forget, and J. W. Head (2015), Comparison of “warm and wet” and “cold and icy” scenarios for early Mars in a 3-D climate model, *J. Geophys. Res. Planets*, *120*(6), 2015JE004787, doi:10.1002/2015JE004787.

Wray, J. J., S. L. Murchie, S. W. Squyres, F. P. Seelos, and L. L. Tornabene (2009), Diverse aqueous environments on ancient Mars revealed in the southern highlands, *Geology*, *37*, 1043–1046, doi:10.1130/G30331A.1.

Ziegler, K., J. C. Hsieh, O. A. Chadwick, E. F. Kelly, D. M. Hendricks, and S. M. Savin (2003), Halloysite as a kinetically controlled end product of arid-zone basalt weathering, *Chem. Geol.*, *202*(3), 461–478.

2.9 Tables

Table 1. Summary of Terrestrial Mineralogy

Volcanic Environment	Clay Minerals	Sulfates	Fe-Oxides	Zeolites	Other Phases	Hypothesized formation	References
Subglacial Hydrothermal	illite, kaolinite, smectite	gypsum, jarosite, alunogen	hematite, goethite,	heulandite, laumonite, stilbite, erioite, analcime **(zeolites most abundant minerals)**	**Palagonite (most abundant rock)**, sideromelane	low-temperature, high water-to-rock ratio	*Golden et al.*, 1993; *Bishop et al.*, 2002b; *Warner and Farmer*, 2010; *Cousins et al.*, 2013; *Massey et al.*, 2017
Subglacial Weathering	kaolinite				**silica (most abundant),** x-ray amorphous material	Carbonate dissolution, sulfide oxidation, silicate weathering	*Berkley and Drake*, 1981; *Anderson*, 2005; *Crompton et al.*, 2015; *Rampe et al.*, 2017; *Smith et al.*, 2017; *Scudder et al.*, 2017

Table 1 continued

Volcanic Environment	Clay Minerals	Sulfates	Fe-Oxides	Zeolites	Other Phases	Hypothesized formation	References
Subaerial Hydrothermal	kaolinite, smectites, illite **(clay minerals most abundant minerals)**	gypsum, jarosite, alunite	hematite, goethite, ferrihydrite		carbonates, silica	Warm water/ steam percolating through the edifice post eruption	*Ugolini*, 1974; *Wolfe et al.*, 1997; *Swayze et al.*, 2002; *Ehlmann et al.*, 2012; *Rice et al.*, 2013
Subaerial Weathering	**smectites, kaolinite (most abundant),** halloysite, Mg-montmorillanite,		goethite, gibbsite, ferrihydrite, hematite		allophane, imoglite, calcite	Leaching due to infiltration of rainfall and snowmelt into rocks	*Claridge*, 1965; *Singer*, 1974, 1980; *Berkley and Drake*, 1981; *Delvaux et al.*, 1989; *Alexander et al.*, 1993; *Arnalds and Kimble*, 2001; *Ugolini and Dahlgren*, 2002; *Ziegler et al.*, 2003; *Arnalds*, 2004; *Ugolini and Bockheim*, 2008; *Tsai et al.*, 2010;

Table 2. CRISM Regions of Interest.

CRISM Image ID	Numerator (x,y)[a]	Denominator (x,y)[a]	Latitude, Longitude[b]	Mineral Interpretation	Notes
FRT00006DE7	219, 118	28, 118	-70.744, 15.609	Mg sulfate	Figure 2, 4
FRT00007588	260, 437 265, 225	12, 437 5, 225	-70.741, 16.057 -70.731, 16.221	zeolite mixture zeolite mixture	Figure 2, 4
FRT000079E4	337, 61	14, 61	-59.933, 1.761	Mg sulfate	Figure 2
FRT00007A8C	153, 572	27, 572	-70.778, 15.967	zeolite mixture	Figure 2, 4
FRT00007AE6	248, 247	33, 247	-63.162, 18.224	gypsum	Figure 2, 3
FRT00007E11	256, 246	12, 246	-63.162, 18.225	gypsum	Figure 2, 3
FRT00007EB5	367, 568	37, 568	-63.453, 2.690	Mg sulfate	Figure 2
HRL000086DE	228, 74 233, 64 238, 65	97, 74 36, 64 177, 65	-59.943, 1.845 -59.939, 1.855 -59.936, 1.854	Mg sulfate zeolite mixture zeolite mixture	Figure 2
HRL00011898	386, 305	345, 305	-63.417, 17.422	Mg sulfate	Figure 2, 3
HRL000122A0	98, 53	45, 53	-66.586, 4.085	zeolite mixture	Figure 2
HRL000126C5	268, 48	49, 48	-66.501, 4.061	Mg sulfate	Figure 2

[a] (X,Y) pixel coordinates are the center of the 5x5 (25 pixel) Region of Interest (ROI) within which average spectra were extracted from the unprojected CRISM L-detector Targeted Reduced Data Record (TRDR).

[b] Latitude (°N) and longitude (°E) coordinates are planetocentric, positive east and International Astronomical Union 2000 standard.

2.10 Figures

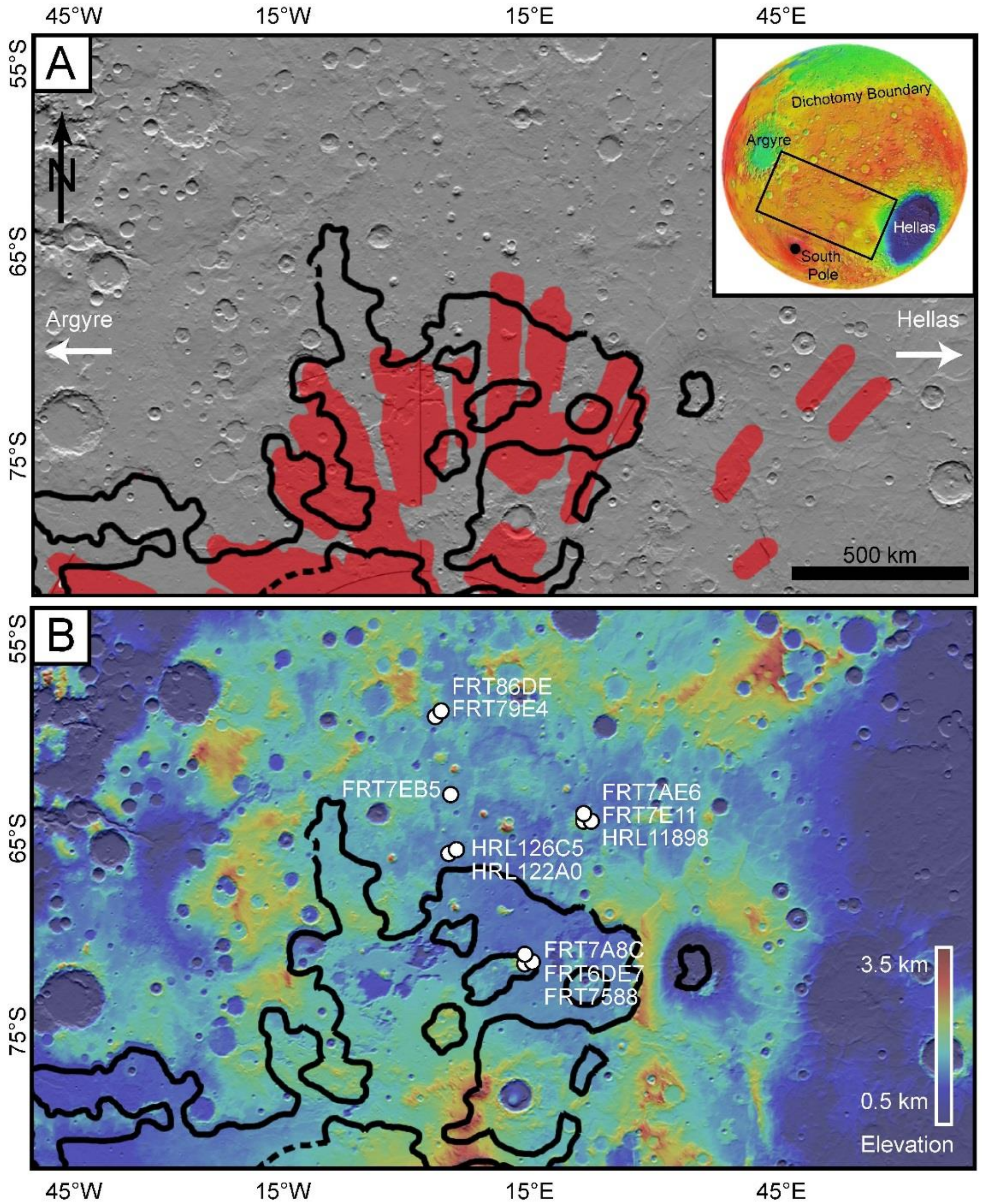

Figure 1. Context for the Sisyphi Montes region. (a) Thermal Emission Imaging System (THEMIS) daytime infrared (IR) background of the Sisyphi Planum. Black outlines show the extent of the Dorsa Argentea Formation (DAF). Regions marked in red show data from the Mars Advanced Radar for Subsurface and Ionospheric Sounding (MARSIS) [*Plaut et al.*, 2007]. Inset shows global context of Sisyphi Planum. (b) Mars Orbiter Laser Altimeter (MOLA) data overlying THEMIS daytime IR. Black outlines show the extent of the DAF. White dots show the locations of the 11 CRISM images used in this study.

Figure 2. Spectral classes in the Sisyphi Montes region. (a) Comparison of visible/near-infrared (VNIR) spectral signatures from MRO CRISM for all three classes from the Sisyphi Montes region. X-axis shows wavelength in nanometers and y-axis shows corrected reflectance. Colors are coordinated to match dots in part (a). (b) MOLA data overlying THEMIS daytime IR. Blue dots show the locations of Class 1: gypsum-dominated material, red dots show the locations of Class 2: polyhydrated sulfate-dominated material, and green dots show the locations of Class 3: smectite-zeolite-iron oxide-dominated material. Edifices are labeled using the labeling scheme in Ghatan and Head [2002]. Figure insets are also shown. (c-g) THEMIS data showing the edifices close up. CRISM footprints used in this study are also shown in black.

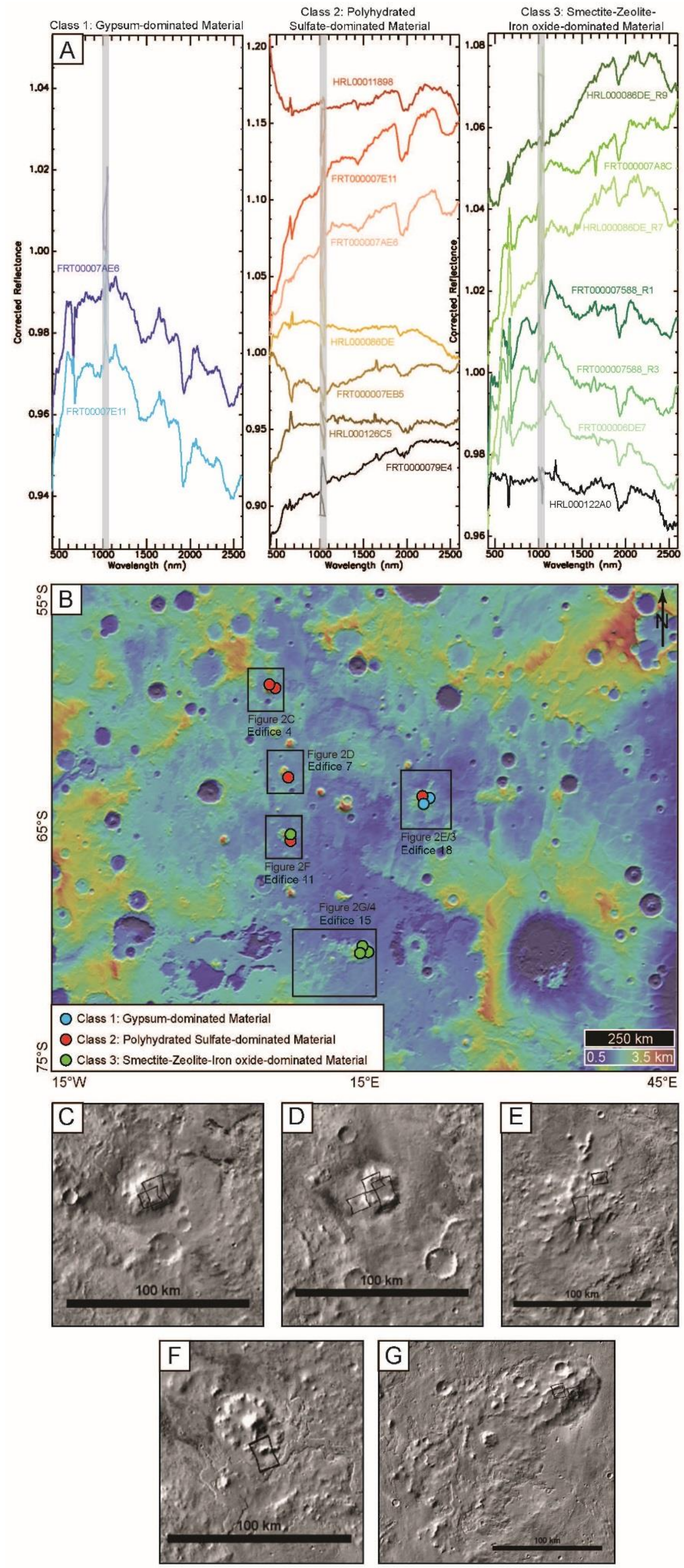

Class 1: Gypsum-dominated Material
Class 2: Polyhydrated Sulfate-dominated Material
Class 3: Smectite-Zeolite-Iron oxide-dominated Material
A
Corrected Reflectance
Wavelength (nm)
FRT00007AE6
FRT00007E11
HRL00011898
FRT000007E11
FRT000007AE6
HRL000086DE
FRT000007EB5
HRL000126C5
FRT0000079E4
HRL000086DE_R9
FRT000007A8C
HRL000086DE_R7
FRT000007588_R1
FRT000007588_R3
FRT000006DE7
HRL000122A0
B
55°S
65°S
75°S
15°W
15°E
45°E
N
Figure 2C
Edifice 4
Figure 2D
Edifice 7
Figure 2E/3
Edifice 18
Figure 2F
Edifice 11
Figure 2G/4
Edifice 15
Class 1: Gypsum-dominated Material
Class 2: Polyhydrated Sulfate-dominated Material
Class 3: Smectite-Zeolite-Iron oxide-dominated Material
250 km
0.5
3.5 km
C
D
E
F
G
100 km
100 km
100 km
100 km
100 km

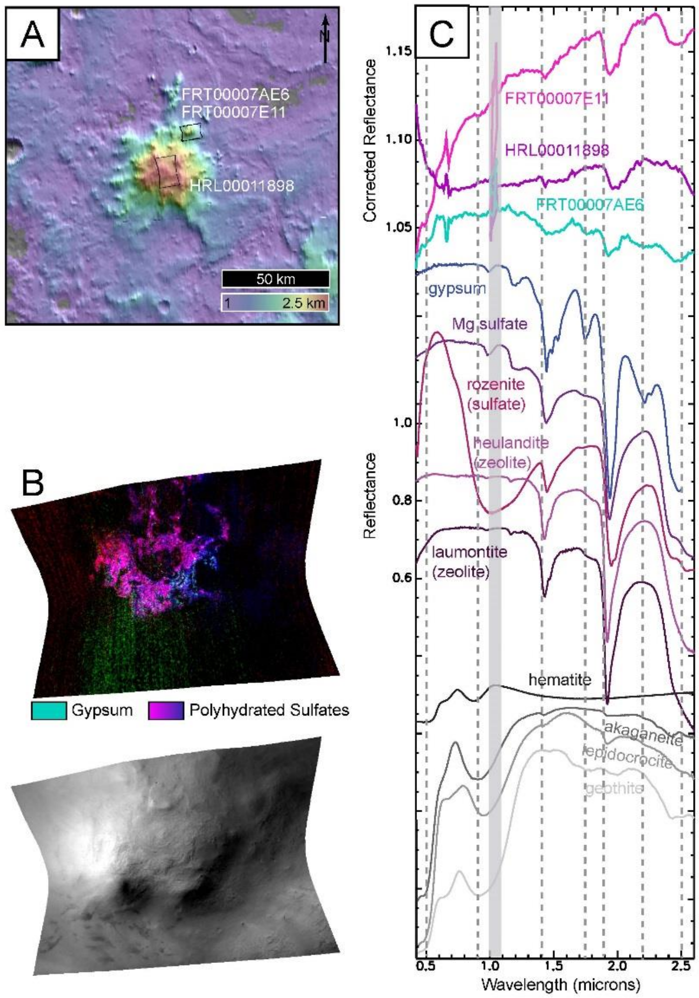

Figure 3. Type location for Class 1: gypsum-dominated material and Class 2: polyhydrated sulfate-dominated material. (a) Regional context for edifice 18 showing the locations of CRISM images FRT00007AE6, FRT00007E11, and HRL00011898. (b) Summary parameter map of FRT00007AE6 (red, SINDEX; green, BD1750; blue, BD1900) so that gypsum is cyan and polyhydrated sulfate-bearing material ranges from pink to purple. A greyscale albedo map is also shown for morphologic context (grey, R1330). (c) Spectra from gypsum-dominated and polyhydrated sulfate-dominated materials. CRISM spectra are ratioed and labeled. Library spectra of gypsum, mg sulfate, rozenite, heulandite, laumontite, hematite, akaganeite, lepidocrocite, and goethite are labeled and included for comparison. Vertical lines are included at 0.5, 0.9, 1.4, 1.75, 1.9, 2.2, and 2.5 μm showing Fe-oxides, hydration, and sulfate signatures, respectively. Wavelengths affected by a detector artifact are greyed out.

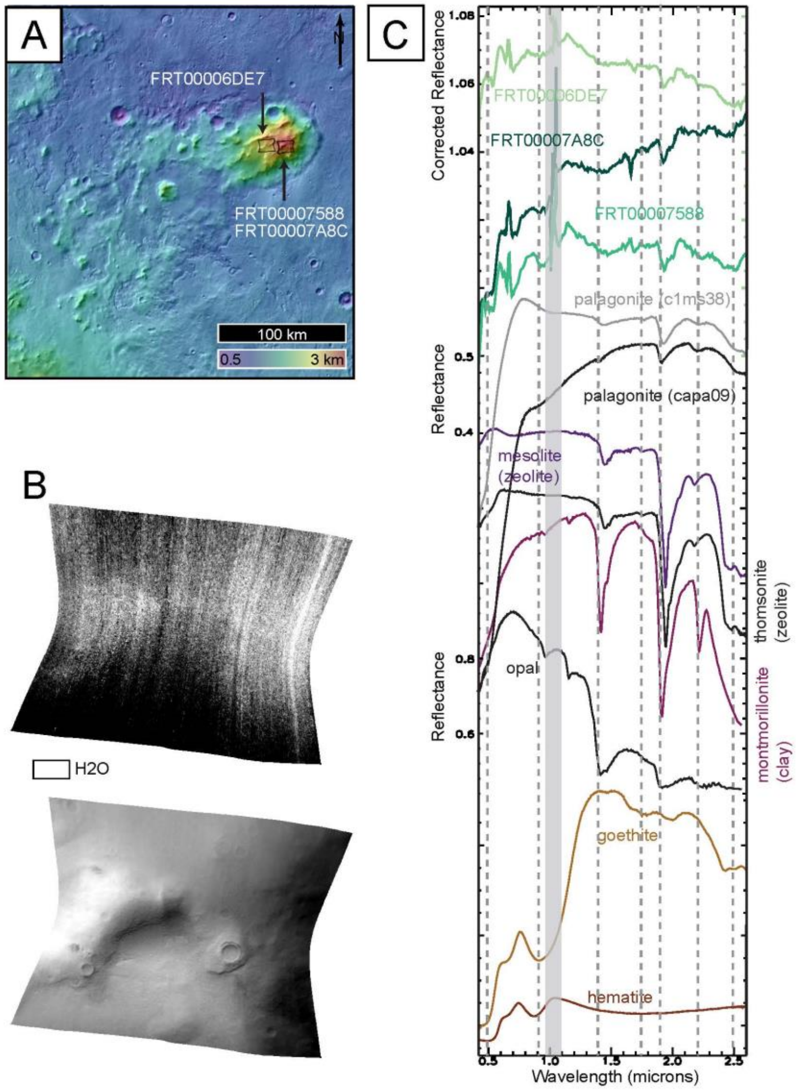

Figure 4. Type location for Class 3: smectite-zeolite-iron oxide-dominated material. (a) Regional context for edifice 15 showing the locations of CRISM images FRT00006DE7, FRT00007588, and FRT00007A8C. (b) Greyscale summary parameter map of FRT00007588 (grey, BD1900) so that smectite/zeolite-dominated material is shown. A greyscale albedo map is also shown for morphologic context (grey, R1330). Note the correlation of the ridge with the mineralogic signature and that the signature on the right hand side of the image is mostly spectral noise. (c) Spectral from smectite-zeolite-iron oxide-dominated materials. CRISM spectra are ratioed and labeled. Library spectra of palagonite, mesolite, thomsonite, montmorillanite, opal, goethite, and hematite are labeled and included for comparison. Vertical lines are included at 0.5, 0.9, 1.4, 1.75, 1.9, 2.2, and 2.5 μm showing Fe-oxides, hydration, clay signatures, and sulfate signatures, respectively. Wavelengths affected by a detector artifact are greyed out.

2.11 Supplemental Tables

Table 3. CRISM images evaluated in this study.

CRISM Image ID	Notes[a]
FRT00006DE7	Figure 2, 4
FRT00007588	Figure 2, 4
FRT000079E4	Figure 2
FRT00007A8C	Figure 2, 4
FRT00007AE6	Figure 2, 3
FRT00007E11	Figure 2, 3
FRT00007EB5	Figure 2
HRL000086DE	Figure 2
HRL00011898	Figure 2, 3
HRL000122A0	Figure 2
HRL000126C5	Figure 2
FRT00013D9A	Ice covered (H2O ice)
FRT00013B01	No L detector observation
FRT0001F95D	No L detector observation
FRT00007C28	Noise of undetermined origin
FRT00013437	Noise of undetermined origin
FRT00006149	Ice covered (CO2 ice)
FRT000064E4	Ice covered (CO2 ice)
FRT000074E9	Spectrally bland

[a]All 24 images were processed through the MTDR pipeline. If the image was used in the study, the figure in which it is featured is noted. Otherwise, the reason for its elimination is noted.

CHAPTER 3. THE COMPOSITION AND CRYSTALLINITY OF ICELANDIC PALAGONITES: AN ANALOG FOR MARS

3.1 Introduction

In volcanic eruptions beneath ice sheets and glaciers on Earth, the combination of heat and large quantities of melt water lead to the production of steep sided and flat topped edifices (tuyas or table mountains), shaped by the confining ice pressure. This environment creates a unique stratigraphic sequence of three lithostratigraphic units, which was originally defined within the Móberg formation in Iceland [*Pjeturss* 1900, 1902, 1904; *Peacock*, 1926a, b; *Noe-Nygaard,* 1940, 1951; *Kjartansson*, 1943; *Bemmelen and Rutten*, 1955; Jakobsson and Gudmundsson, 2008]. The lowermost unit is composed of fragmented subaqueous pillow lavas, which is overlain by a middle unit composed of hyaloclastite: an altered, vesicular, and glassy hydroclastic tephra of basaltic to intermediate composition. The top unit consists of subaerial lava flows, although this unit is not always present [Tuffen, 2007; Jakobsson and Gudmundsson, 2008]. This stratigraphic sequence has been identified in subglacial and intraglacial edifices with associated sediments, including tuyas (table mountains), tindars, and active volcanoes [Jakobsson and Gudmundsson, 2008].

The mineralogy produced during these eruptions is also unique because of the interaction of the hot lava and cold glacial meltwater. The meltwater causes quenching of lava to form glass (sideromelane) as well as *in situ* hydrothermal alteration of the glass to form hyaloclastites [*Stroncik and Schmincke*, 2002]. As the glass in the hyaloclastites starts to dissolve, a mineral assemblage called palagonite is formed [*Drief and Schiffman*, 2004]. Palagonite is an assemblage of crystalline and amorphous secondary phases formed from the alteration of basaltic glass, including clay minerals, zeolites, oxides, and amorphous material [*Pauly et al.*, 2011]. The composition of palagonite is strongly controlled by the composition of the basaltic glass [*Massey*, 2017] and the rate of palagonitization [*Stroncik and Schmincke*, 2001].

Palagonite is common in many martian analog volcanic regions on Earth (e.g., Hawaii and Iceland), and for this reason, palagonite has been used as a type example of altered basalt in Mars studies. The JSC-Mars1 (palagonite-rich) sample, for example, is a common martian regolith simulant collected from the ash of a cinder cone on the island of Hawaii [Allen et al., 1998]. JSC-Mars1 is used to simulate martian dust because of its visible/near-infrared spectral similarities to the bright regions of Mars [Evans and Adams, 1979; Singer, 1982; Morris et al., 1993]. With respect to Mars, palagonite has been used to study: the composition of martian dust and soil [Singer, 1982; Morris et al., 1990; Clancy et al., 1995; Morris et al., 2001], the origin of nanophase and crystalline iron in mineral assemblages [Bell et al., 1990; Morris et al., 1993], clay mineral mixtures [Banin and Margulies, 1983; Orenberg and Handy, 1992], basaltic glass properties [Allen et al., 1981; Bishop et al., 1995; Bishop et al., 2002], and remote sensing applications [Crisp et al., 1992; Farrand et al., 1992; Morris et al., 2003]. While these studies were focused on characterizing the martian surface andused palagonite as a soil analog, they have also revealed significant information about palagonite that was previously unknown.

One of the reasons that palagonite has been proposed as an analog for martian soils is that basaltic volcanism and aqueous alteration have been the dominant processes in producing the observed surface mineralogy of Mars. Volcanism is observed in large provinces including Tharsis, Elysium, Syrtis, and the volcanic plains occupying ~44% of the southern hemisphere [Greeley and Spudis, 1978]. Weathering and alteration of these volcanics under past climatic regimes has resulted in the formation of many types of hydrated silicates and salts: phyllosilicates, sulfates, carbonates, chlorides, and hydrated silica [e.g., *Bibring et al.*, 2005; *Murchie et al.*, 2009; *Ehlmann and Edwards*, 2014]. These secondary minerals are a record of the environmental conditions present at the time of their formation (e.g., pressure, temperature, geochemistry), and therefore offer insight into the history of water and habitability on Mars [e.g. *Ehlmann et al.*, 2011].

However, palagonite is unlikely to be present as a major component of martian soil, because palagonite formation requires specific formation conditions that are unlikely to have been prevalent across the surface of Mars. Palagonite formation requires volcanic eruptions with significant contact with water, either in lakes and oceans (hydrovolcanic) or under glaciers, (glaciovolcanic). While palagonite is most likely not a major soil component on Mars, there are some landforms on Mars that have been hypothesized to be derived from subglacial volcanism based on their morphologies, at both northern [*Fagan et al.*, 2010] and southern high latitudes [Ghatan & Head, 2002]. Recent spectral analysis of the southern high latitude edifices in the Sisyphi Montes region, between the Argyre and Hellas impact basins, has shown that these edifices exhibit visible/near-infrared spectra possibly consistent with palagonite [*Ackiss et al.*, 2018]. However, definitively identifying palagonite from orbital datasets on Mars is challenging due to limited previous studies assessing the range of mineralogical variability of the assemblage [Peacock and Fuller, 1928; Eggleton and Keller, 1982; Furnes, 1984; Jercinovic et al., 1990; Zhou et al., 1992]. In addition, we hypothesize that mineralogical variability can arise from different environmental conditions at the time of formation, and that the resulting palagonite mineralogy could be used as an indicator of those conditions [Ackiss et al., 2017]; in particular, differences in palagonite compositions could potentially elucidate whether a palagonite was formed in a submarine or subglacial environment.

Identifying palagonite on Mars is also challenging because martian mineralogy is characterized by a somewhat different set of techniques than are typically applied on the Earth, including *in situ* rover measurements as well as orbital remote sensing observations. *In situ* rover instrumentation includes the alpha particle X-ray spectrometer (APXS) providing elemental composition [Gellert et al., 2006], Mössbauer spectroscopy (MIMOS II) quantifying iron-bearing mineralogy [Morris et al., 2004], thermal infrared emission spectroscopy (Mini-TES) characterizing mineralogy [Christensen et al., 2004], laser induced breakdown spectroscopy (ChemCam) providing elemental composition [Wiens et al., 2012], X-ray diffraction (CheMin) characterizing mineralogy [Blake et al., 2012], and visible spectroscopy (e.g., MastCam) focusing on iron-bearing mineralogy [Malin et al., 2010; Bell et al., 2012]. Orbital techniques include visible and near-infrared reflectance spectroscopy (CRISM and OMEGA) [Murchie et al., 2007; Poulet et al., 2007] and thermal infrared emission spectroscopy (THEMIS and TES) [Christensen et al., 2001; Christensen et al., 2004]. Here, we focus on X-ray powder diffraction, visible and near-infrared spectroscopy, and thermal infrared spectroscopy to study the variability of the mineralogy, crystallinity, and clay mineral composition of palagonite in our sample suite to provide a direct comparison to martian datasets. Because this methodology explores different aspects of composition than traditional terrestrial methods, we can provide additional insight into the composition of palagonite and methods for constraining environmental conditions.

In this study, we utilize Mars orbiter and rover-type instrumentation to characterize the variability of the mineralogy, crystallinity, and composition of Icelandic palagonite samples in order to (1) determine how well we can detect and characterize the variability of palagonite in Mars orbital and rover datasets, and (2) determine whether composition can be used to constrain the formation conditions of palagonite (e.g. differentiating palagonite formed in submarine versus subglacial regions). The investigation of the spectral, mineralogical, and crystalline variability of palagonite on Earth will help to constrain the range of possible mineral assemblages of palagonite, building valuable datasets that can be applied to Earth as well as Mars.

3.2 Review of Palagonite

3.2.1 Palagonite Formation

Palagonite is formed through the partial dissolution of glass and concurrent precipitation of smectite-like material under low temperature hydrothermal conditions [*Drief and Schiffman*, 2004]. Palagonite initially forms within micro-fractures in hyaloclastites. The glass in the hyaloclastites starts to dissolve and fills the fractures with leached layers. The fractures expand and the glass continues to alter until a mixture of an amorphous to poorly crystalline smectite-like material (palagonite) dominates the rock [*Drief and Schiffman*, 2004]. This process can take 2-3 days following the volcanic activity and requires temperatures between 80-100°C, as observed at Surtsey [*Jakobson and Gudmundson*, 2008]. Because palagonite is formed as an *in situ* alteration product from hyaloclastites, it first starts out as an alteration rind. Rind thickness is related to alteration duration [*Moore*, 1996; *Stroncik and Schmincke*, 2001], temperature [*Moore et al.*, 1985; *Jakobsson and Moore*, 1986], and porosity [*Pauly et al.*, 2011]. As palagonitization increases, porosity decreases [*Pauly et al.*, 2011], and because the water to rock ratio decreases with decreasing porosity [*Walton and Schiffman*, 2003], the water to rock ratio within the deposit is thus inversely related to palagonitization [*Pauly et al.*, 2011].

The amorphous portion of palagonite is a gel thought to form during dissolution-reprecipitation of glass where the primary material is dissolved and the secondary phases are precipitated at the contact with the glass. As palagonite ages, it evolves into fibro-palagonite, which is a mixture of amorphous gel-palagonite and crystalline smectites. Jercinovic et al., [1990] proposed that zeolites are formed in the middle phase of palagonite alteration as it progresses from 1) saponite (Mg-smectite), to 2) zeolites in the order of phillipsite to chabazite, and 3) finally to nontronite (Fe-smectite). Some palagonite compositions have also been observed to reflect primary magma compositions based on immobile elements [*Massey*, 2017]. However, the details of the formation, evolution, and mineralogic composition of palagonite are still highly debated [*Stroncik and Schmincke*, 2002; *Drief and Schiffman*, 2004].

Palagonite has frequently been misinterpreted as a weathering product produced during sub-aerial oxidation and weathering of volcanic rocks [*Hay and Iijima*, 1968; *Hay and Jones*, 1972; *Gooding and Keil*, 1978; *Singer*, 1982; *Banin and Margulies*, 1983]; however, the volcanological literature specifically defines palagonite as a poorly crystalline, hydrated, and oxidized hydrothermal alteration product of basaltic volcanic glass made exclusively at low hydothermal temperatures (typically <120°C) and high water-to-rock ratios [*Allen et al.*, 1981; *Morris et al.*, 1990; *Stroncik and Schmincke*, 2002; *Michalski et al.*, 2005; *Warner and Farmer*, 2010; *Cousins et al.*, 2013]. Because palagonite requires the presence of high abundances of glass, low temperatures, and high water-to-rock ratios, the main environments that it forms in are thus subglacial and submarine volcanic eruptions. Palagonite composition is known to vary based on the composition of the magma it is produced from (e.g. basaltic vs. andesitic). In addition, because palagonite is formed in a turbulent aqueous environment, we hypothesize that local and site-to-site changes in environmental conditions could cause composition to vary both within a single outcrop and within palagonite of different formation environments. Based on past studies, it is unclear how the composition and temperature of the water and overburden pressure affects the composition of palagonite, thus it is unclear how palagonite varies between specific types of aqueous environments (e.g., subglacial, submarine, sublacustrine). In general, while submarine volcanism produces very different volcanic morphologies than subglacial volcanism [*Mitchell et al.*, 2002; *Jakobsson and Gudmundsson*, 2008; *Russell et al.*, 2014; *Romagnoli and Jakobsson*, 2015], the composition of the palagonite in both environments has been assumed to be similar [*Jakobsson*, 1978; *Jakobsson and Moore*, 1986]. However, this hypothesis has not been tested with detailed investigations and robust data collection of the mineralogy of the palagonite.

3.2.2 Mineralogy of Palagonite

Altered basaltic glass samples from Iceland, Alaska, Antarctica, Hawaii, New Mexico, and Mexico were analyzed by Allen et al., [1981] using a number of techniques including optical and scanning electron microscopy, electron microprobe analysis, X-ray diffraction, and VNIR spectroscopy. Their results showed that visible and near infrared (VNIR; ~0.3-2.5 µm in planetary science nomenclature) spectroscopic analyses of palagonite are consistent with a nontronite (Fe smectite) composition. Additionally, palagonite was only observed as an alteration rind around the glass grains and had a complex and variable composition between samples; however, crystalline smectites and zeolites (at <100 μm particle size) were observed in all samples [*Allen et al.*, 1981]. Pleistocene-aged palagonite samples from Mauna Kea in Hawaii show rinds consisting of smectite and zeolites (erionite), and that glass and plagioclase content decrease while the amount of smectite increases with decreasing particle size [*Golden et al.*, 1993]. Icelandic studies of altered pillow basalts and hyaloclastite tuffs show that palagonite-rich tuffs contain more crystalline clay, fewer iron oxides, and have a higher Al/Fe ratio when compared to underlying altered pillow basalts [*Bishop et al.*, 2002].

Consistent with this observation, Farrand et al. [1992] noted that as palagonitization progresses, the final stages consist of a mineral assemblage including clay, ferric oxide, and zeolite minerals, all interpreted to be crystalline in nature. Nanophase ferric oxides have been shown to be the dominant pigmenting agent causing color at VNIR wavelengths, which form via oxidative weathering of mafic glass in water [*Morris et al.*, 1993]. Nano-crystalline oxide phases in Askja volcanic samples in Iceland are seen in association with amorphous palagonite phases and randomly oriented glass fragments [*Cousins et al.*, 2013]. Bell et al. [1993] collected palagonite samples in increasing distance from a geologically recent lava flow in Hawaii to investigate the alteration of palagonite during the emplacement of lava. The results show that volcanism or heating from a source produces crystalline ferric oxides from a poorly crystalline palagonite.

3.2.3 Effects of Eruption Environment

Both submarine and subglacial palagonites have been studied by previous researchers to identify differences in the formation environments; however, the mineral assemblage that is most characteristic of different environments is debated. A small sample set from Iceland showed that glaciovolcanic hyaloclastite ridges are devoid of zeolites and clays and tend to be less hydrated, whereas lacustrine hydrovolcanic hyaloclastites have large amounts of smectites and void-filling zeolites [*Farrand et al.*, 2017]. In contrast, many studies of submarine hydrovolcanic palagonitized tephras from Mauna Kea have shown that these palagonites tend to be phyllosilicate-poor [Hay and Iikima, 1967; Morris et al., 1990; Bell et al., 1993; Morris et al., 1993; Roush and Bell, 1995; Morris et al., 2001; Hamilton et al., 2008]. Pauly et al., [2011] suggests that zeolite-bearing hyaloclastites are associated with subglacial tuya deposits; however, Farrand et al., [2017] suggests that the samples from the Pauly et al., [2011] study are not subglacial in origin but instead are a part of the subaerial beds in the Móberg formation. In addition, the clay mineralogy of palagonites may vary: Golden et al., [1993] noted that glaciovolcanic palagonite from remnant Pleistocene deposits is composed of smectites that are low in structural iron, while other studies have shown that hydrovolcanic palagonites contain Fe-rich smectites.

To rectify these disparate results, Pauly et al., [2011] hypothesized instead two different formation mechanisms for palagonite over two different timescales: 1) burial-diagenetic palagonitization and 2) hydrothermal palagonitization. Burial-diagenetic palagonitization is defined by long-durations, low water/rock ratios, and passive fluid circulation, usually forming palagonite some time after the initial eruption and deposition of the hyaloclastite. Pauly et al., [2011] suggested that this type of formation is common in submarine volcanics. Hydrothermal palagonitization is defined by short-durations, high water/rock, and hydrothermal fluid circulation, which happens either during the eruption or immediately after and is commonly seen in phreatomagmatic and subglacial samples [*Pauly et al.*, 2011]. Mineralogy that correlates to these timescales was not predicted and is still unclear.

Submarine volcanic eruptions are an endmember of hydrovolcanism, which is often inferred in the geologic record by pillow basalts. The presence of pillow basalts can indicate shallow or deep water, ranging in depth from 10-2000 meters [Moore, 1965; Jones, 1969]. A type location for hydrovolcanism is the Columbia River flood basalts in western Washington. The Columbia River flood basalts exposed in the walls of Moses Coulee and the adjacent portion of the Columbia River valley exhibits pillow basalts interlayered with palagonite tuff breccias. Both the pillows and breccias are located at the base of the formation, suggesting that the flood basalts at the Columbia River erupted into a body of water [Fuller, 1931, 1932, 1934, 1950]. This incorporation of the pillows and the breccias as well as their slumping into the water created forset beds indicated relatively deep water (roughly 20-80 meters) [Waters, 1960; Mackin, 1961; Moore et al., 1973; Furnes et al., 1974; Naylor et al., 1999]. Historically this process was also observed at the Mauna Loa flow of 1858 and later described in detail in Green [1887].

3.3 Geologic Setting and Samples

Iceland has experienced a rich history of subglacial and intraglacial activity [Kjartansson, 1960] with more than 50% of historical eruptions occurring underneath glaciers [Larsen, 2002]. During the Pleistocene, almost the entire island of Iceland was covered by up to ~1.5 km of ice [*Saemundsson*, 1980]. The subglacial and intraglacial volcanism left behind deposits which became known as the Móberg Formation, a stratigraphic unit formed in the upper-lower Pleistocene (0.78-3.3Ma), composed primarily of palagonite [*Jóhannesson and Saemundsson*, 1998; *Geirsdottir and Eiriksson*, 1994**;** *Saemundsson*, 1979]. At present, the formation covers 20,000 km^2 (not including presently ice-covered areas or subglacially-formed rhyolites), which is roughly 11% of the country [*Chapman et al.,* 2000; *Jakobsson and Gudmundsson*, 2008; *Jóhannesson and Saemundsson*, 1998]. The Móberg Formation is so vast that it has not yet been characterized in detail. Where small (200 km^2) portions have been studied, they are described as "palagonite highlands" [*Preusser*, 1976], and are characterized by multiple eruptions under ice sheets that have coalesced to form one continuous palagonite-rich deposit. These highlands include the Pleistocene palagonite-rich hyaloclastite mountains [*Jakobsson and Gudmundsson, 2008*]. The Móberg Formation is a subset of the "Palagonite Formation" of Iceland, which contains fragmented basaltic lavas, glacial moraines, tuffs, and alluvial deposits (jökulhlaups) [Kjartansson, 1943]. The widespread occurrence of these formations throughout Iceland is a testament to the amount of ice cover in the past [*Jóhannesson and Saemundsson*, 1998; *Geirsdottir and Eiriksson*, 1994**;** *Saemundsson*, 1979].

There are massive palagonite outcrops spread throughout Iceland; however, a detailed geologic map of those palagonite outcrops has still not been created [Gudmundsson, 2005]. Some radiometric dating of the Northern and Western Volcanic Zones in Iceland has been conducted [*Licciardi et al.*, 2007], but more data would help to constrain the timing, distribution, and thickness of the paleo-ice sheet that once covered the country [*Preusser*, 1976]. Volatiles in volcanic glass can be studied to infer confining pressure and thus ice thickness at the time of eruption [*Garcia et al.*, 1989; *Dixon et al.*, 2002; *Moune et al.*, 2007]; however detailed studies of the palagonite highlands [*Preusser*, 1976] in Iceland have not been conducted. It is clear from the literature that while palagonite has been extensively studied, it remains a complex material that has not yet been well-characterized [*Gudmundsson*, 2006].

Subglacial and intraglacial volcanic rocks are found in the Western, Eastern, Northern, Snæfellsnes, and Öræfajökull Volcanic Zones [Jakobsson and Gudmundsson, 2008]. In this study, we sampled 12 locations (Figure 5): 8 locations in the Western Volcanic Zone, 3 locations in the Northern Volcanic Zone, and 1 location in the Eastern Volcanic Zone, all from glaciovolcanic outcrops in the Móberg Formation, giving us a variety of samples from the same inferred formation environment. The Western Volcanic Zone samples were collected outside of Reykjavik (Lake01, Lake02, Lake03, Lake04, DB01, DB02, 41701, and 41702), the Northern Volcanic Zone samples were from the Herðubreið and Askja volcanoes (Her01, Her02, and Ask01), and the Eastern Volcanic Zone sample was collected on the southern coast of Iceland (SCoast01). While all of the samples are Pleistocene in age, they vary in their degree of surface weathering.

The Western Volcanic Zone samples were all collected from the Móberg Formation located south and southeast of Reykjavik. It is unclear what volcanic edifice these outcrops originated from, as the palagonite outcrops in this area all interfinger from similarly timed eruptions, similar to the "palagonite highland" region north of Vatnajokull [*Preusser*, 1976]. However, all 8 samples vary significantly in color and texture (Figures 6-9).

Samples Lake01-04 were collected from the Hellutindar (mapped as subglacial hyaloclastite [Saemundsson et al., 2010]) near the modern day Kleifarvatn Lake and are the most variable samples when viewing in hand sample. Lake01 is red in color with crosshatched cemented layers that overprint the horizontal layering of the hyaloclastite (Figure 6a,b). Lake 02 is brown in color and has multiple horizontal layers with varying grain size. Between the horizontal layers is heterolithic bedding in a wavy pattern (Figure 6c,d). Lake03 is black in color on the outside and brown/red on the inside (Figure 7). It is a layered hyaloclastite with fracture fill. Lake04 is sourced from the fill within a fracture (Figure 7). The fracture fill is hyaloclastite with a brecciated matrix and is more brown in color than the Lake03 sample with little to no black coloring.

Samples DB01 and DB02 (Figure 8) were collected on the Draugahlíðar subglacial hyaloclastite ridge [Saemundsson et al., 2010], just above the Bolalda Motocross Park (off of Route 1 southeast of Reykjavik). DB01 is brown in color with smooth horizontal layers and a uniform grain size. DB02 is a brecciated layer adjacent to DB01 with ~1.5 cm chunks of pillow basalt, brown in color, and a uniform grain size matrix. It also contains regions that are brown/gold-colored, possibly indicating alteration.

Samples 41701 and 41702 (Figure 9) are mapped as subglacial hyaloclastite [Saemundsson et al., 2010] and were collected on Route 417, a road connecting Route 42 and Route 1 (Ring Road), south of Reykjavik. Sample 41701 is very similar to DB02, with ~1.5 cm chunks of pillow basalt, brown in color, and a uniform grain size matrix. Sample 41702 is brown/gold in color, lighter in color than sample 41701, has very few chunks of volcanic glass and is sandy in comparison to 41701.

The Northern Volcanic Zone samples were collected from well-defined, well-studied subglacial edifices [Saemundsson et al., 2010]. Samples Her01 and Her02 (Figure 10) were collected from the Herðubreið volcano, just north of the Vatnajokull ice cap. Herðubreið is a 1.68 km high tuya (1.68 km above sea-level but ~1.3 km above the surroundings), a classic structure made from an eruption underneath ice that breached the surface [*Van Bemmelen and Rutten*, 1955; *Werner et al.*, 1996]. Herðubreið has also been age dated using cosmogenic ^{3}He concentrations and associated exposure ages, giving an age of 10.5 +/-06 ka [*Licciardi et al*., 2007]. Sample Her01 varies in color from brown to orange to yellow and has a uniform grain size with ~3 cm chunks of pillow basalt. Within the sample, there are consistently spaced layers, usually more orange in color than the surrounding hyaloclastite, possibly indicating more Fe(III)-rich mineral phases. Sample Her02 is mostly beige/yellow/light orange in color and has a platey/blocky texture. This portion of the hyaloclastite breaks easily into chunks/blocks but is well-cemented and unlike other more fine-grained and friable hyaloclastite outcrops we observed.

Sample Ask01 (Figure 11) was collected from the Dyngjufjöll massif [Saemundsson et al., 2010] under the Askja volcano. The Dyngjufjöll massif significantly predates the modern Askja volcano and therefore the hyaloclastites are likely to be more than 4,000 years in age [*Thorarinsson*, 1974; *Sigvaldason*, 1992; *Björnsson and Einarsson, 1990*]. The Dyngjufjöll massif and the rest of the Askja edifice is made up of basaltic lavas that range in composition from olivine tholeiites to quartz tholeiites [*Sigvaldason*, 1992]. Sample Ask01 is grey to brown in color, has mostly uniform grain size, and includes layered pillow basalt fragments.

The Eastern Volcanic Zone sample was collected from a location near the town of Vik on the south coast of Iceland. This sample was collected from a large subglacial hyaloclastite [Saemundsson et al., 2010] outcrop south of the Mýrdalsjökull ice cap and thus the exact volcanic edifice that this sample originates from is unclear. Sample SCoast01 (Figure 12) is very light brown in color and all of the vugs in the sample are filled with moss. The outcrop has a rounded/smooth texture with very large scale layers (~3m layers vs ~3cm layers in other samples), unlike the hyaloclastite outcrops we observed at the other sites. This sample is the most physically weathered sample (started to deteriotate to form soil) in the suite that we collected.

3.4 Methodology

After samples were collected, they were dried in a fume hood for 14 days. Drying the samples guaranteed that any water remaining in the sample was contained in the crystalline structure of the minerals in the rocks and not adsorbed water on the exterior of the sample. "Hand sample" VNIR and thermal infrared (TIR; ~7-25 μm in planetary science nomenclature) spectra were acquired of the fresh hand sample surfaces, in flat regions cleaned with compressed air to remove dust particles. Preliminary VNIR spectra (where one spectrum is the average of 100 spectra) taken on multiple surfaces of the same sample were used to choose the most representative surface. "Sieved" samples were generated by hand grinding the rock samples using a mortar and pestle and then sieving to <125 microns, similar to the sieve in the Sample Acquisition, Processing, and Handling (SA/SPaH) onboard the Mars Science Laboratory (MSL) rover. For TIR measurements, the sieved samples were pressed into compact pellets at 10,000 psi in a hydraulic hand press, to increase the contrast of their infrared spectra and to remove fine particulate spectral features [Salisbury and Wald, 1992; Johnson et al., 1998; Ruff et al., 2004; Glotch et al., 2007]. Measurements were acquired of all sieved samples using VNIR spectroscopy, TIR spectroscopy (pellets), and X-ray powder diffraction (XRD) for consistency and comparison. The differences between the hand samples and sieved samples can be seen in Figures 13 (VNIR comparison) and 14 (TIR comparison).

3.4.1 Visible and Near-Infrared (VNIR) Spectroscopy

VNIR reflectance spectra were acquired with an ASD (Analytical Spectral Devices, Inc.) FieldSpec Pro 3 in the Planetary Spectroscopy Laboratory at Purdue University. This device measured the samples from 350-2500 nm at 3 and 10 nm resolution (at 700 nm and 1400/2100 nm respectively). Both the hand samples and sieved samples were measured using the ASD Contact

Probe attachment, which has a spot size of 10 mm, an emission angle of 30°, and an incidence angle of 0°. Each spectrum was constructed by averaging 100 scans over the same surface area on the sample. Splice Correction in ViewSpec Pro was applied to the raw data after collection to account for small differences in calibration between detectors.

3.4.2 Thermal Infrared (TIR) Spectroscopy

TIR emission spectra were acquired using a Nicolet Nexus 670 spectrometer at the Arizona State University Mars Space Flight Facility. This device measured the samples from 4000 to 400 cm^{-1} at 4 cm sampling resolution [*Ruff et al.*, 1997]. Both the hand samples and sieved pressed pellet samples were measured using the same techniques, including heating the samples to 80°C prior to measurement to increase the signal to noise ratio. The sample chamber is external to the spectrometer and is purged with air scrubbed of H_2O and CO_2 [Lane et al., 2007], which also have absorption features in the 2000-400 cm^{-1} region of the spectrum. Samples were placed on a heater to help maintain the 80°C temperature during the measurement, as this technique is based on the amount of heat a rock emits. The heater and sample were then raised into a chamber that closely approximates a blackbody cavity. Energy emitted from a ~1 cm spot of the sample in a 37° cone is reflected off a paraboloid mirror and directed into the spectrometer through an emission port. Each measurement was taken by averaging 260 scans over the same surface area on the sample to get a clear spectrum of the sample. After data collection, mineral assemblages of all samples were modeled from 1400-400 cm^{-1} using quantitative deconvolution of the spectra [Ramsey and Christensen, 1998] in the open source Davinci programming language, following the non-negative linear least squares method described by Rogers and Aharonson [2008]. This deconvolution method is typically accurate to about the 5-10 vol.% level for phase abundance retrieval in natural unweathered igneous samples [Feely and Christensen, 1999; Hamilton and Christensen, 2000; Wyatt et al., 2001], and phases modeled with abundances lower than this are considered below the detection limit. Somewhat larger errors on the order of 15 vol% have been found for both glass-rich synthetic mixtures and natural tephras [McBride et al., submitted].

The endmember library used to model the spectra was newly designed for this study to include all major phases potentially present in the palagonite samples or observed in other palagonites (Table S1). It comprises 77 spectra of primary minerals, volcanic glasses, phyllosilicates, zeolites, sulfates, oxides, and secondary amorphous products, collected variously from hand samples, coarse particulates, and pressed pellets. This library is appropriate for modeling the palagonite hand sample and pressed pellet spectra while avoiding complications from fine, loose particulate spectral artifacts [e.g. Ruff et al., 2004; Glotch et al., 2007]. A blackbody endmember is included and normalized out of final abundance estimates to account for spectral contrast differences between endmember and rock spectra [Hamilton et al., 1997; Hamilton et al., 2000]. Fits were tested to exclude modeled endmembers that were extremely unlikely to be present in the sample or were incorrectly being modeled (e.g. carbonates and sulfates that were unlikely to be present in the study environment due to specific pressure/temperature/formation conditions).

The amorphous composition of palagonite is likely a highly variable mixture of volcanic glass and amorphous weathering products. The TIR spectra of amorphous silicates varies depending on silica content, cation content, and degree of devitrification [Crisp et al., 1990; Koeppen and Hamilton, 2005; Byrnes et al., 2007; Lee et al., 2010; Minitti and Hamilton, 2010; Farrand et al., 2016; Farrand et al., 2018]. Thus, we include primary glass between basaltic and rhyolitic composition with varying degrees of devitrification, as well as allophane, aluminosilicate gel, and opal endmembers to capture this variability.

Nonlinear spectral mixing behavior occurs in fine-grained material with grains <65 µm [Salisbury and Wald, 1992; Moersch and Christensen, 1995] and can increase the error associated with linear deconvolutions [Ramsay and Christensen, 1998; Thorpe et al., 2015; Pan et al., 2015]. However, nonlinearity is minimal in fine-grained rocks such as basalt, where component minerals have similar absorption regions and strengths [Thorpe et al., 2015]. Although our palagonite samples are fine-grained, we expect them to consist predominantly of silicate material that will mix linearly even at small grain sizes.

3.4.3 Quantitative X-ray Powder Diffractioon (XRD)

XRD patterns were used to assess the crystalline mineralogy of the samples. XRD should be regarded as semi-quantitive [Vassilev and Vassileva, 1997] due to the inherent variability of some crystalline structures, the way the sample is prepared, crystal lattice orientation, grain size, and absorption of X-rays [Klug and Alexander, 1974]. To counteract some of these effects, a known and measured substance, in this case corundum, can be added to the sample to provide more quantitative measurements [McCarthy and Johansen, 1988; Seung et al., 1999].

An aliquot of our sieved samples were reserved for XRD, to which 20% corundum (grain size of 1 micron) was added to our sample ("spiked") for quantitative mineral assemblage modeling. The spiked sample was micronized in ethanol using a McCrone micronizer for 5 minutes to combine the corundum and the sample as well as to make the sample a uniform grain size of ~10 microns [*Locock et al.*, 2012]. The X-ray diffractogram of each sample was acquired by back-loading the sample into a random powder mount [*Bish and Reynolds,* 1989]. The sample was then examined from 5 to 80° 2θ using CoKα_1 radiation (λ = 1.789010 Å) at a scan rate of 2°/min using a PANalytical X'pert Pro MPD X-ray diffractometer (XRD) at the Center for Agronomy Science at Purdue University. A 1° anti scatter slit was used for smaller theta values and was removed at ~12 2θ. The X-ray tube worked at 45 kV and 40 mA. After data collection, mineral assemblages of samples containing clear crystalline mineral peaks (only SCoast01) were modeled using HighScore Plus.

3.5 Observations

3.5.1 Visible and Near-Infrared (VNIR) Spectroscopy

All samples have broad absorption bands near 1000nm, narrow absorptions bands at 1400, 1780, and 1900 nm, and an absorption band or band combination between 2200-2300 nm (Figure 13). Hand samples have lower reflectance (are darker) than sieved samples, consistent with increased surface area due to smaller particle sizes in the sieved samples. The sieved samples also have "cleaner" (less noisy) spectra because of the consistent grain size and will be the focus of our analyses in this section; however, hand sample spectra are included for comparison.

The center of the broad ~1000 nm band varies in the samples from 956 to 1070 nm, and most of the samples are centered near 1036 nm. Absorption bands ranging from 1050-1070 nm are usually attributed to olivine [Horgan et al., 2014]; however, olivine also has a combination of three bands seen at 850, 1050, and 1150 nm [Sunshine et al., 1990; Sunshine and Pieters, 1998], caused by Fe^{2+} ions in both the M1 and M2 coordination sites in the olivine crystal lattice [Burns, 1970a, 1970b, 1970c]. We do not see shoulders from those three bands within the ~1000 nm absorption and thus have ruled out a major contribution from olivine. Orthopyroxenes (otherwise known as low calcium pyroxene in the extraterrestrial literature) exhibit broad absorptions at ~900 and ~1900 nm due to Fe^{2+} in the M2 crystallographic site [Burns, 1970a, 1970b, 1970c], which are inconsistent with the bands we observe. Clinopyroxenes (also known as high calcium pyroxene in the planetary literature) have an absorption at 1000-1050 nm based on the Ca^{2+} cations partially or completely filling the M2 site, and forcing Fe^{2+} cations into the M1 site, which could be contributing to our observed bands. Glass bands are shifted to longer wavelengths (usually above 1100 nm) [Pollack et al., 1973; Dyer and Burns, 1982; Klima et al., 2007; Bishop et al., 2008; Horgan et al., 2014], which is not what we observe here.Thus, we suggest two possible interpretations for the band centers we observe in the palagonitized hyloclastite samples: (1) that these bands are consistent with a mixture of clinopyroxene and glass [Horgan et al., 2014], or (2) that these bands are due to partial devitrification of the glass. Glass/clinopyroxene mixtures could produce a range of band centers, where the range could differentiate compositions or amounts of pyroxenes. However, we also note that the spectral properties of devitrified glass have not yet been studied in detail, so we cannot rule out that local restructuring due to devitrification is also causing a shortward shift in the glass absorption band. In either case, the position of the band is likely related to the amount of vitric glass in the sample. The ~1000 nm band in the Lake01 sample is the shortest band center at 956 nm and is narrower than most of the other samples; however, the SCoast01 sample is the most shallow and narrow, with a band center at 1015 nm, all of which is consistent with less glass in the sample.

The positions of hydration bands in these samples range from 1403-1426 nm and 1913-1923 nm. The positions of the narrow ~1400 and 1900 nm bands often correlate with each other (e.g. if a sample has an absorption at 1426 nm, then the ~1900 nm absorption will be located on/around 1926 nm). These bands are due to the O-H stretch in the crystalline structure at 1400 nm and the H_2O bend + stretch at the 1900 nm absorption [Hunt, 1977; Clark et al., 1990; Bishop et al., 1994]. The narrow ~1790 nm band is associated with the presence of liquid water in the crystal structure of minerals and is a combination band of the fundamental water stretch at ~2900 nm, which is itself a component of the large fundamental water band at ~3000 nm [Ellis, 1931; Collins 1937; Whiting et al., 2004; Milliken et al., 2007]. The position of the ~1790 nm band observed in our samples ranges from 1784 to 1799 nm, where the majority of the bands are centered at 1791 nm. Minerals with bands at these locations include sulfates, silica, and zeolites.

The ~1790 nm band combined with the ~1400 and 1900 nm bands are characteristic of zeolite and are due to water bound in the molecular structure [*Cloutis et al.*, 2002; *Clark et al.*, 2007; *Ehlmann et al.*, 2009; *Rice et al.*, 2013; *Viviano-Beck et al.*, 2014] and will not be observed unless the material is sufficiently hydrated. Thus, the identification of zeolites has been shown to be difficult based on VNIR spectroscopy alone because of their similarity to other hydrated minerals (e.g. sulfates and silica [*Ehlmann et al.*, 2009]); however, zeolites can be distinguished by careful analysis of their hydration absorption bands, as they are usually shifted toward longer wavelengths compared to hydrated sulfates and silica [*Cloutis et al.*, 2002; *Viviano-Beck et al.*, 2014]. The ~1790 nm band in our samples are interpreted to be consistent with a zeolite mineral.

All samples in this suite exhibit a narrow ~2200 nm feature attributed to Al-OH stretching. The samples in this paper have absorptions ranging from 2206-2247 nm, and most samples have a 2213 nm absorption. The ~2200 nm feature observed here is not accompanied by a doublet or a shoulder feature as seen in kaolinite or chlorite, respectively [Clark et al., 1990; Bishop et al., 2008]. While silica has an absorption at ~2210 nm, it is often accompanied by a secondary feature at ~2260nm feature [Rice et al., 2013], which we do not see here. Additionally, hydrated glass has a ~2200 nm feature from Si-OH that can look similar to silica or to montmorillonite if the Al-OH bands are widened from poor crystallinity [Swayze, 2007; Smith et al., 2013]. Thus a mixture of of hydrated glass and Al-smectite is a possible interpretation. Overall, we have interpreted this band to denote that the samples are rich in Al-smectite such as montmorillonite.

Six of the samples (SCoast01, Ask01, DB01, DB02, Lake04, and Her02) exhibit a combination of 2200 and 2300 nm bands. The 2300 nm band is indicative of Fe/Mg phyllosilicates, typically smectites, and is attributed to Fe(III)-OH stretching [Bishop et al., 2008]. The positions of the ~2300 nm bands in these samples range from 2281-2301 nm. While there are 6 samples that exhibit both of these absorptions, in the majority, the ~2300 nm band is present as a shoulder on the deeper ~2200 nm band (e.g. DB01, DB02, Her02, and Lake04). Two of the samples (SCoast01 and Ask01) exhibit the strongest ~2300 nm bands. The Ask01 sample has a deeper 2220 nm band in comparison to its 2281 nm band whereas the SCoast01 sample has a shallower 2213 in comparison to it’s narrower and deeper 2295 nm band. For these 6 samples, we suggest either a physical mixture of Al and Fe/Mg smectites where Al smectites are more prevalent, or perhaps Fe-substitution in Al-smectites [e.g., Bristow et al., 2018]. However, the SCoast01 spectra indicate that the sample is dominated by Fe/Mg smectites.

Lastly, it is worth noting a phase that is not detected in the VNIR - crystalline oxide minerals. Many oxides act as pigments and thus dominate VNIR spectra even at low abundances. Typically, we would expect to see strong absorptions near 600-700 nm and 850-980 nm and an absorption edge near 450-550 nm for crystalline oxides like hematite, goethite, maghemite, lepidocrocite, and other similar oxides and oxyhydroxides [Morris et al., 1985; Townsend, 1987]; however, these absorptions are not clearly present in our spectra. The strong downward slope below 700 nm and subtle shoulders in many of the VNIR spectra near 500 nm are instead potentially consistent with less crystalline phases, such as nanophase ferric oxides and ferrihydrite [Morris et al., 1985; Morris et al., 1993].

3.5.2 Thermal Infrared (TIR) Spectroscopy

All of the samples in this sample suite have absorption bands at ~1024 and ~ 440 cm^{-1}. In the hand sample analyses, 11 out of 12 (all except the Her01 sample) of the samples exhibit a strong shoulder on this primary band at ~890 cm^{-1}. However, in the sieved analyses, the ~890 cm^{-1} feature only appears in half of the samples (Lake01, Lake02, Lake03, Lake04, Her02, Ask01). The hand samples tend to have shallower bands (lower spectral contrast), most likely due to greater pore space in the hand samples compared to the sieved samples, which were analyzed as pressed pellets [Salisbury and Wald, 1992; Johnson et al., 1998]. Because of this effect, the hand sample spectra also tend to be noisier and exhibit less consistent emission band shapes and centers than the sieved samples (Figure 14).

The ~1024 cm^{-1} (~9.7 microns) emissivity minimum is present in all of the samples. In the hand samples it ranges from 1014-1045 cm^{-1} (~9.5 - ~9.8 microns) and in the sieved samples the minimum ranges from 1002-1037 cm^{-1} (~9.6 - ~9.9 microns), shifting the band slightly to longer wavelengths. Igneous silicates exhibit bands in the thermal infrared from 909-1250 cm^{-1} (~8-11 microns) due to the Si-O stretching modes of silicates [Lyon, 1965; Christensen et al., 2004]. Because the bands between 909-1250 cm^{-1} (8-11 microns) are so crucial for silicate identification in the thermal infrared, the Thermal Emission Imaging System (THEMIS) studying Mars has a band at 1035 cm^{-1} (9.66 microns) [Christensen et al., 2004; Bandfield et al., 2004]. Additionally, Rogers and Nekvasil [2015] note that mafic/anorthositic rocks tend to have emission minimums around this region (e.g. basalt at 1020 cm^{-1} [~9.8 microns], norite at 990 cm^{-1} [~10.1 microns], and anorthosite at 980 cm^{-1} [~10.2 microns]). In our samples, the emission minima near 1030 cm^{-1} (~9.7 microns) are consistent with a silicate of mafic composition like basalt or basaltic glass.

The position of the ~890 cm^{-1} (~11.2 microns) shoulder observed in 11 out of 12 (all except the Her01 sample) hand samples and 6 of the 12 (Lake01, Lake02, Lake03, Lake04, Her02, Ask01) sieved samples ranges from 858-927 cm^{-1} and 860-923 cm^{-1}, respectively. This feature was initially identified in basaltic glass from lava flows in Hawaii [Crisp et al., 1990]. Crisp et al., [1990] showed that this feature is only present in partially devitrified glass, and suggested that this feature appears due to the change from disordered silica in fresh glass to more ordered chains and sheets of silica tetrahedra during devitrification. Bands due to the chains of silica tetrahedra are observed between 860-920 cm^{-1} (10.9-11.3 microns) whereas bands due to sheets of silica tetrahedra are observed at ~1040-1050 cm^{-1} (~9.5-9.6 microns). In TIR spectra, SiO_4 sheet and chain structural changes have been shown to be correlated with degree of aqueous alteration during palagonitization[*Farrand et al.*, 2016]. Farrand et al., [2016] also observed these features in minimally altered, glass-rich lacustrine hydrovolcanic samples. The ~11 micron SiO_4-chain feature is present in the majority of our hand samples (Lake01, Lake02, Lake03, Lake04, 41701, 41702, DB01, DB02, Her02, Ask01, and SCoast01) and some of our sieved samples (Lake01, Lake02, Lake03, Lake04, Her02, and Ask01) from our glaciovolcanic sites. The ~9.5 micron SiO_4-sheet feature, if present in our sample spectra, is largely obscured by the deeper band due to tetrahedra in vitric glass at ~9.7 microns. In some cases, the ~11 micron devitrification feature disappears when the samples are ground and sieved (in the case of 41701, 41702, DB01, DB02, and SCoast01).

The ~440 cm^{-1} (~22.7 microns) emission band is present in all of the samples. In the hand samples it ranges from 439-458 cm^{-1} and from 430-453 cm^{-1} in the sieved samples. Like we see in the ~1024 cm^{-1} minimum band, sieving the samples shifts the minima to slightly longer wavelengths. A minimum at ~470 cm^{-1} corresponds to silicate bending vibrations related to tetrahedral sheets in the thermal infrared whereas a minimum between ~250 - 450 cm^{-1} shows M-O bonds and interlayer cation absorptions [Farmer, 1974; Michalski et al., 2005] possibly related to glass in the samples. However, interlayer cation absorptions occurs at <250 cm^{-1} and thus may not be detectable in our samples [Michalski et al., 2006].

The combination of these three minima, as well as the overall band shapes, suggest that our samples are primarily composed of basaltic glass with the addition of devitrified glass, similar to those in Farrand et al., [2016]. Olivine and pyroxene have square and complex bands with multiple absorptions surrounding the band center; however, glass tends to have a broad, smooth U-shaped band with no other accompanying features, a shape we commonly see in our samples. To confirm this, we used the quantitative deconvolution method of Rogers and Christensen [2007] to create a model of the bulk mineral assemblage and abundances for our samples. The models have specific minerals lumped into mineral groups for clarify. Clay minerals here include nontronite (Fe phyllosilicate), illite (Al/Mg/Fe phyllosilicate), hectorite (Mg phyllosilicate), chlorite (Mg/Fe phyllosilicate), saponite (Mg/Fe phyllosilicate), and kaolinite (Al phyllosilicate). Zeolite minerals include thomsonite, analcime, and stilbite. Percentage abundances for each sample can be found in the supplementary material (Table S2). Overall, the models produce relatively accurate fits of the data, where hand samples root-mean-square (RMS) errors range from 0.0014-0.0032 and sieved pellet samples RMS errors range from 0.0017-0.0038. Robust TIR models typically require RMS errors <0.005, and higher RMS errors often indicates that critical end members are missing from the spectral library [e.g., Feely & Christensen, 1999]. Based on the relatively low RMS errors for our samples, we infer that the new spectral library developed for this study (Table S1) contains reasonable approximations of most critical endmembers in our palagonite samples.

The sieved TIR models (Figure 15) show that the samples are all dominated by partially devitrified glass (typically 30-50%) and a similar or smaller fraction of unaltered glass. All of the modeled assemblages also include oxides (typically 5-10%), and typically also contain both zeolites and smectites (<15%). The Lake01, Lake02, and 41701 samples contain an additional amorphous component (8-16%) that the other samples do not contain. Lake 03 and Lake 04 have a very similar modeled assemblage, as expected because Lake 04 is a fracture fill within the Lake03 outcrop; however, Lake03 does contain a slightly larger amount of zeolites. Her02 has a modeled component of amphibole (3%) that the other samples do not contain. Additionally, samples Lake01, Lake02, DB02, and SCoast01 are modeled to contain olivine (1-5%). Mica is modeled to be present in samples Lake03, Lake04, Her02 and Ask01 (1% in all samples); however, we note that the low abundance of the modeled mica in the above samples is below the detection limit and therefore might not actually be a part of the modeled assemblages. The most strikingly different modeled assemblage is that of the SCoast01 sample. While the assemblage is similar to that of the other samples (partially devitrified glass, unaltered glass, oxides, clay minerals, and zeolites), the proportions of each group are different. The SCoast sample is made of 37% glass, 12% partially devitrified glass, 20% oxides, 13% zeolites, 13% clay minerals, and 5% of olivine.

The models of the surface spectra of the hand samples (Figure 16) show that the samples contain mostly partially devitrified glass (36-90%), olivine (4-10%), and secondary alteration minerals. Lake 01 and Lake02 continue to show a modeled component of amorphous material (13% and 1% respectively), however, it is not seen in the 41701 sample. Comparing samples Lake03 and Lake04 to the sieved samples, the hand samples vary considerably. In the sieved samples, the composition was similar but in the hand sample models, the two samples have completely different assemblages. Here, Lake03 is composed of only partially devitrified glass (90%) and clay (10%) while Lake04 has an assemblage consistent with the other samples (partially devitrified glass, olivine, and secondary alteration minerals). Olivine is a major component of the hand sample models, different from the sieved samples where it was only present in a small subset of the samples (Lake01, Lake02, DB02, and SCoast01). Mica is modeled to be present in samples Her01, DB01, and 41702 (1-3%), which is not consistent with what is seen in the sieved sample models. Again, this could be due to a modeled abundance below the detection level of the model. A major difference compared to the sieved samples is that the hand samples contain very little unaltered glass - only samples DB01, 41702, and Her01 have a modeled portion of unaltered glass (7-20%). SCoast01 has a similar assemblage to the rest of the hand samples, however, like in the sieved samples, the abundance percentages are different. The SCoast sample is made of 51% partially devitrified glass, 20% oxides, 15% zeolites, 10% of olivine, and 4% clay minerals.

Compared to the hand sample modeled spectra, the sieved modeled spectra fit the data slightly better (see RMS errors above). This is most likely due to the greater spectral contrast in the sieved samples, caused by creating a uniform grain size. Her02, SCoast01, and Lake01 samples have the worst model fits in both the sieved and hand samples and therefore the modeled assemblages for those samples are less accurate than the other samples. Overall, the largest differences between the hand sample and sieved modeled assemblage are the significant component of vitreous glass in the sieved samples compared to the largely devitrified glass in the hand samples, and the generally higher overall abundances of non-glass primary and secondary phases in the hand samples.

3.5.3 X-ray Powder Diffraction (XRD)

All of the samples had 20% corundum added, and large corundum peaks are observed at ~30, 41, 44, 51, 52, 62, 68, 72, 73, and 79° 2θ ($CoK\alpha_1$) in all samples (Figure 17). All samples also contain a large amorphous hump around ~30° 2θ ($CoK\alpha_1$), consistent with basaltic glass [e.g., Warren, 1990; Rampe et al., 2013; Achilles et al., 2013]. Samples 41701, 41702, and Ask01 have no additional peaks in their diffractograms and thus we interpret these samples as composed almost entirely of poorly crystalline phases. Samples Lake01, Lake02, Lake03, DB01, Her01, and Her02 have additional peaks at 32, and 33° 2θ ($CoK\alpha_1$), attributed to plagioclase feldspar. Samples Lake04 and DB02 have additional peaks at 35° 2θ ($CoK\alpha_1$) attributed to pyroxene (in this case the best match is hedenbergite). However, these peaks are very small relative to the corundum peaks and suggest crystalline phases are still only present at low abundances in all of these samples.

A clay peak at ~7° 2θ ($CoK\alpha_1$) is observed very clearly in one sample (SCoast01) and weakly in two samples (Lake03 and Ask01); however, the type of clay is unknown. In generaly, the SCoast01 sample exhibits many distinct peaks due to crystalline phases, and thus is drastically different than the rest of the samples. Because of the vast difference between this sample and the rest in the sample suite, this sample was modeled using HighScore Plus and showed a composition of 0.86% analcime (zeolite), 6.93% hedenbergite (pyroxene), 17.84% ferrosilite (pyroxene), and 73.47% amorphous phases, normalized to the known 20% addition of corundum added to the sample. However, we also know there is a crystalline clay phase and feldspar phase present due to the observed peaks that the model did not correctly identify.

3.6 Discussion

Overall, the samples are dominated by poorly crystalline ferric oxides, glass, Al-phyllosilicates, and zeolites in the VNIR; glass, devitrified glass, zeolites, clays, and oxides in the TIR; and almost exclusively X-ray amorphous material in the XRD measurements. The SCoast01 sample is the exception in all measurements, as it also displays pyroxene and Fe/Mg phyllosilicates in the VNIR, higher abundances of secondary alteration minerals in the TIR, and clearly crystalline pyroxene, clay, feldspar, and zeolites in the XRD measurements (Table 2).

3.6.1 Effect of Formation Environment on Mineralogy

SCoast01 is consistently different compared to the other glaciovolcanic samples throughout the methods used, both in that it contains more clearly crystalline primary and secondary phases and more Fe/Mg-rich smectites. Here we investigate two non-exclusive hypotheses for this difference in mineralogy: (1) SCoast01 was emplaced via hydrovolcanism (submarine/sublacustrine) as opposed to via glaciovolcanism, and (2) SCoast01 is more weathered due to longer surface exposure.

In terms of mineralogy, hydrovolcanic palagonite has been previously observed to exhibit a stronger ~2300 nm band indicative of Fe/Mg smectites [Farrand et al., 2017] with an almost nonexistent ~2200 nm band. Additionally, Summers [1976] showed that nontronite (Fe member of the smectite group) was the dominant clay in the palagonite associated with the Columbia River pillow basalts. However, Farrand et al., [1992] showed that clay composition in hydrovolcanic palagonites varies with water depth based on the presence of the ~2200 and ~2300 nm bands within multiple samples of hydrovolcanic palagonites collected in the southwest United States. They found that tuff ring samples (erupted near the water-air interface) exhibit a ~2200nm band and tuff cone samples (erupted in somewhat deeper water) exhibit a ~2300nm band. Thus, tuff rings, which erupt near the water-air interface, contain more Al-rich clays, whereas tuff cones, which erupt in somewhat deeper water, contain more Fe-rich clays.

As shown in this study and previous studies, this variability contrasts strongly with the clay mineralogy inferred for subglacial palagonite, which is consistently Al-smectite bearing [Bishop et al., 2002; Farrand et al., 2017]. Thus, we hypothesize that glaciovolcanic and deep hydrovolcanic palagonites may represent end members on a continuum of palagonite clay composition, as suggested by Crovisier et al., [1992].

Based on this apparent relationship between clay composition and formation environment, SCoast01 is potentially consistent with a hydrovolcanic palagonite erupted into relatively deep water, but potentially still in the near-shore environment. The SCoast01 sample is located on the emergent southern coastline of Iceland, which has been rebounding since the last ice age due to glacial retreat [Árnadóttir et al., 2009]. The sample was collected at elevations below the wave cut cliffs along the southern coast that correspond to the shoreline during the last ice age, so it is plausible that the eruption that created the SCoast01 sample occurred offshore and was thus submarine instead of subglacial.

We suggest that the observed difference in clay composition between deep water hydrovolcanic palagonite, dominated by Fe/Mg-smectite, vs. shallow water hydrovolcanic and glaciovolcanic palagonite, both dominated by Al-smectite, is due to differences in alteration style across the environments. Previous studies have shown that smectite composition is largely determined by whether the alteration system is an open or closed system. Open systems with high water to rock ratios experience high chemical fractionation, where after cations are leached from primary minerals, the more mobile monovalent and divalent cations (e.g., Na, Ca, Mg, Fe^{2+}) are rapidly removed from the system, and Fe^{3+} and Al are incorporated into aluminum clays and iron oxides [Ehlmann et al., 2011]. In closed systems, the combination of typically reducing conditions and limited fluid flow leads to retention of Fe^{2+}. If sufficient Fe is present in the system due to either a mafic parent material or infiltration by Fe-bearing fluids, significant Fe/Mg-smectite can be formed [Ehlmann et al., 2011; Baker et al., 2017]. Note that closed systems are rare on Earth and are usually constrained to the subsurface [Ehlmann et al., 2011; Baker et al., 2017]; however, this type of alteration is also observed in seafloor hydrothermal systems where the parent rock is basalt [Cann and Vine, 1966] and in subaerial hydrothermal systems in Iceland [Franzon et al., 2008; Ehlmann et al., 2011b].

Applying this distinction in clay mineralogies between open vs. closed systems to palagonites suggests that glaciovolcanic and shallow water hydrovolcanic palagonites are dominated by Al-smectites formed in a largely open system, whereas deep water hydrovolcanic palagonites are dominated by Fe/Mg-smectites formed in a largely closed system. Deep water effectively creates a closed system due to isolation from the atmosphere, often reducing conditions, and consistent temperature and pressure [Ehlmann et al., 2011].

Alternatively, we must also consider whether or not the difference in composition between SCoast01 and the other Icleandic palagonites in this study could be due to recent surface weathering. Subaerial chemical weathering is driven by leaching due to infiltration of rainfall and snowmelt into rocks and soils, and the alteration mineral assemblage in these environments is highly dependent on climate (specifically the amount of precipitation), duration of alteration, and element mobility. In very humid climates, like Iceland, subaerial weathering of volcanic terrain is initially dominated by poorly crystalline materials (e.g. allophane, imoglite, and ferrihydrite) [*Claridge*, 1965; *Singer*, 1974, 1980; *Arnalds and Kimble*, 2001; *Arnalds*, 2004; *Ugolini and Bockheim*, 2008]. This is because the humid climate and the glass-rich nature of the parent materials both encourage rapid leaching of immobile elements (e.g. K^+, Na^+, Ca^{2+}, Mg^{2+}) and formation of Al-, Fe-, and Si-rich poorly crystalline weathering products. The poorly crystalline weathering products mature into more crystalline clay minerals and oxides (e.g., halloysite, kaolinite, gibbsite) over a period of tens of thousands to millions of years [*Ugolini and Dahlgren*, 2002; *Ziegler et al.*, 2003; *Tsai et al.*, 2010]. Al-smectites are more commonly produced during weathering under somewhat more arid climates [e.g., Johnsson et al., 1993]. However, Fe/Mg-smectites are rarely produced during open-system pedogenic leaching, and tend to be restricted to the base of deep weathering profiles, where limited pore space restricts fluid flow at small scales [Baker et al., 2017]. The cliff where SCoast01 was collected exhibits clear evidence for surface exposure (well-developed mosses, etc.), so any leaching likely took place in the near surface. Thus, because near-surface subaerial weathering of volcanic terrains usually produces either poorly crystalline phases or crystalline Al-rich phyllosilicates, the SCoast01 sample, spectrally dominated by Fe/Mg phyllosilicates, is inconsistent with this interpretation.

We suggest that the SCoast01 sample is more consistent with a hydrovolcanic origin than a subaerial weathering origin. If the SCoast01 sample is indeed hydrovolcanically sourced, our sample set now reflects a subset of 11 glaciovolcanic samples and 1 hydrovolcanic sample.

3.6.2 Inconsistencies Between Datasets and Crystallinity

The analyses of three separate datasets produces three distinct views of the mineral assemblage that make our glaciovolcanic palagonites initially appear not entirely consistent. While some inconsistencies between analytical methods are expected based on the nature of each instrument and what phases they are most sensitive to (e.g. VNIR is very sensitive to secondary mineralogy and Fe-bearing materials while TIR can identify most phases at moderate abundances), many of the inconsistencies may instead be related to the crystallinity of the samples.

Models of the TIR spectra of the hand and sieved pellet samples produce two different assemblages. The hand sample models show that the samples contain mostly partially devitrified glass, olivine, and secondary alteration minerals including zeolites, clay minerals, and oxides.

The sieved sample models show that the samples contain mostly partially devitrified glass, unaltered glass, clay, oxides, and zeolites. The largest differences are the small amount of olivine modeled in the hand samples and the significant unaltered glass modeled in the sieved pellet samples. While the difference in olivine abundance could be due to the presence of one or several olivine phenocrysts in the hand sample, we attribute the difference in glass crystallinity to a real difference between sample interiors and exteriors. The hand samples are a relatively pristine samples composed of intact grains of palagonite, whereas the sieved samples were crushed and ground to create a uniform grain size, exposing the interiors of the palagonite grains. This suggests that more devitrified glass is present at the surface of the grains that make up the palagonite hand sample, and that more unaltered or vitric glass is present in the interiors of the grains exposed in the sieved samples. This would be consistent with devitrification due to heating of the grains during and shortly after eruption that only progressed far enough to affect the surfaces of the grains but not the interiors.

Another hypothesis for the differences in the modeled mineral assemblages between hand and sieved samples could be based on texture. TIR spectral measurements can be very sensitive to sample texture as demonstrated by Farrand et al., [2016] where a bulk hand sample and a slice/cut of the sample was compared, showing two different TIR spectra. Thus it is possible that the model isn't actually matching a mineral/mineraloid but instead it is matching the shape of the bands caused by different textures. The differences in natural and cut samples have also been observed to be attributed to weathering rinds [Michalski et al., 2005] and could likely be what we are seeing here.

VNIR and TIR spectra show clear detections of phyllosilcate minerals in all palagonites in this study; however, most samples do not show evidence for phyllosilicates in their XRD patterns. VNIR and TIR spectral measurements essentially detect individual Fe/Mg/Al-OH or Si-O bonds that can exist outside of a crystalline structure. However, only materials with long-range atomic structure can be definitively detected using XRD. Therefore the lack of crystalline clay mineral detection in XRD data suggests that the phyllosilicates in the palagonites are mostly poorly crystalline. Additionally, many other minerals are detected in VNIR and TIR but not in the XRD analysis (e.g., zeolites), suggesting that the entire palagonite assemblage is poorly crystalline. The lack of crystalline minerals in palagonites has been well-documented in previous research [*Allen et al.*, 1981; *Morris et al.*, 1990; *Stroncik and Schmincke*, 2002; *Michalski et al.*, 2005; *Warner and Farmer*, 2010; *Cousins et al.*, 2013], suggesting that the combination of both spectral and XRD techniques is a valid technique for identifying and more fully characterizing the composition of poorly crystalline materials.

For terrestrial studies, this suggests that these non-traditional techniques (VNIR and TIR) could be used to better identify and characterize poorly crystalline materials, supplementing more traditional techniques such as XRD, XRF (X-ray fluorescence), EMP (electron microbe), thin section analysis, TEM (transmission electron microscopy), SEM (scanning electron microprobe), and ICP-MS (Inductively Coupled Plasma Mass Spectrometry). In addition, VNIR and TIR techniques are usually less time-consuming, less destructive, and less expensive than the traditional terrestrial techniques listed above.

This method of investigating crystallinity using VNIR, TIR, and XRD together also has major implications for extraterrestrial research. Mineral identification on Mars has primarily been accomplished using VNIR and TIR spectra, however, this study illustrates the need for caution when interpreting alteration phases on Mars using VNIR and TIR techniques alone. These materials could actually be poorly crystalline in nature, and thus potentially very different from traditional terrestrial analogs selected based on the presence of their crystalline counterparts. This may be a major issue on Mars, as recent findings from the Mars Science Laboratory mission show that a majority of the sediments in Gale crater studied via XRD contain high abundances of poorly crystalline and/or amorphous phases [Bish et al., 2013; Vaniman et al., 2014; Morris et al., 2016; Yen et al., 2017; Rampe et al., 2017; Archilles et al., 2017a, 2017b].

The SCoast01 sample is the general exception to our general finding that the palagonites in this study are dominated by poorly crystalline phases. The SCoast01 sample is composed of a significant fraction of crystalline minerals that we were able to detect and model using XRD. The fact that SCoast01 is more crystalline than and has a different mineralogy from the rest of the sample suite could help place constraints on SCoast01's formation and alteration history. While subaerial weathering causes amorphous material to become crystalline overtime, the Fe-smectitic mineralogy of SCoast01 is not consistent with a subaerial weathering formation environment, as discussed above. In general, we cannot attribute crystallinity to any long-term maturation process. Daux et al., [1994] noted that the crystallinity of weathering products in glaciovolcanic samples is not simply related to the age of the samples, based on the observation that some of the oldest samples in their glaciovolcanic collection from Iceland are amorphous and some of the youngest samples are highly crystallized. If SCoast01 is indeed hydrovolcanically-sourced, this implies that crystallinity could be a differentiating factor in glaciovolcanic versus hydrovolcanically sourced palagonite. Perhaps consistent with the analogous formation of the Columbia River hydrovolcanic palagonites, this sample could indicate an intrusive production in deep water where the crystallization is due to the isolation from the atmosphere and therefore limited leaching, constant temperature and pressure, and more time to cool and crystallize [Waters, 1960; Mackin, 1961; Moore et al., 1973; Furnes, 1974; Naylor et al., 1999].

3.7 Conclusions

Results show the sampled palagonites contain partially devitrified glass, unaltered glass, and secondary minerals including clay minerals, poorly crystalline ferric oxides, and zeolites. However, one sample (SCoast01) shows a vastly different mineral assemblage in all sample techniques, including well-crystalline Fe/Mg-clays as opposed to the poorly-crystalline Al-clays observed in our other samples. Based on previous studies of subaqueous palagonites and the location this sample was collected from, we hypothesize that the SCoast01 sample was formed in a submarine environment rather than subglacial. This suggests that it may be possible to differentiate submarine vs. subglacial palagonite on Earth based on composition and from remote sensing observations on Mars. Definitively identifying palagonite on the martian surface would be vital in constraining past environments and the history of the surface.

There are two major implications of this work: while both glaciovolcanic and hydrovolcanic palagonites contain an assemblage including devitrified and unaltered glass, smectites, zeolites, and oxides, (1) both the composition and crystallinity of glacio- and hydrovolcanically sourced palagonites differ, and (2) these differences can be detected with Mars-relevant in situ and orbital instruments. The clay composition in glaciovolcanic palagonite is mostly composed of Al-smectites, which we hypothesize is due to leaching in an open system created by the flow of water and atmosphere under the melting glacier. In comparison, hydrovolcanic palagonite formed at depth in water has additional smectites rich in Fe/Mg, possibly due to alteration underwater in a closed system created by the reducing conditions well below the water surface. Hydrovolcanic eruptions in shallow water environments (e.g., tuff rings) may exhibit intermediate clay compositions between these two endmembers.

These results were made possible due to the combined application of both spectral (VNIR and/or TIR) and XRD techniques, which together provide valuable information on the composition and crystallinity of rocks and sediments. These results show that, in addition to the composition, the crystallinity of palagonites is variable. Based on our sample set, hydrovolcanic palagonites appear to contain more crystalline assemblages than glaciovolcanic palagonites. Our study implies that for both terrestrial and extraterrestrial studies of palagonite, the variable mineralogy and crystallinity of the rocks can be used to place constraints on the formation environment of the palagonite and thus the climatic regime in which it was formed. Thus, the mineralogy of palagonite may serve as a valuable record of past surface environments on both Earth and Mars.

3.8 Acknowledgements and Data

This work was supported by the NASA Earth and Space Science Fellowship, the Purdue Doctoral Fellowship, and the Pierazzo International Student Travel Award. We would like to thank Cliff Johnston, Heather Pasley, and Darryl Schultz for their generosity in sharing their XRD facilities as well as Thor Thordarson for useful discussions. Lastly, we note that data from this manuscript is available at the Data Center Hub (https://datacenterhub.org/).

3.9 References

Ackiss, S., Horgan, B., Seelos, F., Farrand, W., Wray, J., 2018. Mineralogic evidence for subglacial volcanism in the Sisyphi Montes region of Mars. Icarus 311, 357–370.

Allen, C.C., Gooding, J.L., Jercinovic, M., Keil, K., 1981. Altered basaltic glass: A terrestrial analog to the soil of Mars. Icarus 45, 347–369. https://doi.org/10.1016/0019-1035(81)90040-3

Allen, C.C., Jager, K.M., Morris, R.V., Lindstrom, D.J., Lindtsrom, M.M., Lockwood, J.P., 1998. Martian soil simulant available for scientific, educational study. Eos Trans. Am. Geophys. Union 79, 405–409. https://doi.org/10.1029/98EO00309

Árnadóttir, T., Lund, B., Jiang, W., Geirsson, H., Björnsson, H., Einarsson, P., Sigurdsson, T., 2009. Glacial rebound and plate spreading: results from the first countrywide GPS observations in Iceland. Geophys. J. Int. 177, 691–716.

Arnalds, O., 2004. Volcanic soils of Iceland. CATENA, Volcanic Soil Resources: Occurrence, Development and Properties 56, 3–20. https://doi.org/10.1016/j.catena.2003.10.002

Arnalds, O., Kimble, J., 2001. Andisols of deserts in Iceland. Soil Sci. Soc. Am. J. 65, 1778–1786.

Baker, L.L., Neill, O.K., 2017. Geochemistry and mineralogy of a saprolite developed on Columbia River Basalt: Secondary clay formation, element leaching, and mass balance during weathering. Am. Mineral. J. Earth Planet. Mater. 102, 1632–1645.

Banin, A., Margulies, L., 1983. Simulation of Viking biology experiments suggests smectites not palagonites, as martian soil analogues. Nature 305, 523–525. https://doi.org/10.1038/305523a0

Bell, J.F., C. Malin, M., A. Caplinger, M., A. Ravine, M., S. Godber, A., Jungers, M., Rice, M., Anderson, R., 2012. Mastcam Multispectral Imaging on the Mars Science Laboratory Rover: Wavelength Coverage and Imaging Strategies at the Gale Crater Field Site. Lunar Planet. Inst. Sci. Conf. Abstr. 2541.

Bell, J.F., McCord, T.B., Owensby, P.D., 1990. Observational evidence of crystalline iron oxides on Mars. J. Geophys. Res. Solid Earth 95, 14447–14461.

Bell, J.F., Morris, R.V., Adams, J.B., 1993. Thermally altered palagonitic tephra: A spectral and process analog to the soil and dust of Mars. J. Geophys. Res. Planets 98, 3373–3385.

Bibring, J.-P., Langevin, Y., Gendrin, A., Gondet, B., Poulet, F., Berthé, M., Soufflot, A., Arvidson, R., Mangold, N., Mustard, J., Drossart, P., OMEGA Team, Erard, S., Forni, O., Combes, M., Encrenaz, T., Fouchet, T., Merchiorri, R., Belluci, G., Altieri, F., Formisano, V., Bonello, G., Capaccioni, F., Cerroni, P., Coradini, A., Fonti, S., Kottsov, V., Ignatiev, N., Moroz, V., Titov, D., Zasova, L., Mangold, M., Pinet, P., Douté, S., Schmitt, B., Sotin, C., Hauber, E., Hoffmann, H., Jaumann, R., Keller, U., Duxbury, T., Forget, F., 2005. Mars Surface Diversity as Revealed by the OMEGA/Mars Express Observations. Science 307, 1576–1581. https://doi.org/10.1126/science.1108806

Bish, D.L., Reynolds, R.C., 1989. Sample preparation for X-ray diffraction. Rev. Mineral. Geochem. 20, 73–99.

Bishop, J.L., Lane, M.D., Dyar, M.D., Brown, A.J., 2008. Reflectance and emission spectroscopy study of four groups of phyllosilicates: smectites, kaolinite-serpentines, chlorites and micas. Clay Miner. 43, 35–54.

Bishop, J.L., Pieters, C.M., Burns, R.G., Edwards, J.O., Mancinelli, R.L., Fröschl, H., 1995. Reflectance Spectroscopy of Ferric Sulfate-Bearing Montmorillonites as Mars Soil Analog Materials. Icarus 117, 101–119. https://doi.org/10.1006/icar.1995.1145

Bishop, J.L., Schiffman, P., Southard, R., 2002. Geochemical and mineralogical analyses of palagonitic tuffs and altered rinds of pillow basalts in Iceland and applications to Mars. Geol. Soc. Lond. Spec. Publ. 202, 371–392. https://doi.org/10.1144/GSL.SP.2002.202.01.19

Björnsson, H., Einarsson, P., 1990. Volcanoes beneath Vatnajökull, Iceland: Evidence from radio echo-sounding, earthquakes and jökulhlaups. Jökull 40, 147–168.

Blake, D., Vaniman, D., Achilles, C., Anderson, R., Bish, D., Bristow, T., Chen, C., Chipera, S., Crisp, J., Des Marais, D., 2012. Characterization and calibration of the CheMin mineralogical instrument on Mars Science Laboratory. Space Sci. Rev. 170, 341–399.

Burns, R.G., 1993. Mineralogical applications of crystal field theory. Cambridge University Press.

Burns, R.G., 1970a. Site preferences of transition metal ions in silicate crystal structures. Chem. Geol. 5, 275–283.

Burns, R.G., 1970b. Crystal field spectra and evidence of cation ordering in olivine minerals. Am. Mineral. 55, 1608–1632.

Byrnes, J.M., Ramsey, M.S., King, P.L., Lee, R.J., 2007. Thermal infrared reflectance and emission spectroscopy of quartzofeldspathic glasses. Geophys. Res. Lett. 34.

Cann, J.R., Vine, F.J., 1966. A discussion concerning the floor of the northwest Indian Ocean-An area on the crest of the Carlsberg Ridge: petrology and magnetic survey. Phil Trans R Soc Lond A 259, 198–217.

Chapman, M.R., Shackleton, N.J., 2000. Evidence of 550-year and 1000-year cyclicities in North Atlantic circulation patterns during the Holocene. The Holocene 10, 287–291.

Christensen, P.R., Bandfield, J.L., Hamilton, V.E., Ruff, S.W., Kieffer, H.H., Titus, T.N., Malin, M.C., Morris, R.V., Lane, M.D., Clark, R.L., Jakosky, B.M., Mellon, M.T., Pearl, J.C., Conrath, B.J., Smith, M.D., Clancy, R.T., Kuzmin, R.O., Roush, T., Mehall, G.L., Gorelick, N., Bender, K., Murray, K., Dason, S., Greene, E., Silverman, S., Greenfield, M., 2001. Mars Global Surveyor Thermal Emission Spectrometer experiment:

Investigation description and surface science results. J. Geophys. Res. 106, 23823–23872. https://doi.org/10.1029/2000JE001370

Christensen, P.R., Jakosky, B.M., Kieffer, H.H., Malin, M.C., McSween, H.Y., Nealson, K., Mehall, G.L., Silverman, S.H., Ferry, S., Caplinger, M., Ravine, M., 2004. The Thermal Emission Imaging System (THEMIS) for the Mars 2001 Odyssey Mission. Space Sci. Rev. 110, 85–130. https://doi.org/10.1023/B:SPAC.0000021008.16305.94

Clancy, R.T., Lee, S.W., Gladstone, G.R., McMillan, W.W., Rousch, T., 1995. A new model for Mars atmospheric dust based upon analysis of ultraviolet through infrared observations from Mariner 9, Viking, and Phobos. J. Geophys. Res. Planets 100, 5251–5263.

Claridge, G.G.C., 1965. The clay mineralogy and chemistry of some soils from the Ross Dependency, Antarctica. N. Z. J. Geol. Geophys. 8, 186–220.

Clark, R., Swayze, G.A., Wise, R., Livo, E., Hoefen, T., Kokaly, R., Sutley, S.J., 2007. USGS digital spectral library splib06a: U.S. Geological Survey. Digit. Data Ser. 231.

Clark, R.N., King, T.V.V., Klejwa, M., Swayze, G.A., Vergo, N., 1990. High spectral resolution reflectance spectroscopy of minerals. J. Geophys. Res. 95, 12653–12680. https://doi.org/10.1029/JB095iB08p12653

Cloutis, E.A., Asher, P.M., Mertzman, S.A., 2002. Spectral reflectance properties of zeolites and remote sensing implications. J. Geophys. Res. Planets 107, 5067. https://doi.org/10.1029/2000JE001467

Collins, J.R., 1937. The Near Infrared Absorption Band of Liquid Water at 1.79μ. Phys. Rev. 52, 88–90. https://doi.org/10.1103/PhysRev.52.88

Cousins, C.R., Crawford, I.A., Carrivick, J.L., Gunn, M., Harris, J., Kee, T.P., Karlsson, M., Carmody, L., Cockell, C., Herschy, B., Joy, K.H., 2013. Glaciovolcanic hydrothermal environments in Iceland and implications for their detection on Mars. J. Volcanol. Geotherm. Res. 256, 61–77. https://doi.org/10.1016/j.jvolgeores.2013.02.009

Crisp, J., Bartholomew, M.J., 1992. Mid-infrared spectroscopy of Pahala ash palagonite and implications for remote sensing studies of Mars. J. Geophys. Res. Planets 97, 14691–14699.

Crisp, J., Kahle, A.B., Abbott, E.A., 1990. Thermal infrared spectral character of Hawaiian basaltic glasses. J. Geophys. Res. Solid Earth 95, 21657–21669.

Crovisier, J.-L., Honnorez, J., Fritz, B., Petit, J.-C., 1992. Dissolution of subglacial volcanic glasses from Iceland: laboratory study and modelling. Appl. Geochem. 7, 55–81.

Daux, V., Crovisier, J.L., Hemond, C., Petit, J.C., 1994. Geochemical evolution of basaltic rocks subjected to weathering: fate of the major elements, rare earth elements, and thorium. Geochim. Cosmochim. Acta 58, 4941–4954.

Drief, A., Schiffman, P., 2004. Very Low-Temperature Alteration of Sideromelane in Hyaloclastites and Hyalotuffs from Kilauea and Mauna Kea Volcanoes: Implications for the Mechanism of Palagonite Formation. Clays Clay Miner. 52, 622–634. https://doi.org/10.1346/CCMN.2004.0520508

Eggleton, R.A., Keller, J., 1982. The palagonitization of limburgite glass - A TEM study. Neues Jahrb. Mineral. Monatshefte 7, 321–336.

Ehlmann, B.L., Edwards, C.S., 2014. Mineralogy of the Martian Surface. Annu. Rev. Earth Planet. Sci. 42, null. https://doi.org/10.1146/annurev-earth-060313-055024

Ehlmann, B.L., Mustard, J.F., Murchie, S.L., Bibring, J.-P., Meunier, A., Fraeman, A.A., Langevin, Y., 2011a. Subsurface water and clay mineral formation during the early history of Mars. Nature 479, 53–60. https://doi.org/10.1038/nature10582

Ehlmann, B.L., Mustard, J.F., Murchie, S.L., Bibring, J.-P., Meunier, A., Fraeman, A.A., Langevin, Y., 2011b. Subsurface water and clay mineral formation during the early history of Mars. Nature 479, 53–60. https://doi.org/10.1038/nature10582

Ehlmann, B.L., Mustard, J.F., Swayze, G.A., Clark, R.N., Bishop, J.L., Poulet, F., Des Marais, D.J., Roach, L.H., Milliken, R.E., Wray, J.J., Barnouin-Jha, O., Murchie, S.L., 2009. Identification of hydrated silicate minerals on Mars using MRO-CRISM: Geologic context near Nili Fossae and implications for aqueous alteration. J. Geophys. Res. Planets 114. https://doi.org/10.1029/2009JE003339

Ellis, J.W., 1931. Polymers and New Infrared Absorption Bands of Water. Phys. Rev. 38, 693.

Evans, D.L., Adams, J.B., 1979. Comparison of Viking Lander multispectral images and laboratory reflectance spectra of terrestrial samples, in: Lunar and Planetary Science Conference Proceedings. pp. 1829–1834.

Fagan, A.L., Sakimoto, S.E.H., Hughes, S.S., 2010. Formation constraints on Martian north polar volcanic edifices. J. Geophys. Res. Planets 115.

Farmer, V.C., 1974. Infrared spectra of minerals. Mineralogical society.

Farrand, W.H., Singer, R.B., 1992. Alteration of hydrovolcanic basaltic ash: Observations with visible and near-infrared spectrometry. J. Geophys. Res. Solid Earth 97, 17393–17408.

Farrand, W.H., Wright, S.P., Glotch, T.D., Schröder, C., Sklute, E.C., Dyar, M.D., 2018. Spectroscopic examinations of hydro- and glaciovolcanic basaltic tuffs: Modes of alteration and relevance for Mars. Icarus 309, 241–259. https://doi.org/10.1016/j.icarus.2018.03.005

Farrand, W.H., Wright, S.P., Rogers, A.D., Glotch, T.D., 2016. Basaltic glass formed from hydrovolcanism and impact processes: Characterization and clues for detection of mode of origin from VNIR through MWIR reflectance and emission spectroscopy. Icarus 275, 16–28.

Feely, K.C., Christensen, P.R., 1999. Quantitative compositional analysis using thermal emission spectroscopy: Application to igneous and metamorphic rocks. J. Geophys. Res. Planets 104, 24195–24210.

Franzson, H., Zierenberg, R., Schiffman, P., 2008. Chemical transport in geothermal systems in Iceland: evidence from hydrothermal alteration. J. Volcanol. Geotherm. Res. 173, 217–229.

Fuller, R.E., 1950. Structural features in the Columbia River basalt. Northwest Sci. 24, 65–73.

Fuller, R.E., 1934. Structural features in the Columbia River lavas of central Washington: a criticism. J. Geol. 42, 311–328.

Fuller, R.E., 1932. Concerning basaltic glass. Am. Mineral. 17, 104–107.

Fuller, R.E., 1931. The aqueous chilling of basaltic lava on the Columbia River Plateau. Am. J. Sci. 281–300.

Furnes, H., 1984. Chemical changes during progressive subaerial palagonitization of a subglacial olivine tholeiite hyaloclastite: a microprobe study. Chem. Geol. 43, 271–285.

Furnes, H., Fridleifsson, I.B., 1974. Tidal effects on the formation of pillow lava/hyaloclastite deltas. Geology 2, 381–384.

Garcia, M.O., Muenow, D.W., Aggrey, K.E., O’Neil, J.R., 1989. Major element, volatile, and stable isotope geochemistry of Hawaiian submarine tholeiitic glasses. J. Geophys. Res. Solid Earth 94, 10525–10538.

Geirsdóttir, Á., Eiriksson, J.O.N., 1994. Sedimentary facies and environmental history of the Late-glacial glaciomarine Fossvogur sediments in Reykjavík, Iceland. Boreas 23, 164–176.

Gellert, R., Rieder, R., Brückner, J., Clark, B.C., Dreibus, G., Klingelhöfer, G., Lugmair, G., Ming, D.W., Wänke, H., Yen, A., 2006. Alpha Particle X-ray Spectrometer (APXS): Results from Gusev crater and calibration report. J. Geophys. Res. Planets 111.

Ghatan, G.J., Head, J.W., 2002. Candidate subglacial volcanoes in the south polar region of Mars: Morphology, morphometry, and eruption conditions. J. Geophys. Res. Planets 107, 5048. https://doi.org/10.1029/2001JE001519

Glotch, T.D., Bandfield, J.L., Christensen, P.R., Calvin, W.M., McLennan, S.M., Clark, B.C., Rogers, A.D., Squyres, S.W., 2006. Mineralogy of the light-toned outcrop at Meridiani Planum as seen by the Miniature Thermal Emission Spectrometer and implications for its formation. J. Geophys. Res. Planets 111.

Golden, D.C., Morris, R.V., Ming, D.W., Lauer, H.V., Yang, S.R., 1993. Mineralogy of three slightly palagonitized basaltic tephra samples from the summit of Mauna Kea, Hawaii. J. Geophys. Res. Planets 98, 3401–3411. https://doi.org/10.1029/92JE02590

Gooding, J.L., Keil, K., 1978. Alteration of glass as a possible source of clay minerals on Mars. Geophys. Res. Lett. 5, 727–730. https://doi.org/10.1029/GL005i008p00727

Green, W.L., 1887. Vestiges of the molten globe, pt. 2. Earths Surf. Featur. Volcan. Phenom. Honol. Gaz. Publ. Co 337.

Gudmundsson, 2005. Subglacial volcanic activity in Iceland. Icel. Mod. Process. Past Environ. Elsevier In: C. Caseldine, A. Russell, J. Hardardóttir and Ó. Knudsen eds., 127–151.

Hamilton, V.E., Christensen, P.R., 2000. Determining the modal mineralogy of mafic and ultramafic igneous rocks using thermal emission spectroscopy. J. Geophys. Res. Planets 105, 9717–9733.

Hamilton, V.E., Christensen, P.R., McSween, H.Y., 1997. Determination of Martian meteorite lithologies and mineralogies using vibrational spectroscopy. J. Geophys. Res. Planets 102, 25593–25603.

Hamilton, V.E., Morris, R.V., Gruener, J.E., Mertzman, S.A., 2008. Visible, near-infrared, and middle infrared spectroscopy of altered basaltic tephras: Spectral signatures of phyllosilicates, sulfates, and other aqueous alteration products with application to the mineralogy of the Columbia Hills of Gusev Crater, Mars. J. Geophys. Res. Planets 113, E12S43. https://doi.org/10.1029/2007JE003049

Hay, R.L., Iijima, A., 1968. Nature and Origin of Palagonite Tuffs of the Honolulu Group on Oahu, Hawaii. Geol. Soc. Am. Mem. 116, 331–376. https://doi.org/10.1130/MEM116-p331

Hay, R.L., Jones, B.F., 1972. Weathering of Basaltic Tephra on the Island of Hawaii. Geol. Soc. Am. Bull. 83, 317–332. https://doi.org/10.1130/0016-7606(1972)83[317:WOBTOT]2.0.CO;2

Horgan, B.H.N., Cloutis, E.A., Mann, P., Bell, J.F., 2014. Near-infrared spectra of ferrous mineral mixtures and methods for their identification in planetary surface spectra. Icarus 234, 132–154. https://doi.org/10.1016/j.icarus.2014.02.031

Hunt, G.R., 1977. Spectral signatures of particulate minerals in the visible and near infrared. Geophysics 42, 501–513. https://doi.org/10.1190/1.1440721

Jakobsson, S., 1978. Environmental factors controlling the palagonization of the Surtsey tephra, Iceland. Bull Geol Soc Den. 27, 91–105.

Jakobsson, S., Gudmundsson, M., 2008. Subglacial and intraglacial volcanic formations in Iceland. Jökull 58, 179–196.

Jakobsson, S.P., Moore, J.G., 1986. Hydrothermal minerals and alteration rates at Surtsey volcano, Iceland. Geol. Soc. Am. Bull. 97, 648–659. https://doi.org/10.1130/0016-7606(1986)97<648:HMAARA>2.0.CO;2

Jercinovic, M.J., Keil, K., Smith, M.R., Schmitt, R.A., 1990. Alteration of basaltic glasses from north-central British Columbia, Canada. Geochim. Cosmochim. Acta 54, 2679–2696. https://doi.org/10.1016/0016-7037(90)90004-5

Jóhannesson, H., Saemundsson, K., 1998. Jardfraedikort af Islandi. Hoggun Geol. Map Icel. Tecton. Náttúrfraedistofunu Isl. Icel. Inst. Nat. Hist. Reykjavık.

Johnsson, M.J., Ellen, S.D., McKittrick, M.A., 1993. Intensity and Duration of Chemical Weathering: An Example from Soil, Clays of the Southeastern Koolau Mountains, Oahu, Hawaii. Spec. Pap.-Geol. Soc. Am. 147–147.

Jones, J.G., 1969. Pillow lavas as depth indicators. Am. J. Sci. 267, 181–195.

Kjartansson, G., 1960. Geological map of Iceland. 1: 250.000. Reyk. Icel. Surv. Dep.

Kjartansson, G., 1943. Arnesingasaga I. Reykjavik.

Klima, R.L., Pieters, C.M., Dyar, M.D., 2007. Spectroscopy of synthetic Mg-Fe pyroxenes I: Spin-allowed and spin-forbidden crystal field bands in the visible and near-infrared. Meteorit. Planet. Sci. 42, 235–253. https://doi.org/10.1111/j.1945-5100.2007.tb00230.x

Klug, H.P., Alexander, L.E., 1974. X-ray diffraction procedures: for polycrystalline and amorphous materials. X-Ray Diffr. Proced. Polycryst. Amorph. Mater. 2nd Ed. Harold P Klug Leroy E Alexander Pp 992 ISBN 0-471-49369-4 Wiley-VCH May 1974 992.

Koeppen, W.C., Hamilton, V.E., 2008. Global distribution, composition, and abundance of olivine on the surface of Mars from thermal infrared data. J. Geophys. Res. Planets 113, E05001. https://doi.org/10.1029/2007JE002984

Lane, M.D., 2007. Mid-infrared emission spectroscopy of sulfate and sulfate-bearing minerals. Am. Mineral. 92, 1–18.

Larsen, G., 2002. A brief overview of eruptions from ice-covered and ice-capped volcanic systems in Iceland during the past 11 centuries: frequency, periodicity and implications. Geol. Soc. Lond. Spec. Publ. 202, 81–90.

Licciardi, J.M., Kurz, M.D., Curtice, J.M., 2007. Glacial and volcanic history of Icelandic table mountains from cosmogenic 3He exposure ages. Quat. Sci. Rev. 26, 1529–1546.

Locock, A.J., Chesterman, D., Caird, D., Duke, M.J.M., 2012. Miniaturization of mechanical milling for powder X-ray diffraction. Powder Diffr. 27, 189–193.

Lyon, R.J.P., 1965. Analysis of rocks by spectral infrared emission (8 to 25 microns). Econ. Geol. 60, 715–736.

Mackin, J.H., 1961. stratigraphic section in the Yakima Basalt and the Ellensburg Formation in south-central Washington.

Malin, M.C., Caplinger, M.A., Edgett, K.S., Ghaemi, F.T., Ravine, M.A., Schaffner, J.A., Baker, J.M., Bardis, J.D., DiBiase, D.R., Maki, J.N., 2010. The Mars Science Laboratory (MSL) mast-mounted cameras (Mastcams) flight instruments, in: Lunar and Planetary Science Conference. p. 1123.

Massey, E., 2017. A comparative study of glaciovolcanic palagonitization of tholeiitic and alkaline sideromelane at Helgafell, Iceland and Wells Gray-Clearwater Volcanic Field, BC Canada. Assoc. Miner. Explor. Br. Columbia.

McCarthy, G.J., Johansen, D.M., 1988. X-ray powder diffraction study of NBS fly ash standard reference materials. Powder Diffr. 3, 156–161.

Michalski, J.R., Kraft, M.D., Sharp, T.G., Christensen, P.R., 2005. Palagonite-like Alteration Products on the Earth and Mars I: Spectroscopy (0.4-25 microns) of Weathered Basalts and Silicate Alteration Products. Presented at the 36th Annual Lunar and Planetary Science Conference.

Milliken, R.E., Mustard, J.F., Poulet, F., Jouglet, D., Bibring, J.-P., Gondet, B., Langevin, Y., 2007. Hydration state of the Martian surface as seen by Mars Express OMEGA: 2. H2O content of the surface. J. Geophys. Res. Planets 112. https://doi.org/10.1029/2006JE002853

Minitti, M.E., Hamilton, V.E., 2010. A search for basaltic-to-intermediate glasses on Mars: Assessing martian crustal mineralogy. Icarus 210, 135–149.

Mitchell, N.C., Masson, D.G., Watts, A.B., Gee, M.J., Urgeles, R., 2002. The morphology of the submarine flanks of volcanic ocean islands: a comparative study of the Canary and Hawaiian hotspot islands. J. Volcanol. Geotherm. Res. 115, 83–107.

Moersch, J.E., Christensen, P.R., 1995. Thermal emission from particulate surfaces: A comparison of scattering models with measured spectra. J. Geophys. Res. Planets 100, 7465–7477.

Moore, J., 1966. Rate of palagonitization of submarine basalt adjacent to Hawaii. US Geol. Surv. Prof. Pap.

Moore, J.G., 1965. Petrology of deep sea basalt near Hawaii. Am. J. Sci. 263, 40–52.

Moore, J.G., Phillips, R.L., Grigg, R.W., Peterson, D.W., Swanson, D.A., 1973. Flow of lava into the sea, 1969–1971, Kilauea Volcano, Hawaii. Geol. Soc. Am. Bull. 84, 537–546.

Morris, R.V., Golden, D.C., Bell, J.F., Lauer, H.V., Adams, J.B., 1993. Pigmenting agents in Martian soils: Inferences from spectral, Mössbauer, and magnetic properties of nanophase and other iron oxides in Hawaiian palagonitic soil PN-9. Geochim. Cosmochim. Acta 57, 4597–4609.

Morris, R.V., Golden, D.C., Ming, D.W., Shelfer, T.D., Jørgensen, L.C., Bell, J.F., Graff, T.G., Mertzman, S.A., 2001. Phyllosilicate-poor palagonitic dust from Mauna Kea Volcano (Hawaii): A mineralogical analogue for magnetic Martian dust? J. Geophys. Res. Planets 106, 5057–5083.

Morris, R.V., Gooding, J.L., Lauer, H.V., Singer, R.B., 1990. Origins of Marslike spectral and magnetic properties of a Hawaiian palagonitic soil. J. Geophys. Res. Solid Earth 95, 14427–14434. https://doi.org/10.1029/JB095iB09p14427

Morris, R.V., Graff, T.G., Mertzman, S.A., Lane, M.D., Christensen, P.R., 2003. Palagonitic (not andesitic) Mars: Evidence from thermal emission and VNIR spectra of palgonitic alteration rinds on basaltic rock, in: Sixth International Conference on Mars. p. 3211.

Morris, R.V., Klingelhoefer, G., Bernhardt, B., Schröder, C., Rodionov, D.S., De Souza, P.A., Yen, A., Gellert, R., Evlanov, E.N., Foh, J., 2004. Mineralogy at Gusev Crater from the Mössbauer spectrometer on the Spirit Rover. Science 305, 833–836.

Morris, R.V., Ming, D.W., Blake, D.F., Vaniman, D.T., Bish, D.L., Chipera, S.J., Downs, R.T., Gellert, R., Treiman, A.H., Yen, A.S., 2013. The amorphous component in martian basaltic soil in global perspective from MSL and MER missions.

Moune, S., Sigmarsson, O., Thordarson, T., Gauthier, P.-J., 2007. Recent volatile evolution in the magmatic system of Hekla volcano, Iceland. Earth Planet. Sci. Lett. 255, 373–389.

Murchie, S., Arvidson, R., Bedini, P., Beisser, K., Bibring, J.-P., Bishop, J., Boldt, J., Cavender, P., Choo, T., Clancy, R.T., Darlington, E.H., Des Marais, D., Espiritu, R., Fort, D., Green, R., Guinness, E., Hayes, J., Hash, C., Heffernan, K., Hemmler, J., Heyler, G., Humm, D., Hutcheson, J., Izenberg, N., Lee, R., Lees, J., Lohr, D., Malaret, E., Martin, T., McGovern, J.A., McGuire, P., Morris, R., Mustard, J., Pelkey, S., Rhodes, E., Robinson, M., Roush, T., Schaefer, E., Seagrave, G., Seelos, F., Silverglate, P., Slavney, S., Smith, M., Shyong, W.-J., Strohbehn, K., Taylor, H., Thompson, P., Tossman, B., Wirzburger, M., Wolff, M., 2007. Compact Reconnaissance Imaging Spectrometer for Mars (CRISM) on Mars Reconnaissance Orbiter (MRO). J. Geophys. Res. Planets 112. https://doi.org/10.1029/2006JE002682

Murchie, S.L., Mustard, J.F., Ehlmann, B.L., Milliken, R.E., Bishop, J.L., McKeown, N.K., Noe Dobrea, E.Z., Seelos, F.P., Buczkowski, D.L., Wiseman, S.M., Arvidson, R.E., Wray, J.J., Swayze, G., Clark, R.N., Des Marais, D.J., McEwen, A.S., Bibring, J.-P., 2009. A synthesis of Martian aqueous mineralogy after 1 Mars year of observations from the Mars Reconnaissance Orbiter. J. Geophys. Res. Planets 114, E00D06. https://doi.org/10.1029/2009JE003342

Naylor, P.H., Bell, B.R., Jolley, D.W., Durnall, P., Fredsted, R., 1999. Palaeogene magmatism in the Faeroe–Shetland Basin: influences on uplift history and sedimentation, in: Geological Society, London, Petroleum Geology Conference Series. Geological Society of London, pp. 545–558.

Orenberg, J., Handy, J., 1992. Reflectance spectroscopy of palagonite and iron-rich montmorillonite clay mixtures: Implications for the surface composition of Mars. Icarus 96, 219–225.

Pan, C., Rogers, A.D., Thorpe, M.T., 2015. Quantitative compositional analysis of sedimentary materials using thermal emission spectroscopy: 2. Application to compacted fine-grained mineral mixtures and assessment of applicability of partial least squares methods. J. Geophys. Res. Planets 120, 2015JE004881. https://doi.org/10.1002/2015JE004881

Pauly, B.D., Schiffman, P., Zierenberg, R.A., Clague, D.A., 2011. Environmental and chemical controls on palagonitization. Geochem. Geophys. Geosystems 12.

Peacock, M.A., Fuller, R.E., 1928. Chlorophaeite, sideromelane and palagonite from the Columbia River Plateau. Amer Min 13, 360–382.

Pollack, J.B., Toon, O.B., Khare, B.N., 1973. Optical properties of some terrestrial rocks and glasses. Icarus 19, 372–389. https://doi.org/10.1016/0019-1035(73)90115-2

Preusser, H., 1976. landscapes of Iceland. W. Junk.

Rampe, E.B., Ming, D.W., Blake, D.F., Bristow, T.F., Chipera, S.J., Grotzinger, J.P., Morris, R.V., Morrison, S.M., Vaniman, D.T., Yen, A.S., Achilles, C.N., Craig, P.I., Des Marais, D.J., Downs, R.T., Farmer, J.D., Fendrich, K.V., Gellert, R., Hazen, R.M., Kah, L.C., Morookian, J.M., Peretyazhko, T.S., Sarrazin, P., Treiman, A.H., Berger, J.A., Eigenbrode, J., Fairén, A.G., Forni, O., Gupta, S., Hurowitz, J.A., Lanza, N.L., Schmidt, M.E., Siebach, K., Sutter, B., Thompson, L.M., 2017. Mineralogy of an ancient lacustrine mudstone succession from the Murray formation, Gale crater, Mars. Earth Planet. Sci. Lett. 471, 172–185. https://doi.org/10.1016/j.epsl.2017.04.021

Rampe, E.B., Morris, R.V., Ruff, S.W., Horgan, B.H., Dehouck, E., Achilles, C.N., Ming, D.W., Bish, D.L., Chipera, S.J., 2014. AMORPHOUS PHASES ON THE SURFACE OF MARS. Eioght Int. Conf. Mars 1239.

Ramsey, M.S., Christensen, P.R., 1998. Mineral abundance determination: Quantitative deconvolution of thermal emission spectra. J. Geophys. Res. Solid Earth 103, 577–596.

Rice, M.S., Cloutis, E.A., Bell III, J.F., Bish, D.L., Horgan, B.H., Mertzman, S.A., Craig, M.A., Renaut, R.W., Gautason, B., Mountain, B., 2013. Reflectance spectra diversity of silica-rich materials: Sensitivity to environment and implications for detections on Mars. Icarus 223, 499–533. https://doi.org/10.1016/j.icarus.2012.09.021

Rogers, A.D., Aharonson, O., 2008. Mineralogical composition of sands in Meridiani Planum determined from Mars Exploration Rover data and comparison to orbital measurements. J. Geophys. Res. Planets 113.

Rogers, A.D., Christensen, P.R., 2007. Surface mineralogy of Martian low-albedo regions from MGS-TES data: Implications for upper crustal evolution and surface alteration. J. Geophys. Res. Planets 112, E01003. https://doi.org/10.1029/2006JE002727

Rogers, A.D., Nekvasil, H., 2015. Feldspathic rocks on Mars: Compositional constraints from infrared spectroscopy and possible formation mechanisms. Geophys. Res. Lett. 42, 2619–2626.

Romagnoli, C., Jakobsson, S.P., 2015. Post-eruptive morphological evolution of island volcanoes: Surtsey as a modern case study. Geomorphology 250, 384–396.

Roush, T.L., Bell, J.F., 1995. Thermal emission measurements 2000–400 cm− 1 (5–25 μm) of Hawaiian palagonitic soils and their implications for Mars. J. Geophys. Res. Planets 100, 5309–5317.

Ruff, S.W., 2004. Spectral evidence for zeolite in the dust on Mars. Icarus 168, 131–143. https://doi.org/10.1016/j.icarus.2003.11.003

Ruff, S.W., Christensen, P.R., Barbera, P.W., Anderson, D.L., 1997. Quantitative thermal emission spectroscopy of minerals: A laboratory technique for measurement and calibration. J. Geophys. Res. Solid Earth 102, 14899–14913.

Russell, J.K., Edwards, B.R., Porritt, L., Ryane, C., 2014. Tuyas: a descriptive genetic classification. Quat. Sci. Rev. 87, 70–81. https://doi.org/10.1016/j.quascirev.2014.01.001

Saedmundsson, K., Einarsson, S., 1980. Geological map of Iceland, sheet 3, Southwest-Iceland, 1: 250 000, in: Icelandic Mus. Nat. Hist. and Iceland Geodetic Survey.

Sæmundsson, K., 1979. Outline of the geology of Iceland.

Sæmundsson, K., Hjartarson, K., Kaldal, A., Sigurgeirsson, I., Kristinsson, M., Víkingsson, S., 2012. Geological Map of Northern Volcanic Zone, Iceland. Northern Part.

Sæmundsson, K., Sigurgeirsson, M., Hjartarson, A., Kaldal, I., Kristinsson, S., 2016. Geological Map of of Southweast Iceland.

Salisbury, J.W., Wald, A., 1992. The role of volume scattering in reducing spectral contrast of reststrahlen bands in spectra of powdered minerals. Icarus 96, 121–128.

Sigurgeirsson, M., Hjartarson, A., Kaldal, I., Sæmundsson, K., Kristinsson, S., Víkingsson, S., 2015. Geological Map of the Northern Volcanic Zone, Iceland. Southern Part.

Sigvaldason, G.E., 1992. Recent hydrothermal explosion craters in an old hyaloclastite flow, central Iceland. J. Volcanol. Geotherm. Res. 54, 53–63.

Singer, A., 1980. The paleoclimatic interpretation of clay minerals in soils and weathering profiles. Earth-Sci. Rev. 15, 303–326.

Singer, A., 1974. Mineralogy of palagonitic material from the Golan Heights, Israel. Clays Clay Miner. 22, 231–240.

Singer, R.B., 1982. Spectral evidence for the mineralogy of high-albedo soils and dust on Mars. J. Geophys. Res. Solid Earth 87, 10159–10168. https://doi.org/10.1029/JB087iB12p10159

Stroncik, N.A., Schmincke, H.-U., 2002. Palagonite – a review. Int. J. Earth Sci. 91, 680–697. https://doi.org/10.1007/s00531-001-0238-7

Stroncik, N.A., Schmincke, H.-U., 2001. Evolution of palagonite: Crystallization, chemical changes, and element budget. Geochem. Geophys. Geosystems 2, 1017. https://doi.org/10.1029/2000GC000102

Summers, K.V., 1976. The clay component of the Columbia River palagonites. Am. Mineral. 61, 492–494.

Sunshine, J.M., Pieters, C.M., 1998. Determining the composition of olivine from reflectance spectroscopy. J. Geophys. Res. Planets 103, 13675–13688.

Sunshine, J.M., Pieters, C.M., Pratt, S.F., 1990. Deconvolution of mineral absorption bands: An improved approach. J. Geophys. Res. Solid Earth 95, 6955–6966.

Thorpe, M.T., Rogers, A.D., Bristow, T.F., Pan, C., 2015. Quantitative compositional analysis of sedimentary materials using thermal emission spectroscopy: 1. Application to sedimentary rocks. J. Geophys. Res. Planets 120, 1956–1983.

Tsai, C.C., Chen, Z.S., Kao, C.I., Ottner, F., Kao, S.J., Zehetner, F., 2010. Pedogenic development of volcanic ash soils along a climosequence in Northern Taiwan. Geoderma 156, 48–59.

Tuffen, H., 2007. Models of ice melting and edifice growth at the onset of subglacial basaltic eruptions. J. Geophys. Res. Solid Earth 112, B03203. https://doi.org/10.1029/2006JB004523

Ugolini, F.C., Bockheim, J.G., 2008. Antarctic soils and soil formation in a changing environment: a review. Geoderma 144, 1–8.

Ugolini, F.C., Dahlgren, R.A., 2002. Soil development in volcanic ash. Glob. Environ. Res.-Engl. Ed.- 6, 69–82.

van Bemmelen, R.W., Rutten, M.G., 1955. Tablemountains of northern Iceland. Brill.

Viviano-Beck, C.E., Seelos, F.P., Murchie, S.L., Kahn, E.G., Seelos, K.D., Taylor, H.W., Taylor, K., Ehlmann, B.L., Wisemann, S.M., Mustard, J.F., Morgan, M.F., 2014. Revised CRISM spectral parameters and summary products based on the currently detected mineral diversity on Mars. J. Geophys. Res. Planets 119, 2014JE004627. https://doi.org/10.1002/2014JE004627

Walton, A.W., Schiffman, P., 2003. Alteration of hyaloclastites in the HSDP 2 Phase 1 Drill Core 1. Description and paragenesis. Geochem. Geophys. Geosystems 4.

Warner, N.H., Farmer, J.D., 2010. Subglacial Hydrothermal Alteration Minerals in Jökulhlaup Deposits of Southern Iceland, with Implications for Detecting Past or Present Habitable Environments on Mars. Astrobiology 10, 523–547. https://doi.org/10.1089/ast.2009.0425

Warren, B.E., 1990. X-ray Diffraction. Dover. N. Y. 253.

Waters, A.C., 1960. Determining direction of flow in basalts. Am. J. Sci. 258, 350–366.

Werner, R., Schmincke, H.-U., Sigvaldason, G., 1996. A new model for the evolution of table mountains: volcanological and petrological evidence from herdubreid and Herdubreidartögl volcanoes (Iceland). Geol. Rundsch. 85, 390–397. https://doi.org/10.1007/BF02422244

Whiting, M.L., Li, L., Ustin, S.L., 2004. Predicting water content using Gaussian model on soil spectra. Remote Sens. Environ. 89, 535–552. https://doi.org/10.1016/j.rse.2003.11.009

Wiens, R.C., Maurice, S., Barraclough, B., Saccoccio, M., Barkley, W.C., Bell, J.F., Bender, S., Bernardin, J., Blaney, D., Blank, J., 2012. The ChemCam instrument suite on the Mars Science Laboratory (MSL) rover: Body unit and combined system tests. Space Sci. Rev. 170, 167–227.

Wyatt, M.B., Hamilton, V.E., McSween, H.Y., Christensen, P.R., Taylor, L.A., 2001. Analysis of terrestrial and Martian volcanic compositions using thermal emission spectroscopy: 1. Determination of mineralogy, chemistry, and classification strategies. J. Geophys. Res. Planets 106, 14711–14732.

Zhou, Z., Fyfe, W.S., Tazaki, K., Van der Gaast, S.J., 1992. The structural characteristics of palagonite from DSDP Site 335. Can. Mineral. 30, 75–81.

Ziegler, K., Hsieh, J.C., Chadwick, O.A., Kelly, E.F., Hendricks, D.M., Savin, S.M., 2003. Halloysite as a kinetically controlled end product of arid-zone basalt weathering. Chem. Geol. 202, 461–478.

3.10 Tables

Table 4. Description of samples in this study including their locations (volcanic zones and coordinates) and what figures they can be seen in.

Sample ID	**Volcanic Zone**	**UTM Zone**	**UTM Coordinates**	**Figure #**	**Description**
Lake01	Western	27V	0452740 7091801	6	Red in color; crosshatched cemented layers overprinting the horizontal layering
Lake02	Western	27V	0452700 7091780	6	Brown in color; multi horizontal layers with varying grain size; wavy pattern between layers
Lake03	Western	27V	0452665 7091781	7	Black coloring on the outside and brown/red on the inside; layered hyaloclastite with fracture fill
Lake04	Western	27V	0452665 7091781	7	Fracture fill within the fault; hyaloclastite with brecciated matrix; more brown than Lake03 with little to no black coloring
DB01	Western	27W	0475389 7102839	8	Brown in color; smooth layers with uniform grain size
DB02	Western	27W	0475389 7102839	8	Layer within DB01 with thumb-size chunks of pillow basalt; brown in color with uniform grain size matrix and brown/gold-colored alteration regions
41701	Western	27W	0469965 7100021	9	Many layers of breccia; Similar to DB02
41702	Western	27W	0469976 7100087	9	Brown/gold in color; lighter in color than 41701 possibly showing more alteration; a sandy “clean” piece in comparison to 41701
Her01	Northern	28W	0439122 7229993	10	Color varies from brown to orange to yellow; uniform grain size with larger chunks of pillow basalt; consistently spaced layers, usually more orange in color than the surrounding hyaloclastite

Table 4 Continued

Sample ID	Volcanic Zone	UTM Zone	UTM Coordinates	Figure #	Description
Her02	Northern	28W	0439119 7229995	10	Color is mostly beige/yellow/light orange; texture is plated and rock breaks easily into chunks/blocks; well-cemented; unlike other hyaloclastite outcrops we've observed
Ask01	Northern	28W	0422778 7214627	11	Color is grey to brown; mostly uniform grain size with layered pillow basalt fragments included
SCoast01	Eastern	27V	0593409 7031951	12	Very light brown in color; vugs all filled with moss; rounded/smooth texture; very large scale layers, unlike the hyaloclastite outcrops we observed that have thin layers

Table 5. Overall assemblages of samples.

Measurement Technique	Glaciovolcanic Samples*	Hydrovolcanic Sample (SCoast01 Sample)
VNIR	glass, clays (Al smectite), zeolites	pyroxene, clays (Fe/Mg smectite)
TIR	glass (20-50%), devitrified glass (40-50%), zeolites (~10%), clays (<5%), oxides (~5%)	higher abundances of clays, zeolites, and oxides (~15-20%)
XRD	only XRD amorphous material	pyroxene, clay, and minor zeolite peaks

* Sample suite includes Lake01, Lake02, Lake03, Lake04, DB01, DB02, 41701, 41702, Her01, 1355 Her02, Ask01

3.11 Figures

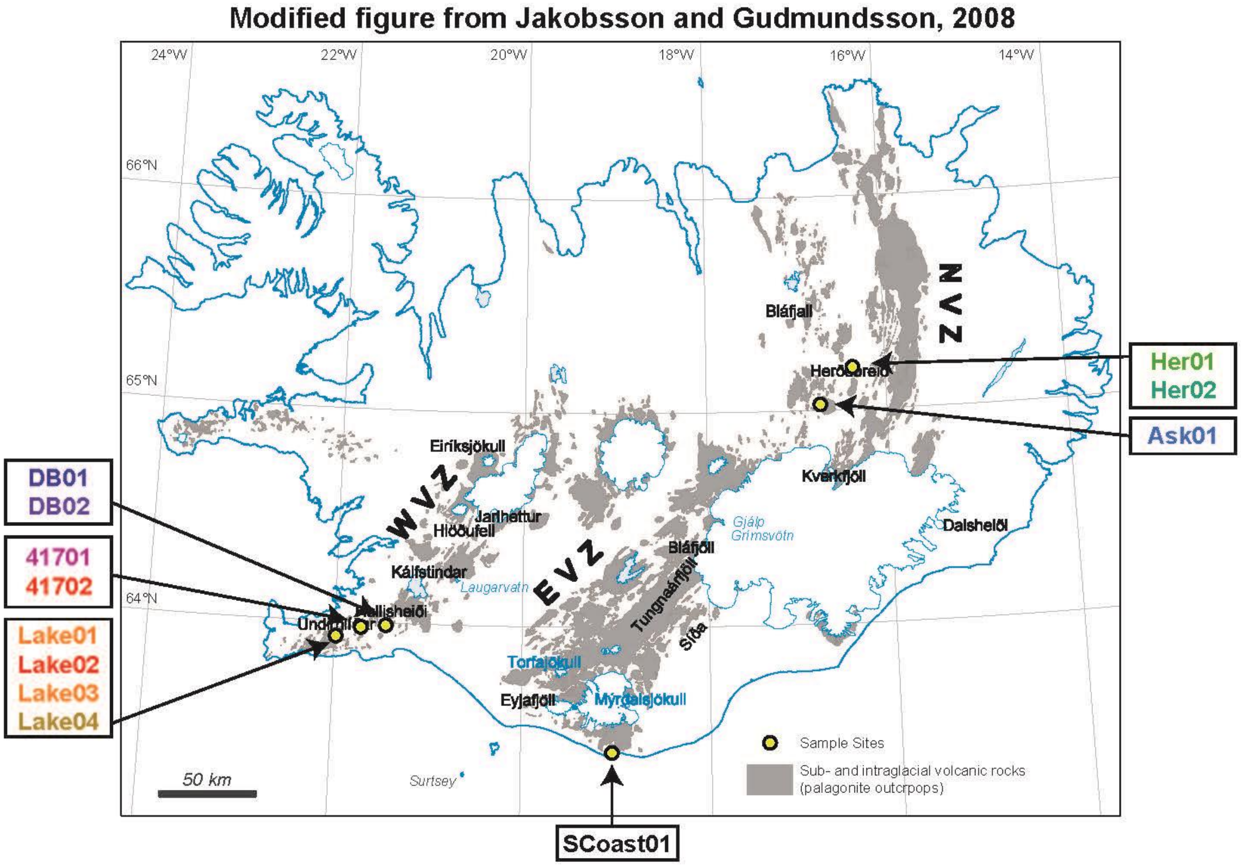

Figure 5. Sample locations in Iceland, modified from Jakobsson and Gudmundsson [2008]. Palagonite outcrops from Pleistocene-aged volcanic rocks in Iceland, as mapped by Jóhannesson and Saemundsson [1998] and modified by Jakobsson and Gudmundsson [2008]. The Western, Eastern, and Northern Volcanic Zones are labeled. Sample locations from this study are denoted by yellow dots. Eight samples are located in the Western Volcanic Zone (DB01, DB02, 41701, 41702, Lake01, Lake02, Lake03, and Lake04), 1 sample in the Eastern Volcanic Zone (SCoast01), and 3 samples in the Northern Volcanic Zones (Her01, Her02, and Ask01). Sample labels are color-coded and consistent throughout the figures for clarity.

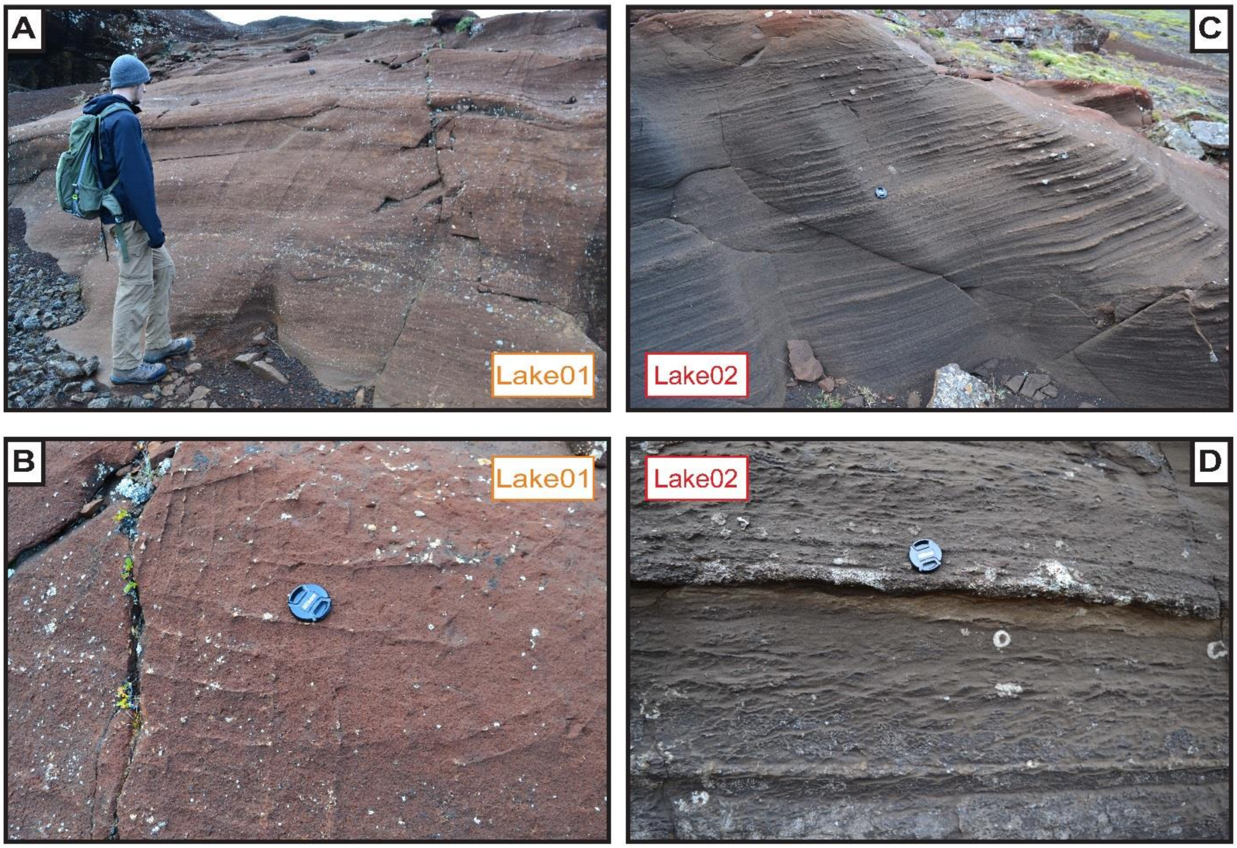

Figure 6. Lake01 and Lake02 sample locations. (a) Lake01 contextual view with person for scale (1.85 meters). (b) Lake01 close-up view showing crosshatched cemented layers with camera lens for scale. (c) Lake02 contextual view with camera lens for scale. (d) Lake02 close-up view showing wavy patterns between the layers. Camera lens for scale.

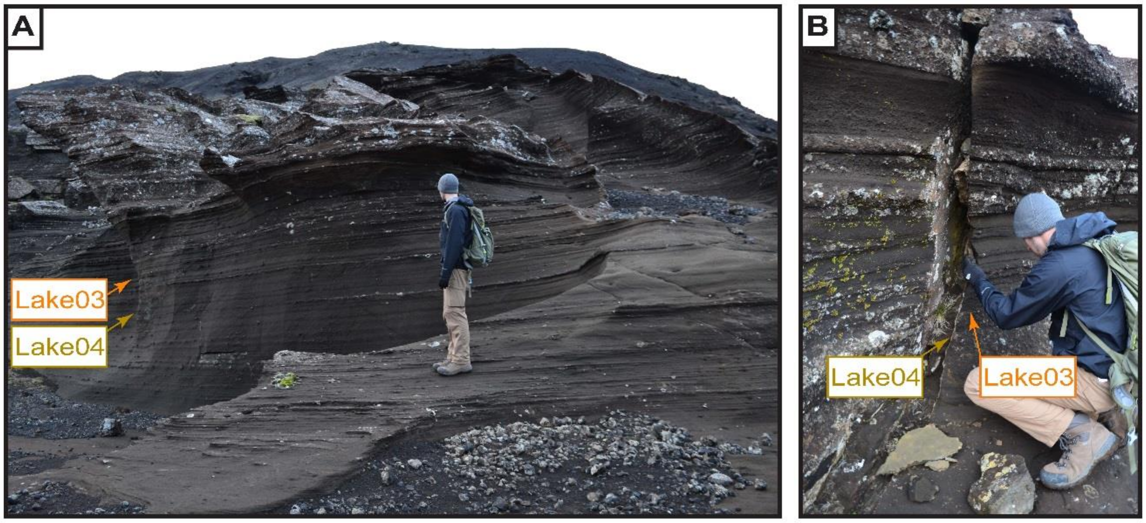

Figure 7. Lake03 and Lake04 sample locations. (a) Contextual view of Lake03 and Lake04 samples with person for scale (1.85 meters). (b) Close-up view of sample locations showing the black hyaloclastite, Lake0, sample and the Lake04, fracture fill, sample.

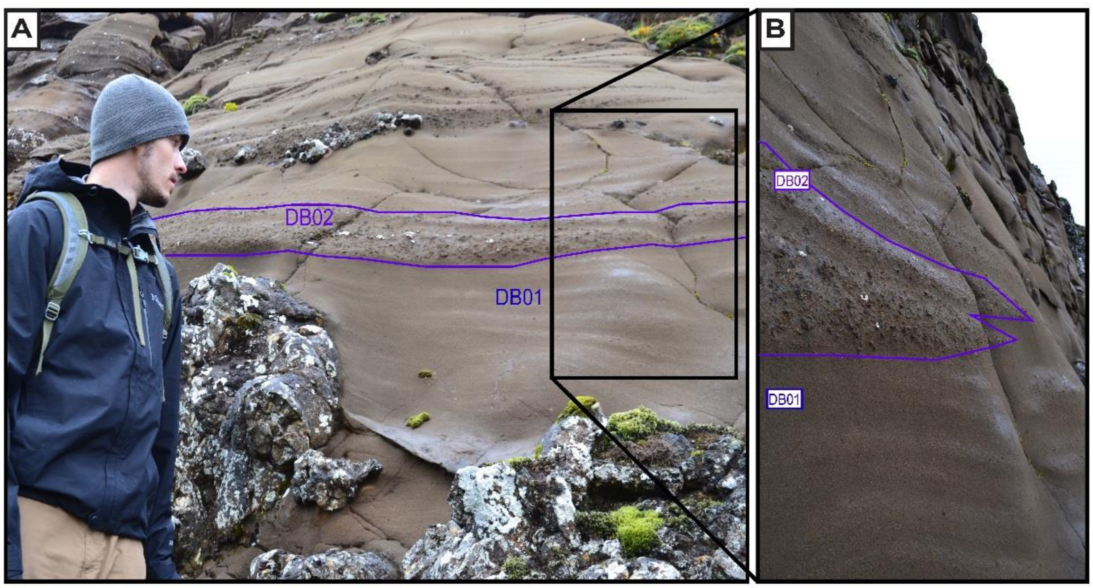

Figure 8. DB01 and DB02 sample locations. (a) Contextual view of DB01 and DB02 samples with person for scale. DB02 sample layer is outlined in purple for clarity. Inset shows (b) close-up of the layering and matrix of the samples.

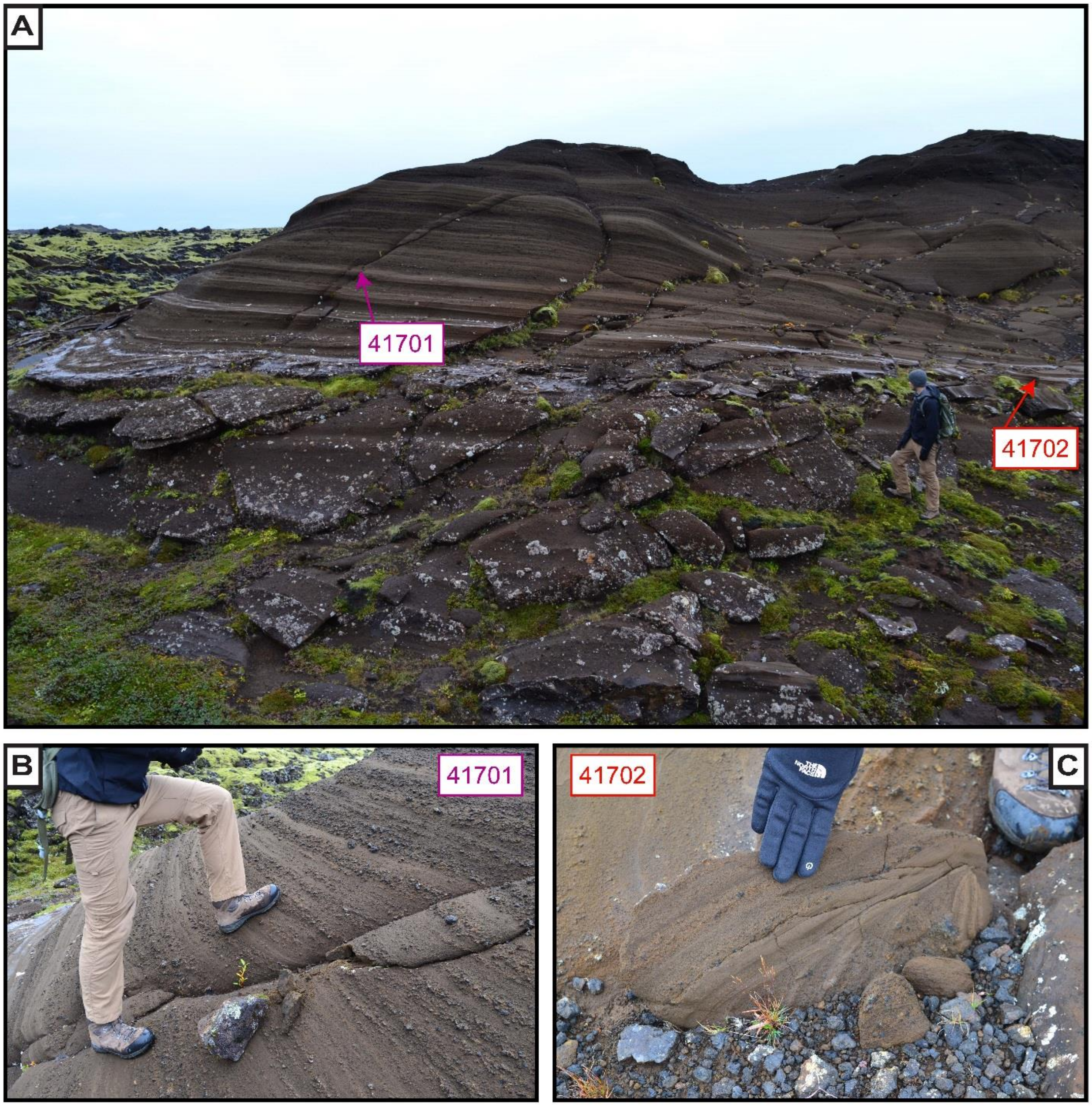

Figure 9. 41701 and 4102 sample locations. (a) Contextual view of 41701 and 41702 samples with person for scale (1.85 meters). (b) Close-up view of sample 41701 with size 13 shoes (boots measure 33cm in length) for scale. (c) Close-up view of sample 41702 with hand for scale.

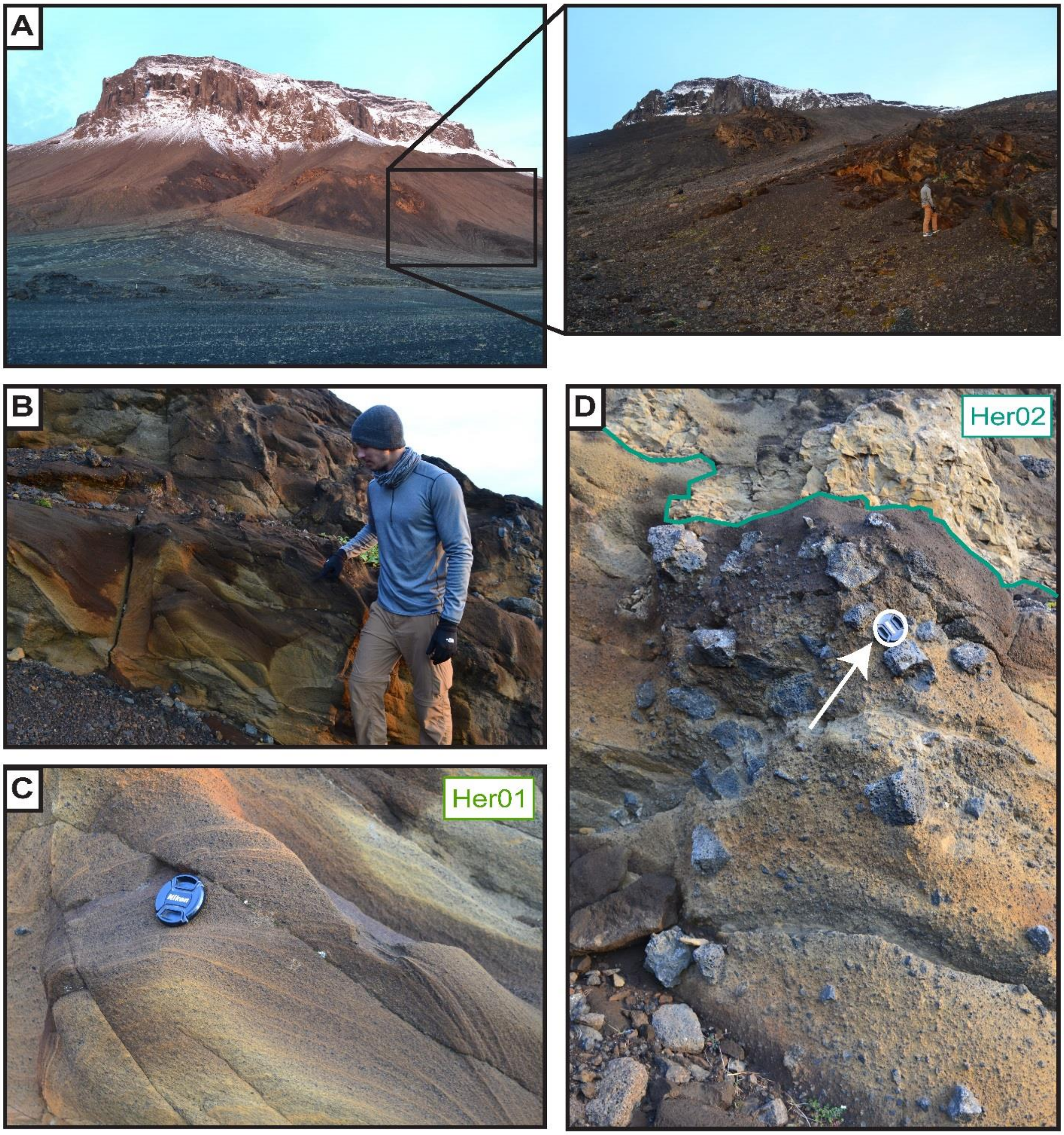

Figure 10. Her01 and Her02 sample locations. (a) Contextual view of the Herðubreið volcano with an inset of the sample location with person for scale (1.85 meters). (b) Close-up view of sample location with person for scale. (c) Sample Her01 layering with camera lens for scale. (d) Light-toned, platy hyaloclastite, sample Her02, outlined in green in the upper portion of the image. Camera lens for scale as denoted by the white outline and arrow.

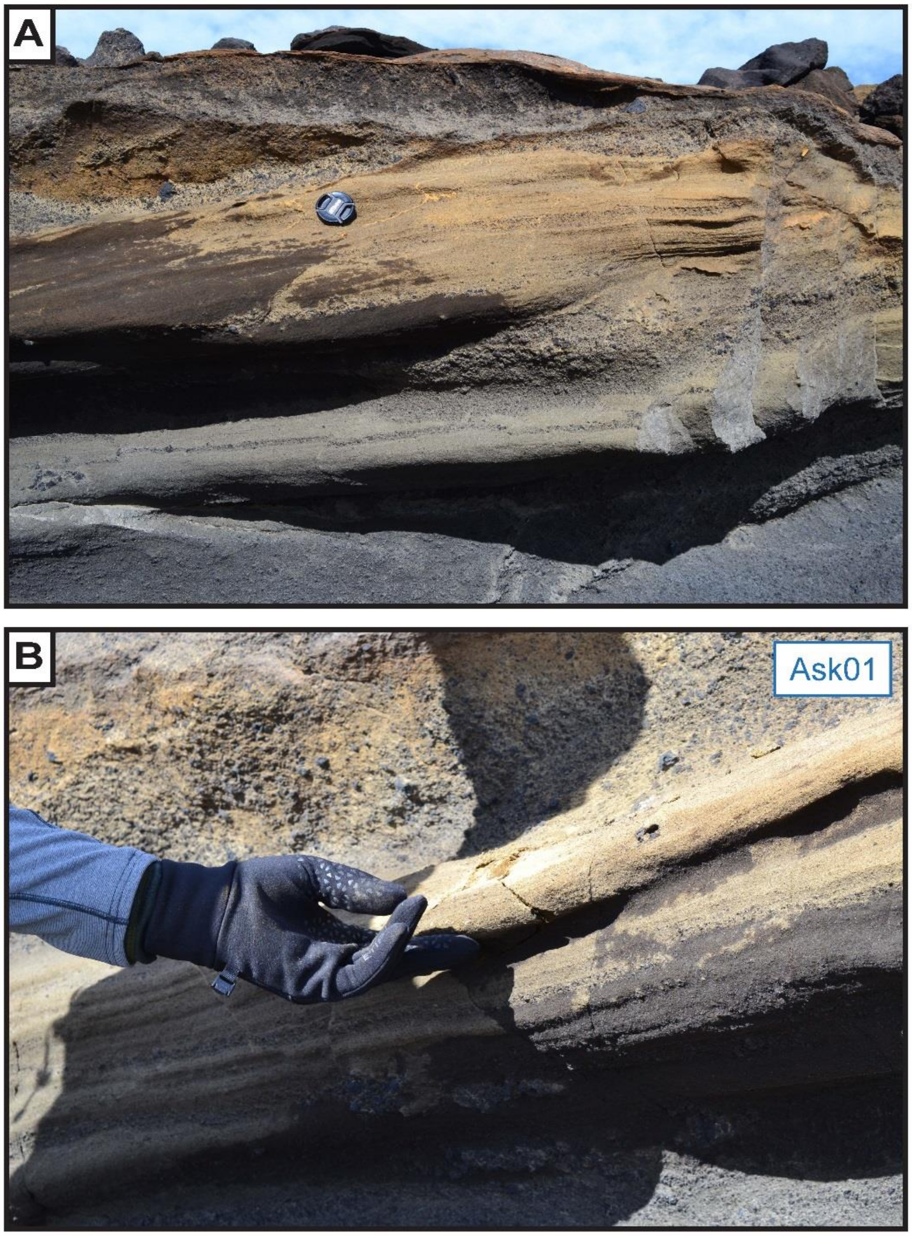

Figure 11. Ask01 sample location. (a) Contextual view of Ask01 sample site. (b) Close-up view of Ask01 showing layering with hand for scale.

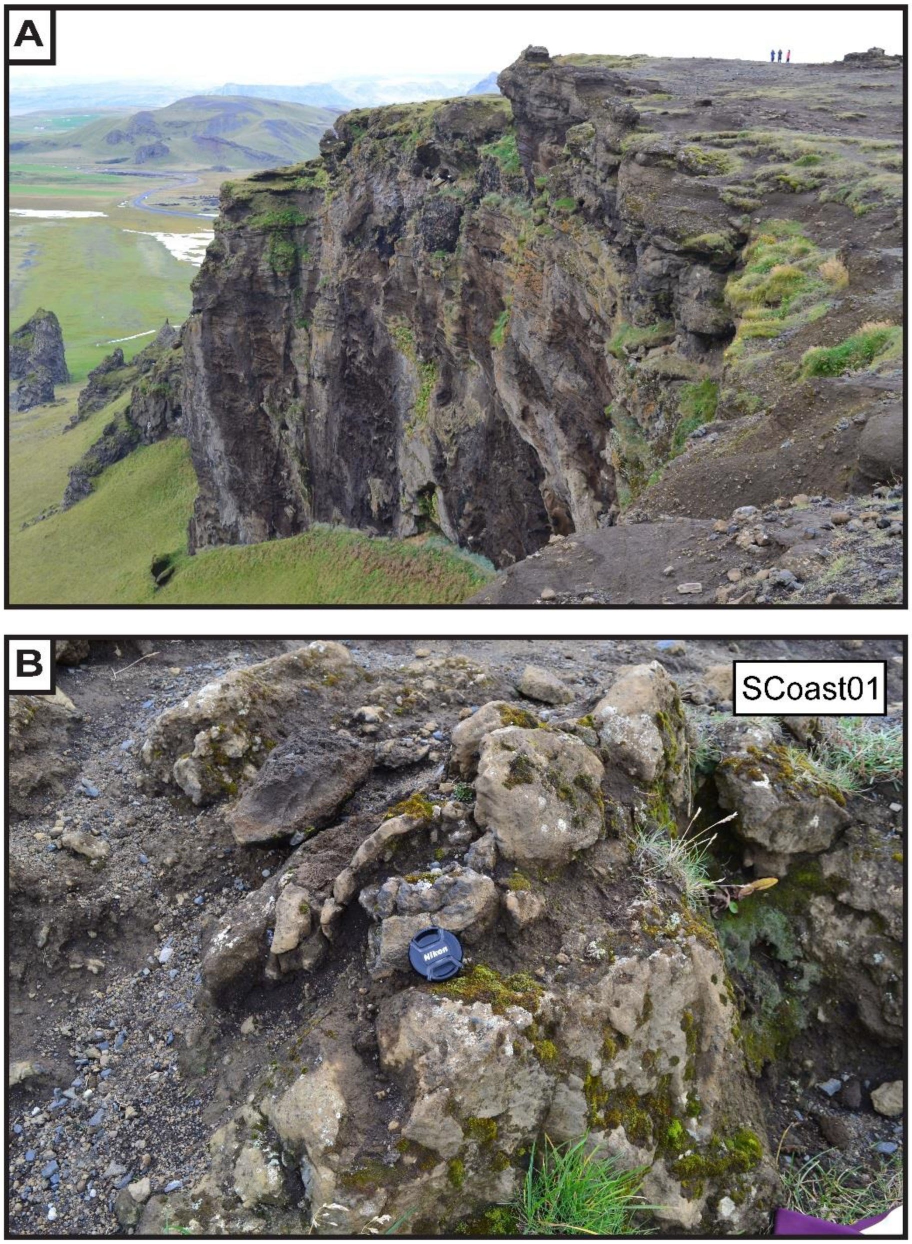

Figure 12. SCoast01 sample location. (a) Contextual view of SCoast01 sample site. (b) Close-up view of SCoast01 showing degradation of fine-scale layering. Camera lens for scale.

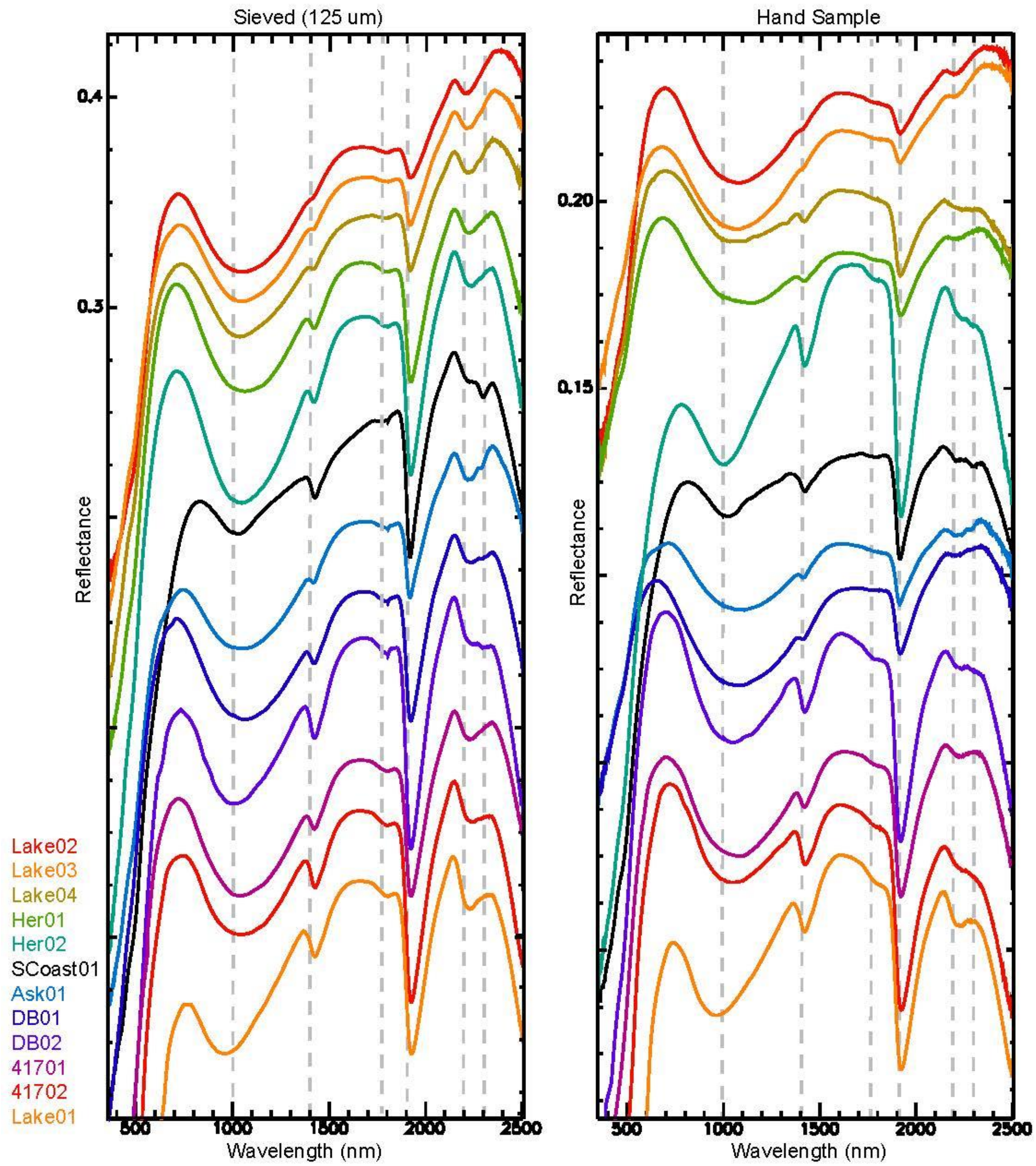

Figure 13. Visible and near-infrared spectroscopy with wavelengths from 0.35-2.50 um and offset reflectance for clarity of all samples in this study. Left side shows samples that were sieved to 125 um grain size for consistency. Right side shows samples as bulk hand samples (only dusted with pressurized air before analysis).

Figure 14. Thermal infrared spectroscopy with wavelengths from 7.14-25.00 um and offset emissivity for clarity of all samples in this study. Left side shows samples that were sieved to 125 um grain size for consistency and pressed into pellets. Right side shows samples as bulk hand samples (only dusted with pressurized air before analysis).

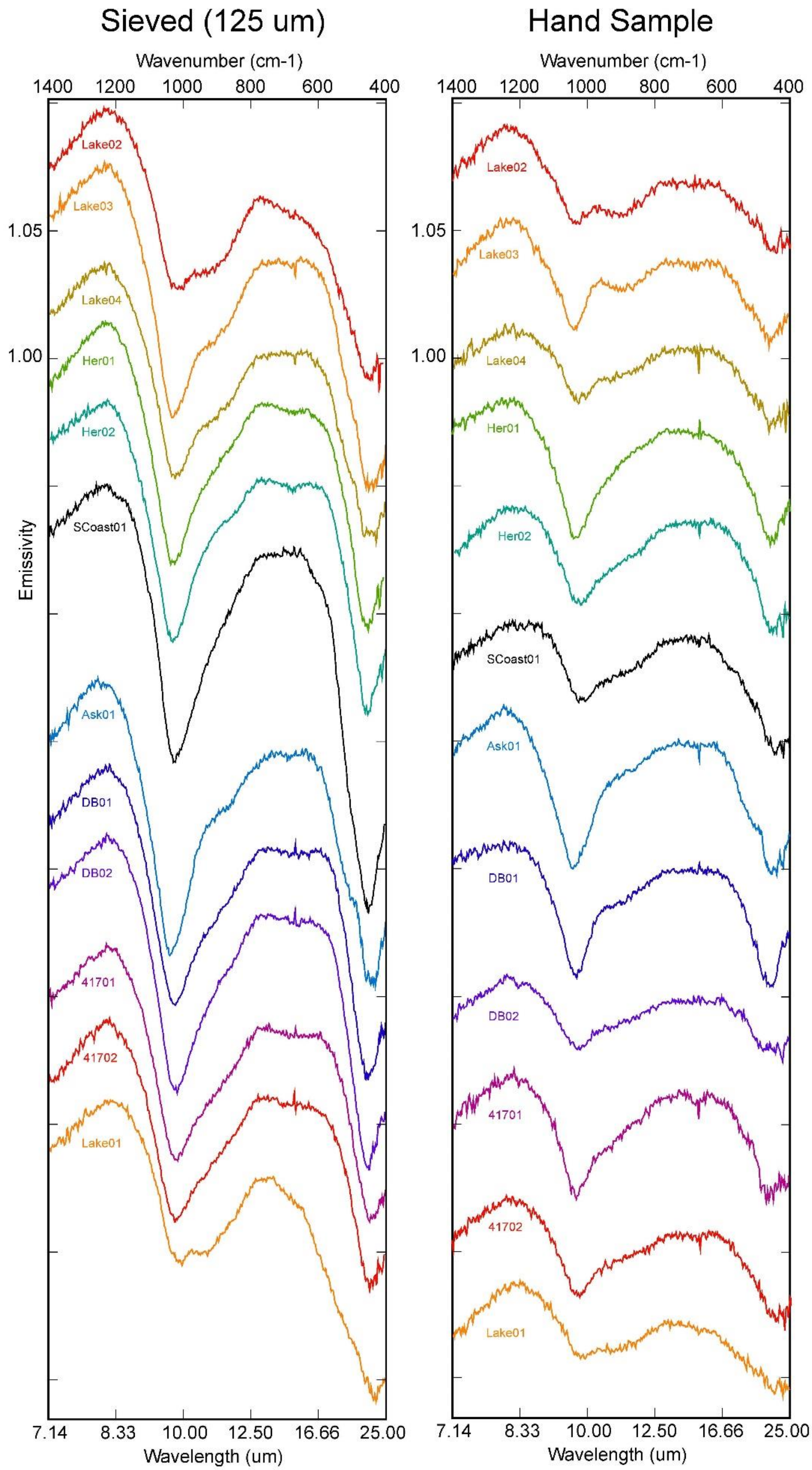

Sieved (125 um)
Hand Sample
Wavenumber (cm-1)
1400
1200
1000
800
600
400
Emissivity
1.05
1.00
Lake02
Lake03
Lake04
Her01
Her02
SCoast01
Ask01
DB01
DB02
41701
41702
Lake01
7.14
8.33
10.00
12.50
16.66
25.00
Wavelength (um)

Figure 15. Modeled mineral/mineraloid abundances for sieved samples in this study. Left side shows samples that were sieved to 125 um grain size for consistency and pressed into pellets. Colored spectra show the data and black spectra show the associated model. Right side shows a breakdown of the percentages and types of minerals/mineraloids in the models. All modeled minerals/mineraloids are color coded for clarity (partially devitrified glass = black, glass = grey, clay = pink, zeolite = blue, sulfate = purple, pyroxene = yellow, mica = brown, amorphous = white, olivine = green, and oxide = red).

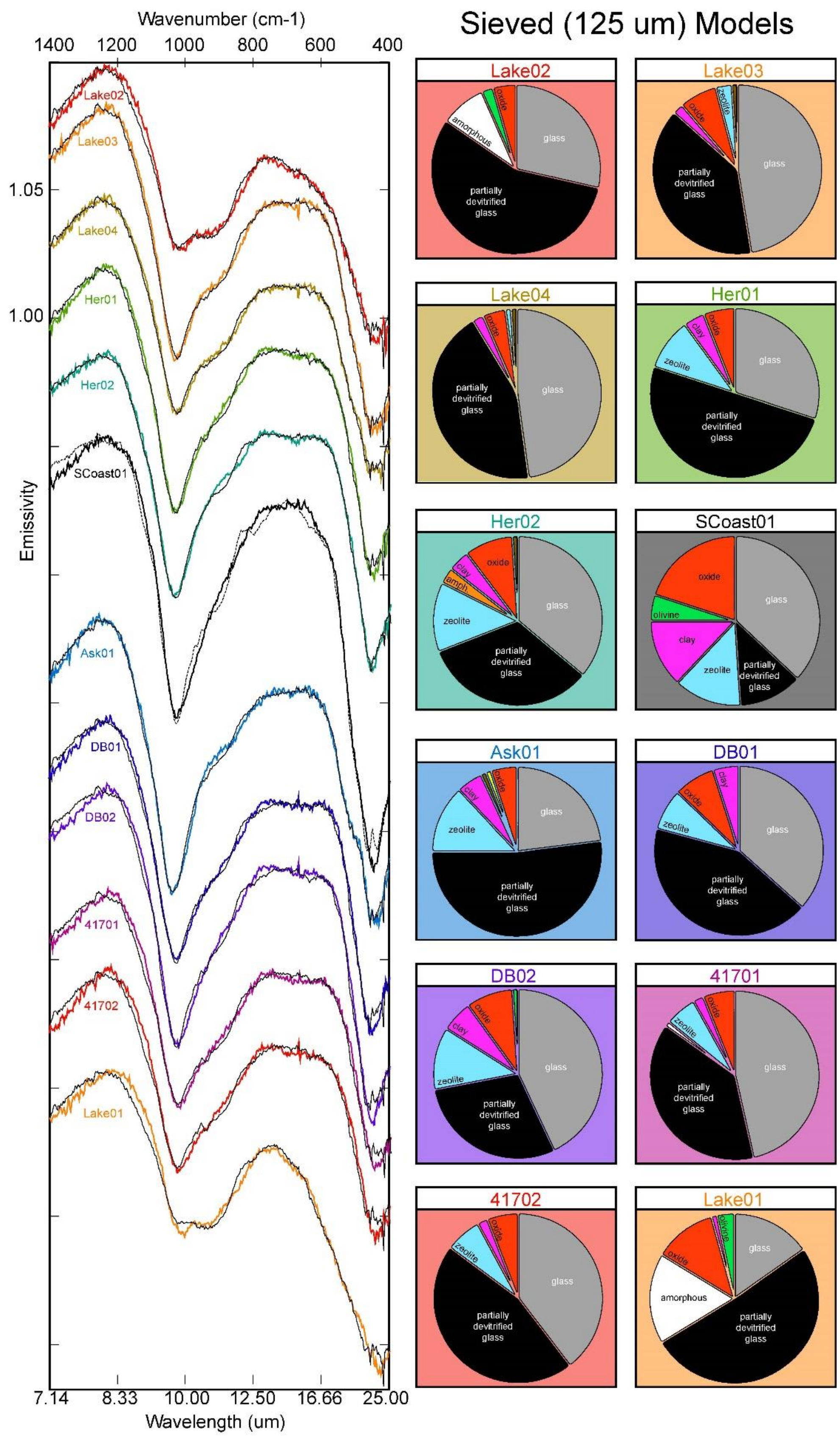

Wavenumber (cm-1)
1400
1200
1000
800
600
400
1.05
1.00
Emissivity
Lake02
Lake03
Lake04
Her01
Her02
SCoast01
Ask01
DB01
DB02
41701
41702
Lake01
7.14
8.33
10.00
12.50
16.66
25.00
Wavelength (um)
Sieved (125 um) Models
Lake02
amorphous
oxide
glass
partially devitrified glass
Lake03
oxide
zeolite
glass
partially devitrified glass
Lake04
oxide
glass
partially devitrified glass
Her01
clay
oxide
zeolite
glass
partially devitrified glass
Her02
oxide
clay
amph
zeolite
glass
partially devitrified glass
SCoast01
oxide
olivine
clay
zeolite
glass
partially devitrified glass
Ask01
clay
oxide
zeolite
glass
partially devitrified glass
DB01
oxide
clay
zeolite
glass
partially devitrified glass
DB02
oxide
clay
zeolite
glass
partially devitrified glass
41701
zeolite
oxide
glass
partially devitrified glass
41702
zeolite
oxide
glass
partially devitrified glass
Lake01
oxide
olivine
glass
amorphous
partially devitrified glass

Figure 16. Modeled mineral/mineraloid abundances for bulk hand samples in this study based on linear deconvolutions of TIR emission spectra with a suite of laboratory endmember spectra. The left side shows emissivity spectra of bulk hand samples (only dusted with pressurized air before analysis), where colored spectra show the data and black spectra show the associated model. The right side shows a breakdown of the percentages and types of minerals/mineraloids in the models. All modeled minerals/mineraloids are color coded for clarity (partially devitrified glass = black, glass = grey, clay = pink, zeolite = blue, sulfate = purple, pyroxene = yellow, mica = brown, amorphous = white, olivine = green, and oxide = red).

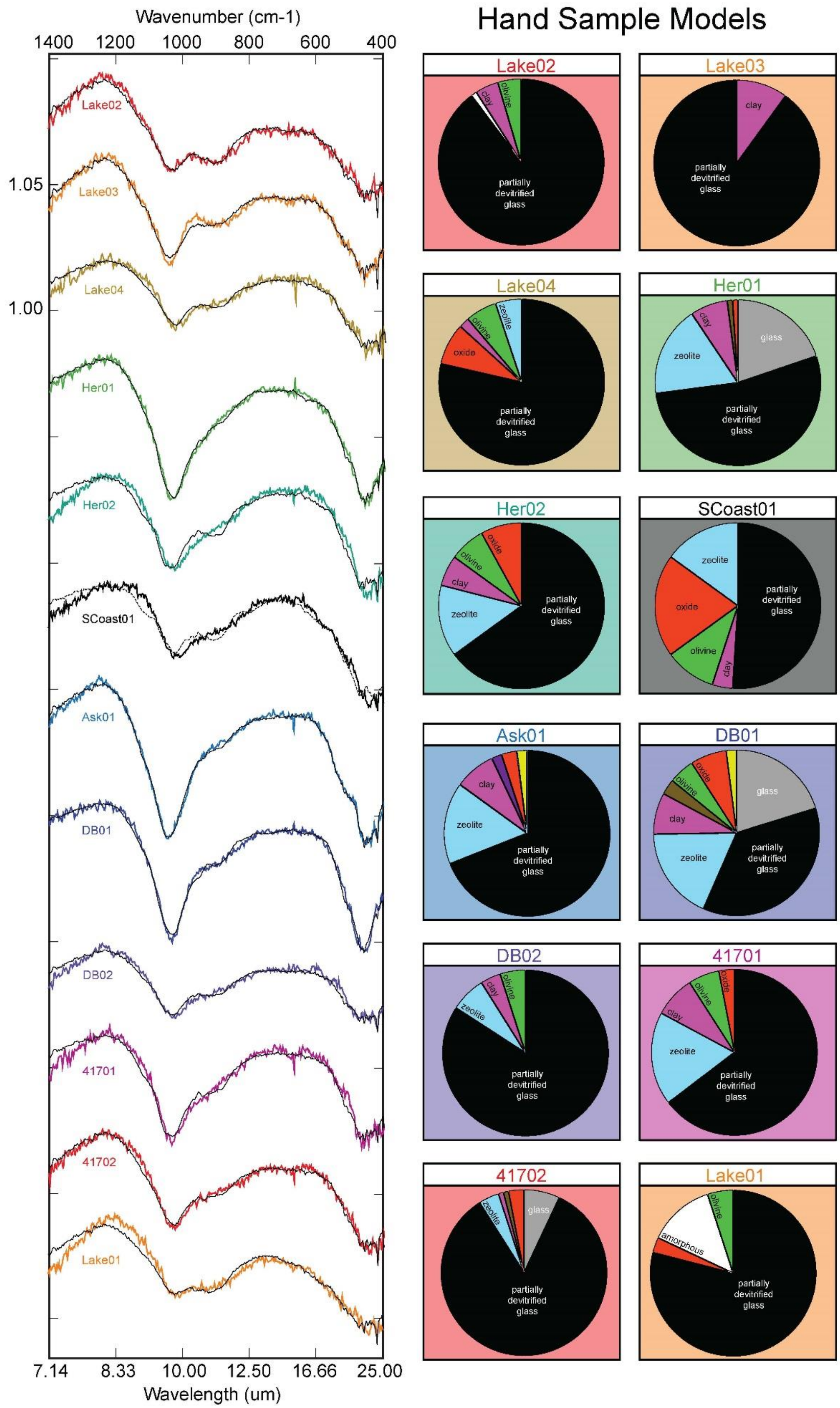
Wavenumber (cm-1)
1400 1200 1000 800 600 400
1.05
1.00
Lake02
Lake03
Lake04
Her01
Her02
SCoast01
Ask01
DB01
DB02
41701
41702
Lake01
7.14 8.33 10.00 12.50 16.66 25.00
Wavelength (um)
Hand Sample Models
Lake02
clay
olivine
partially devitrified glass
Lake03
clay
partially devitrified glass
Lake04
zeolite
olivine
oxide
partially devitrified glass
Her01
clay
glass
zeolite
partially devitrified glass
Her02
oxide
olivine
clay
zeolite
partially devitrified glass
SCoast01
zeolite
oxide
olivine
clay
partially devitrified glass
Ask01
clay
zeolite
partially devitrified glass
DB01
oxide
olivine
glass
clay
zeolite
partially devitrified glass
DB02
olivine
clay
zeolite
partially devitrified glass
41701
oxide
olivine
clay
zeolite
partially devitrified glass
41702
zeolite
glass
partially devitrified glass
Lake01
olivine
amorphous
partially devitrified glass

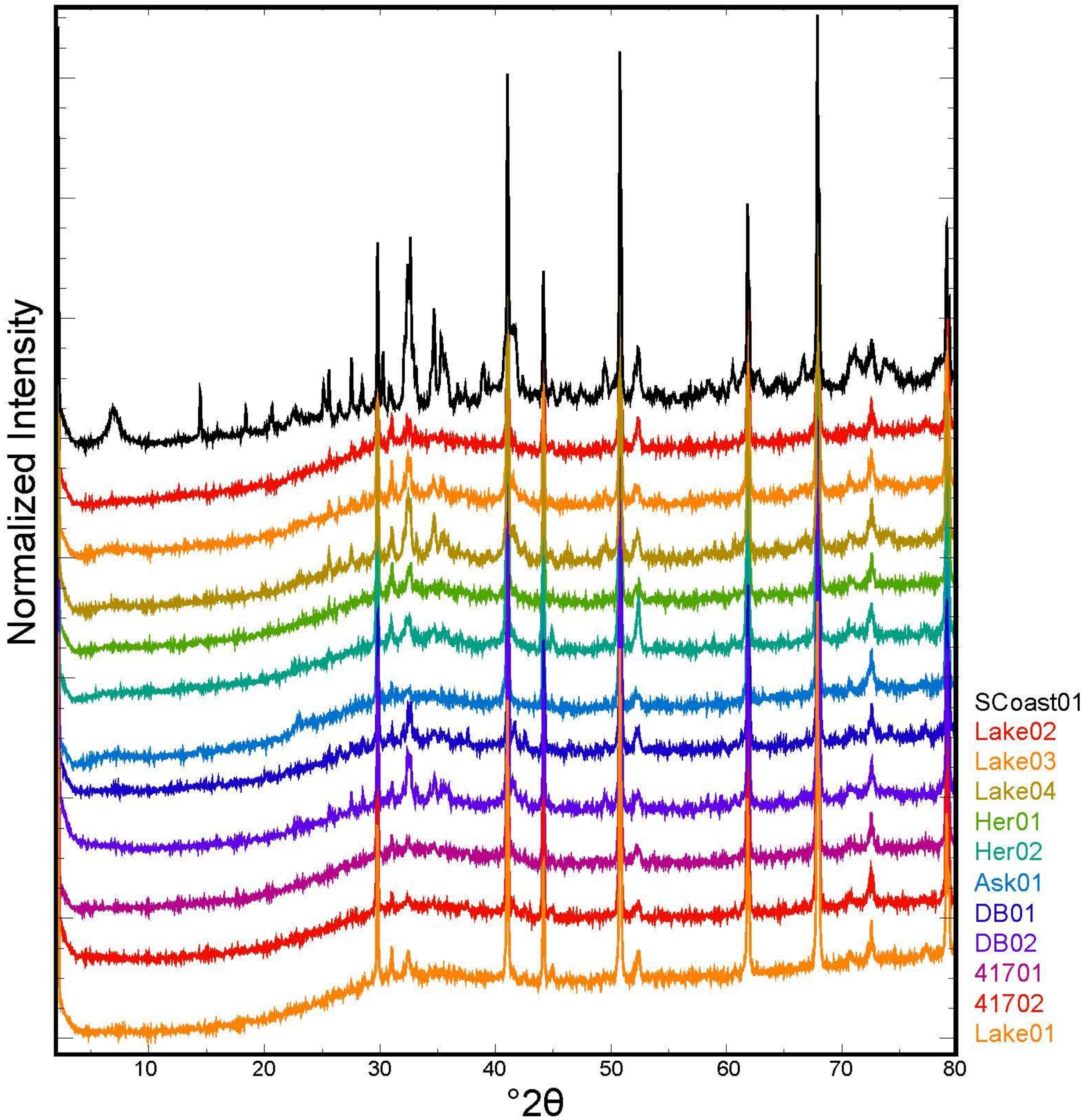

Figure 17. XRD diffractograms for all samples in this study. Measurements were taken from 2-80 degrees 2 theta with intensity normalized and offset for clarity.

3.12 Supplemental Tables

Table 6. Table of thermal infrared spectra used to model mineral abundances

Class	#	Sample Name	Sample ID	ASU ID	Citation
Amorphous	1	Allophane Si:Al 0.44	ALLO044	2398	Rampe et al (2012)
	2	Allophane Si:Al 0.92	ALLO092	2399	Rampe et al (2012)
	3	Aluminosilicate Gel Si:Al 5.6	ALLO560	2401	Rampe et al (2012)
	4	Opal-A	Opal-A	1966	Joe Michalski 2003
Amphibole	5	Hornblende	BUR-1380A	488	Christensen et al. (2000)
	6	Hornblende-biotite granodiorite	ELF	658	Feely & Christensen (1999)
Phyllo-silicate	7	Beidellite [pellet]	SBId-1	2170	-
	8	Chlorite	WAR-1924	466	Christensen et al. (2000)
	9	Halloysite	ECL:HAL001	2191	-
	10	Hectorite [pellet]	ECL:HEC102	2179	-
	11	illite <0.2um (Imt-1)	lmt-1	1830	-
	12	Illite/Smectite Layer	ECL:ILS104	2377	-
	13	Kaolinite	KGa-1b	569	Christensen et al. (2000)
	14	Kaolinite	KGa-1b	570	Christensen et al. (2000)
	15	Kaolinite (well ordered) [pellet]	ECL:KAO103	2152	-
	16	Montmorillonite (Ca)	STx-1	581	Christensen et al. (2000)
	17	Montmorillonite (Na Rich) [pellet]	ECL:MON107	2153	-
	18	Nontronite [pellet]	ECL:NON104	2174	-

Table 6 continued

Class	#	Sample Name	Sample ID	ASU ID	Citation
	19	Saponite	Saponite	579	Christensen et al. (2000)
	20	saponite <0.2um (Mg-smectite)	Eb-1	1831	-
	21	Smectite	SWa-1	590	Christensen et al. (2000)
	22	Smectite	SWa-1	592	Christensen et al. (2000)
Feldspar	23	Albite	WAR-0235	560	Christensen et al. (2000)
	24	Andesine	WAR-0024	561	Christensen et al. (2000)
	25	Anorthite	BUR-340	564	Christensen et al. (2000)
	26	Bytownite	WAR-1384	563	Christensen et al. (2000)
	27	Labradorite	BUR-3080A	562	Christensen et al. (2000)
	28	Mircocline (Perthite)	WAR-5802	490	Christensen et al. (2000)
	29	Oligoclase	WAR-5804	493	Christensen et al. (2000)
Glass	30	Andesite interstitial glass	MEM-5	1046	Minitti and Hamilton, 2010
	31	Dacite interstitial glass	MEM-4	1045	Minitti and Hamilton, 2010
	32	K-rich Glass	K-rich Glass	1736	Wyatt et al., 2001
	33	Martian meteorite basalt proxy glass	MEM-3	1044	Minitti and Hamilton, 2010
	34	NMB12-14 (cut surface average)	NMB12-14	3662	Farrand et al. 2016

Table 6 continued

Class	#	Sample Name	Sample ID	ASU ID	Citation
	35	TES andesite proxy glass	MEM-2	1043	Minitti and Hamilton, 2010
	36	TES basalt proxy glass	MEM-1	1042	Minitti and Hamilton, 2010
Heater	37	Heater Spectrum 2	Heater Spectrum 2	3681	-
Mica	38	Biotite	BUR-840	453	Christensen et al. (2000)
	39	Muscovite	WAR-5474	449	Christensen et al. (2000)
Olivine	40	Fayalite	WAR-FAY01	557	Christensen et al. (2000)
	41	Olivine Fo10	KI 3008	960	Hamilton, 2010; Koeppen and Hamilton, 2008
	42	Olivine Fo35	KI 3373	957	Hamilton, 2010; Koeppen and Hamilton, 2008
	43	Olivine Fo60	KI 3362	954	Hamilton, 2010; Koeppen and Hamilton, 2008
	44	Olivine Fo68	KI 3115	953	Hamilton, 2010; Koeppen and Hamilton, 2008
Oxide	45	Goethite	GTS4	3740	Glotch et al. (2004)
	46	Goethite-Derived Hematite	GTSH4-300	1810	-
	47	Hematite	BUR-2600	474	Christensen et al. (2000)
	48	Hematite Substrate - Clean	DC700-4-T (HMRE1)	665	-
	49	Magnetite	MTS4	3741	Glotch et al. (2004)

Table 6 continued

Class	#	Sample Name	Sample ID	ASU ID	Citation
Partially Devitrified Glass	50	CH-02	CH-02	3659	Farrand et al. 2016
	51	NMB12-14 bulk (uncut surface average)	NMB12-14 bulk (uncut surface average)	3661	Farrand et al., 2016
	52	Obsidian - Devitrified	OBS-Div	3664	-
Pyroxene	53	Augite	NMNH-119197	540	Christensen et al. (2000)
	54	Bronzite	BUR-1920	439	Christensen et al. (2000)
	55	Diopside	HS-15.4B	445	Christensen et al. (2000)
	56	Enstatite	HS-9.4B	458	Christensen et al. (2000)
	57	Enstatite	NMNH-R14440	546	Christensen et al. (2000)
	58	Enstatite	WAR-2889	602	Christensen et al. (2000)
	59	Hedenbergite	NMNH-16168	600	Christensen et al. (2000)
	60	Hedenbergite (Manganoan)	NMNH-R11524	544	Christensen et al. (2000)
	61	Pigeonite	Wo10En36Fs54, 33,34	3668	Hamilton (2000)
Slope	62	Slope 250/247	Slope 250/247	3678	-
Sulfate	63	Anhydrite	S9	498	Christensen et al., 2000
	64	Anhydrous Magnesium Sulfate	Anhydrous Magnesium Sulfate	756	Baldridge, 2006
	65	Bassanite	S11	643	Lane, 2006
	66	Epsomite	Epsomite	759	Baldridge, 2006

Table 6 continued

Class	#	Sample Name	Sample ID	ASU ID	Citation
	67	Gypsum	S11	496	Christensen et al. (2000)
	68	Gypsum	S8	644	Lane, 2006
	69	Jarosite	S51	627	Lane, 2006
	70	Kieserite	152959	636	Lane, 2006
Zeolite	71	Analcime	WAR49-0672	2136	-
	72	Clinoptilolite	27031	3734	Che et al. (2011, 2012)
	73	Heulandite	agu_heu1	1840	Ruff, 2004
	74	Rozenite	JB626	635	Lane, 2006
	75	Stilbite	agu_stil	1841	Ruff, 2004
	76	Thomsonite	thom4	1839	-

Table 7. Table of thermal infrared spectra modeled mineral abundances/percentages.

Sample ID	**Sample Type**	**Glass (%)**	**Partially Devitrified Glass (%)**	**Zeolite (%)**	**Clay (%)**	**Olivine (%)**	**Oxide (%)**	**Sulfate (%)**	**Pyroxene (%)**	**Mica (%)**	**Amorphous (%)**	**Amphibole (%)**	**Total (%)**
Lake01	Hand Sample	0	79	0	0	5	3	0	0	0	13	0	100
Lake02*	Hand Sample	0	79	0	4	4	0	0	0	0	1	0	88
Lake03	Hand Sample	0	90	0	10	0	0	0	0	0	0	0	100
Lake04	Hand Sample	0	77	5	2	6	8	0	0	1	0	0	99
DB01	Hand Sample	20	36	18	8	5	7	0	2	3	0	0	99
DB02	Hand Sample	0	85	7	4	5	0	0	0	0	0	0	101
41701	Hand Sample	0	64	18	8	6	3	0	0	0	0	0	99
41702	Hand Sample	7	84	4	1	0	3	0	0	1	0	0	100
Her01	Hand Sample	19	51	17	7	0	1	0	3	1	0	0	99
Her02	Hand Sample	0	65	14	6	7	8	0	0	0	0	0	100

Table 7 continued

Sample ID	Sample Type	Glass (%)	Partially Devitrified Glass (%)	Zeolite (%)	Clay (%)	Olivine (%)	Oxide (%)	Sulfate (%)	Pyroxene (%)	Mica (%)	Amorphous (%)	Amphibole (%)	Total (%)
Ask01	Hand Sample	0	69	16	8	0	3	2	2	0	0	0	100
SCoast01	Hand Sample	0	51	15	4	10	20	0	0	0	0	0	100
Lake01	Sieved Pellet Sample	14	47	0	1	3	11	0	0	0	16	0	92
Lake02	Sieved Pellet Sample	26	51	0	0	2	4	0	0	0	8	0	91
Lake03	Sieved Pellet Sample	46	38	3	2	0	7	0	0	1	0	0	97
Lake04	Sieved Pellet Sample	44	40	1	2	0	4	0	0	1	0	0	92
DB01	Sieved Pellet Sample	37	43	8	5	0	8	0	0	0	0	0	101
DB02	Sieved Pellet Sample	43	29	12	6	1	9	0	0	0	0	0	100

Table 7 continued

Sample ID	Sample Type	Glass (%)	Partially Devitrified Glass (%)	Zeolite (%)	Clay (%)	Olivine (%)	Oxide (%)	Sulfate (%)	Pyroxene (%)	Mica (%)	Amorphous (%)	Amphibole (%)	Total (%)
41701	Sieved Pellet Sample	46	38	6	2	0	6	0	0	0	1	0	99
41702	Sieved Pellet Sample	40	46	7	2	0	6	0	0	0	0	0	101
Her01	Sieved Pellet Sample	30	50	10	4	0	6	0	0	0	0	0	100
Her02	Sieved Pellet Sample	35	32	13	4	0	9	0	0	1	0	3	97
Ask01	Sieved Pellet Sample	23	52	13	5	0	5	0	1	1	0	0	100
SCoast01	Sieved Pellet Sample	37	12	13	13	5	20	0	0	0	0	0	100

* a = 12% “slope mineral” was also included in the model, affecting the lower “total” percentage

CHAPTER 4. GEOMORPHOLOGIC MAPPING OF A POSSIBLE HESPERIAN SUBGLACIAL ENVIRONMENT IN THE SISYPHI MONTES, MARS

4.1 Introduction

The history of ice on modern Mars is well constrained by direct observations of glacial and periglacial processes in the Amazonian, but hypotheses surrounding ice in the Noachian time period are poorly constrained. In the most extreme scenario predicted by climate models, the Noachian has been proposed to be covered in ice, experiencing what has been referred to as a "snowball Mars" [Fastook and Head, 2015]. Some answers may lie in the history of ice on the surface during the transition between these periods, the Hesperian, where some features attributed to ice remain but the extent of the ice is not well understood. While there have been a large number of studies surrounding the role of liquid water in the Hesperian [Baker 1982; Baker et al. 1992; Tanaka, 1986; Tribe and Clifford 1993; Masursky et al. 1977; Carr 1979; Tanaka and Chapman 1990; Clifford and Parker, 2001], ice-related features from this time period are rare. The most compelling ice-related features are located in the southern highlands of Mars in the vicinity of the Dorsa Argentea Formation (DAF). Thus, this particular Hesperian region is a critical location to study the history of ice on Mars as it provides a link between the proposed but poorly constrained extensive ice sheets of the Noachian and the more restricted mid latitude glaciation that has been directly observed in Amazonian terrains.

The DAF is a remnant formation characterized by a smooth surface that has a mantling relationship with underlying topography [Tanaka and Kolb, 2001; Head and Pratt, 2001; Bleacher et al., 2003]. There have been two different proposed origins for the DAF: (1) a debris flow made of friable or weak materials resulting from local impacts, igneous activity, or basal melting of the polar units [Tanaka and Kolb, 2001] or (2) a volatile-rich mantling deposit, such as an ancient ice sheet [Head and Pratt, 2001]. The major lines of evidence for the ice sheet hypothesis include braided sinuous ridges that are morphologically similar to subglacial eskers and the proximity of the deposit to the present day south polar deposits [Head and Pratt, 2001]. Head and Pratt [2001] suggest that the DAF was simply a volatile-rich deposit and not necessarily a flowing glacier. However, based on the lack of more widespread paleoglacial morphologies, Tanaka and Kolb [2001] suggest that ridges in the DAF could instead be remnant volcaniclastic deposits.

Climate models suggest that an ice sheet could have formed at the current location of the DAF after the valley-network forming era and after the emplacement of Tharsis, most likely during the Early Hesperian (~3.7 billion years ago) [Scanlon et al., 2018]. Previous researchers have suggested that the DAF dates to roughly 3 billion years ago (Late Hesperian) based on geomorphologic evidence [Sharp, 1973; Condit and Soderblom, 1978; Tanaka and Scott, 1987; Plaut et al., 1988]. MARSIS (Mars Advanced Radar for Subsurface and Ionospheric Sounding) [*Picardi et al.,* 2004] detections of shallow subsurface ice interfaces in this area are highly correlated with the DAF, suggesting remnant subsurface ice is still present within this feature [*Plaut et al.,* 2007].

Another important set of possibly ice-related features in proximity to the DAF are the Sisyphi Montes, which, as previously mapped, are a collection of several dozen 20-60 km wide and ~1 km tall edifices spread throughout Sisyphi Planum to the north of the DAF [Tanaka and Scott, 1987]. The edifices display unique morphologies, including steep sides and flat tops not observed anywhere else on the planet. These morphologies have been proposed to be consistent with subglacial volcanoes, also known as tuyas [Russell et a., 2014] and extend well beyond the modern extent of the DAF. If they are indeed subglacial constructs, they would provide an additional constraint on the history of ice in the region.

In order to better constrain the origin of the Dorsa Argentea Formation and its possible history of ice, we address an overarching question: What is the relationship between the Sisyphi Montes and the past presence of ice in this region? The morphology of subglacial volcanoes is directly related to the presence of the surrounding ice and on Earth has been used to infer the past extent and thickness of ice sheets (e.g., Russell et al., [2014]). The Sisyphi Montes show variability in their heights and shapes, and here we conduct detailed geomorphologic analyses of the edifices to determine (1) whether they are indeed subglacial in origin, and (2) which characteristics can be used to constrain their formation environment. In addition, the edifices are associated with a variety of geomorphologic features that may be related to their formation or other ice-related processes, such as moat-like features, smooth mantling terrain, and regions of deep depressions.

Here we construct a geomorphic map of the area in order to decipher the relationship between the edifices and other potentially ice-related features on the surrounding plains. From this, we can determine whether or not there was ice in the region and subsequently constrain the extent of the proposed ice sheet. We can also evaluate the history of the ice, by determining where the melted ice might have drained and how significant melting was across the region. Overall, the analysis of the region can help to determine the relationship between the Dosa Argentea Formation and the edifices.

4.2 Background and Study Region

Sisyphi Planum (55-75°S, 335-40°E; Figure 18) is located in the southern highlands between the Argyre and Hellas basins. It is a region of low topography that includes isolated domical features known as the Sisyphi Montes [Ghatan and Head, 2002; Farrand et al., 2008] and a unit interpreted to be portions of the ancient ice sheet, the Dorsa Argentea Formation [Ghatan and Head, 2002; Scanlon and Head, 2015].

4.2.1 Sisyphi Montes

The edifices of the Sisyphi Planum were first identified by Murray et al., [1972]. Later, Tanaka and Scott, [1987] mapped the region from Viking data at a 1:2,000,000 scale and described the Sisyphi Planum edifices (also known as the Sisyphi Montes) as mountainous terrain that could be interpreted as degraded volcanoes, tectonic mountains, and/or remnants of polar plateau sequence materials. Seventeen edifices were initially identified and mapped by Tanaka and Scott, [1987]. Ghatan and Head [2002] expanded the number of identified edifices to 21 and interpreted the Sisyphi Montes to be volcanic in nature, possibly glaciovolcanic due to their inclusion in the DAF. Ghatan and Head, [2002] classified the 21 edifices into five categories based on the shape of their peak: (1) low-domed, (2) flat-topped, (3) flat-topped with a cone, (4) cone-shaped with a summit crater, and (5) cone-shaped. These categories were used to determine the origin of the edifices specifically, to differentiate between remnants of impact craters, central peaks, rootless cones, and volcanoes. The Sisyphi Montes predominantly fall into one of the cone-shaped varieties (4 and 5) with a smaller number of flat-topped edifices, which suggested to the authors that the morphologies were consistent with volcanoes that were built and erupted under a more extensive Hesperian-aged ice sheet. After classifying the edifices by height, width, basal and summit elevations, Ghatan and Head, [2002] calculated a minimum ice sheet thickness of ~1.4 km based on the flat-topped and cone-shaped edifices, with the assumption that, unlike the flat- topped edifices, the cone- shaped edifices never breached the surface of a subglacial lake made within the melting ice sheet. Fagan et al. (2010) recalculated the thickness of the Sisyphi Planum paleo-ice sheet using methods from Gudmundsson, [2005] and determined a minimum ice sheet thickness of 500–2200 m with an average value of 1.4 km, consistent with the findings from Ghatan and Head, [2002].

Rodiriguez and Tanaka, [2006] identified additional edifices in the region, reclassified their peak shapes, measured their heights, and noted moat-like features around the edifices. Forty features were identified, where roughly half were surrounded with a moat-like feature. The moat-like features were observed to be about three times the diameter of the associated edifices. Additionally, some of the edifices classified as cone-peaked were associated with hummocky blankets and rampart margins [Rodiriguez and Tanaka, 2006]. This reclassification of the Sisyphi Montes led to new interpretations for their origin. Rodiriguez and Tanaka [2006] suggested the edifices could be either highly degraded impact craters or areas of volcanism controlled by tectonic structures generated by large impact craters. The authors favored the hypothesis that the edifices are degraded impact craters with central volcanic zones. They further suggested that the moat-like features could be due to enhanced volatile loss and subsidence within the craters [Rodiriguez and Tanaka, 2006].

Mineralogic studies support the hypothesis that the Sisyphi Montes are subglacial in origin (Figure 19). Wray et al., [2009] first identified sulfates and hydrated minerals associated with the Sisyphi Montes, suggesting formation due to volcanic hydrothermal or acid fog systems. Ackiss and Wray [2014] followed up by studying the latitude range of 55-75°S including the Sispyhi Montes, the Thyles Rupes, the Ulyxis Rupes, and a region around Chamberlin Crater in search of hydrated minerals. Overall, their results showed that hydrated minerals were not unique to the Sisyphi Planum edifices; however, the strongest signatures were found associated with the edifices. The authors concluded that the hydrated minerals were most consistent with dissolution, transport and re-precipitation of the soluble Mg-sulfates by regional groundwater but could also be explained by volcanogenic alteration, ice-dust weathering, subglacial weathering, or playa evaporation. Ackiss et al., [2018] conducted a more in-depth analysis of the mineralogy of only the Sisyphi Montes, specifically looking at the mineral assemblages to further characterize a formation environment. The authors compared terrestrial mineral assemblages of environments including glaciovolcanic hydrothermal regions, glaciovolcanic weathering, subaerial hydrothermal volcanism, and subaerial weathering to that of the Sisyphi Montes. They identified gypusm-dominated, smectite–zeolite–iron oxide-dominated (possibly palagonite), and polyhydrated sulfate-dominated material on the edifices and suggested that the combination of these observed minerals strongly suggests formation during subglacial eruptions or alteration in associated hydrothermal systems [Ackiss et al., 2018].

4.2.2 Dorsa Argentea Formation

The Dorsa Argentea Formation (DAF) is a remnant formation that was once a massive volatile-rich debris deposit [Tanaka and Kolb, 2001; Head and Pratt, 2001; Bleacher et al., 2003]. The DAF was mapped initially by Tanaka and Scott [1987] at a scale of 1:2,000,000 using Viking data. The lower member of the DAF was mapped as occurring around cavi units (deep depressions), specifically the Sisyphi and Angusti Cavis. Cavis within the Dorsa Argentea are deep (~1 km), and penetrate through the DAF into the underlying rocks [Tanaka and Scott, 1987]. The authors hypothesized that these depressions were volcanic in origin, and that the DAF was a volcanic deposit sourced from local fissures, which have since been buried [Tanaka and Scott, 1987]. While Cavi Sisyphi hasn't been studied in detail, Cavi Angusti contains edifices and flow-like structures suggesting the cavi formed from melting of the volatile-rich substrate, draining liquid water [Howard, 1981; Ghatan and Head, 2002]. The melting could be associated with magmatic activity in the region [Clifford, 1987]. The upper member of the DAF was hypothesized to also be sourced from buried fissures and included possible dome-shaped volcanoes, mapped as mountains. The upper member contains braided ridges that follow the gradient of the region, which have been interpreted to be eskers [Howard, 1981] or lava flow features [Tanaka and Scott, 1987].

A revised and updated geologic map [Tanaka et al., 2014] mapped the region in broad geologic units at a scale of 1:20,000,000 [*Tanaka et al.*, 2014]. Higher resolution datasets including the Mars Global Surveyor (MGS) Mars Orbiter Laster Altimeter (MOLA) [*Smith et al.*, 2001], Thermal Emission Imaging System (THEMIS) [*Christensen et al.*, 2004c] mid-infrared day and night-time images, and the Mars Reconnaissance Orbiter (MRO) Context Camera (CTX) [*Malin et al.*, 2007] were used to further characterize the geology at a global scale. The revised map suggested that the surface of Sisyphi Planum is Noachian in age, but does not differentiate the Sisyphi Montes from the plains. Tanaka et al., [2014] also confirmed a Hesperian age for the DAF, but combined the upper and lower members of the DAF into one unit and renamed it the Hesperian Polar Unit. While initially mapped as volcanic in origin [Tanaka and Scott, 1987], the majority of more recent studies have concluded that the DAF was most likely glacial in origin [Tanaka et al., 2014]. The Hesperian Polar Unit is observed to be a plains-forming deposit with a relatively low radar dialectic constant. It is interpreted to be a water-ice sheet formed by cryovolcanism or atmospheric precipitation that is covered by a thin mantling deposit [Tanaka et al., 2014]. Other major geologic constructs in the area include Pituysa Patera, a large volcanic complex proximal to the DAF, which formed in the Late Noachian to Early Hesperian [Tanaka and Kolb, 2001], before the DAF was emplaced.

4.3 Methodology

4.3.1 Geomorphologic Mapping

While the previous maps [*Tanaka and Scott, D.L.*, 1987; *K. L. Tanaka et al.*, 2014] have contributed to the interpretation of the region, there are still some major knowledge gaps that could be answered using a finer-scale, higher-resolution geomorphologic map. Here, we create a geomorphologic map focusing on the Sisyphi Montes and surrounding features.

The map was created at scales between 1:600,000 and 1:250,000 using MOLA and THEMIS. In addition to these datasets, derived products including slope and hillshade maps were used to differentiate edifices, ejecta blocks, and craters. The slope map was used to quickly identify edifices and map out their base. Topographic highs with a slope greater than 4.5 degrees were examined to determine if the topographic high was consistent with a possible volcanic edifice, a plateau, or an ejecta block. Edifices were then identified based on their lack of proximity to a large crater (to differentiate from ejecta blocks) and the presence of surrounding features (e.g. if the region was hummocky with many topographic highs, the high in question would not be mapped as an edifice). To view the base morphology with no additional information, a hillshade map was produced and utilized. This was used to look at morphology of edifices without the distraction from the thermal information obtained from THEMIS.

Standard geomorphologic mapping methods were utilized along with Planetary Geologic Mapping Protocols [*Skinner et al.,* 2018]. Specifically, four types of contacts were used: certain, approximate, inferred, and concealed. Certain contacts were used to map features that were confidently observed and located. Approximate contacts were used to map features that were known to exist but the location wasn't confidently identified. Inferred contacts were drawn where unit boundaries were hypothesized to occur but there was insufficient evidence available to confirm. Concealed contacts were used to map features that were traceable but subdued. Linear features such as crater rims, buried craters, and sinuous channels were also mapped. Units were mapped and divided based on their different morphologies including textural and color changes. As suggested by Tanaka et al, [2009], care was taken when evaluating possible volcanic features and units were named as non-interpretively as possible. We also recognize that surficial materials are likely undermapped [Tanaka et al., 2009]. Regional Noachian plains units that were previously mapped were not mapped in this study because we focused on Hesperian-aged features and/or features related to the Sisyphi Montes.

Creating and utilizing a map at this scale (between 1:600,000 and 1: 250,000), identifying all of the edifices in the region, and evaluating the map with respect to the results from spectral analysis done by previous studies [Wray et al., 2009; Ackiss and Wray, 2014; Ackiss et al., 2018], will help to construct a more complete and detailed history of the Sisyphi Montes region.

4.3.2 Edifice Classification

To catalogue the martian Sisyphi Montes, we acquired one to three topographic profiles from the Mars Orbital Laser Altimeter (MOLA; 128 pix/deg or ~460 m/pix) [*Smith et al*., 1999] over each edifice. All profiles crossed the edifice in a different direction for a complete three-dimensional view. The edifices were then categorized by their peak structures, using the MOLA topographic profiles, and analyzed to look for trends in the data (size, shape, clustering, etc.). The shapes and sizes of the peaks were categorized into five groups: 1) flat topped, 2) rounded tops, 3) sharp peaks, 4) cratered peaks, and 5) height less than 300 meters – a "catch-all" category for all features below the specified height, which exhibit less distinctive morphologies in MOLA topography (Figure 20). These classifications are different from the Ghatan and Head [2002] study which included: (1) low-domed, (2) flat-topped, (3) flat-topped with a cone, (4) cone-shaped with a summit crater, and (5) cone-shaped. Our study identified the edifices and made an effort to categorize the peaks off of what was observed without the bias from a previous study. We have chosen these five categories to closer align with the data that we observed in the region. We also note that we classified more than five times the amount of data than Ghatan and Head [2002], which could also explain why the categories differ. If an edifice had a flat top with an additional peak, that was noted (Supplemental Table 1) but was still classified as a flat topped edifice (Figure 21). Heights of the edifices and the elevations that they are located at were also extracted from the MOLA data. Additionally, not all edifices identified in previous studies [Ghatan and Head, 2002; Rodriguez and Tanaka, 2006] were included in this study. These edifices were excluded because they did not align with the requirements used to identify edifices in this study. The edifices excluded from this study but included in previous studies are detailed in Table 1.

4.4 Results

4.4.1 Geomorphologic Mapping

Eleven units were observed and mapped based on their geomorphology (Figure 22; Table 2). There are four units that we interpret to be associated with older (possibly Noachian in age) and/or cratering events including the Crater Unit, the Ejecta Unit, the High Elevation Plateau Unit, and the Patera Unit. Four units including the Polygonally Patterned Unit, the Braided Feature Unit, the Mantled Unit, and the Cavi Unit, are interpreted to be ice-related. Two edifice-related units were mapped including the Monte Unit and the Circular Depression Unit. The final unit that was mapped is the Surficial Sediments Unit. Each unit is described below (Figure 23).

Craters larger than 10km in diameter were mapped to show the extent of large-scale cratering in the region. The 10km lower limit was chosen based on the significant increase in crater density for diameters below this size in this region, so that the large number of smaller craters did not consume the entire map. The majority of the mapped craters are located in the northern region of the map. Ejecta is mapped as a separate unit that is associated with the Crater Unit (Figure 24). The majority of mapped craters lack visible associated ejecta; however, ejecta is present in the southern and eastern regions of the map. The craters with ejecta have smaller diameters than craters without ejecta.

The High Elevation Plateau (HEP; Figure 25) unit is composed of high elevation plains that surround the Sisyphi Planum region. Sisyphi Planum appears to be in a regional low (Figure 18). The low areas are similar in elevation to other low areas within the highlands, specifically near Argyre and northward into Terra Sabaea. The MOLA topography shows that Sisyphi Planum is not a regional low but instead a relatively uniform topographic surface surrounded by localized high elevation regions.

The Patera Unit is an elevated terrain surrounding a circular depression corresponding to the Pityusa Patera volcanic complex [Williams et al., 2009]. This unit comprises the topographic highs in the eastern portion of the map (Figure 26). This unit contains flow-like features and "fingers" that extend up into the northern portion of the map. A depressed region, a region that seems to have sourced the flows, can be seen on the edge of the study region. On the southwestern edge of the Patera Unit, this unit forms a sharp scarp above the Mantled Unit. However, no overlap of the two units occurs, thus relative ages cannot be assessed. Some smaller craters superpose the Patera Unit, which is dated to be ~3.8 billion years old [Williams et al., 2009].

There are many units in the region that could be attributed to ice-related processes. The Polygonal Patterned Unit is located in the southwest region of the map near the margin of the southern ice cap (Figure 17). The polygonally patterned region shows both high albedo (bright) and low albedo (dark) terrain, where the high albedo terrain forms the polygon centers and the low albedo terrain forms the lines between the polygons. The polygons tend to transition from polygons into longer linear features throughout the unit.

The Braided Unit is composed of topographically elevated sinuous structures that appear braided (Figure 18). They do not, however, resemble the features southward of the Sisyphi Planum that have been mapped as eskers by other researchers [Butcher et al., 2016; Head and Hallet, 2001]. The Braided Unit is variable between the northern portion of the map and the southern portion of the map. The northern braided terrain is on a higher plateau feature, in this case the High Elevation Plateau (HEP) unit. The terrain is less muddled and more defined, where channels can be observed. The braided features do not lead anywhere and instead seem to be contained in a depressed region with chaotic patterns. The southern portion of the Braided Unit is composed of long braided features on plateaus, with some linear features crosscutting the braided terrain. Like the northern Braided Unit, the channels are chaotic and do not lead to an end/drainage area. Unlike the north, the southern Braided Unit does not seem to be confined in a local depression and instead, based on shadowing, appears to be slightly raised above the surrounding unit. The Braided Unit seems to carve into underlying units (HEP Unit in the north) or sit on top of underlying units (Mantled Unit in the south).

The Mantled unit is located on a slightly raised plateau and marked by a distinct contact with surrounding terrains (Figures 28b, 29). The surface is composed of smooth debris that appear to cover underlying units, and includes many small craters distributed sparsely across the unit.

The Cavi Unit cuts into the Mantled Unit, and are depressed regions marked by a distinct contact with the Mantled Unit (Figure 29). The Cavi Unit is always observed within or surrounded by the Mantled Unit. The boundary of the Cavi Unit (specifically of the Sisyphi Cavi) exhibits a sharp scarp that cuts ~1 km into the underlying units [Tanaka and Scott, 1987] with gullies and slumping on the walls. While the floors are largely flat, some areas exhibit some small craters that appear to be buried or very degraded as well as cone-like mound features. Smaller occurrences of the Cavi Unit (excluding the Sisyphi Cavi) cut into the Mantled Unit but are not as deep. Gullies and slumping are not observed in the smaller portions of the Cavi Unit.

The edifice-related units include the Monte Unit and the Circular Depressions Unit. The Monte Unit is composed of isolated edifices ranging in heights with different top shapes. This unit is discussed in detail in Section 4.3.

The Circular Depressions Unit is observed as depressed regions surrounding the Monte Unit (Figure 30). The moat-like features tend to be circular to semi-circular regions surrounding the edifices. Some have steep walls similar to impact craters, while others do not exhibit a noticeable change in elevation compared to the surrounding terrains. This variation in topography is present even within the same circular depression, where one side of the feature exhibits a rim and the other side grades down into surrounding regions. The texture of the bottoms of the circular depressions (moat-like features) is similar to the surrounding plains/unmapped regions. There are circular depressions surrounding 19 of the mapped edifices in our study region (Figure 31), which is a substantially smaller fraction than those mapped by some previous researchers - 18% in our study (19/106), compared to roughly half (~20/40) in the Rodriguez and Tanaka [2006] study and 43% (9/21) in the Ghatan and Head [2002] study.

The youngest unit in the map is the Surficial Sediments Unit which is composed of dune fields that overlie other geomorphologic units (Figures 24, 29). This unit is often found in low depressions such as craters and the Cavi Unit. The material within the Dunes Unit has a bright signature in the THEMIS daytime IR.

4.4.2 Edifice Identification and Classification

Ghatan and Head [2002] initially mapped 22 edifices in the Sisyphi Planum. Rodriguez and Tanaka [2006] later mapped >40 edifies. Here, we expand the number of edifices to >100 (Figure 31) and examine the edifices in detail to verify their nature and origin. We have identified and analyzed 106 edifices in the Sisyphi Planum. Of those, 8% (9/106) have flat peaks, 8% (9/106) are topped by crater-like depressions, 10% (11/106) have rounded peaks, 31% (33/106) have sharp peaks and 42% (45/106) have heights less than 300 meters (Figure 31). The last classification was created because the small size of the edifices prevented clear classification of their tops in the 128 pixels per degree resolution MOLA global maps. While the lack of topographic detail on the edifices that are less than 300 meters in height means that they cannot be used to characterize a formation environment, here we included these features in our map to show the full extent of possible volcanic edifices within the Sisyphi Planum. Excluding the smaller edifices, the majority of the edifices in the region have a sharp peak. The flat-topped edifices and the edifices with crater-like depressions are the least common type of all of the mapped classifications. There is no clear pattern in the distribution of the various categories within the region, with the exception that the flat-topped edifices are generally located in the north central portion of the study region.

Approximate heights relative to surrounding terrains and summit elevations of the edifices were derived from the MOLA global map. The cratered peaks category had an average elevation of 2090 meters, maximum elevation of 2697 meters, and minimum elevation of 1714 meters. The flat top category had an average elevation of 2566 meters, maximum elevation of 3049 meters, and minimum elevation of 1841 meters. The rounded peaks category had an average elevation of 1880 meters, maximum elevation of 2460 meters, and minimum elevation of 1582 meters. The sharp peaks category had an average elevation of 1941 meters, maximum elevation of 3410 meters, and minimum elevation of 1398 meters. And the category of edifices with heights less than 300 meters had an average elevation of 1532 meters, maximum elevation of 2086 meters, and minimum elevation of 1233 meters. Overall, the minimum elevations of the edifices is 1233 meters with only a few hundred meters of fluctuation (Table 3). This is consistent with the average elevation of the region which is around 1500 meters. The average, maximum, and minimum heights and elevations of each classification can be seen in Table 3.

We plotted the edifices in a histogram of different elevation bins to determine if there was a trend in type of edifice and at what elevation it most often occurred in (Figure 32). The smaller edifices (heights less than 300 meters) were seen at lower elevations with a large number of them occurring at 1500 meters - the average elevation of the region. The sharp peaked edifices also followed an approximate Gaussian distribution with the maximum frequency observed between 1700 and 1800 meters. The other classifications don't exhibit a significant distribution; however, we note that the flat topped edifices are observed at much higher elevations with respect to the other classifications. The flat topped edifices are consistently the tallest features with an average height of 1334 meters, a maximum height of 1900 meters, and a minimum height of 700 meters. The exception to this is that the sharp peaked category has one edifice with a height of 2400 meters (-68.76°S, 5.22°E), the tallest edifice in the region. If this edifice is removed from the calculations, the highest edifice in the sharp peaks category is 1900 meters, the same as the flat topped category. Thus, the flat topped edifices are the highest edifices in the region.

Additionally, we measured the flank slopes for a representative subset of the edifices. Some of the larger edifices have slopes up to ~31 degrees; however the majority of the edifices have slopes between ~15 and 24 degrees.

4.5 Discussion

4.5.1 Geomorphologic Mapping Interpretations

Geomorphologic unit descriptions are detailed above in Section 5.1 and unit interpretations are discussed here. Each unit is addressed below:

1) The Crater and Ejecta Units - We hypothesize that the lack of ejecta around larger craters is due to the age of the craters where the larger ones are typically older and thus more degraded (e.g., Mangold et al., 2012). Craters that have ejecta could be younger and less degraded or could have impacted regions with subsurface ice creating lobate ejecta and debris

flows that are more erosionally resistant, as suggested by previous researchers [Baratoux et al., 2002; Weiss and Head, 2013].

2) The High Elevation Plateau Unit (HEP) - The High Elevation Plateau Unit here is hypothesized to be constructional, perhaps built up by cratering processes and layering of ejecta. Some of these areas can be plausibly attributed to ejecta from specific large and ancient craters in the area – for example, near Russell crater on the northern edge of the region and Lyell crater on the western edge of the region, as labeled in Figure 18. This unit comprises most of the southern cratered highlands units in the previous maps of this region.

3) The Patera Unit - The Patera Unit borders the Mantled Unit in the southwest portion of the mapped region, and a large scarp is present at the contact of the two units (Figure 26). Previous researchers have suggested that this particular area was created when Pityusa Patera chilled against the Dorsa Argentea Formation (DAF), indicating the location of the margin of an ice sheet [Scanlon and Head, 2014]. Pityusa Patera is ~3.8 billion years old [Williams et al., 2009] and the DAF is Late Hesperian (~3 billion years) in age [Scanlon et al., 2018; Sharp, 1973; Condit and Soderblom, 1978; Tanaka and Scott, 1987; Plaut et al., 1988; Thomas et al., 1992]. In order for Pityusa Patera and the modern DAF to coexist and create the chilled margin, this would require that the DAF was an active ice sheet that erased craters for at least 700 million years, which may not be consistent with climate models suggesting volatile climate changes on Mars on much shorter timescales [Laskar et al., 2004]. However, it is clear that something abruptly stopped the flow of the Patera Unit in the southwest region of the mapped unit.

4) The Polygonally Patterned Unit – The polygonal texture of these terrains may be caused by the sublimation of ice and/or dry thermal expansion/contraction of ice-cemented soil [Mangold, 2005; Mellon et al., 2008], which is observed at higher latitudes closer to the southern ice cap and in the northern polar regions. The transition from polygons to linear features could suggest different thermal regimes due to local temperatures and/or winds.

5) The Mantled Unit - Due to the lack of observed craters on this unit, it is interpreted to be young in age. The Mantled Unit coincides with previously mapped Dorsa Argentea Formation [Tanaka et al., 2014; Scott and Tanaka, 1987] and regions that have subsurface ice, as discovered by the Mars Advanced Radar for Subsurface and Ionospheric Sounding (MARSIS) [Plaut et al., 2007]. While the Mantled Unit mapped here is less extensive than the DAF mapped by previous researchers [Tanaka et al., 2014; Scott and Tanaka, 1987], we have interpreted that the Mantled

Unit and the Dorsa Argentea Formation are essentially the same formation. We attribute the smooth morphology to be a mantling of regolith that covers subsurface ice. It is possible that the Mantled Unit/DAF extends beyond the regions we have mapped here but we have not seen geomorphic evidence for it (e.g. the distinctly sharp contact used to map the entirety of the unit).

6) The Cavi Unit – Because the Cavi Unit is always associated with the Mantled Unit and the Mantled Unit is inferred to be the subsurface ice-rich DAF, we have interpreted the Cavi Unit to be depressed regions where ice has melted or sublimated from the subsurface layer and the top exposed layer collapsed. Mapped occurrences of the Cavi Unit can be thought of as remnants of the Mantled Unit.

7) The Braided Unit – While grouped into the same unit, the braided terrain differs between the north and the south occurrences. The northern portion of the terrain resembles inverted channels. Here, we hypothesize that this is a remnant of inverted channels exposed by differential weathering patters [Pain et al., 2007]. The southern portion of this terrain occurs in association with the Cavi and Montes units. We have interpreted the braided unit in the southern portion of the map to be related to a volcanic events. Structures resembling dykes and fractures [Head et al., 2006] are observed throughout the unit, which cross hummocky terrain. Hummoky terrain similar to what we observe in the braided unit has been observed in Elysium Planitia and is said to be associated with volcano/ground-ice interaction [Malin, 1977; Mouginis-Mark, 1985; Mouginis-Mark et al., 1984; Squyres et al., 1987], consistent with regional interpretations of the unit (the ice-rich Mantled unit and the collapsed Cavi unit).

8) The Circular Depression Unit – The circular depressions (or moat-like features) have been hypothesized to be caused by the response of the lithosphere due to the emplacement of the volcano [Campbell et al., 2016], similar to flexural moats observed around terrestrial volcanoes [Collier and Watts, 2001; McGovern et al., 2004; Isherwood et al., 2013]. However, the circular depressions are not seen around all of the edifices. Thus, this feature could not be a response to the extra load. Instead, we hypothesize that the circular depressions around the edifices could be due to permafrost. Permafrost on Mars can extend as deep into the surface as 7km and some of these circular depressions are ~1km deep or more (Figure 30). Permafrost could explain the size and depths of the moat-like features as well as why they do not surround all of the edifices. Previous researchers, such as Ghatan and Head [2002], did not suggest permafrost but did

suggest that the circular depressions could be made by a loss in volatiles, consistent with our interpretation of permafrost.

9) The Surficial Sediments Unit - We interpret this unit to be surficial debris mobilized by aeolian processes, otherwise known as dunes. Dunes are observed throughout the Sisyphi Planum and are not localized to any particular region of the map.

The lack of superposition between these units makes determining relative ages challenging. We suggest that the Braided Unit is younger than the HEP Unit, the Cavi Unit is younger than the Mantled Unit, and Circular Depression Unit is younger than the Cavi Unit, and the Surficial Sediment Unit is the youngest unit in the region. This timeline of relative age is consistent with our crater counting ages as well, which shows that the Circular Depression Unit is younger than the Cavi Unit. The oldest units (in no particular order) are the HEP, Patera, Crater, and Ejecta Units. Followed by the Mantled Unit, the Cavi Unit, the Circular Depressions Unit, and the Surficial Sediments Unit. The age of the Polygonal Patterned Unit, the Braided Unit, and the Montes Unit is still unclear.

4.5.2 Edifice Classification Interpretations

While the morphologies of the Sisyphi Montes of the Sisyphi Planum are most consistent with volcanism, other possible morphologies must also be ruled out. In addition to volcanic features as suggested by Ghatan and Head [2002], these edifices could also have been interpreted to be impact-related or erosionally-resistant remnants such as mesas. Mesas are possible but the large diversity in elevations and heights is inconsistent with one or even several resistant units controlling erosion in the area. There are also no other erosional features supporting this hypothesis. In terms of relationships to impacts, not enough of the edifices are surrounded by circular depressions (also known as moat-like features) to be characterized as sourced from an impact crater, as suggested by Rodriguez and Tanaka [2006]. Thus, here we consider two volcanic hypotheses for the origin of the high latitude edifices:

1) Subglacial volcanism: Previous research in this area has suggested that these edifices are subglacial in origin [Ghatan and Head, 2002; Farrand et al., 2008; Scanlon and Head, 2015; Ackiss et al., 2018]. In volcanic eruptions beneath ice sheets and glaciers on Earth, the combination of heat and large quantities of melt water lead to the production of unique morphologies. These morphologies include “tuyas” or table

mountains that are steep sided and flat topped edifices as well as “tindars” or ridges that are flat-topped and linear [Russell et al., 2014]. Subglacial mounds, which are conical in shape, are created when the eruption does not breach the ice-sheet [Russell et al., 2014]. A possible smectite-zeolite-iron oxide mixture consistent with terrestrial palagonite has been recently identified on the edifices using CRISM spectra [Ackiss et al., 2018], also supporting a subglacial volcanic origin.

2) Subaerial volcanism: Subaerial volcanism includes stratovolcanoes, complex volcanoes, compound volcanoes, somma volcanoes, shield volcanoes, pyroclastic shields, lava cones, and lava domes [Grosse et al., 2014]. The morphologies of these edifices are typically cone-, dome-, or shield-shaped and generally have flank slopes that are less steep than glaciovolcanic edifices (<30 degrees) [Pedersen and Grosse, 2014].

To evaluate these two hypotheses, we have identified and classified all of the edifices in the Sisyphi Planum based on their profiles, which were extracted from a digital elevation model (DEM). While the edifices have been previously classified [Ghatan and Head, 2002; Rodriguez and Tanaka, 2006], not all of the edifices were identified in those studies. Here, we strive to identify and classify all of the edifices in the regi, creating a complete view of the Sisyphi Montes. Additionally, we constructed a geomorphologic map to characterize the relationship of the Montes and the surrounding plains units of the region. The goal of geomorphologic maps is to show the spatial distribution of landforms and surface deposits in order to constrain the processes that act on those landforms and better understand how a landscape has developed over time. This is in contrast to geologic maps, which focus on characterizing rock units and/or geologic strata, and may not differentiate between surfacial landforms. In this study we are primarily interested in the evolution of the surface over time and the processes that have affected the surface, so we have chosen to map based only on the surface geomorphology of the region.

One of the distinctive characteristics of the Sisyphi Montes is their variable top shape, which has been attributed to subglacial processes in previous studies [Ghatan and Head, 2002]. However, this characteristic alone is insufficient to determine whether the edifices are subglacially or subaerially formed structures. Subglacial volcanoes on Earth can have a variety of top classifications based on where they erupted in the ice and whether or not they breached the ice sheet. Subglacial mounds and tindars, or volcanoes that do not breach the ice sheet, tend to exhibit cone-like tops that would be classified as “Rounded Peaks” in this study [Russell et al., 2014; Blankenship et al., 1993; Hickson, 2000; Lescinsky and Fink, 2000]. Subglacial tuyas, or volcanoes that do breach the ice sheet, exhibit flat tops that would be classified as “Flat-Topped” in this study [Russell et al., 2014]. Subglacial volcanoes that breach the ice sheet, form flat tops, and continue to erupt forming sharp peaks are classified as complex volcanic structures [Russell et al., 2014]. In this study, if any flat top/flat elevation on an edifice was observed, that edifice was classified as a flat-topped edifice. However, stratovolcanoes not formed in the presence of ice or water with little degradation will have sharp tops due to the combination of viscous (usually felsic) magmas and deposition of tephra at the angle of repose [Karatson et al., 2010]. Both subaerial and subglacial volcanoes can experience internal subsidence and form a crater at the peak, consistent with the “Cratered Peak” classification in this study [Branney, 1995].

Thus, cratered and rounded peaks on edifices could be interpreted to be either subglacial or subaerial in origin, while flat-topped edifices are most likely subglacial in origin. Sharp peaked edifices are most likely subaerial; however, it is also possible that they could be subglacial but continued to erupt either while the ice was present or later during an interglacial period, obscuring the underlying subglacial construct. Therefore, of the edifice classifications within this study, the most important category for constraining the history of ice in the region is the flat-topped category, as they are the only class that has a uniquely subglacial morphology. The sharp peaked edifices are more common and scattered throughout the study region with a similar distribution as the smaller edifices. The flat-topped edifices are concentrated in the center of Sisyphi Planum. From this information, it is plausible that the flat-topped edifices were formed under ice and the sharp peaked edifices were formed either before or after the ice was present. However, it is important to note that many sharp peaked edifices are located within the previously mapped DAF and the Mantled Unit of this study. Within the Mantled Unit, most of the larger edifices are either sharp- or rounded-peaks, with a high density of the smaller (<300 m height) edifices as well. This could either suggest that some of the sharp peaked and small edifices were indeed erupted subglacially under the modern DAF, or that they erupted subaerially prior to emplacement of the modern DAF. In constrast, the flat-topped edifices are located within the undivided/unmapped Noachian-aged plains to the north, unrelated to the modern ice-rich regions. As previous studies have proposed, this implies that ice once covered this north central portion of Sisyphi Planum.

In addition to the peaks of the edifices, the slopes could also indicate formation environment. Slopes of the edifices in this region range from roughly 4.5-40 degrees, where the majority have slopes between 12-23 degrees. On Earth, slopes can be used to differentiate volcanic types where shield volcanoes have slopes up to 5 degrees, stratovolcanoes have slopes between 10-30 degrees, cinder cones have up to ~30 degree slopes (at the angle of repose) [Rossi, 1996], and subglacial volcanoes often have slopes greater than 30 degrees [Russell et al., 2014]. The observed slopes within the Sisyphi Montes region fall within the range of terrestrial stratovolcano slopes. An experimental study by Kleinhans et al., [2011] suggested that the angle of repose may be dependent on the gravity of the body. If this is correct, it could provide evidence showing that the angles of volcanoes we observe on Earth may be slightly different than what we should expect of possible martian volcanic edifices. This could suggest that 3+ billion years of degradation via mass wasting, small impacts, and periglacial processes may have modified these slopes.

Ackiss et al., [2018] noted the presence of a smectite-zeolite-iron oxide-dominated material, interpreted as possible palagonite on a subset of the Sisyphi Montes edifices. Combing the results of that study and this study, we see the smectite-zeolite-iron oxide-dominated material (possibly palagonite) was located on both flat topped and rounded edifices (Figure 33). Of those edifices identified with smectite-zeolite-iron oxide-dominated material [Ackiss et al., 2018], none were associated with the previously mapped DAF [Tanaka et al., 2014; Tanaka and Scott, 1987]. While palagonite is not restricted to strictly subglacial environments, as it also forms in subaqueous environments [Waters 1960; Mackin 1961; Moore et al., 1973; Furnes 1974; Naylor et al., 1999], this suggests the past presence of abundant water in some form. Regardless, the presence of the possible palagonite provides additional evidence that the edifices are most likely volcanic in origin, and together with the morphologies identified in this study and previous studies, it is likely that the edifices were formed subglacially.

4.5.3 Relationships between the montes and the regional ice

The DAF within the Sisyphi Planum region has two proposed hypotheses for formation: 1) a debris flow made of friable or weak materials resulting from local impacts, igneous activity, or basal melting of the polar units [Tanaka and Kolb, 2001] or 2) a volatile-rich deposit such as an ancient ice sheet [Head and Pratt, 2001]. Here, we have mapped the region specifically focusing on the Sisyphi Montes and the surrounding units to further narrow down the origin of the DAF and help answer the question: What is the relationship between the Sisyphi Montes and the ice in the region?

Combining the edifice top classifications with the results from the geomorphologic map, we have interpreted that the Mantled Unit was previously more extensive in Mars' history. Here we have interpreted the Mantled Unit to be a remnant of an ancient ice sheet, the Dorsa Argentea Formation. We also observe the flat topped edifices, having morphologies consistent with subglacial volcanism, outside of the Mantled Unit. This implies that the ancient ice sheet was once present in the region to the north, in central Sisyphi Planum, where the flat-topped edifices are located. However, our results do not uniquely indicate that the ancient ice sheet was the same as the modern DAF. It is also possible that the DAF represents the most recent icy deposit in this area, and that other, perhaps more extensive, ice sheets preceded it at different times in Mars history.

It is important to remember that this region is unique, as morphologies like this are not seen in any other region of the planet, and also very well preserved. The uniqueness is important because there are many volcanic environments in the southern highlands but none that have morphologies like the Sisyphi Planum. If the icy highlands "snowball Mars" model [Fastook and Head, 2015] is correct, we should expect to see regions like this – covered in flat topped edifices – throughout the southern highlands. The fact that we do not suggests either that the model overestimates the amount of ice coverage on ancient Mars, or that older regions are much more degraded compared to the Sisyphi Planum. The preservation likely suggests that this region is either very young or was covered in ice/regolith and thus preserved.

Based on what was observed in the Sisyphi Planum, we have concluded that an ancient ice sheet was present and most likely more extensive than the DAF today. Further work will be needed to tie this region to the history and distribution of ice sheets on the planet, and to understand the exceptional levels of preservation of both the ice and underlying geomorphology.

4.6 Conclusion

In this study, we have identified and classified the tops of the Sisyphi Montes as well as geomorphologically mapped the Sisyphi Planum region of Mars. While many of the edifices could be subglacial in origin, we find that the only morphologic class that exhibits uniquely subglacial morphologies are the flat-topped edifices. These edifices are similar to terrestrial tuyas, which form when a subglacial volcano breaches an ice sheet and erupts a plateau of subaerial lavas [Russell et al., 2014]. Based on these maps and topographic data, we have shown that flat-topped edifices are all located outside of regions that we map as the Mantled Unit, which we infer to be related to the Dorsa Argentina Formation, a modern buried icy mantle that is likely a remnant of a more extensive Hesperian ice sheet. The combination of the flat-topped edifices and their location outside of the mapped ice-related regions strongly suggests that the ice in the region was once more extensive than what is currently observed. While this has been proposed in the past, the combination of a detailed map at this resolution and how far the ice sheet could have extended has not been produced. Here we show that the ice must have extended to at least as far as the flat-topped edifices in the region.

While the work and interpretations here have led to a further classification of the region, future measurements and more detailed studies such as higher resolution radar mapping of the subsurface ice, higher resolution mineralogy studies, and detailed (CTX/HiRISE scale) morphology studies of the edifices and any related glacial features would be useful.

4.7 References

Ackiss, S. E., and J. J. Wray (2014), Occurrences of possible hydrated sulfates in the southern high latitudes of Mars, *Icarus*, *243*, 311–324, doi:10.1016/j.icarus.2014.08.016.

Ackiss, S., Horgan, B., Seelos, F., Farrand, W., Wray, J., 2018. Mineralogic evidence for subglacial volcanism in the Sisyphi Montes region of Mars. Icarus 311, 357–370.

Baker, Victor R. "The channels of Mars." *Research supported by NASA, NSF, and Australian-American Educational Foundation Austin, TX, University of Texas Press, 1982. 204 p.* (1982).

Baker, Victor R., et al. "Channels and valley networks." *Mars* (1992): 493-522.

Baratoux, David, Christophe Delacourt, and Pascal Allemand. "An instability mechanism in the formation of the Martian lobate craters and the implications for the rheology of ejecta." *Geophysical Research Letters* 29.8 (2002): 51-1.

Branney, Michael J. "Downsag and extension at calderas: new perspectives on collapse geometries from ice-melt, mining, and volcanic subsidence." *Bulletin of Volcanology* 57.5 (1995): 303-318.

Blankenship, Donald D., et al. "Active volcanism beneath the West Antarctic ice sheet and implications for ice-sheet stability." *Nature* 361.6412 (1993): 526.

Bleacher, Jacob E., et al. "Deflation/erosion rates for the Parva Member, Dorsa Argentea Formation and implications for the south polar region of Mars." *Journal of Geophysical Research: Planets* 108.E7 (2003).

Butcher, Frances EG, Susan J. Conway, and Neil S. Arnold. "Are the Dorsa Argentea on Mars eskers?." *Icarus* 275 (2016): 65-84.

Carr, Michael H. "Formation of Martian flood features by release of water from confined aquifers." *Journal of Geophysical Research: Solid Earth* 84.B6 (1979): 2995-3007.

Campbell, A., S. Ackiss, and B. H. Horgan (2016), Morphology of possible subglacial volcanoes in the Sysphi Montes region of Mars, vol. 47, p. 1554.

Collier, J. S., and A. B. Watts. "Lithospheric response to volcanic loading by the Canary Islands: constraints from seismic reflection data in their flexural moat." *Geophysical Journal International* 147.3 (2001): 660-676.

Christensen, Philip R., et al. "The thermal emission imaging system (THEMIS) for the Mars 2001 Odyssey Mission." *Space Science Reviews* 110.1-2 (2004): 85-130.

Clifford, Stephen M. "Polar basal melting on Mars." *Journal of Geophysical Research: Solid Earth* 92.B9 (1987): 9135-9152.

Clifford, Stephen M., and Timothy J. Parker. "The evolution of the Martian hydrosphere: Implications for the fate of a primordial ocean and the current state of the northern plains." *Icarus* 154.1 (2001): 40-79.

Condit, Christopher D., and Laurence A. Soderblom. *Geologic map of the Mare Australe area of Mars*. No. 1076. 1978.

Fastook, J. L., and J. W. Head (2015), Glaciation in the Late Noachian Icy Highlands: Ice accumulation, distribution, flow rates, basal melting, and top-down melting rates and patterns, *Planet. Space Sci.*, *106*, 82–98.

Farrand, W. H., M. D. Lane, and B. R. Edwards (2008), North and South: Possible Tuyas and Hyaloclastite Hills on the Northern Plains and in the Southern Dorsa Argentea Region of Mars, vol. 39, p. 1761.

Furnes, H., Fridleifsson, I.B., 1974. Tidal effects on the formation of pillow lava/hyaloclastite deltas. Geology 2, 381–384.

Ghatan, G. J., and J. W. Head (2002), Candidate subglacial volcanoes in the south polar region of Mars: Morphology, morphometry, and eruption conditions, *J. Geophys. Res. Planets*, *107*, 5048, doi:10.1029/2001JE001519.

Grosse, Pablo, et al. "A global database of composite volcano morphometry." *Bulletin of Volcanology* 76.1 (2014): 784.

Gudmundsson, 2005. Subglacial volcanic activity in Iceland. Icel. Mod. Process. Past Environ. Elsevier In: C. Caseldine, A. Russell, J. Hardardóttir and Ó. Knudsen eds., 127–151.

Hickson, Catherine J. "Physical controls and resulting morphological forms of Quaternary ice-contact volcanoes in western Canada." *Geomorphology* 32.3-4 (2000): 239-261.

Head III, J. W., and B. Hallet. "Origin of sinuous ridges in the Dorsa Argentea Formation: New observations and tests of the esker hypothesis." *Lunar and Planetary Science Conference*. Vol. 32. 2001.

Head, James W., and Stephen Pratt. "Extensive Hesperian- aged south polar ice sheet on Mars: Evidence for massive melting and retreat, and lateral flow and ponding of meltwater." *Journal of Geophysical Research: Planets* 106.E6 (2001): 12275-12299.

Isherwood, Ryan J., et al. "The volcanic history of Olympus Mons from paleo-topography and flexural modeling." *Earth and Planetary Science Letters* 363 (2013): 88-96.

Karátson, Dávid, et al. "The regular shape of stratovolcanoes: a DEM-based morphometrical approach." *Journal of Volcanology and Geothermal Research* 193.3-4 (2010): 171-181.

Kolb, Eric J., and Kenneth L. Tanaka. "Geologic history of the polar regions of Mars based on Mars Global Surveyor data: II. Amazonian Period." *Icarus* 154.1 (2001): 22-39.

Kleinhans, M. G., et al. "Static and dynamic angles of repose in loose granular materials under reduced gravity." *Journal of Geophysical Research: Planets* 116.E11 (2011).

Laskar, Jacques, et al. "Long term evolution and chaotic diffusion of the insolation quantities of Mars." *Icarus* 170.2 (2004): 343-364.

Lescinsky, David T., and Jonathan H. Fink. "Lava and ice interaction at stratovolcanoes: use of characteristic features to determine past glacial extents and future volcanic hazards." *Journal of Geophysical Research: Solid Earth* 105.B10 (2000): 23711-23726.

Mackin, J.H., 1961. stratigraphic section in the Yakima Basalt and the Ellensburg Formation in south-central Washington.

Mangold, Nicolas. "High latitude patterned grounds on Mars: Classification, distribution and climatic control." *Icarus* 174.2 (2005): 336-359.

Masursky, Harold, et al. "Classification and time of formation of Martian channels based on Viking data." *Journal of Geophysical Research* 82.28 (1977): 4016-4038.

Malin, Michael C., et al. "Context camera investigation on board the Mars Reconnaissance Orbiter." *Journal of Geophysical Research: Planets* 112.E5 (2007).

McGovern, Patrick J. "Flexural stresses beneath Hawaii: Implications for the October 15, 2006, earthquakes and magma ascent." *Geophysical Research Letters* 34.23 (2007).

Mellon, Michael T., et al. "Periglacial landforms at the Phoenix landing site and the northern plains of Mars." *Journal of Geophysical Research: Planets* 113.E3 (2008).

Murray, Bruce C., et al. "Geological framework of the south polar region of Mars." *Icarus* 17.2 (1972): 328-345.

Moore, J.G., Phillips, R.L., Grigg, R.W., Peterson, D.W., Swanson, D.A., 1973. Flow of lava into the sea, 1969–1971, Kilauea Volcano, Hawaii. Geol. Soc. Am. Bull. 84, 537–546.

Naylor, P.H., Bell, B.R., Jolley, D.W., Durnall, P., Fredsted, R., 1999. Palaeogene magmatism in the Faeroe–Shetland Basin: influences on uplift history and sedimentation, in: Geological Society, London, Petroleum Geology Conference Series. Geological Society of London, pp. 545–558.

Pedersen, G. B. M., and Pablo Grosse. "Morphometry of subaerial shield volcanoes and glaciovolcanoes from Reykjanes Peninsula, Iceland: effects of eruption environment." *Journal of Volcanology and Geothermal Research* 282 (2014): 115-133.

Picardi, G., et al. "Performance and surface scattering models for the Mars Advanced Radar for Subsurface and Ionosphere Sounding (MARSIS)." *Planetary and Space Science* 52.1-3 (2004): 149-156.

Plaut, J. J., et al. "Accumulation of sedimentary debris in the south polar region of Mars and implications for climate history." *Icarus* 76.2 (1988): 357-377.

Plaut, J. J., A. Ivanov, A. Safaeinili, S. M. Milkovich, G. Picardi, R. Seu, and R. Phillips (2007), Radar Sounding of Subsurface Layers in the South Polar Plains of Mars: Correlation with the Dorsa Argentea Formation, vol. 38, p. 2144.

Rodriguez, J. A. P., and K. L. Tanaka (2006), Sisyphi Montes and Southwest Hellas Paterae: Possible Impact, Cryotectonic, Volcanic, and Mantle Tectonic Processes and Hellas Basin Rings, *LPI Contrib.*, *1323*, 8066.

Rossi, M. J., and A. Gudmundsson. "The morphology and formation of flow-lobe tumuli on Icelandic shield volcanoes." *Journal of Volcanology and Geothermal Research* 72.3-4 (1996): 291-308.

Russell, J. K., B. R. Edwards, L. Porritt, and C. Ryane (2014), Tuyas: a descriptive genetic classification, *Quat. Sci. Rev.*, *87*, 70–81, doi:10.1016/j.quascirev.2014.01.001.

Scanlon, K. E.; Head, J. W. The Dorsa Argentea Formation: Synthesis of Glacial Features and History of Late Noachian-Early Hesperian Martian Climate Change. (2014) 45th Lunar and Planetary Science Conference, LPI Contribution No. 1777, p.1477

Scanlon, Kathleen E., James W. Head, and David R. Marchant. "Volcanism-induced, local wet-based glacial conditions recorded in the Late Amazonian Arsia Mons tropical mountain glacier deposits." *Icarus* 250 (2015): 18-31.

Scanlon, K. E., et al. "The Dorsa Argentea formation and the Noachian-Hesperian climate transition." *Icarus* 299 (2018): 339-363.

Sharp, Robert P. "Mars: South polar pits and etched terrain." *Journal of Geophysical Research* 78.20 (1973): 4222-4230.

Skinner Jr, J. A., et al. "Planetary geologic mapping protocol–2018." *United States Geologic Survey: Flagstaff, AZ* (2018).

Smith, David E., and Maria T. Zuber. "The relationship of the MOLA topography of Mars to the mean atmospheric pressure." *Bulletin of the American Astronomical Society*. Vol. 31. 1999.

Smith, David E., et al. "Mars Orbiter Laser Altimeter: Experiment summary after the first year of global mapping of Mars." *Journal of Geophysical Research: Planets* 106.E10 (2001): 23689-23722.

Tanaka, Kenneth L. "The stratigraphy of Mars." *Journal of Geophysical Research: Solid Earth* 91.B13 (1986).

Geological Survey (US), Kenneth L. Tanaka, and David Holcomb Scott. *Geologic map of the polar regions of Mars*. The Survey, 1987.

Tanaka, Kenneth L., and Mary G. Chapman. "The relation of catastrophic flooding of Mangala Valles, Mars, to faulting of Memnonia Fossae and Tharsis volcanism." *Journal of Geophysical Research: Solid Earth* 95.B9 (1990): 14315-14323.

Tanaka, Kenneth L., et al. "Assessment of planetary geologic mapping techniques for Mars using terrestrial analogs: The SP Mountain area of the San Francisco Volcanic Field, Arizona." *Planetary and Space Science* 57.5-6 (2009): 510-532.

Tanaka, K. L., et al. "The digital global geologic map of Mars: Chronostratigraphic ages, topographic and crater morphologic characteristics, and updated resurfacing history." *Planetary and Space Science* 95 (2014): 11-24.

TRIBE, S., and SM CLIFFORD. "Temporal changes in the geographic distribution, elevation, and potential origin of the Martian outflow channels(Abstract Only)." *Lunar and Planetary Inst, Mars: Past, Present, and Future. Results from the MSATT Program, Part 1 p 51-52(SEE N 94-33190 09-91)* (1993).

Waters, A.C., 1960. Determining direction of flow in basalts. Am. J. Sci. 258, 350–366.

Weiss, David K., and James W. Head. "Formation of double- layered ejecta craters on Mars: A glacial substrate model." *Geophysical Research Letters* 40.15 (2013): 3819-3824.

Williams, David A., et al. "The circum-Hellas volcanic province, Mars: overview." *Planetary and Space Science* 57.8-9 (2009): 895-916.

Wray, J. J., S. L. Murchie, S. W. Squyres, F. P. Seelos, and L. L. Tornabene (2009), Diverse aqueous environments on ancient Mars revealed in the southern highlands, *Geology, 37*, 1043–1046, doi:10.1130/G30331A.1.

4.8 Tables

Table 8. Edifices not included in this study but were previously identified in the Sisyphi Montes region.

Longitude	Latitude	Previous Study	Reasoning for Removal
1.7348	-57.54894	Ghatan and Head, 2002	Nothing; Crater
4.71361	-57.2741	Ghatan and Head, 2002	Mapped as part of high plateau in this study; Previously mapped as mountainous in Tanaka and Scott, 1987
34.51217	-67.70068	Ghatan and Head, 2002	Pitusa Patera; Not part of the Sisyphi Plateau edifices
20.15834	-65.02546	Rodriguez and Tanaka, 2006	High plateau feature between two craters; Not definitive
20.6422	-64.2918	Rodriguez and Tanaka, 2006	High plateau feature between two craters; Not definitive
23.91739	-63.82743	Rodriguez and Tanaka, 2006	Inverted Plateau; Possibly inverted ejecta
24.37284	-62.18288	Rodriguez and Tanaka, 2006	High plateau region - portion of a ridge; Previously mapped as Plateau Sequence in Tanaka and Scott, 1987and Middle Noachian Highland Crust in Tanaka et al., 2014
29.12886	-61.01667	Rodriguez and Tanaka, 2006	High region on edge of crater; Not definitive
38.33672	-69.30086	Rodriguez and Tanaka, 2006	Outside of study area

Table 9. Descriptions of Mapped Units

Unit Name	**Unit Description**	**Unit Interpretation**
Cavi	Depressed region marked by a distinct contact associated with the Mantled Unit.	Regions of depressions where ice has sublimated from the subsurface layer and the top exposed layer collapses.
Crater	Crater with circular rims; Includes all stages of the cratering process including degraded, buried, and fresh craters; Craters mapped are larger than 10 km in diameter	Large craters that are geologically old. Noachian in age [Tanaka et al., 2014].
Surficial Sediments	Dune fields overlying other geomorphologic units; often associated in low depressions such as craters and cavi units; high albedo THEMIS signature	Surficial debris mobilized by aeolian processes.
Ejecta	Ejecta associated with regional craters	Ejecta from large craters that are geologically old. Noachian in age [Tanaka et al., 2014].
High Elevation Plateau	Regional highlands surrounding the Sisyphi Planum	Unclear whether the Sisyphi Planum is a regional low or if it is just surrounded by regional highs. This unit represents the highly cratered plateau units surrounding the Sisyphi Planum

Table 9 continued

Unit Name	**Unit Description**	**Unit Interpretation**
Circular Depressions	Depressed region marked by a distinct contact associated with the Monte Unit.	Depressed regions around the edifices possibly caused by the response of the lithosphere due to the emplacement of the volcano (similar to terrestrial flexural moats) and/or depressions from the loading of water due to the melting ice sheet.
Monte	Isolated edifices ranging in heights with different top shapes	Possibly volcanic edifices. Interpreted to be both subglacial and intraglacial in origin.
Patera	Elevated material surrounding a circular depression	Volcanic complex Pituysa Patera.
Braided Feature	Long braided features on plateaus associated with high elevation units such as the High Elevation Plateau Unit and the Mantled Unit; Linear features crosscut by linear features.	Possibly inverted braided channels, volcanic cones/pits crosscut by dike-like features.
Mantled	Slightly raised plateau region marked by a distinct contact; smooth debris covering underlying units	Correlates to regions mapped as the Dorsa Argentea Formation [Tanaka et al., 2014] as well as data from MARSIS [Plaut et al., 2007] and interpreted to be the location of subsurface ice.
Polygonal Patterned	Terrain with high and low albedo associated with the Mantled Unit; Polygonal geometric shapes in high albedo terrain separated by low albedo terrain	Possibly caused by the sublimation of ice and/or dry thermal expansion and contraction of ice-cemented soil [Mellon et al., 2008]. Only seen at higher latitudes closer to the southern ice cap.

Table 10. Elevations and heights of classified edifices

Edifice Classification	**Average Elevation (m)**	**Maximum Elevation (m)**	**Minimum Elevation (m)**	**Average Height (m)**	**Maximum Height (m)**	**Minimum Height (m)**
Cratered Top	2090	2697	1714	689	1250	325
Flat Top	2566	3049	1841	1334	1900	700
Rounded Peak	1880	2460	1582	641	1250	325
Sharp Peak	1941	3410	1398	592	2400	325
Heights less than 300 m	1532	2086	1233	195	300	70

4.9 Figures

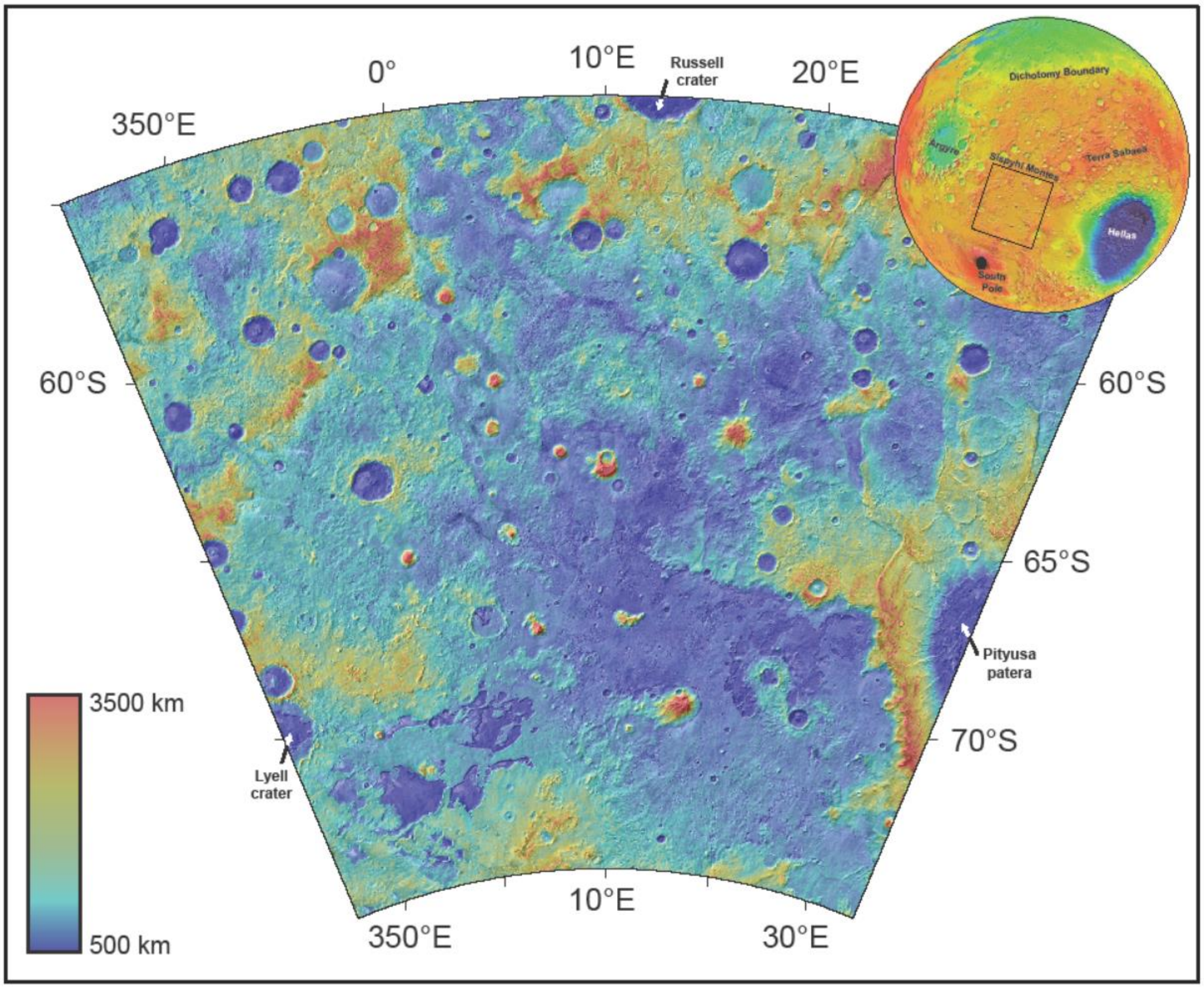

Figure 18. Topographic view of the Sisyphi Planum. MOLA topography overlying THEMIS daytime thermal infrared. Cooler colors show low elevation regions of (dark blue is 500km) and warm colors show high elevation regions (red is 3500km). Inset shows the region in a global perspective, between the Argyre and Hellas basins and northward of the South Pole.

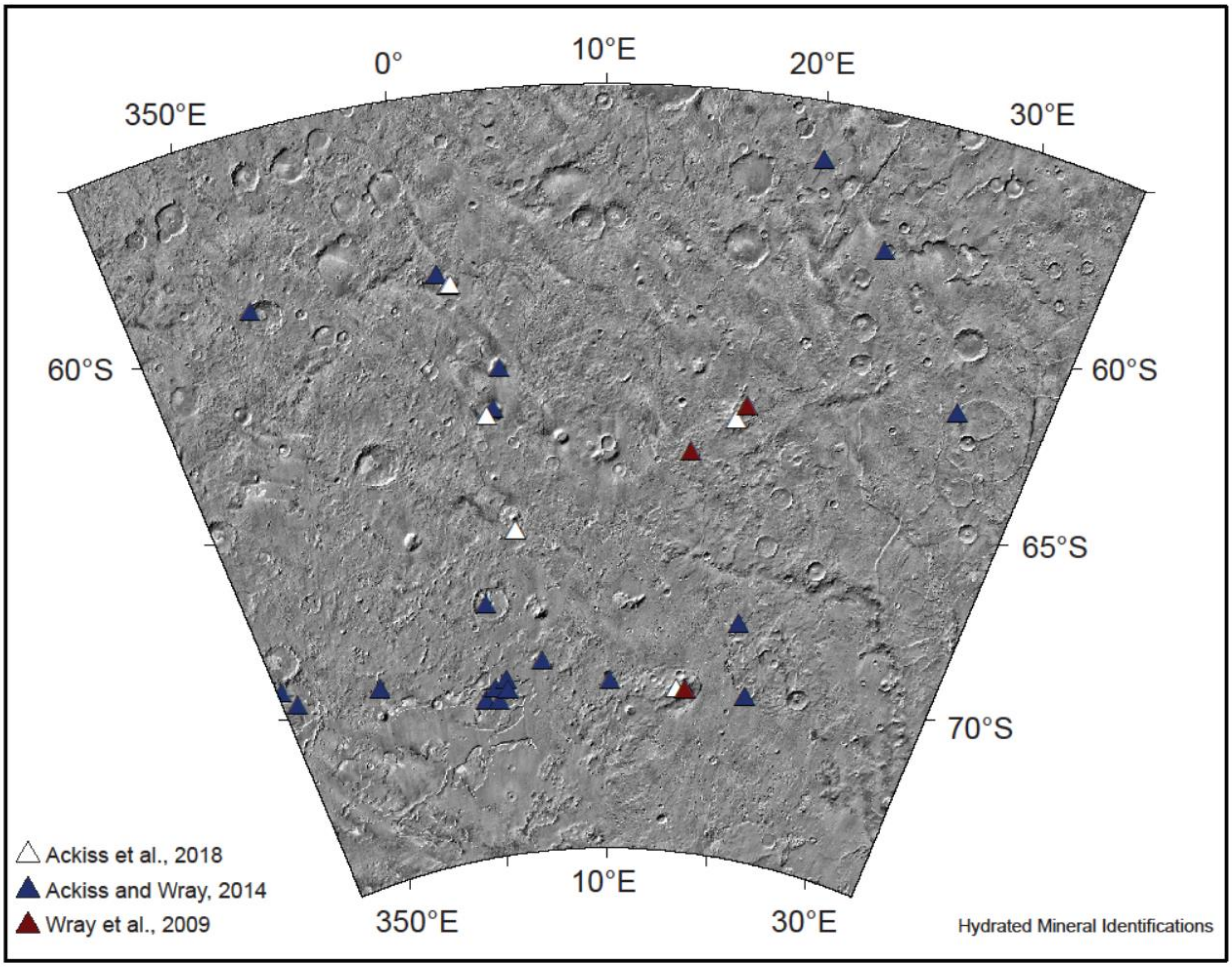

Figure 19. Map of hydrated mineral occurences within the Sisyphi Planum. Observations from Wray et al., [2009] (red), Ackiss and Wray [2014] (blue), and Ackiss et al., [2018] (white) are shown.

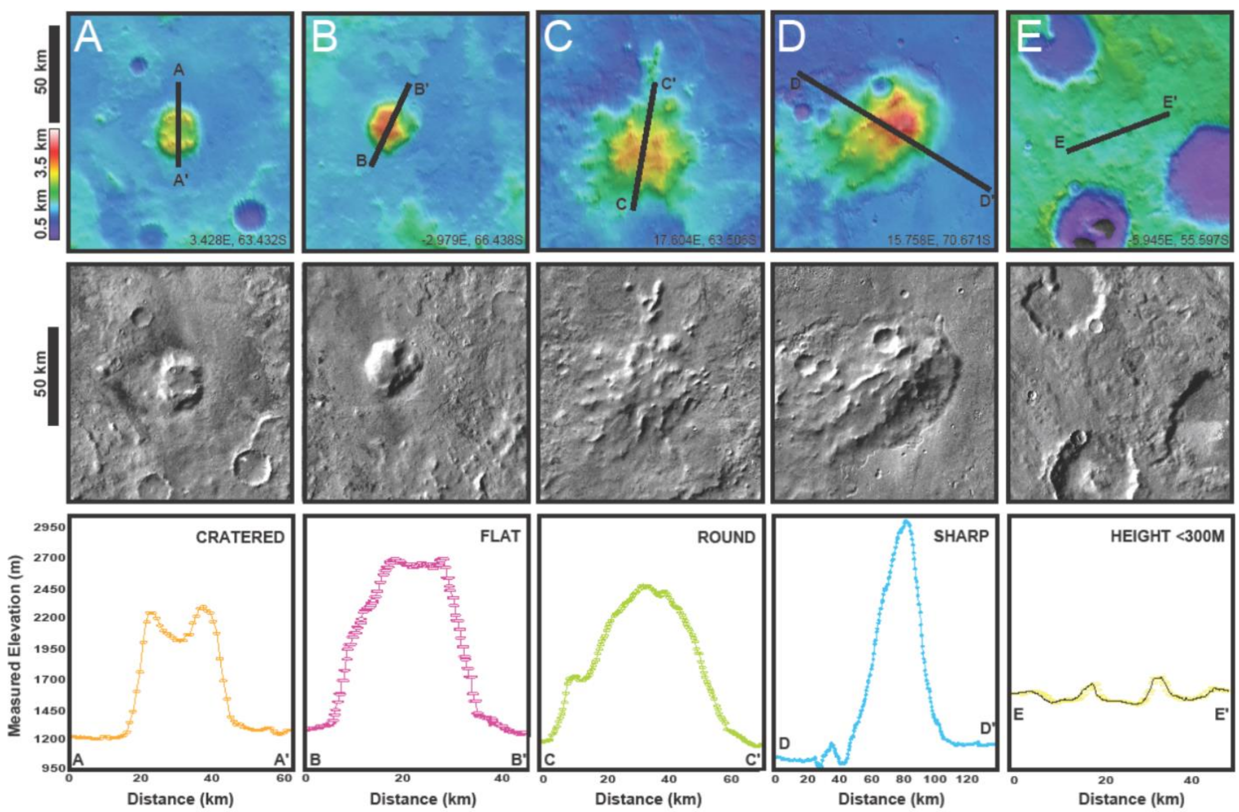

Figure 20. Type locations for the edifice top classifications. Top panel shows MOLA elevation from 0.5 km (blue) to 3.5 km (red), middle panel shows morphology in THEMIS daytime thermal infrared, and bottom panel shows the elevation profile. Scale bar is 50 km in top and middle panel. Here the five classifications are shown as (a) cratered peaks, (b) flat tops, (c) rounded peaks, (d) sharp peaks, and (e) edifices with heights less than 300 meters.

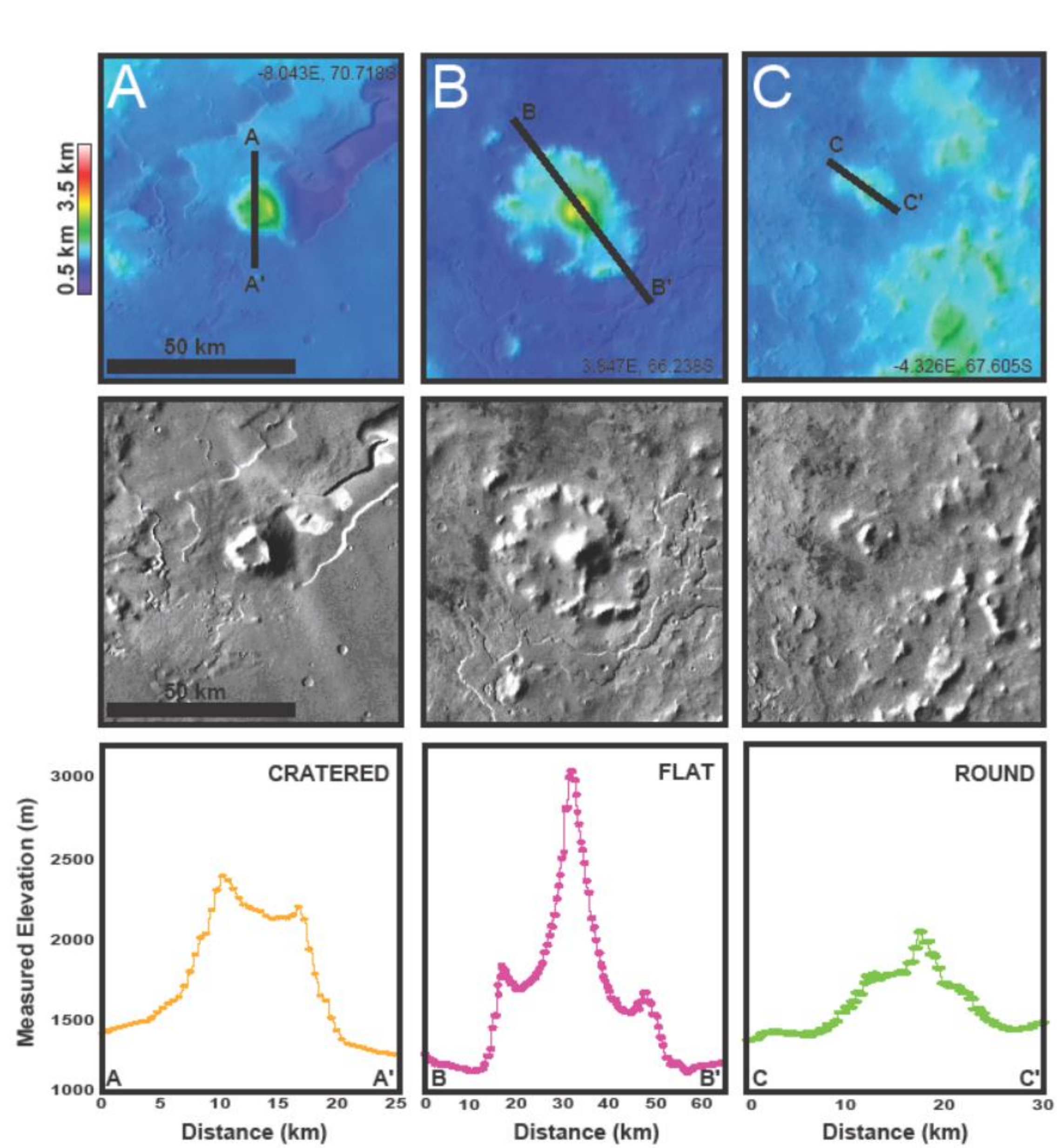

Figure 21. Examples of atypical edifices. Top panel shows MOLA elevation from 0.5 km (blue) to 3.5 km (red), middle panel shows morphology in THEMIS daytime thermal infrared, and bottom panel shows the elevation profile. Scale bar is 50 km in top and middle panel. Here we show a cratered peak with uneven edges (a), a flat topped edifice with a peak (b), and a rounded edifice with a peak (c).

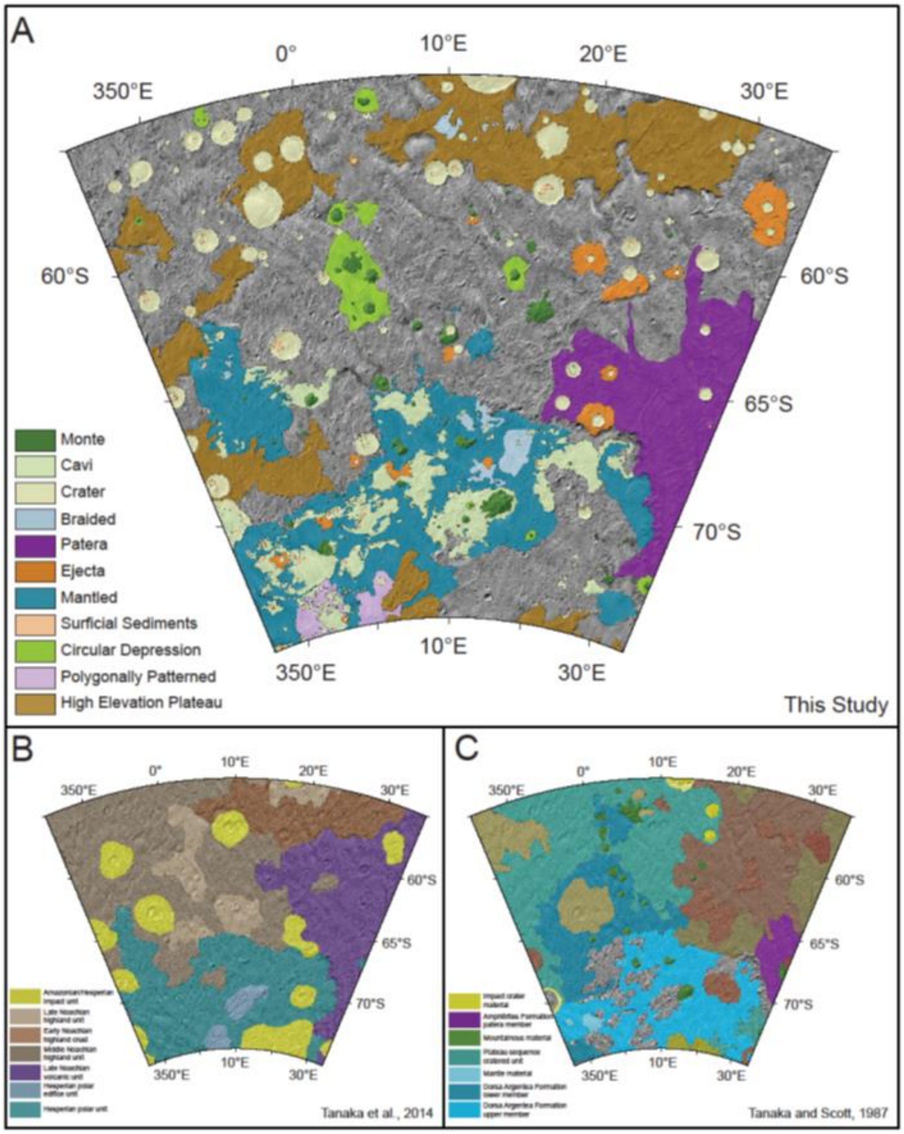

Figure 22. Maps of the Sisyphi Planum region. Colors from the maps were changed from previous digital maps [Tanaka et al., 2014; Tanaka and Scott, 1987] for easier comparison between units. (a) Geomorphologic map from this study where the twelve mapped units are labeled. THEMIS daytime thermal infrared basemap. Regions with no coloring were not mapped. (b) Tanaka et al., [2014] global map with relevant units labeled. Only the Sisyphi Planum region is shown for comparison. (c) Tanaka and Scott [1987] south polar map with relevant units labeled. “Undivided” terrain was removed from the map for comparisons with our unmapped/undivided regions. Only the Sisyphi Planum region is shown for comparison.

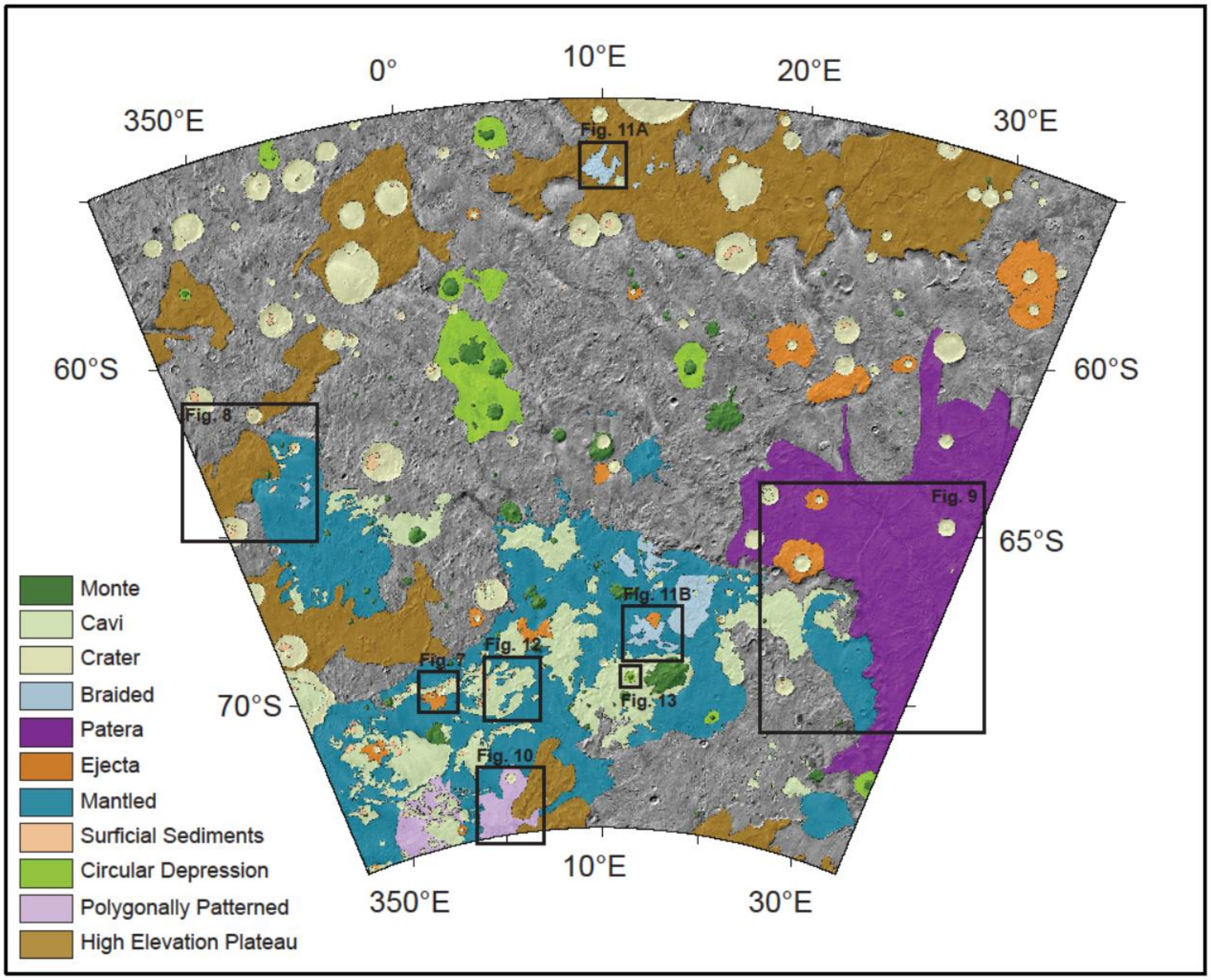

Figure 23. Geomorphologic map produced from this study. Insets show where later figures are located.

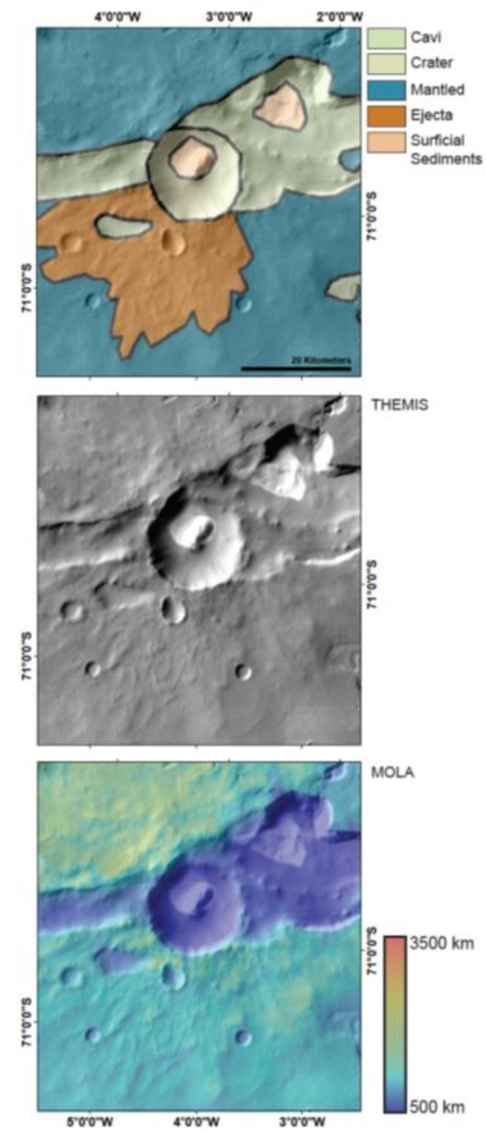

Figure 24. Crater and Ejecta Units type location. (top panel) Region of map produced in this study. THEMIS daytime thermal infrared basemap. (middle panel) THEMIS daytime thermal infrared. (bottom panel) MOLA topography overlying THEMIS daytime thermal infrared.

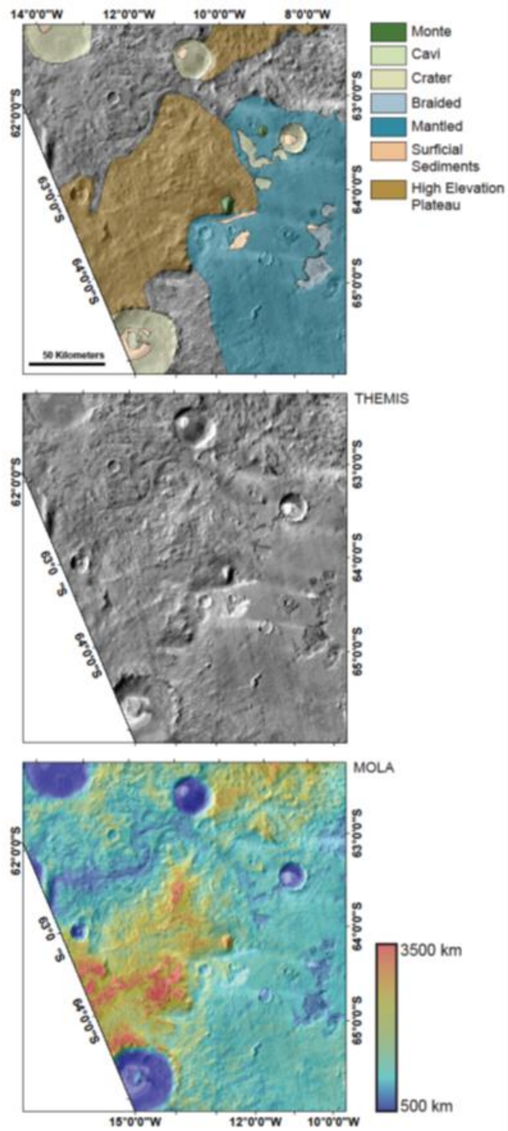

Figure 25. High Elevation Plateau Unit type location. (top panel) Region of map produced in this study. THEMIS daytime thermal infrared basemap. (middle panel) THEMIS daytime thermal infrared. (bottom panel) MOLA topography overlying THEMIS daytime thermal infrared.

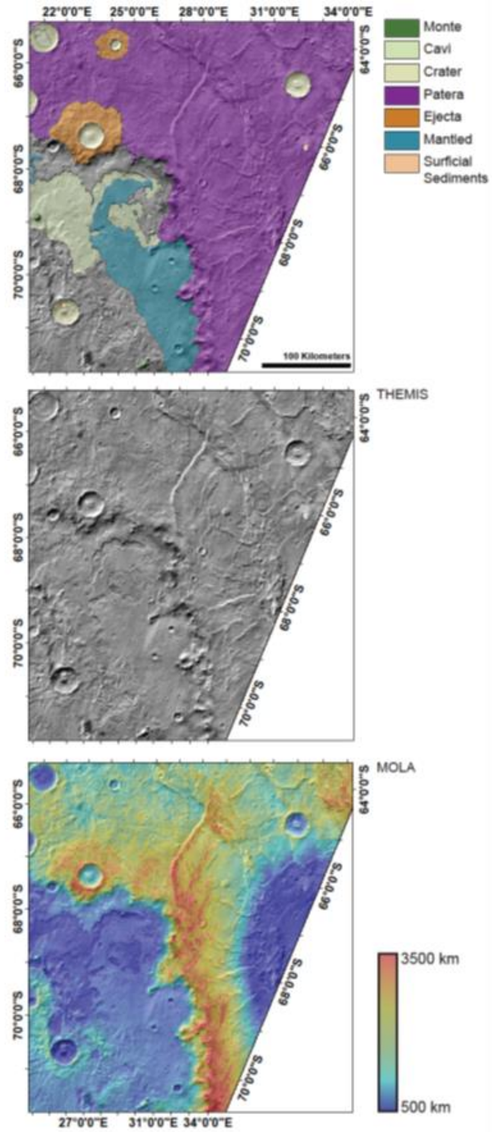

Figure 26. Patera Unit type location. (top panel) Region of map produced in this study. THEMIS daytime thermal infrared basemap. (middle panel) THEMIS daytime thermal infrared. (bottom panel) MOLA topography overlying THEMIS daytime thermal infrared.

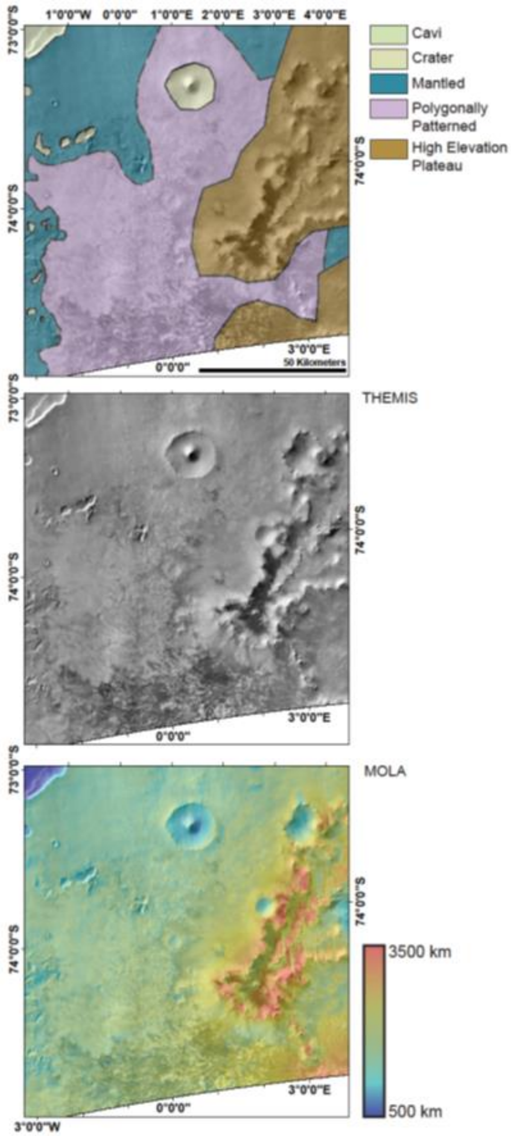

Figure 27. Polygonal Patterned Unit type location. (top panel) Region of map produced in this study. THEMIS daytime thermal infrared basemap. (middle panel) THEMIS daytime thermal infrared. (bottom panel) MOLA topography overlying THEMIS daytime thermal infrared.

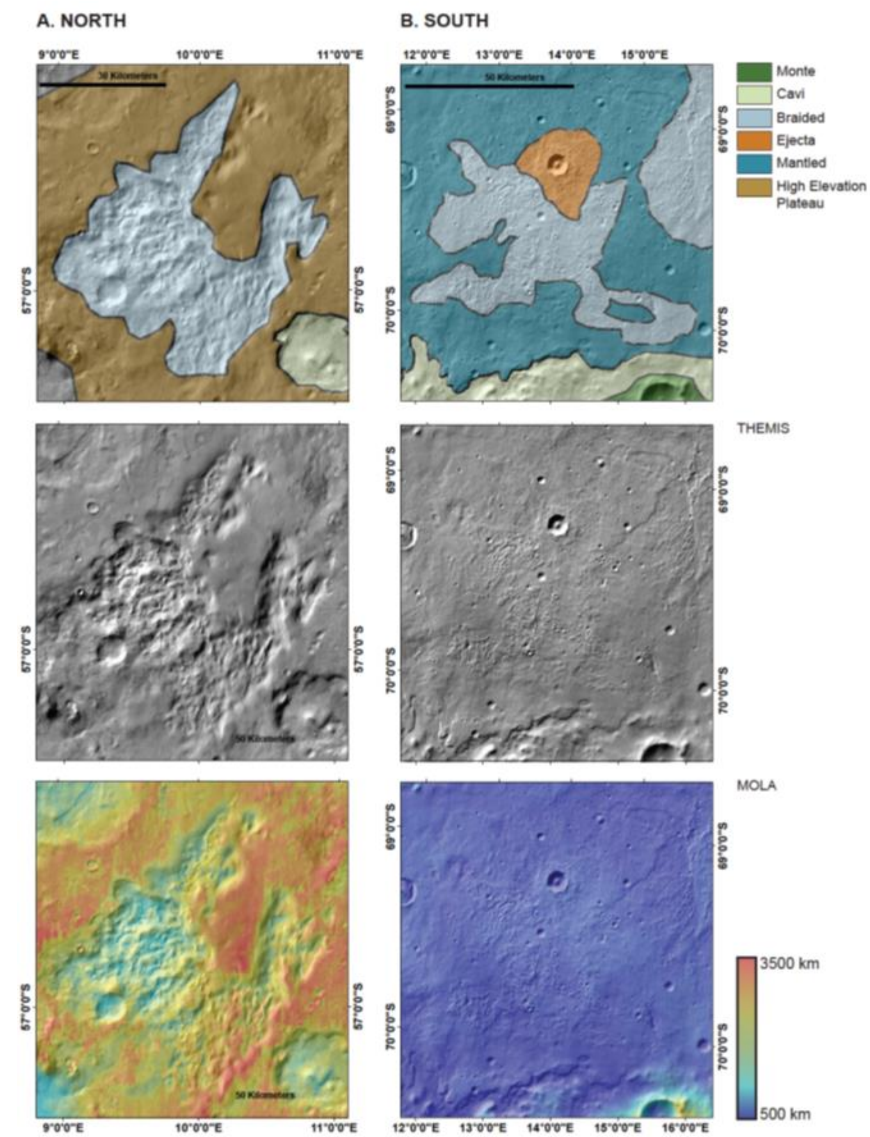

Figure 28. Braided Unit type location showing occurrences in the north (a) and south (b). (top panel) Region of map produced in this study. THEMIS daytime thermal infrared basemap. (middle panel) THEMIS daytime thermal infrared. (bottom panel) MOLA topography overlying THEMIS daytime thermal infrared.

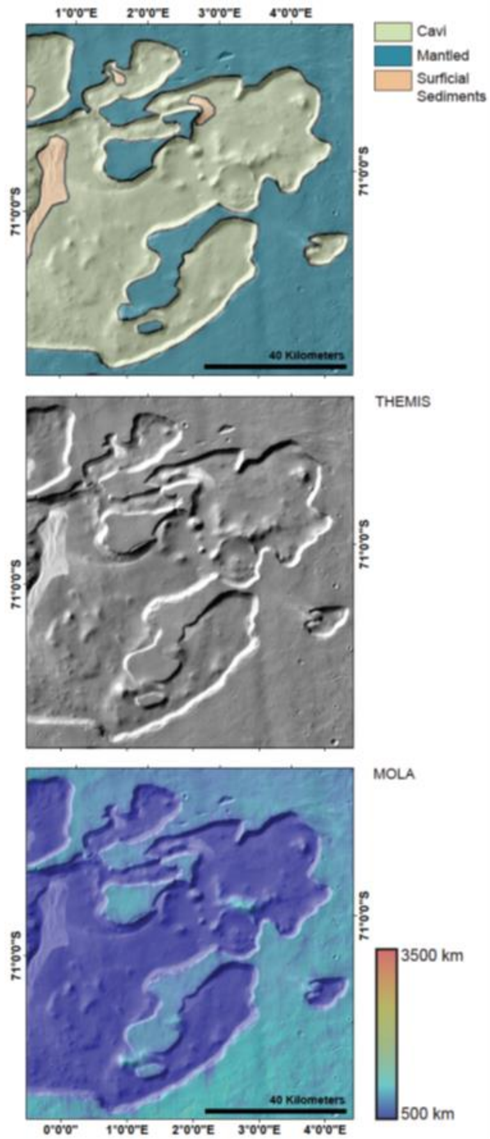

Figure 29. Mantled, Cavi, and Surficial Sediment Units type location. (top panel) Region of map produced in this study. THEMIS daytime thermal infrared basemap. (middle panel) THEMIS daytime thermal infrared. (bottom panel) MOLA topography overlying THEMIS daytime thermal infrared.

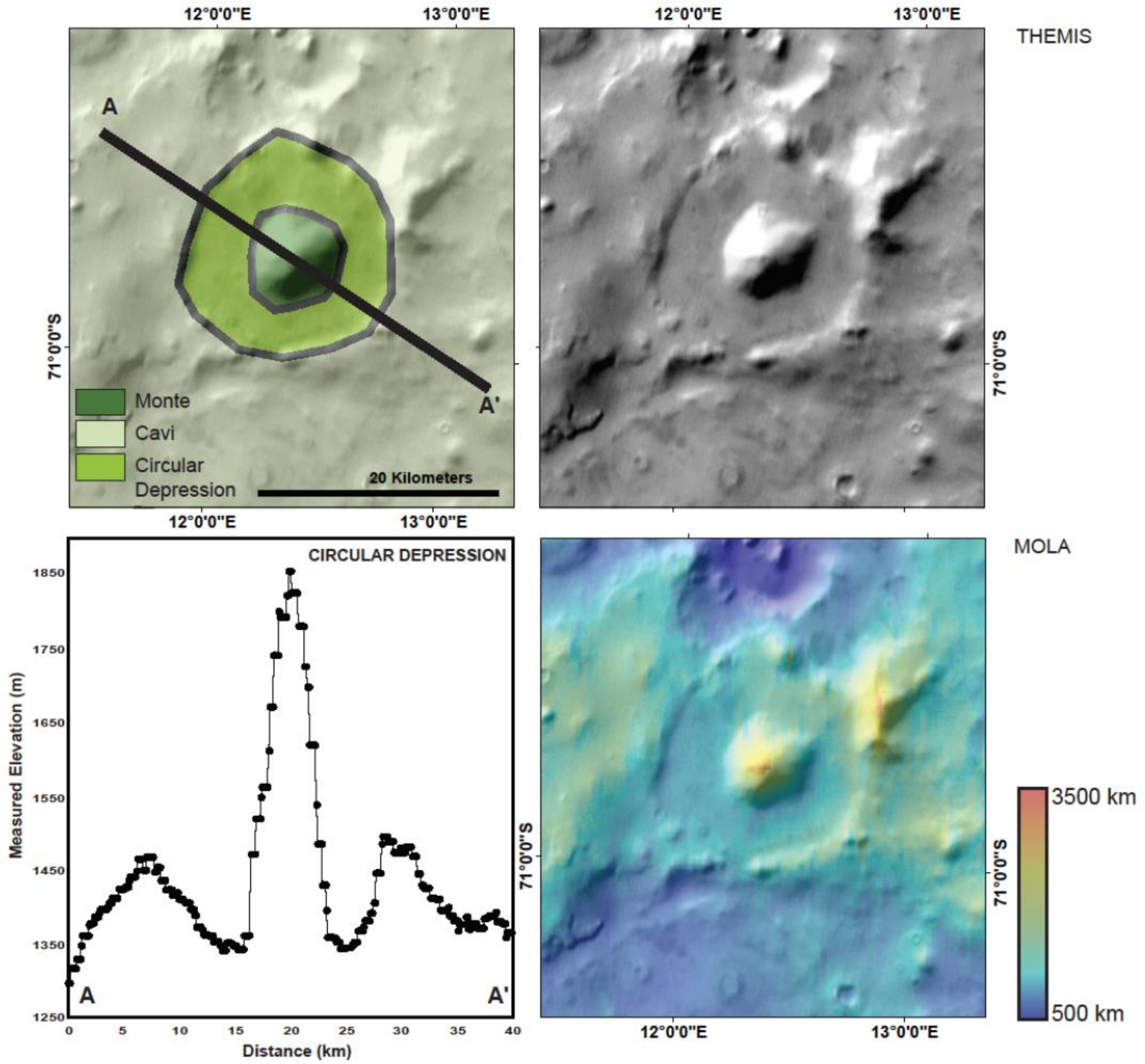

Figure 30. Circular Depression Unit type location. (top left) Region of map produced in this study. THEMIS daytime thermal infrared basemap. (top right) THEMIS daytime thermal infrared. (bottom left) Profile of the circular depression shown. (bottom right) MOLA topography overlying THEMIS daytime thermal infrared.

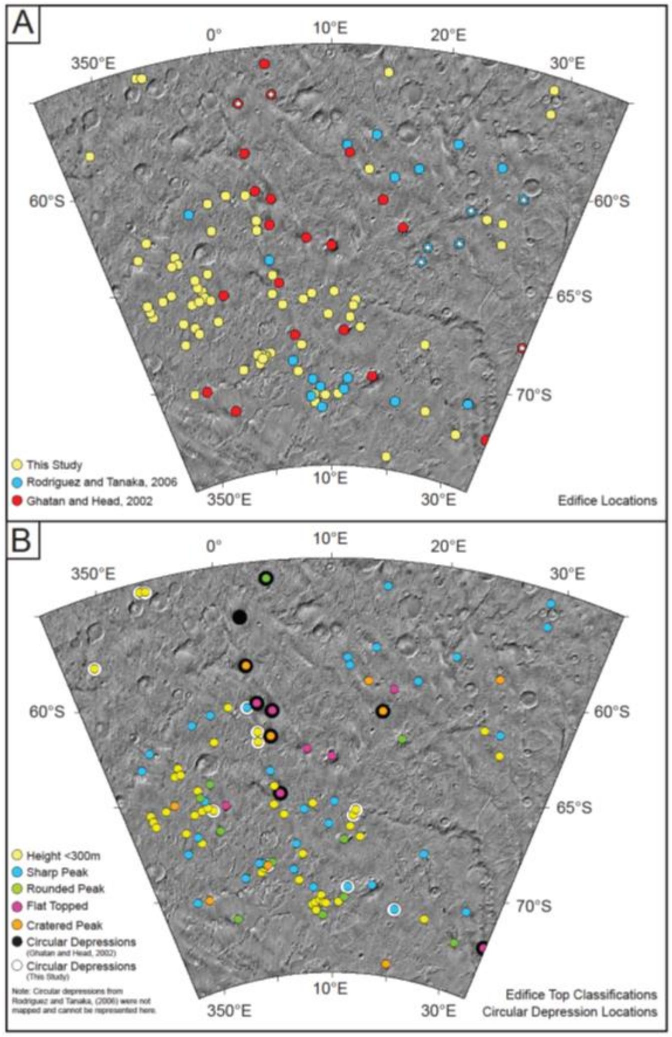

Figure 31. Locations of the edifices mapped within the Sisyphi Planum. THEMIS daytime thermal infrared basemap. (a) Edifices mapped in this study are shown in yellow dots. Edifices mapped in Ghatan and Head [2002] are shown in red dots. Edifices mapped in Rodriguez and Tanaka [2006] are shown in blue dots. Dots with white stars show edifices from previous studies that were removed (e.g. we do not agree that these are edifices). (b) Locations of the edifices surrounded by the Circular Depression Unit and top shape classification. Circular Depressions mapped in this study are shown in white dots while those mapped in Ghatan and Head [2002] are shown in black dots. Moat-like features from Rodriguez and Tanaka [2006] were not mapped and thus are not represented on this chart. Each colored dot is an edifice that was included and classified in this study. Yellow dots are edifices that have a height less than 300 meters. Blue dots are edifices that have sharp peaks. Green dots are edifices that have rounded peaks. Pink dots are edifices that have flat tops. Orange dots are edifices that have cratered peaks.

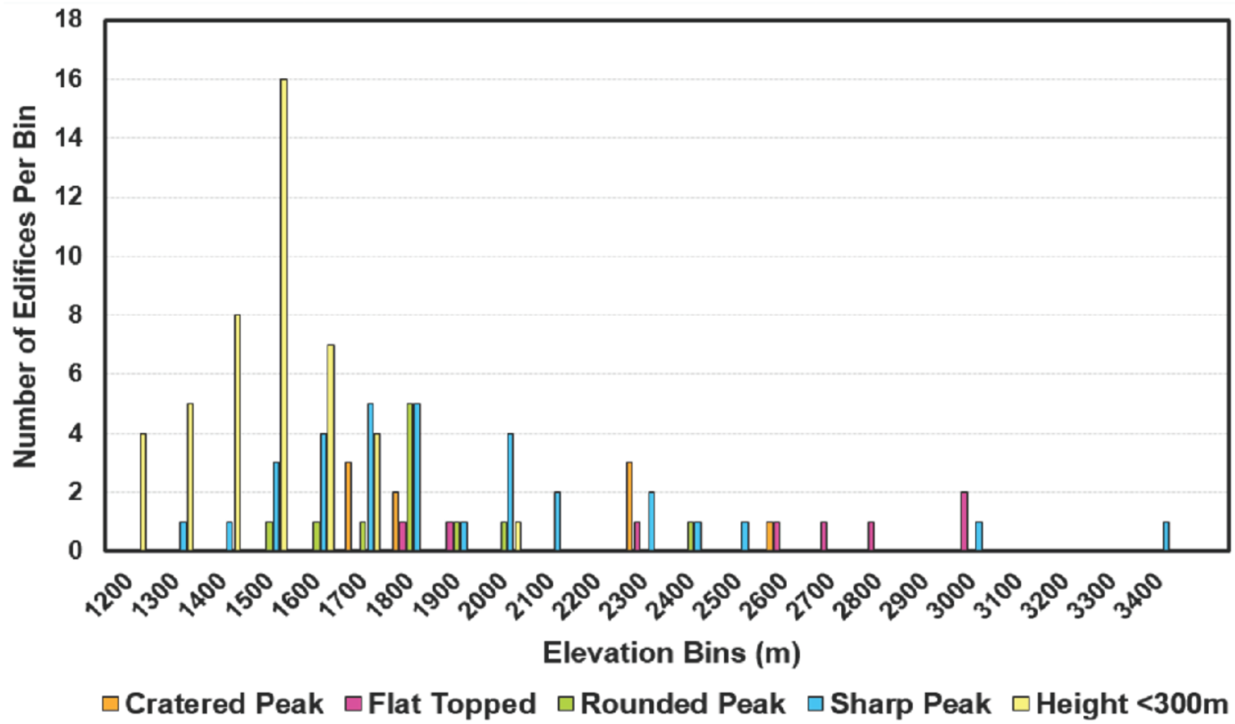

Figure 32. Histogram of edifices classified by top structure and elevation. X-axis is elevation in bins of 100 meters, y-axis is the number of edifices per bin. Edifices of all classifications are shown (heights less than 300 meters in yellow, sharp peaks in blue, rounded peaks in green, flat topped peaks in pink, and cratered peaks in orange).

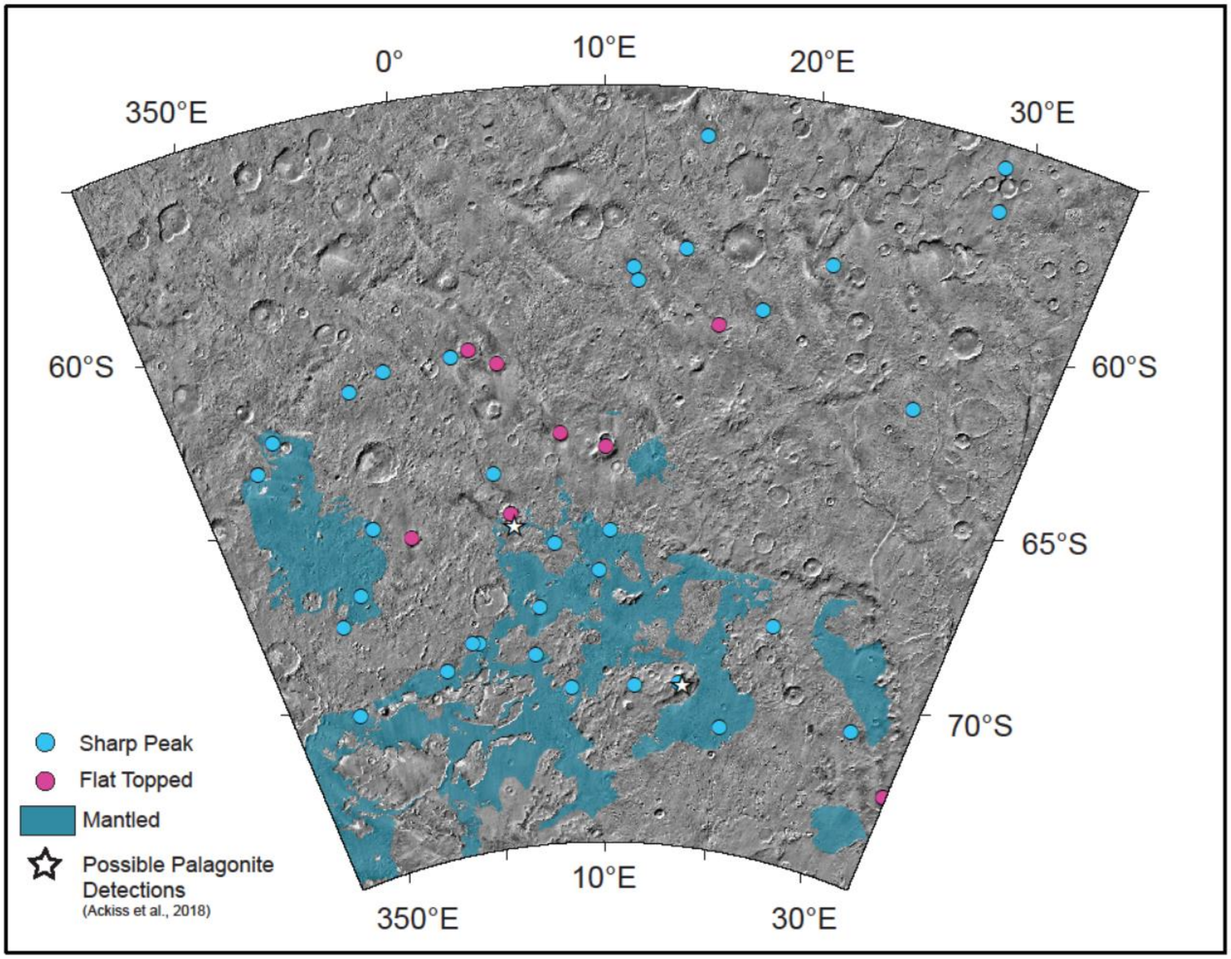

Figure 33. Overview of ice and monte relationship. Mapped Mantled Unit, sharp peaks, flat topped, and locations of possible palagonite showing the relationship between the DAF and the edifices.

4.10 Supplemental Tables

Table 11. Sisyphi Planum edifices classified by their peaks

Longitude	Latitude	Top Classification	Elevation (m)	Approximate Height (m)	Notes
1.06539	-69.6351	Crater	1714	325	Uneven crater edges
3.37733	-63.4426	Crater	2312	1000	
1.70917	-59.9143	Crater	2697	1200	
13.67779	-60.88	Crater	1885	500	Uneven crater edges
15.31078	-62.2915	Crater	2372	1250	
26.33504	-59.8373	Crater	1780	375	Uneven crater edges
351.942	-70.7205	Crater	2383	800	Uneven crater edges
19.58894	-74.4052	Crater	1785	325	Uneven crater edges
351.0995	-65.8517	Crater	1883	425	Uneven crater edges
2.27294	-61.7711	Flat Peak	1972	775	
3.79611	-62.2082	Flat Peak	2812	1500	Flat with peak; low region at elevation 2282m
34.69576	-72.3954	Flat Peak	2355	1000	
3.77962	-66.2421	Flat Peak	3034	1800	Flat with peak; low region at elevation 1834m
7.24442	-64.1781	Flat Peak	2769	1600	
10	-64.5469	Flat Peak	3049	1900	
357.0568	-66.4538	Flat Peak	2695	1400	
16.2616	-61.1697	Flat Peak	1841	700	Flat with peak; low region at elevation 1714m

Table 11 continued

Longitude	Latitude	Top Classification	Elevation (m)	Approximate Height (m)	Notes
4.37719	-55.8108	Rounded Peak	1864	600	
8.57281	-72.2452	Rounded Peak	1671	325	
11.63124	-68.6023	Rounded Peak	2038	1200	
11.85979	-71.386	Rounded Peak	1931	700	
17.65898	-63.5338	Rounded Peak	2460	1250	
29.92604	-72.6531	Rounded Peak	1832	500	
354.2587	-65.8232	Rounded Peak	1708	375	
355.3576	-71.93	Rounded Peak	1853	700	
355.7521	-67.6163	Rounded Peak	1892	600	Rounded with peak
355.7631	-65.2856	Rounded Peak	1851	450	
1.75691	-69.5134	Rounded Peak	1582	350	
4.64547	-69.9794	Sharp Peak	2007	575	
11.52092	-59.7724	Sharp Peak	2377	1150	
11.75706	-60.129	Sharp Peak	2102	900	
14.21801	-59.2359	Sharp Peak	2035	450	
18.53717	-60.6603	Sharp Peak	1623	400	
350.9703	-68.3059	Sharp Peak	2066	400	
1.24869	-61.9233	Sharp Peak	1801	450	
12.3528	-70.8649	Sharp Peak	1854	425	
19.61845	-71.7613	Sharp Peak	1676	475	
0.42755	-69.5323	Sharp Peak	1693	350	
2.91942	-65.1292	Sharp Peak	2455	1150	
5.2208	-68.7649	Sharp Peak	3410	2400	
6.55317	-67.0898	Sharp Peak	1507	375	
7.28997	-70.9112	Sharp Peak	1594	325	
9.57961	-67.8257	Sharp Peak	1486	375	

Table 11 continued

Longitude	**Latitude**	**Top Classification**	**Elevation (m)**	**Approximate Height (m)**	**Notes**
10.31451	-66.7536	Sharp Peak	1398	325	
14.85788	-56.2367	Sharp Peak	2144	550	
15.85593	-70.7199	Sharp Peak	3008	1900	
21.82656	-59.2029	Sharp Peak	1685	325	
22.41365	-68.8894	Sharp Peak	1584	425	
27.84246	-62.4169	Sharp Peak	1482	325	
28.85939	-55.6176	Sharp Peak	2518	675	
29.17313	-56.7634	Sharp Peak	2055	325	
30.27992	-71.0754	Sharp Peak	1712	475	
348.774	-63.761	Sharp Peak	2383	850	
350.1665	-70.6792	Sharp Peak	1773	375	
350.1837	-63.0993	Sharp Peak	1700	325	
352.7749	-67.6451	Sharp Peak	1813	450	
354.6921	-66.0344	Sharp Peak	1741	325	
355.2422	-62.3248	Sharp Peak	1833	375	
357.3631	-62.0136	Sharp Peak	1834	400	
357.6841	-70.111	Sharp Peak	1963	500	
359.938	-69.5063	Sharp Peak	1739	425	
1.95322	-63.6499	Height < 300m	1590	200	
2.03006	-63.174	Height < 300m	1633	250	
12.70306	-67.4083	Height < 300m	1241	220	
12.97438	-67.1418	Height < 300m	1277	220	
347.7782	-58.3057	Height < 300m	2086	110	
353.5883	-55.4603	Height < 300m	1667	160	
354.0624	-55.5112	Height < 300m	1724	150	
355.4488	-66.5615	Height < 300m	1488	140	

Table 11 continued

Longitude	Latitude	Top Classification	Elevation (m)	Approximate Height (m)	Notes
0.07629	-69.9524	Height < 300m	1616	225	
0.57753	-69.7334	Height < 300m	1654	210	
0.83391	-69.6001	Height < 300m	1591	175	
2.85571	-66.7374	Height < 300m	1516	300	
3.12966	-65.8535	Height < 300m	1540	275	
3.97172	-67.2838	Height < 300m	1361	120	
5.25536	-70.5009	Height < 300m	1485	230	
5.99244	-69.2533	Height < 300m	1503	250	
6.98818	-71.7124	Height < 300m	1553	260	
7.43052	-71.6237	Height < 300m	1490	180	
7.5625	-72.0093	Height < 300m	1587	225	
7.63328	-66.8348	Height < 300m	1261	170	
8.17751	-71.5075	Height < 300m	1596	200	
8.38767	-71.2905	Height < 300m	1531	250	
8.71263	-71.6366	Height < 300m	1625	300	
9.09117	-71.6728	Height < 300m	1360	90	
10.98249	-71.6109	Height < 300m	1567	275	
12.36062	-67.9528	Height < 300m	1340	275	
13.72136	-68.422	Height < 300m	1233	120	
24.42842	-71.9652	Height < 300m	1510	250	
26.151	-62.4122	Height < 300m	1449	250	
28.35694	-63.3978	Height < 300m	1382	200	
348.0247	-65.9711	Height < 300m	1570	200	
348.1177	-66.2775	Height < 300m	1648	125	
348.2096	-66.5751	Height < 300m	1526	110	
349.9408	-65.9938	Height < 300m	1553	260	

Table 11 continued

Longitude	**Latitude**	**Top Classification**	**Elevation (m)**	**Approximate Height (m)**	**Notes**
351.4959	-67.3016	Height < 300m	1722	275	
352.0824	-64.5233	Height < 300m	1475	110	
352.6988	-64.1507	Height < 300m	1473	100	
352.7715	-64.5149	Height < 300m	1552	190	
353.0774	-67.9665	Height < 300m	1694	140	
353.0996	-66.551	Height < 300m	1475	120	
354.0915	-66.4742	Height < 300m	1427	70	
354.1897	-65.4403	Height < 300m	1535	180	
354.8348	-66.3649	Height < 300m	1356	85	
357.1903	-63.3194	Height < 300m	1749	275	
359.295	-61.8027	Height < 300m	1732	250	

CHAPTER 5. CONCLUSION

The work in this dissertation has strived to answer the questions: 1) Is the mineralogy of the Sisyphi Montes region consistent with a subaerial, submarine, or subglacial origin?; 2) Can the spectral variability of Icelandic palagonites be used to constrain the identification of palagonite on the martian surface?; 3) What formation environments are the features surrounding the Sisyphi Montes edifices consistent with?; and 4) Are the volcanic morphologies and mineralogies of Noachian Mars consistent with volcanism on a "snowball Mars"?

By studying the Sisyphi Planum region of Mars as well as palagonite outcrops in Iceland, we are able to add scientific insight to the history of Mars and to propose possible answers to the above questions. Significant outcomes of this thesis include:

1) The first direct identification of possible palagonite on Mars from orbital spectral data in the Sisyphi Montes. This indicates water-magma interactions in the past at these sites, based on the spectral identification of an assemblage of smectites, zeolites, and iron oxides as shown in Chapter 2.
2) The identification of glaciovolcanic hydrothermal systems, as seen in Chapters 2-4, has significant implications for the long-term habitability of Mars. Locations of ice-magma interactions are present from the Noachian through the Amazonian, suggesting that these habitable surface environments spanned much of Mars' history and may have provided a refuge when much of the surface became uninhabitable due to atmospheric loss.
3) Both the composition and crystallinity of glacio- and hydrovolcanically sourced palagonites differ, and these differences can be detected with Mars-relevant in situ and orbital instruments, as shown in Chapter 3.
4) Edifice height and location of the Sisyphi Montes provide regional information about the history of ice sheets in the region and the origin of the Dorsa Argentea Formation, as well as surrounding volcanic features such as Pityusa Paterae, as shown in Chapter 4.

5.1 Future Work

While the major questions regarding the surface history of the Sisyphi Planum region of Mars have been mostly addressed by this body of work, there is always more to do. In particular, it would be useful to make detailed geologic maps of each edifice itself to investigate the volcanic properties of the structures, including layering and possible flows within/near the edifices. A larger spectroscopic study of the entire region using visible and near-infrared multispectral mapping strips would also provide more information about the volcanic history and ice-magma interactions in the region; however, there are still processing procedures that need to be developed to proceed with that work.

The small field/laboratory study within this thesis (Chapter 2) conducted in Iceland can also be expanded to answer larger overarching questions with applications to fundamental geological principles, such as: How does palagonite change with parent magma composition? And, How does the properties of palagonite change with local environmental conditions? While many studies of palagonite have been conducted, few have succeeded in fully classifying the range of composition and crystallinity of the rock across a range of eruption environments. Iceland experiences hotspot volcanism and is also situated between a major spreading center. Because of this, Iceland experiences a chemical range of lavas including basalt, andesite, and rhyolite. Palagonite is created exclusively by altering basaltic glass; however, studying all three compositions in Iceland can help to constrain the formation mechanism and percentage of basaltic glass needed for production. In addition, palagonite forms in both sub-aerial and subglacial environments, and here we suggest that these may result in distinct compositions that could be used to tease apart these paleoenvironments on Mars. However, this hypothesis needs to be tested with additional samples from a broader variety of sites, both subglacial in Iceland and subaqueous in lakes and oceans in more temperate climates. Measurements of palagonite including visible and near-infrared (VNIR), thermal infrared (TIR), X-ray powder diffraction (XRD), X-ray fluorescence (XRF), microprobe, thin section, and inductively coupled plasma mass spectrometry (ICP-MS) can be used to characterize the composition of palagonite as well as the degree of palagonitization. Traditional terrestrial techniques can be related to observations from spectral analysis in order to better understand how classic terrestrial methods are related to Mars remote sensing data. These relationships can be used to create a database of palagonite characteristics, which can be used to study and identify the degree of palagonitization on Earth and Mars. The results of this proposed future work are likely to reveal that there is a compositional difference between palagonites formed in different parent materials and eruption environments which can be uniquely identified.

Additionally, the techniques used in this body of work have inspired other volcanology-centered martian analog projects that are not subglacial but instead subaerial. In particular, the same techniques that I used in my PhD thesis can be used to answer the question: What is the relationship between lava flows, soils, and trace gases that drive both biotic and abiotic methanogenesis on Earth and possibly Mars? The Craters of The Moon National Monument and Preserve (COTM) is located in southern Idaho in a depression once created by the movement of the North American plate over the Yellowstone hotspot. Initially the region experienced rhyolitic eruptions; however, subsequent eruptions have been primarily basaltic. This region is a prime martian analog because 1) the lavas are Fe-rich in comparison to other Martian basalt analogs and 2) the region experiences seasonal deposition of evaporites. Secondary soils in this region have been extensively mapped and characterized. Primary basaltic flow maps of the region have been created; however, mineralogic and petrographic characteristics of each flow have not been studied in detail. Ideally this would be a two-part project where a team of field geologists sample and subsequently map the characteristics of each flow using VNIR, TIR, XRD, XRF, EGA (evolved gas analysis), and ICP-MS. This would create a robust database of the parent flows which could be linked to the daughter soil profiles. The second portion of the project would be led by an expert biogeochemist who would sample the soils, knowing their exact parent compositions, and link the soils to methanogenesis through trace gas studies. The results of this proposed future work are likely to reveal important information on the role of chemistry from soils influenced by basaltic inputs.

VITA

Dept. of Earth, Atmospheric, and Planetary Sciences
550 Stadium Mall Drive
West Lafayette, IN 47907

Purdue University
HAMP 2263
sackiss@purdue.edu

Education:

- Ph.D. Candidate in Earth, Atmospheric, and Planetary Sciences, Purdue University, 2019
- Non-degree (Geology), George Washington University, 2013
- B.S., Applied Mathematics, Georgia Institute of Technology, 2012

Research-based Employment:

- Postdoctoral Research Associate, University of Idaho, 2019-2022
  -*Investigating micro crystallinity of volcanic products with Professor Erika Rader*
- Graduate Research Assistant, Purdue University, 2014-2019
  -*Studying the mineralogy and morphology of subglacial eruptions on Earth and Mars with Professor Briony Horgan*
- Postgraduate Research Assistant, Johns Hopkins University/Applied Physics Lab, 2013-2014
  -*Sponsored by the Oak Ridge Institute for Science and Education (ORISE)*
  -*Compact Reconnaissance Imaging Spectrometer for Mars (CRISM) Featured Images production and website renovation with Dr. Scott Murchie*
  -*Mineralogic mapping of Huygens crater, Mars with Dr. Kim Seelos*
  -*Geologic mapping of the Caloris basin, Mercury with Dr. Debra Buczkowski*
- Undergraduate Research Assistant, Georgia Institute of Technology, 2011-2012
  -*Mapping the southern high latitudes of Mars through aqueous mineralogy and stratigraphy with Professor James Wray*

- Undergraduate Student Research Program, NASA Goddard Space Flight Center, 2011
  -Electromagnetic modeling and testing of millimeter-wave detectors for land-based astrophysics with Dr. David Chuss

Teaching/Mentoring Experience:

- Purdue University Gifted Education Resource Institute (GERI), 2017-2018
  -Experiments in Fluids, Course Instructor, Summer 2018
  -STEAM (Science, Technology, Engineering, Art, and Math) Machine Labs, Course Assistant, Summer 2017
  -Experiments in Fluids, Course Assistant, Summer 2017
- Research Mentor for Undergraduates, 2015-2018
  -Mr. Aaron Campbell, B.S. Planetary Science, 2018 (Mentored from Summer 2015-Spring 2016)
  -Ms. Marley Suda, B.S. Planetary Science, 2020 (Mentored from Fall 2017-Fall 2018)
- Purdue University Earth, Atmospheric, and Planetary Sciences Department teaching and course development, 2015-2018
  -Developed and Instructed EAPS 39100: "Applying to Graduate School", Fall 2015, 2016, 2017 (Online)
  -Instructor, EAPS 106: "Geosciences in the Cinema", Summer 2017, 2018
  -Teaching Assistant, EAPS 106: "Geosciences in the Cinema", Spring 2017
  -Guest Lecturer, EAPS 10500: "The Planets", Fall 2016
  -Developed and Instructed EAPS 59100: "Volcanology", Spring 2016
  -Guest Lecturer, EAPS 39100: "Astrobiology", Fall 2015
- Mars Exploration Student Data Teams (MESDT), Mentor, 2013-2016
  - Recipient of the 2014 Johns Hopkins University/Applied Physics Laboratory STEMmy Award
- Graduate Teaching Fellows in K-12 Education (GK–12), Visiting Scientist and Co-Teacher, 2015
  -Recipient of the Purdue University Community Service/Service Learning Grant

- Tutor, Georgia Institute of Technology National Collegiate Athletic Association, 2010
  -*Calculus I, II, and Finite Mathematics*

Awards/Honors:

- Associate Fellow, Purdue Teaching Academy, inducted 2018
- Purdue Doctoral Fellow, 2017-2019
- Indiana Space Grant Consortium Graduate Fellowship, 2017-2018
- NASA Earth and Space Science Fellow, 2014-2017
- Outstanding Presentation for the Purdue University Department of Earth, Atmospheric, and Planetary Science Student Research EXPO, 2016
- Donald W. Levandowski Memorial Scholarship in Geology, 2015
- 3rd Place, Student Poster Competition, Astrobiology Science Conference, 2012
- NASA Headquarters Student Ambassador, Cohort IV, 2012
- National Science Foundation (NSF) Mentoring Through Critical Transition Points in the Mathematical Sciences (MTCP) Scholarship, 2012
- Georgia Helping Outstanding Pupils Educationally (HOPE) Scholarship, 2009-2011

NASA Mission/Panel Experience:

- NASA Review Panel, Executive Secretary, September 2017
- NASA Review Panel, Executive Secretary, February 2017
- Mars 2020 rover Mastcam-Z instrument, Science Team Collaborator, 2015-2018
- Mars Science Laboratory (MSL) Curiosity Rover, Science Team Collaborator, 2015-2016
- Mars Reconnaissance Orbiter (MRO) Compact Reconnaissance Imaging Spectrometer for Mars (CRISM), Science Team Member, 2013-present

Invited Talks:

3. Igneous Processes and the Influence of Tectonics Seminar, Montana State University (10/2018)

2. CRISM Science Team Meeting, Johns Hopkins University Applied Physics Lab (11/2015)
1. MESSENGER 32nd Science Team Meeting, Johns Hopkins University Applied Physics Lab (5/2014)

Laboratory Skills:

- Visible and Near-Infrared Spectroscopy (VNIR), Advanced
- Thermal Infrared Spectroscopy (TIR), Intermediate
- X-ray Powder Diffraction (XRD), Novice

Field Experience:

- Antarctic Search for Meteorites (ANSMET), Field Party Volunteer, 2018-2019 Field Season
- Studying the interaction between volcanism and glaciation in the north, west, and southern regions of Iceland, The Sixth International Conference on Mars Polar Science and Exploration Pre-, Mid-, and Post-Conference Field Trips, 2016
- Investigating mineral coatings on volcanic rocks recently exposed by retreating glaciers at the Three Sisters, Oregon, USA, Field Assistant, 2016
- Investigating the mineralogy of Hogg Rock and Hayrick Butte subglacial volcanoes in central Oregon, USA, Lead researcher, 2016
- Volcanology Field Camp in the Andes and Galapagos Islands, Ecuador, GEOL 512: "Science/Engineering Field Applications," South Dakota School of Mines and Technology, 2016
- Geomorphic mapping of paleoglaciologic landforms in Dalarna, Sweden, EAPS 59100: "Glaciation in Sweden," Purdue University, 2015
- Geologic Mapping of the St. Francios Mountains, Johnson Shut-Ins State Park, Missouri, EAPS 3900: "Geologic Field Methods," Purdue University, 2015
- Studying the geomorphology of central peak impact craters, Kentland Crater, Indiana, EAPS 59100: "Impact Cratering," Purdue University, 2014

- Studying the geomorphology of sand dunes, Indiana Dunes State Park, Indiana, EAPS 55600: "Planetary Geology," Purdue University, 2014
- Mapping the mineralogy of Skyline Drive, Shenandoah National Park, Blue Ridge Mountains, Virginia, GEOL 2111: "Mineralogy," George Washington University, 2013
- Exploring Impact Rocks of the Sudbury Impact Structure, Sudbury, Ontario, Canada, Large Meteorite Impacts and Planetary Evolution V Pre-Conference Field Trip, 2013

Professional Affiliations:

- Member, Hoosier Association of Science Teachers Incorporated, 2015
- Member, Purdue University Graduate Women in Science Program (WISP), 2015
  -Department of Earth, Atmospheric, and Planetary Sciences Representative
- Member, Mineralogical Society of America, 2014-present
- Member, Purdue University Earth Atmospheric and Planetary Sciences Graduate Student Association (EAPS GSA), 2014-2018
  -President and Faculty Meeting Student Representative, 2015-2016
  -Treasurer and Graduate Admissions Committee Student Representative, 2014-2015
- Member, Geological Society of America, Planetary Geology Division, 2013-present
  -Diversity in the Geosciences Committee, Student Member-at-Large, 2018-2020
- Member, American Geophysical Union, Planetary Sciences & Earth and Planetary Surface Processes Sections, 2012-present

Refereed Publications:

4. **S. Ackiss**, B. Horgan, F. Seelos, W. Farrand, J. Wray, "Mineralogic Evidence for Subglacial Volcanism in the Sisyphi Montes Region of Mars", Icarus, ISSN 0019-1035, https://doi.org/10.1016/j.icarus.2018.03.026.
3. **S.E. Ackiss**, D.L. Buczkowski, C.M. Ernst, J.A. McBeck, K.D. Seelos, "Knob heights within circum-Caloris geologic units on Mercury: Interpretations of the geologic history of the region", Earth and Planetary Science Letters, Volume 430, 15 November 2015, Pages 542-550

2. **Sheridan E. Ackiss**, J.J. Wray (2014), "Occurrences of possible hydrated sulfates in the southern high latitudes of Mars", Icarus, Volume 243, Pages 311-324.
1. David T. Chuss, Edward J. Wollack, Giampaolo Pisano, **Sheridan Ackiss**, Kongpop U-Yen, Ming wah Ng (2012), "A Translational Polarization Rotator." Applied Optics, Vol. 51, Issue 28, Pages 6824-6830.

First Authored Abstracts and Presentations (* indicates student mentee):

19. **S. Ackiss**, B. Horgan, J. Gudnason, C. Haberle, and T. Thorsteinsson (2018). "The Mineralogic Variability of Icelandic Palagonites: An Analog Study for Mars." Lunar and Planetary Science Conference 49. Abstract 1773. (Talk)
18. **S. Ackiss**, B. Horgan, J. Gudnason, C. Haberle, and T. Thorsteinsson (2017). "The Mineralogic Variability of Icelandic Palagonites: An Analog Study for Mars." Geological Society of America Annual Meeting. Abstract 296-10. (Talk; Canceled due to Pneumonia)
17. **S. Ackiss**, B. Horgan, J. Gudnason, C. Haberle, T. Thorsteinsson, and T. Thordarson (2017). "The Mineralogic Variability of Icelandic Palagonites: An Analog Study for Mars." Lunar and Planetary Science Conference 48. Abstract 2500. (Poster)
16. **S. Ackiss**, B. Horgan, A. Campbell*, F. Seelos, W. Farrand, J. Wray (2016). "Mineralogic evidence for subglacial volcanoes in the Sisyphi Montes region of Mars." The Sixth International Conference on Mars Polar Science and Exploration. Abstract 6086. (Talk)
    -*Planetary Science Institute's Pierazzo International Student Travel Award*
15. **S. Ackiss**, A. Campbell*, B. Horgan, F. Seelos, J. Wray, J. Michalski (2016). "Mineralogic evidence for subglacial volcanoes in the Sisyphi Montes region of Mars." Lunar and Planetary Science Conference 47. Abstract 1305. (Talk)
    - *Purdue University Earth, Atmospheric, and Planetary Science Departmental Travel Grant*
    -*SETI Institute and NASA Astrobiology Institute Lunar and Planetary Science Conference Travel Funding*

14. **S. E. Ackiss**, J. J. Wray, K. D. Seelos, and P. B. Niles (2015). "Huygens crater: Insights into Noachian volcanism, stratigraphy, and aqueous processes." First Landing Site/Exploration Zone Workshop for Human Missions to the Surface of Mars. Abstract 1032. (Talk)
13. **S. E. Ackiss** and B. Horgan (2015). "Possible Sources of Sulfates in the Sisyphi Montes Region of Mars." Lunar and Planetary Science Conference 46. Abstract 2230. (Poster)
    - *Purdue University Earth, Atmospheric, and Planetary Science Departmental Travel Grant*
    - *Purdue Graduate Student Government Student Travel Grant*
12. **S. E. Ackiss** and James J. Wray (2014). "Occurrences of Possible Hydrated Sulfates in the Southern High Latitude of Mars." Eighth International Conference on Mars. Abstract 1040. (Poster)
11. **S. E. Ackiss**, K. D. Seelos, and D. L. Buczkowski (2014). "Mineralogic Mapping of Huygens Crater, Mars: A Transect of the Highlands Crust and Hellas Basin Rim." Eighth International Conference on Mars. Abstract 1038. (Poster)
10. **S. E. Ackiss**, D. L. Buczkowski, C. Ernst, J. McBeck, S. Edrich, and K. D. Seelos (2014). "Knob Heights within the Circum-Caloris Geologic Units on Mercury: Interpretations of the Geologic History of the Region." Lunar and Planetary Science Conference 45. Abstract 2328. (Poster)
9. **S. E. Ackiss**, K. D. Seelos, and D. L. Buczkowski (2013). "Mineralogic Mapping of Huygens Crater, Mars: A Transect of the Highlands Crust and Hellas Basin Rim." Geological Society of America Annual Meeting. Abstract 233415. (Talk)
    - *Geological Society of America's Northeastern Section Student Travel Grant*
    - *Completed the Sequence Stratigraphy for Graduate Students short course (1.6 CEU)*
    - *Attended the Early Career Workshop on Writing Scholarly Papers*
8. **S. E. Ackiss**, K. D. Seelos, and D. L. Buczkowski (2013). "Mineralogic Mapping of Huygens Crater, Mars: A Transect of the Highlands Crust and Hellas Basin Rim." Large Meteorite Impacts and Planetary Evolution V. Abstract 3095. (Poster)
    - *Barringer Travel Grant*
7. **S. E. Ackiss**, K. D. Seelos, and D. L. Buczkowski (2013). "Mineralogic Mapping of Huygens Crater, Mars." Annual Planetary Geologic Mappers Meeting. (Talk)

6. **S. E. Ackiss** and James Wray (2012). "Hydrated sulfates in the southern high latitude of Mars." American Geophysical Union 2012 Fall Meeting. Abstract ID P11E-1860. (Poster)
   - *American Geophysical Union's Fall Meeting Student Travel Grant*
   - *Georgia Institute of Technology's Presidential Undergraduate Research Travel Award*
5. **S. Ackiss** and James Wray (2012). "Hydrated sulfates in the southern high latitude of Mars." Astrobiology Science Conference. Abstract 4481. (Poster)
4. **S. Ackiss** and James Wray (2012). "Hydrated sulfates in the southern high latitude of Mars." Georgia Institute of Technology, Undergraduate Research Opportunities Program, Spring Symposium 7. (Talk)
3. **S. Ackiss** and James Wray (2012). "Hydrated sulfates in the southern high latitude of Mars." Atlantic Coast Conference (ACC) Meeting of the Minds 7. (Poster)
   - *Chosen as 1 of 7 Georgia Institute of Technology undergraduate students to present research*
2. **S. E. Ackiss** and J. J. Wray (2012). "Hydrated sulfates in the southern high latitudes of Mars." Lunar and Planetary Science Conference 43. Abstract 2434. (Poster)
1. **S. E. Ackiss** and J. J. Wray (2012). "Hydrated sulfates in the southern high latitude of Mars." Undergraduate Planetary Science Research Conference at the Lunar and Planetary Science Conference. Abstract 1009. (Poster)
   - *NASA Science Mission Directorate (SMD) Year of the Solar System (YSS) Undergraduate Student Travel Grant*